TECHNISCHE UNIVERSITÄT MÜNCHEN

MAX-PLANCK-INSTITUT FÜR ASTROPHYSIK

Towards modelling ultracool dwarfs

Laura Porter

Vollständiger Abdruck der von der Fakultät für Physik der Technischen Universität München zur Erlangung des akademischen Grades eines

Doktors der Naturwissenschaften

genehmigten Dissertation.

Vorsitzender: Univ-Prof. Dr. L. Oberauer
Prüfer der Dissertation:
1. Priv-Doz. Dr. E. Müller
2. Univ-Prof. Dr. B. Garbrecht

Die Dissertation wurde am 27.06.2014 bei der Technischen Universität München eingereicht und durch die Fakultät für Physik am 01.08.2014 angenommen.

Abstract

Towards modelling ultracool dwarfs

Numerical modelling of stellar atmospheres enables the complex coupling of thermodynamics, atomic physics and radiative transfer to be probed in order to disentangle the underlying atmospheric structure, chemical composition, atmospheric motion and more. In particular, 3D radiative hydrodynamic simulations have been extremely successful in reproducing observations, in particular for the Sun. The Sun has a convective envelope that joins to the radiative atmosphere. Recent modelling efforts have shown that the inherent inhomogeneity in the convection zone strongly influences both the atmospheric structure and the emergent spectra, even altering the derived chemical composition. Stars cooler than the Sun have a similar structure and therefore inhomogeneity is expected to play a significant role here too. This work explores a sequence of cooler dwarf stars using a 3D radiative hydrodynamic code to study the mixing mechanism, energy transport, atmospheric structure and spectra of these stars. I show that the often employed mixing-length parameterisation for hydrostatic models is inadequate and that convection plays a more prominent role in spectral-line forming layers than was expected. I study the inhomogeneous surface properties, which evolve along the sequence, and develop statistical results that relate the simulation inhomogeneity to observations.

The chemical species present in stellar atmospheres are governed by their effective temperatures. Hot stars are characterised by ionised species, while the atmospheres are increasingly neutral for cooler stars. The coolest stars are characterised by molecule formation, such as metal oxides, water and methane. Molecules possess additional degrees of freedom, presenting greater opportunity for photon absorption. As a result, molecules have large opacities. Thus, the formation of molecules presents a critical new regime in stellar atmospheres, for modelling which a detailed equation-of-state and opacity suite are required. I present the results of a comparison of two such equations-of-state and opacity suites, and the implementation of improved physical data for the modelling of cooler objects. This will allow the detailed modelling of still cooler objects in future.

Across the substellar boundary, molecules grow and condense to form dust, another new regime for model atmospheres. Dust formation is strongly governed by the nucleation phase and the atmospheric mixing present. I present here the first model of dust in stellar atmospheres to simultaneously resolve the full dust cycle and the physical mixing mechanism. This is a crucial step in modelling the transition from star to brown dwarf to planet and remains an outstanding problem in this field.

Hin zu einer Modellierung ultra-kühler Zwergsterne

Numerische Modelle von Sternatmosphären machen es möglich, die komplexen Zusammenhänge von Thermodynamik, Atomphysik und Strahlungstransport zu untersuchen. Dies dient dem Verständnis der zugrundeliegenden Atmosphärenstruktur, chemischer Zusammensetzung, Atmosphärendynamik und anderer Eigenschaften des Sterns. Dreidimensionale Strahlungs-Hydrodynamik Simulationen im Besonderen spiegeln die beobachtbaren Eigenschaften mit grossem Erfolg wieder. Dies gilt speziell für die Sonne. Die Sonne besitzt eine konvektive Hülle, die sich an die strahlungsdominierte Atmosphäre anfügt. Modelluntersuchungen in jüngster Zeit haben gezeigt, dass die der Konvektionszone innewohnende Inhomogenität einen starken Einfluss auf die Struktur der Atmosphäre sowie die beobachtbaren Spektren hat. Dies kann sogar zu einer Veränderung der chemischen Zusammensätzung führen, die aus den theoretischen Modellen abgeleitet wird. Sterne mit niedrigen Temperaturen als die Sonne besitzen eine ähnliche Atmosphärenstruktur. Daher sollte die Inhomogenität auch in diesen Fällen eine significante Rolle spielen.

In dieser Arbeit untersuche ich eine Reihe kühler Zwergsterne mit Hilfe einer dreidimensionalen Strahlungs-Hydrodynamik Software. Das Ziel ist die Untersuchung der Mischungsmechanismen, Energietransport, Atmosphärenstruktur und Spektren dieser Sterne. Ich zeige, dass die häufig benutzte Parametrisierung für die Mischungsweglänge in hydrodynamischen Modellen unzulänglich ist und dass der Einfluss der Konvektion auf die Sternschichten in denen die Spektrallinien gebildet werden grösser ist als erwartet. Ferner untersuche ich die Eigenschaften der inhomogenen Oberfläche und deren Entwicklung entlang der Reihe von Zwergsternen. Mit Hilfe von statistischen Untersuchungen gelingt es mir, die Inhomogenitäten der Simulation den beobachteten Ergebnissen anzupassen.

Die Arten von chemischen Spezies, die in Sternatmosphären auftreten können, werden durch die effektive Temperatur dieser Sterne bestimmt. Heisse Sterne sind durch ionisierte Spezies gekennzeichnet, während die Atmosphären von kühleren Sterne zunehmend neutraler sind. Die kühlsten Sterne sind durch die Bildung von Molekülen, wie Metalloxide, Wasser oder Methan, gekennzeichnet. Moleküle besitzen zusätzliche Freiheitsgrade und damit mehr Möglichkeiten ein Photon zu absorbieren. Folglich haben Moleküle höhere Opazitäten. Die Molekülbildung ist damit ein neuer, kritischer Zustand der Sternatmosphäre dessen theoretische Beschreibung eine angepasste Zustandgleichung sowie detaillierte Opazitäten erfordert. In dieser Arbeit präsentiere ich die Ergebnisse eines Vergleiches zweier solcher Zustandsgleichungen und Opazitäten sowie die Implementierung von verbesserten physikalischen Werten für die Modellierung von kühlen Objekten. Dies bereitet den Weg für eine zukünftige detaillierte Modellierung von noch kühleren Objekten.

ber die Grenze zu substellaren Objekten hinweg finden Prozesse statt, die zum Wachstum sowie zur Kondensation von Molekülen führen, und damit letztendlich zur Bildung von Staub. Dies ist ein weiterer neuer Zustand in der Beschreibung von astrophysikalischen Atmosphären. Die Bildung von Staub hängt stark von der Keimbildung und dem Ausmass der Mischung innerhalb der Atmosphäre ab. In dieser Arbeit präsentiere ich das erste Modell für Staub in Sternatmosphären, dass gleichzeitig den vollständigen Staubzyklus und die physikalischen Mischungsmechanismen beschreibt. Dies ist ein entscheidender Schritt in der Modellierung des bergangs von Stern zu Braunem Zwerg zu Planet; eines bisher ungelösten Problems in der Beschreibung von astrophysikalischen Atmosphären.

Contents

Chapter 1

Introduction

Stars are self-gravitating balls of plasma that fuse atoms in their cores to sustain themselves against gravity. Formed by the gravitational collapse and fragmentation of a gas cloud (Jeans 1902), protostars contract until their contraction is halted and balanced by the energy release from their core fusion - thus forming a star on the 'main-sequence'. The main-sequence describes the period when a star steadily burns hydrogen in its core to balance gravity and usefully, during this phase in its evolution, the star remains stationary on the effective temperature and luminosity plane - or Hertzsprung-Russell diagram.

The Hertzsprung-Russell diagram shows the luminosity of a star, or its absolute magnitude, versus the effective temperature or equivalently spectral type, see Figure 1.1. The main-sequence forms a strip from hot, luminous stars, in the upper left-hand region of the diagram, to cool, dim stars, at the lower right-hand side. The overall structure, lifetime, final fate and spectral appearance of these stars forms a continuum along this sequence, with hot stars (above ~8,000K) having convective cores and radiative envelopes and atmospheres, while cool stars have radiative cores and convective envelopes that extend to their surfaces.

Main-sequence stars have no solid surface, and therefore the star and its atmosphere are ill-defined, formally consisting of 'the transition from the stellar interior to the interstellar medium' (Gray 2005). More practically it is often taken to mean the photosphere [1]; that is where the atmosphere becomes transparent to radiation. Passing through the star, photons are scattered or absorbed and re-emitted, performing a 'random walk', before finally being emitted into free space. Photons escaping the star carry the distinctive 'fingerprint' of the atmospheric conditions where they were last emitted or scattered, making their spectra rich in physical information about the stellar surface layers.

Stellar spectra are the primary resource available for studying the atmospheric structure and composition of stars [2](Gray 2005). The spectra result from the coupling of thermodynamics in gases, the gas motion, radiative transfer and atomic physics. The coupling can be complex and highly non-linear. As a result, it is not possible, in general, to invert the spectra directly to derive the physical structure, instead forward modelling of the system is required to produce synthetic spectra, which may then be compared with the observed spectra (e.g. Stein & Nordlund 1998).

[1] Typically in the optical as the surface of last emission or scattering can be vary significantly in geometrical depth at different wavelengths.

[2] Asteroseismology can probe some suitable stars through the monitoring of oscillations in their atmospheres.

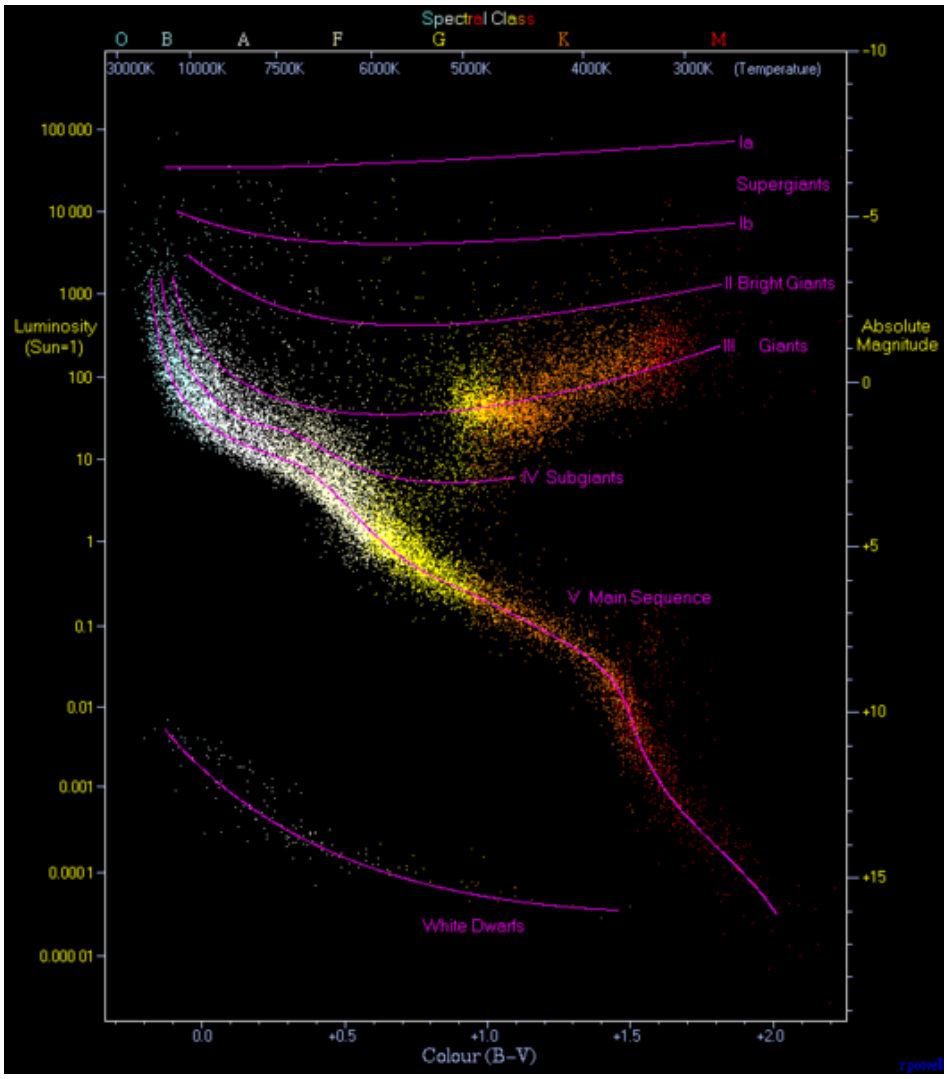

Figure 1.1: A Hertzsprung-Russell diagram showing the variety of variables that may be plotted. The upper x-axis shows spectral class from O to M, while immediately underneath is the equivalent effective temperatures. It should be noted that the temperature scale is reversed and logarithmically spaced. The lower x-axis shows the equivalent 'Colour' index. Colour or colour index is defined as the difference in apparent magnitude of the star in two different spectral bands, in this case B-V - the difference between the blue filter, B, and the visual band filter, V. The left-hand y-axis shows the luminosity of the star on a logarithmic scale normalised to the solar luminosity, while the right-hand y-axis shows the equivalent absolute magnitude. Absolute magnitude is the apparent magnitude the object would appear to have at the standard distance of 10 parsecs (32.6 light-years) and is related to the luminosity of the star. The large strip across the diagram that encompasses the majority of the stars is the main-sequence. A star will appear on the main-sequence when it begins stable core nuclear burning and remain there without moving position on this diagram for most of its lifetime, until the hydrogen fuel in the core has been exhausted. The position along the main-sequence is primarily determined by the mass of the star, with high-mass stars to the upper left and low-mass stars to the lower right. Also marked are giants and supergiants, which represent a later evolutionary epoch in the lifetime of the star, when it exhausts its core hydrogen fuel. Finally, white dwarfs in the lower left-hand region of the diagram represent the final phase for many stars, essentially a burnt out, slowly cooling ember. Figure courtesy of http://upload.wikimedia.org/wikipedia/commons/6/6b/HRDiagram.png

Spectral classes are assigned based on the presence, prominence and appearance of spectral features. The sequence may be understood in terms of atomic physics and temperature. Hot stars are characterised by ionised helium lines, progressing to neutral helium becoming more prominent towards cooler effective temperatures. Cool stars are characterised by the weakening of hydrogen lines, while ionised metal wax then wane towards cooler effective temperatures where neutral metals are dominant and molecular lines begin to become important.

This may be understood in terms of atomic nuclei seeking to minimise their internal energy. When the local ambient conditions become cool enough, atomic nuclei capture electrons to form stable bonds. Helium becomes neutral before the metals as, once captured, its electron are more tightly bound than in metals. Thermal energy equates to energetic collisions in the atmosphere meaning that higher temperatures inhibit the formation of neutral atoms. At cooler temperatures, the atoms can also form bonds to make stable molecules and eventually at the coolest effective temperatures even these molecules can bond to form condensates or dust.

Stellar modelling attempts to infer the atmospheric structure and composition by constructing a physical model with parameters tuned to reproduce certain spectral features (e.g. Gustafsson et al. 1975; Hauschildt et al. 1999; Kurucz 1979). Early modelling attempts relied upon strong assumptions, such as frequency independent or 'Gray' radiative transfer (e.g. Milne 1921), but these were quickly found to be seriously flawed (e.g. Chandrasekhar 1935; Böhm 1954) and more detailed models with better radiative transfer were constructed. Currently there exist a number of competing 1D numerical programs that model stellar atmospheres e.g. MARCS (Gustafsson et al. 1975), PHOENIX (Hauschildt et al. 1999), ATLAS (Kurucz 1979), and are constantly extended and refined to reflect advances in contributing fields and model a larger parameter space.

1.1 Cool stars

Cool stars constitute the majority of the stars in the Universe (e.g. Bastian et al. 2010). With effective temperatures below $\sim 8 \cdot 10^3 K$, the broad structure of a cool star on the main-sequence is a hot, dense core, where hydrogen burning releases energy that is transported by radiation. Further out, the increasing opacity due to hydrogen recombination means that convection overtakes radiation as the dominant energy transport mechanism in the stellar envelope. Finally, the photospheres of these stars are where the atmosphere becomes transparent to radiation and thus radiation reasserts itself as the dominant energy transport mode (Gray 2005). As a result of this structure, the photosphere is a radiative zone directly on top of a convective envelope, meaning that the sub-surface layers will be inhomogeneous as a result of the convective cells, therefore this inhomogeneity would be expected to influence the resultant spectra (e.g. Stein & Nordlund 1998).

1.1.1 Solar-like stars

Sun-like stars cover the spectral range of approximately F-K spectral types. These stars represent the lowermost portion of the initial mass function; a power law describing the initial mass of stars produced by the fragmentation of a gas cloud. While spherically symmetric (1-dimensional) modelling of stellar atmospheres has its successes, solar-like stellar modelling requires more sophisticated models, as the convective envelope immediately below the photosphere strongly influences the resultant

spectra. 3-dimensional models include the dynamics of the gas motion and inhomogeneities that result from the convective cell pattern (e.g. Freytag et al. 2002; Vögler et al. 2005; Muthsam et al. 2010; Stein & Nordlund 1998; Gudiksen et al. 2011). Multi-dimensional models require significantly more computational effort than spherically symmetric ones, but this increasing complexity is rewarded by a greater understanding of the contributing physical processes and improved correspondence between model predictions and observations (e.g. Ramírez et al. 2009; Collet et al. 2007; Chiavassa et al. 2012).

For example, a convective surface pattern leads to net wavelength shifts of spectral lines compared to their laboratory measured wavelengths and gives rise to asymmetries in the profiles that are measurable in high-precision spectral studies. The solar model is particularly well-studied, as the proximity of the Sun allows high-precision spectroscopy and even resolved limb-darkening [3] measurements. Results show that 3D models outperform all the 1D models on the limb-darkening observations (Pereira et al. 2009), while differences in spectral line profiles have led to a downward revision of the chemical composition of the Sun (e.g. Asplund et al. 2009).

Figure 1.2 shows the results of a solar simulation in 3 dimensions. Panel a) displays the emergent intensity intensity from the surface of the simulation, where the convective structure of hot, bright convective cells entrained by cool, dark intergranular lanes can be seen clearly. Panel b) show the structure of the atmosphere in terms of density and temperature; the black dots represent individual simulation datapoints, while the red line shows the mean structure. Again, evidence of the inhomogeneity of the atmosphere is apparent and this justifies the need to investigate the atmosphere multi-dimensionally.

1.2 Ultracool dwarfs

Ultracool dwarfs span the class of objects from low-mass stars through brown dwarfs to giant planets (e.g. Kirkpatrick 2005). Dwarf stars of spectral type M define the low-mass end of the main-sequence. Structurally, this spectral class covers objects with a sun-like radiative core and convective envelope through to cooler objects that are fully convective (e.g. Basri 2000). Spectrally, across the M-dwarf class the importance of molecules becomes increasingly dominant. First discovered in 1996 (Rebolo et al. 1995), brown dwarfs are failed stars as they are insufficiently massive to begin stable hydrogen burning in their core (e.g. Chabrier et al. 2005), although deuterium and lithium fusion may occur. Formed from the collapse and fragmentation of a gas cloud, brown dwarfs form a quasi-main-sequence at the cool, dim end of the Hertzsprung-Russell diagram, and their discovery led to the definition of two new spectral classes, L and T (e.g. Kirkpatrick 2005). In these objects dust and molecules play a dominant role in their spectra. Giant planets, outside our own solar-system, were discovered at around the same time (Mayor & Queloz 1995) and differ from stars and brown dwarfs in that they form from the agglomeration of particles and gas in a proto-planetary disk (e.g. Wuchterl 2004; Blum & Wurm 2008). The largest extra-solar giant planets overlap in mass with brown dwarfs,

[3] Limb-darkening is an effect whereby the intensity of the star appears brightest in the stellar centre and appears to decrease towards the edge. It is the result of the visible surface (optical depth unity) towards the limb being reached in cooler, less dense layers than for the centre.

[4] Metallicity is the fraction of the star that is composed of elements heavier than Helium. It is often expressed as the logarithmic difference between the iron abundance of the considered composition and the solar composition, e.g. the solar metallicity would be expressed as [Fe/H]=0.0 and is computed $[Fe/H] = log_{10}N_{Fe}/N_H - log_{10}(N_{Fe}/N_H)_{\odot}$.

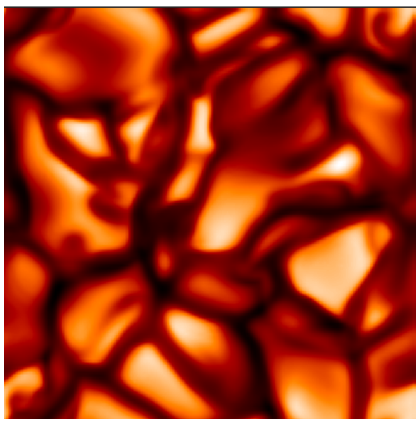

(a) Emergent intensity from the surface of the solar model.

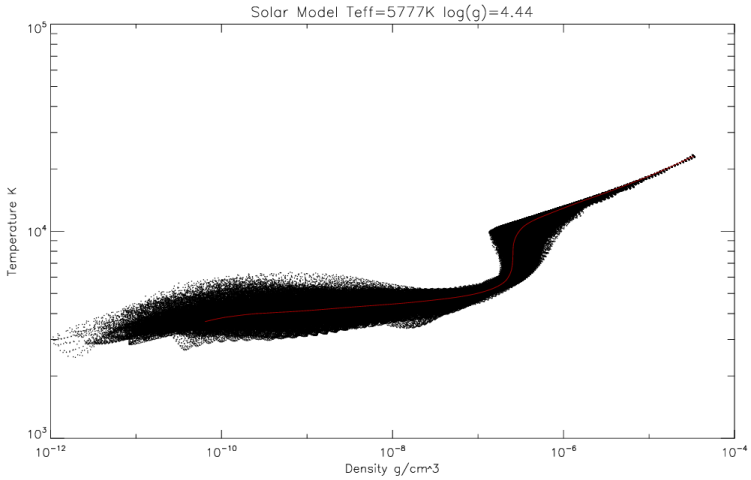

(b) The solar model temperature structure

Figure 1.2: Results of the solar model (T_{eff} = 5777K, log(g)=4.44, solar metallicity [4]). Panel a) shows the emergent intensity of the model, with lighter colours corresponding to hotter temperatures. Panel b) shows the atmospheric structure as a function of density and temperature; the black dots represent datapoints in the solar model and the red line is the mean atmospheric structure for comparison. Figure from results of a solar test calculation that may be compared with Asplund (2005) Figures 1 and 4.

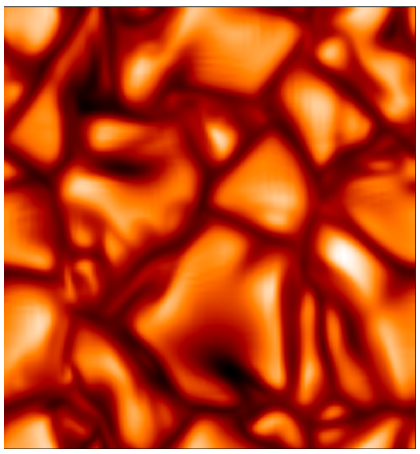

(a) Emergent intensity from the surface of an M dwarf model.

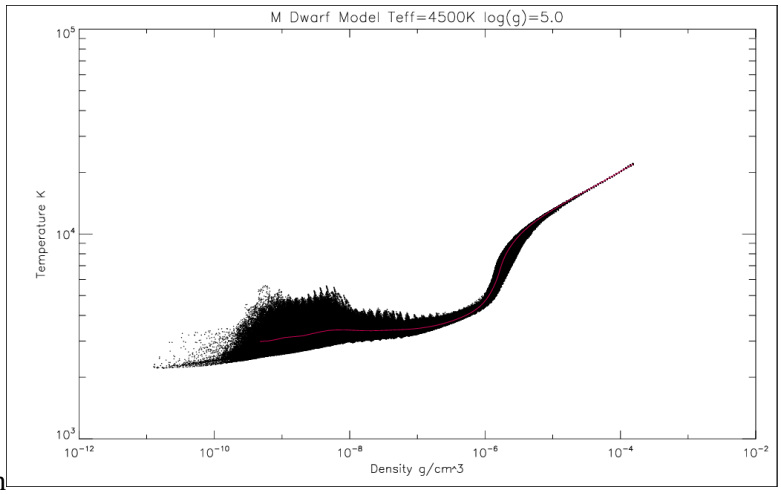

(b) An M dwarf model temperature structure.

Figure 1.3: Results of a hot M dwarf model (T_{eff} = 4500K, log(g)=5.0, solar metallicity). Panel a) shows the emergent intensity of the model, with lighter colours corresponding to hotter temperatures. Panel b) shows the atmospheric structure as a function of density and temperature; the black dots represent datapoints in the M dwarf model and the red line is the mean atmospheric structure for comparison. Figure composed of data from the first model in Table 3.1 and shows figures equivalent to Asplund (2005) Figures 1 and 4.

meaning they too can fuse deuterium and lithium in their cores, leading to difficulty in unambiguous classification (e.g. Béjar et al. 2001; Whitworth & Stamatellos 2006; Johnson et al. 2009). As a result, the umbrella term ultracool dwarf is useful for describing the continuum of objects from star to planet and the evolution of molecular and particulate species in their atmospheres.

Figure 1.3 shows the analogous plots as in Figure 1.2, but for a hot M dwarf model. In the emergent surface intensity in panel a), the inhomogeneous nature of the convective cells is again apparent. The M dwarf atmospheric structure shown in panel b) also displays a high degree of inhomogeneity, most notably in the outermost layers. As this inhomogeneity has been shown to be important in hotter objects, it is reasonable to suppose that it will continue to influence the modelling strongly at cooler effective temperatures and therefore it is necessary to employ more sophisticated 3D models in order to probe the physics in these atmospheres.

1.2.1 L dwarfs

L dwarfs are characterised spectroscopically by the weakening of metal oxide and metal hydride bands that have been strong in the M dwarfs (Basri 2000). The evolution of the L dwarfs spectral type is punctuated by the formation of methane and water in place of carbon monoxide. These spectral changes reflect the formation and thickening of the silicate dust clouds as metal oxide formation is suppressed by the atoms being sequestered into dust (Allard & Hauschildt 1995), while the change of the dominant carbon bearing molecule reflects the increasing gas pressure (e.g. Kirkpatrick 2005).

1.2.2 T dwarfs

T dwarf atmospheres are methane rich with little spectroscopic evidence of dust clouds(e.g. Kirkpatrick 2005) . Physically, this reflects the cooler nature of these atmospheres, where it is believed that dust clouds form, but the cloud base is below the photosphere leaving a cloud-free atmosphere (Burgasser et al. 2002b; Tsuji et al. 1996a).

1.2.3 The L-T Transition

While the hot (early) L dwarfs and the cool (late) T dwarfs are fairly well understood, the transition between the two has yet to be modelled satisfactorily. It is likely to be either that the dust formation and growth becomes suddenly more efficient or that the cloud base develops holes whose areal filling factor rapidly increases until the atmosphere is clear (e.g. Burgasser et al. 2002b). The former explanation has no clear physical mechanism to justify a sudden increase in dust growth efficiency, while the latter explanation contradicts the expected thickening of dust clouds as the temperature drops permitting more stable dust species in the atmosphere. This remains one of the key outstanding problems in stellar atmospheres, impeding progress in understanding the complex atmospheres of ultracool dwarfs and planets.

Figure 1.4 shows an artist's impression of how ultracool dwarfs might look in the visible. On the far left the Sun is shown for a comparison of size, then there is the M dwarf that is the hottest and

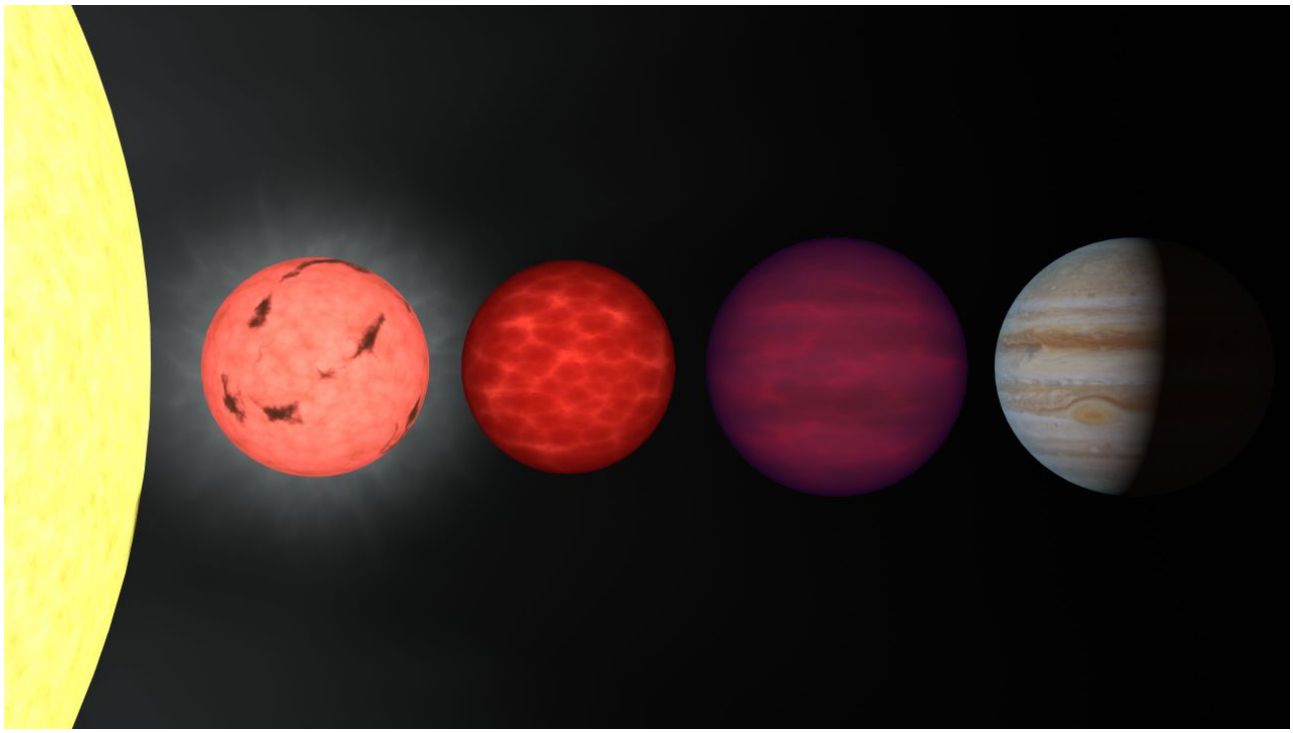

Figure 1.4: Image courtesy of Rob Hurt is an artist's impression showing these objects in the visible: the M and L dwarfs are red, while the T dwarf is dimly magenta, due to absorption by sodium and potassium atoms in the green. The sun (far left) is shown for a comparison of scale, then an M dwarf, an L dwarf, a T dwarf and Jupiter.

brightest of the ultracool dwarfs, has convective surface and is most likely to have some magnetic activity of these objects. Next, comes the cloudy L dwarf that is cooler, making magnetic activity less likely. The T dwarf shows a distinctly purplish hue due to the increasing importance of methane in the atmosphere, and finally Jupiter is shown for comparison.

1.3 Statement of purpose

This project aims to extend the multi-dimensional modelling of stellar atmospheres to cooler effective temperatures in order to better understand the effects of inhomogeneity and dust formation in their atmospheres. Chapter 2 describes the surface convection hydrodynamics and the numerical model that forms the basis for the subsequent modelling in this work. Chapter 3 describes the results of a sequence of the first 3D models at such low effective temperatures, including discussion of the inhomogeneity, structure and synthetic spectra of these objects. Chapter 4 details the requirement for, and implementation of, a new equation-of-state and opacity suite in order to make further progress in modelling the coolest dwarfs. Chapter 5 summarises and critically examines the current state-of-the-art in modelling of dust formation in the atmospheres of ultracool dwarfs. Chapter 6 presents the first model to simultaneously follow the full dust formation cycle (of molecular formation, dust nucleation, growth, settling, evaporation and element replenishment) and resolve the physical mixing mechanism, convection. Chapter 7 presents some statistical results that connect the simulation inhomogeneity and resultant micro-variability with the observable stellar variability and discusses the applications and

limitations of this. Chapter 8 summaries and draws together the conclusions of this body of work. Chapter 9 discusses both the limitations of this work and explores potentially fruitful avenues for future work.

Chapter 2

Convection

Convection is an energy transport mechanism, available only in fluids, that is extremely efficient. It constitutes the dominant energy transfer mechanism and major mode of mass transfer in the envelopes of cool stars. In these objects the photosphere defines the transition between the convective envelope and radiative outer atmosphere. Convection manifests itself horizontally as a characteristic pattern of hot, bright upflows and cool, darker downflows, see Figure 2.1.

The Schwarzschild criterion, $\nabla > \nabla_S$, based on fluid perturbation analysis, describes whether a medium is stable against convection. A stratification is unstable if a perturbed gas parcel continues to rise buoyantly in the atmosphere. Such a parcel, that shares the local conditions (ρ, P, T) requires a greater adiabatic expansion, $-d\rho_S$, than the density change in that medium over the same path, $-d\rho$.

$$\rho - d\rho_S < \rho - d\rho_{med} \qquad \leftrightarrow \qquad d\rho_S > d\rho \tag{2.1}$$

This may be re-expressed as a critical temperature-pressure gradient.

$$d\rho = \left(\frac{\partial \rho}{\partial T}\right)_P dT + \left(\frac{\partial \rho}{\partial P}\right)_T dP, \qquad d\rho = \left(\frac{\partial \rho}{\partial P}\right)_S dP \tag{2.2}$$

$$\Rightarrow \quad \left(\frac{\partial \rho}{\partial P}\right)_S dP > \left(\frac{\partial \rho}{\partial T}\right)_P dT + \left(\frac{\partial \rho}{\partial P}\right)_T dP \tag{2.3}$$

$$\Rightarrow \quad \left(\frac{\partial T}{\partial P}\right) > \left(\frac{\partial T}{\partial P}\right)_S \tag{2.4}$$

$$\tag{2.5}$$

Customarily this is expressed as a log-log gradient which forms the Schwarzschild criterion

$$\left(\frac{\partial \log T}{\partial \log P}\right) > \left(\frac{\partial \log T}{\partial \log P}\right)_S \tag{2.6}$$

$$\nabla \equiv \frac{\partial \log T}{\partial \log P} > \nabla_S \tag{2.7}$$

Physically super-adiabatic gas, gas for which the temperature-pressure gradient is steeper than the adiabatic gradient, experiences continuous buoyancy and rises until it encounters a sub-adiabatic

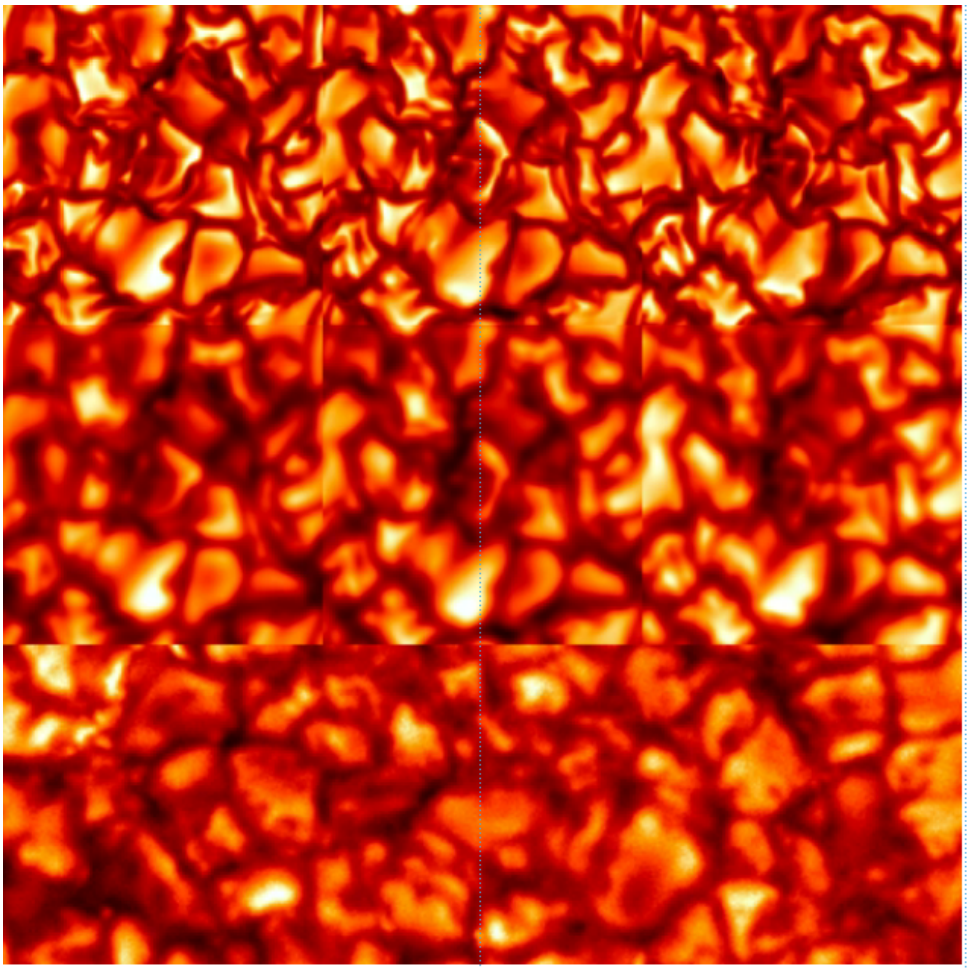

Figure 2.1: The top panel is a mosaic of three snapshots taken from a simulation of the solar atmosphere at one-minute intervals. The middle panel is the simulation mosaic filtered with the point-spread function of the telescope and Earth's atmosphere. The bottom panel is an actual observation from a Swedish solar telescope. Courtesy of Stein 2010

(shallow gradient) region, where the buoyancy ceases and the gas parcel is pulled back by gravity. In cool stars, the sub-surface temperature gradient tends to be fairly close to the adiabatic gradient as the gas flow is dominated by adiabatically expanding upflows, but cool dense downflowing plumes of gas create an ambient medium with a slightly steeper gradient.

Super-adiabatic gas experiences buoyancy and rises until it encounters a sub-adiabatic region, where the fluid parcel is then pulled back by gravity (Stein & Nordlund 1998). Above the surface, with the transition defined by the photosphere, the stratification is sub-adiabatic as the gradient here is set by radiative heating, resulting in a much shallower gradient. The transition from optically thick to the optically thin regime (and convectively to radiatively dominated energy transport) is crucial for understanding both the driving of vigorous surface convection and interpreting the radiation we observe from the star, as most of it originates in these layers. Photons escaping from the optical surface remove entropy, leaving the cooler, denser gas to gather in plumes that sink into the lower atmosphere and provide kinetic energy to drive the upflows (Stein & Nordlund 1998).

The key to modelling this physical problem is to correctly follow the behaviour of the plasma, its

motion under gravity and interaction with the radiation field, and this requires modelling the coupled equations of radiative-hydrodynamics.

2.1 Hydrodynamics

Hydrodynamics deals with the physics of fluid motion. Consisting of highly compressible gas, convective stellar atmospheres are well described by the compressible hydrodynamic equations as the plasma speeds encountered in the medium are typically far from relativistic. The stationary nature of the photosphere means that these equations are most conveniently solved on a stationary Eulerian grid, in contrast to outflows like stellar winds where it may be more appropriate to consider a co-moving frame of reference. The hydrodynamical equations consist of a set of five relations describing the macroscopic properties of the system. The first equation is the continuity equation which expresses the conservation of mass:

$$\frac{\partial \rho}{\partial t} + \nabla \cdot \rho \mathbf{u} = 0 \tag{2.8}$$

where ρ is the total gas density, $\mathbf{u}$ is the gas velocity while the gas momentum density $\rho\mathbf{u}$ is equivalent to the local mass flux. The equation of motion governs the dynamics of the system; this equation is normally solved for each of the components of the gas velocity vector (or equivalently momentum vector). It takes the form

$$\frac{\partial \rho \mathbf{u}}{\partial t} + \nabla \cdot (\rho \mathbf{u}\mathbf{u}) + \nabla P = -\rho g + \nabla \cdot \tau_{visc} \tag{2.9}$$

where P is the total gas pressure (as radiation pressure contributes negligibly, see Figure 2.2), τ_{visc} is the viscosity tensor and $\mathbf{g}$ is the gravitational acceleration. In this form the equation of motion is also called the Navier-Stokes equation and expresses the conservation of momentum. The inertial term $\rho\mathbf{u}\mathbf{u}$ provides kinetic energy flux and and is responsible for complex turbulent behaviour of gas with disparate inertial and viscous length scales. Plasma viscosity in stellar atmospheres is small and could be neglected if numerical stability didn't necessitate smoothing of the hydrodynamic flow for large gradients. Gravitational acceleration is considered as constant across the domain, as the atmospheres of dwarf stars are very thin compared to the extent of the star, $r_{atmosphere} << R_*$.

The final equation is the thermodynamic equation which expresses the conservation of internal energy of the gas:

$$\frac{\partial e}{\partial t} = -\nabla \cdot (e\mathbf{u}) - P(\nabla \cdot \mathbf{u}) + + Q_{rad} + Q_{visc} \tag{2.10}$$

where e is the internal energy per unit volume. The internal energy flux is $e\mathbf{u}$ while $P(\nabla \cdot \mathbf{u})$ is the rate of change of internal energy due to compression and expansion work, Q_{rad} is a source term that accounts for the radiative heating or cooling of the gas and Q_{visc} corrects the energy budget for the viscous dissipation of kinetic energy. The Navier-Stokes equation and conservation of energy equation require closing from an equation-of-state that relates the density, temperature and pressure to one another. The energy equation further requires the radiative heating rates, Q_{rad}, that in turn require the solution of the equation of radiative transfer. Viscous energy dissipation in a real atmosphere is very small and does not contribute significantly.

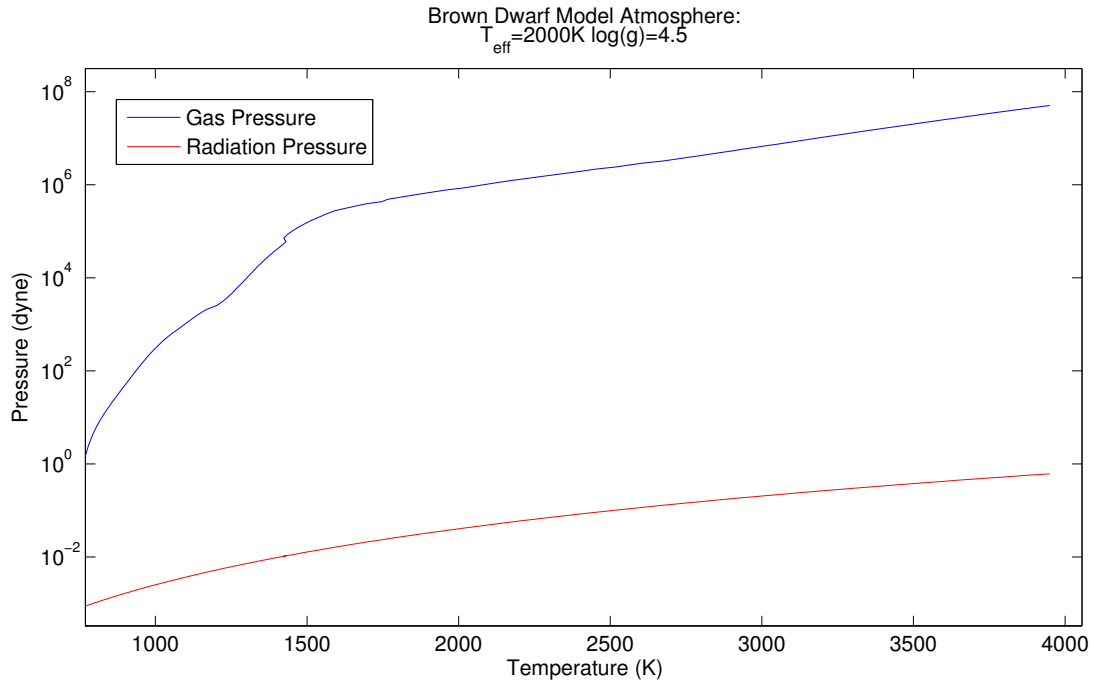

Figure 2.2: Comparison of gas and radiation pressure for a brown dwarf model atmosphere at T_{eff}=2000K, log(g)=4.5 and solar composition. The x-axis shows the local gas temperature at different heights throughout the atmosphere. Note that $P_{gas} >> P_{rad}$ throughout the structure, justifying the neglect of the contribution of the radiation field to the conservation of momentum equation.

2.1.1 Equation of State

An equation-of-state (EOS) is a thermodynamic relation that describes the state of matter under particular physical conditions. An EOS is necessary to close, or help close, the system of hydrodynamic equations. It enters explicitly through the pressure, P, but is also required to provide other thermodynamic data, the ionisation and molecular equilibria, and the level populations.

A truly realistic EOS must account for all permissible micro-physical states of the plasma, reflecting the plasma composition, the radiation field and time-dependent effects on a variety of timescales. Such a model is orders of magnitude beyond current computational capabilities. Equally the simple ideal gas EOS, $PV = NkT$, while perhaps applicable to hotter objects and supernovae, is too simplistic for cooler stars. Solar plasma is only moderately non-ideal, although the abundance of detailed observations makes this more significant, but as you move to cooler objects like low-mass stars, brown dwarfs and white dwarfs the plasma coupling is stronger necessitating a more sophisticated EOS (Cauble et al. 1998).

Beyond the ideal gas law, it is ionisation and molecular formation that lead to strong departures from the ideal gas law. Molecular formation and dust condensation will be particularly significant for ultracool dwarfs. Atomic and molecular electrons populate excited states, while molecules have additional rotational and vibrational degrees of freedom. Including internal energy states is essential as in solar simulations (Nordlund et al. 2009) the convective energy flux near the surface is primarily stored in internal modes like ionisation, rather than thermal motion. An ideal gas with no internal degrees of freedom would have a smaller heat capacity requiring higher flow speeds to reproduce the

solar luminosity. Simplifications based on composition are also possible as hydrogen and helium are naturally of principal interest, due to their abundance, while heavier elements like carbon, nitrogen and oxygen are significant electron donors, affecting the ionisation, and form the abundant molecular species at low temperatures, but minority species may well be of little significance. The exact mix of ions, atoms, molecules and condensates that should be included depends strongly on the problem being considered.

Physically, the radiation field is coupled to the macroscopic state of the plasma, but in these objects the radiation field is not strong and local thermodynamic equilibrium can be assumed. Local thermodynamic equilibrium,(LTE), stated simply says that the distribution function is the Maxwell-Boltzmann function corresponding to thermodynamic equilibrium. In a local volume, or computational cell, the velocity distribution is (approximately) Maxwellian for the local temperature and remains close to thermodynamic equilibrium as the distribution thermalises on timescales shorter than those considered by the simulation.

This assumption drastically simplifies the EOS such that all states then depends only on a pair of macroscopic state variables. It is expedient to exploit this low dimensional parameter space to pretabulate the EOS, to reduce the required runtime of the simulations.

Solar-like simulations using this code have employed the EOS by Mihalas et al. (1988). This implementation accounts for the effects of excitation, ionisation, and dissociation of the 17 most abundant elements as well as of H2 and H2+. The Mihalas, Hummer and Däppen EOS is based on the principle of free energy minimisation (Trampedach et al. 2006) where the free energy is defined as $F = U - TS$ therefore $dU = TdS - PdV + \sum_i (u_i dN_i)$. Designed for solar-like stars it is incomplete at low temperatures and in particular is missing many key molecules at low temperature. For ultracool dwarfs molecules dominate the spectrum therefore it is essential to include them. The Astrophysical Chemical Equilibrium Solver (ACES) is a state-of-the-art equation-of-state for use in stellar atmospheres (Barman, in prep). ACES employs the method of Smith & Missen (1982) and additionally incorporates new experimental and theoretical thermodynamical data for 839 species (84 elements, 289 ions, 249 molecules, 217 condensates). Crucially, it includes all of the most important molecular species pertinent for brown dwarf atmospheres and has been well tested down to temperatures of $\simeq 100K$ (Witte 2011; Husser et al. 2013).

2.1.2 Radiative Transfer

Photon propagation has many physical regimes: in high-energy particle physics quantum mechanical corrections are appropriate, while Maxwell's equations provide an adequate description for most atomic physics applications. The propagation of radiation through stellar atmospheres is affected by absorption, emission and scattering processes. As the radiation field in these objects is only moderately intense, energy transfer through bulk emission and absorption dominates, and as such a macroscopic description using the equation of radiative transfer is appropriate. On the scale of the radiation wavelength $\lambda_{radiation}$ the state variable gradients are small meaning a particle model is suitable.

Opacity is the macroscopic material coefficient that describes the removal of photons, whether by true absorption or scattering, from the incident beam.

$$\chi_\nu = \kappa_\nu + \sigma_\nu \tag{2.11}$$

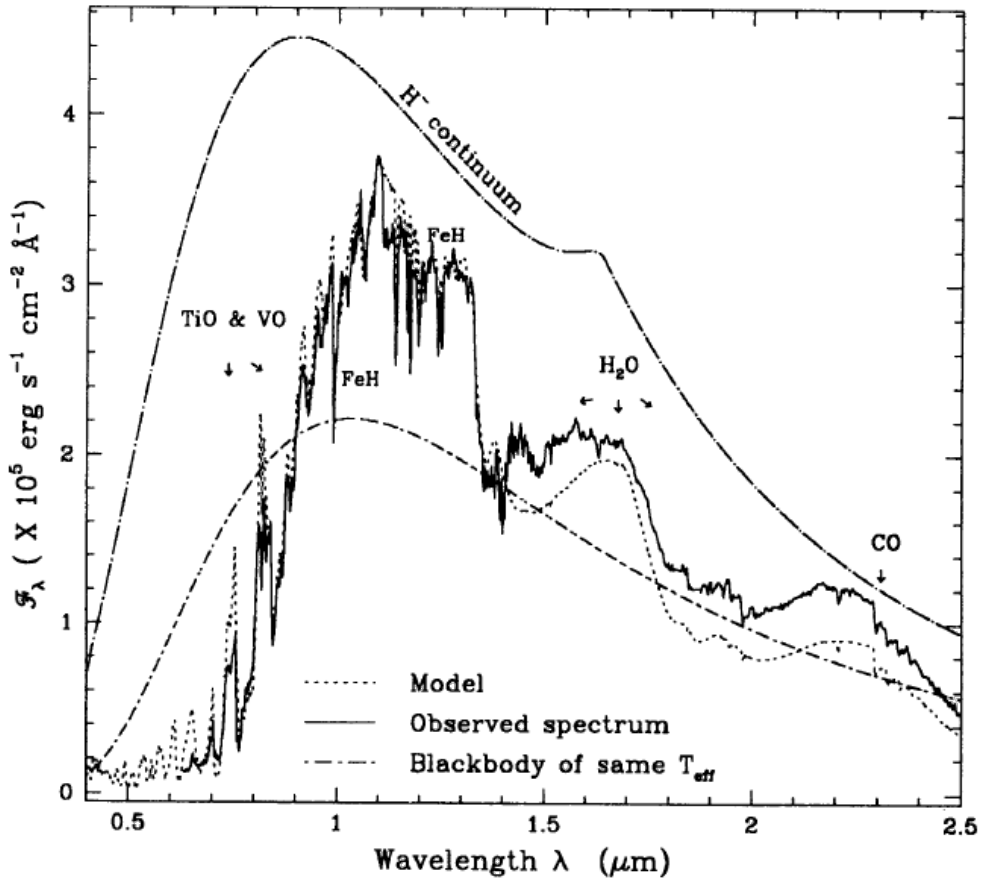

Figure 2.3: Figure from (Allard & Hauschildt 1995). The figure shows the spectrum of the metal-rich M dwarf VB 10 (solid line) (Kirkpatrick et al. 1993). The best fit model (with derived parameters $T_{eff} = 2800K$, $g = 10^5$ and assumed solar metallicity) is shown with the dashed line, while the dash-dotted (lower) line shows a blackbody model at the same temperature. Also shown is the H^- continuum only, obtained by neglecting the molecular opacities in the radiative transfer. It is evident that the spectrum is both far from blackbody and is strongly affected by the molecular opacities.

The total opacity is given by χ_ν and is composed of the absorption coefficient κ_ν and the scattering coefficient σ_ν. For convenience, opacities are often split into continuum opacity, referring to the smoothly varying weakly wavelength dependent component and line opacity which covers the sharply wavelength dependent resonances. As stars are blackbodies to first order, it is the opacity of the surface and overlying layers which governs the formation of the spectrum. For low-mass stars, the description of opacity is crucial in order to produce an accurate photospheric model. While 'Gray' atmospheres, that is a wavelength independent description of opacity, may be sufficient to model some hotter stars, such strong assumptions are deeply inappropriate for brown dwarf photospheres.

Figure 2.3 shows the spectrum of an M dwarf (solid black line). Evidently the observed spectrum deviates drastically from both the blackbody curve (dashed dotted) and the continuum curve from H^-. The discrepancy between the blackbody model and the observed spectrum is the result of opacities. Opacities in stellar modelling are typically calculated separately and tabulated in a suitable form for the solution of radiative transfer. There exist a number of groups who build and maintain databases of spectral line data. When modelling solar-like stars, this convection code has previously used data

from the MARCS opacity package (Gustafsson et al. 2008), however this database was designed for warmer stars and in order to model cooler objects I switch to the opacity package used by the PHOENIX group (Ferguson et al. 2005; Hauschildt et al. 1999) as it has more complete coverage of molecules and extends to lower temperatures.

The photosphere defines the surface where radiation rapidly supersedes convection as the dominant form of energy transport. The radiation field, therefore, plays a crucial role in the photospheric energy balance. While contributing to the energy budget, photons in cool stars have too little energy to contribute significantly to the pressure, which is dominated by gas pressure and gravity, see Figure 2.2.

The radiation field enters the RHD equations solely through the radiative heating rate per unit volume, Q_{rad}, the divergence of the frequency integrated radiative flux.

$$Q_{rad} = -\int_{\nu} \nabla \times F_{\nu} d\nu = 4\pi\rho \int_{\nu} \kappa_{\nu}(J_{\nu} - S_{\nu}) d\nu \tag{2.12}$$

The monochromatic radiative flux F_{ν} requires solving photon propagation through the atmosphere. Radiative transfer describes the beam intensity as it propagates through a medium. It is affected by emission, absorption and scattering processes. The equation of radiative transfer may be cast

$$\frac{dI_{\nu}}{ds} = j_{\nu} - \rho\chi_{\nu} I_{\nu} \tag{2.13}$$

$$= -\rho\chi_{\nu}(I_{\nu} - S_{\nu}) \tag{2.14}$$

$$= -\rho(\kappa_{\nu} + \sigma_{\nu})(I_{\nu} - S_{\nu}) \tag{2.15}$$

where the monochromatic beam intensity, I_{ν}, along path s is augmented by the photon emissivity j_{ν} and reduced by a combination of the beam intensity, the density, ρ, and the extinction coefficient χ_{ν}. The extinction coefficient accounts for radiation removed from the beam due to true absorption and scattering. It may be recast explicitly to include the contribution of true absorption via the absorption coefficient κ_{ν}, and the scattering σ_{ν}. Collet et al. (2011b) showed that the assumption of local thermodynamic equilibrium approximates well the stratification where scattering is correctly modelled provided scattering is excluded from the free-streaming mean opacities. Thus the scattering contribution to the extinction is omitted in the calculation of the opacity table. In stellar atmospheres both the photon emissivity and opacities have approximately exponential behaviour with depth in the atmosphere, therefore it is convenient to introduce the source function, S_{ν}, defined by $S_{\nu} = j_{\nu}/\chi_{\nu}$. The source function forms a material property, like the opacity κ_{ν}, which must be derived from a model. Under the assumption of LTE, the source function may be found via the Planck function, B_{ν}

In order to calculate the radiative heating rate, Q_{rad}, it is necessary to solve the equation of radiative transfer at every grid-point, in every direction at all timesteps.

$$\frac{dI_{\nu}}{ds} = -\chi_{\nu}\rho(I_{\nu} - S_{\nu}) \tag{2.16}$$

Naturally a numerical treatment of this problem is necessitated by the complex and rapidly varying nature of the opacity in these objects, composed of numerous absorption edges and millions of spectral lines from primarily iron and tens of millions of molecular lines, see Figure 4.12 later. For example, to model the solar spectrum $10^6 - 10^7$ frequency points are required to capture the detailed dependence with frequency (Vögler 2004). While solving the Equation of Radiative Transfer for this number of

points may be tolerable for 1D static models, the computational cost is prohibitive for 3D dynamic modelling. Practicability requires that the number of required solutions to the equation of radiative transfer is reduced. Two popular ways of achieving this are opacity distribution functions (ODFs) and the 'Multi-group' method. The former relies on the relevant physical properties of the radiation field being integrals over frequency and therefore should not depend sensitively on the detailed frequency structure of the opacity. The frequency spectrum is divided into frequency intervals (typically $10^2 - 10^3$ $\delta\nu_i$) and the monochromatic opacity within these intervals is replaced by a smooth distribution function. ODFs reduce the computational load by of order $\sim 10^3$. The latter approach divides the frequency spectrum into a few non-contiguous subsets ('bins') according to opacity strength and defines bin integrated quantities, allowing the equation of radiative transfer to be recast for a bin-averaged opacity, $\bar{\kappa_\nu}$. This implies that a large part of the frequency integration has been done before the ray integration takes place. Equation 2.16 need only be solved a single time for each bin resulting in a factor of $10^5 - 10^6$ in computational effort. For this reason, the multi-group method is applied in this work.

2.2 The *Stagger* Code

The equations of fully compressible (magneto-) hydrodynamics are highly non-linear and as such there exist analytical solutions for only a few very simplified scenarios. Realistic models demand a numerical approach and in recent years a number of groups have developed their own codes for this purpose, e.g. CO^{5}BOLD (Freytag et al. 2002), MURaM (Vögler et al. 2005), ANTARES (Muthsam et al. 2010), *stagger* (Stein & Nordlund 1998), BIFROST (Gudiksen et al. 2011).

A stellar atmosphere covers a large dynamic range in length scales, from the km sized flows resolved by the convection models to the viscous length scales which are many orders of magnitude smaller. It remains unfeasible to resolve all these scales simultaneously and so these numerical algorithms follow a 'large-eddy' approach, where only the largest structures are resolved, with small scale structures, approximated through sub-grid scale modelling, suppressed (Hayek 2010; Nordlund et al. 2009).

The nature of the physical problem further constrains the numerical approach as the non-linear and hyperbolic nature of the equations enables shock waves to form leading to discontinuous solutions, even from smooth initial conditions, while low viscosities can lead to turbulent flow and rarefied gas can lead to supersonic flow speeds (Nordlund 1982).

The *Stagger* code is a 3D radiative (magneto-) hydrodynamic code that employs a high-order finite difference solver on a staggered mesh, to obtain a highly accurate solution while retaining the flexibility to include additional physics in the hydrodynamical model, e.g. scattering (Hayek et al. 2010). It models 'box-in-a-star' or representative portion of the stellar atmosphere on a staggered Eulerian grid to sample the atmosphere sufficiently while making the dynamic range of the problem soluble with current computational facilities.

Staggered meshes are structured grids where scalar variables, like density ρ and internal energy per unit volume e, are stored in a mesh placed at the computational cell centres while vector quantities, like momenta $\mathbf{p}$ and magnetic field $\mathbf{B}$, are stored on a mesh at the cell face-centres, displaced by half a grid-point from the scalar mesh. Figure 2.4 shows the geometry of a mesh cell.

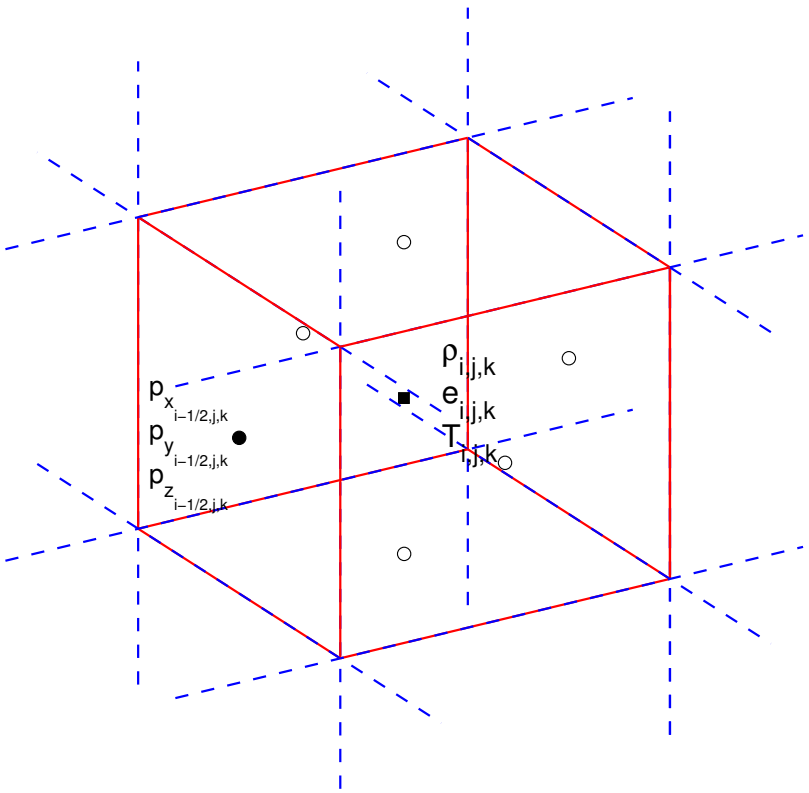

Figure 2.4: Computational cell of *stagger* code. The density, ρ, energy, e, and temperatures, T, are stored in the cell centres (square), while the momenta, p, are stored in the centre of the cell faces (circles).

Staggered grids are more accurate than their collocated counterparts as the derivative operators return a result with an effective step length Δx that is half that of the non-staggered grid. Furthermore staggered grids retain the coupling of neighbouring cells, preventing the odd-even decoupling or checker-board effect that can be a problem for collocated grids. While staggering has the advantage that physical quantities are often naturally calculated where they are required, variables are sometimes needed at other positions, necessitating interpolations not required in non-staggered grids.
The hydrodynamic solver uses 6th order derivative and 5th order interpolation along 3 spatial dimensions, each with a stencil of 6 grid-points and returns the result shifted by half a grid-point with respect to the cell centres of the stencilled points. The explicit interpolation operators are

$$f_{i+\frac{1}{2},j,k} = a(f_{i,j,k} + f_{i+1,j,k}) + b(f_{i-1,j,k} + f_{i+2,j,k}) + c(f_{i-2,j,k} + f_{i+3,j,k}) \tag{2.17}$$

while the derivative operators are

$$f'_{i,j,k} = \frac{a}{\delta x}(f_{i,j,k} - f_{i+1,j,k}) + \frac{b}{\delta x}(f_{i-1,j,k} - f_{i+2,j,k}) + \frac{c}{\delta x}(f_{i-2,j,k} - f_{i+3,j,k}) \tag{2.18}$$

with constants a,b,c fixed in the code.

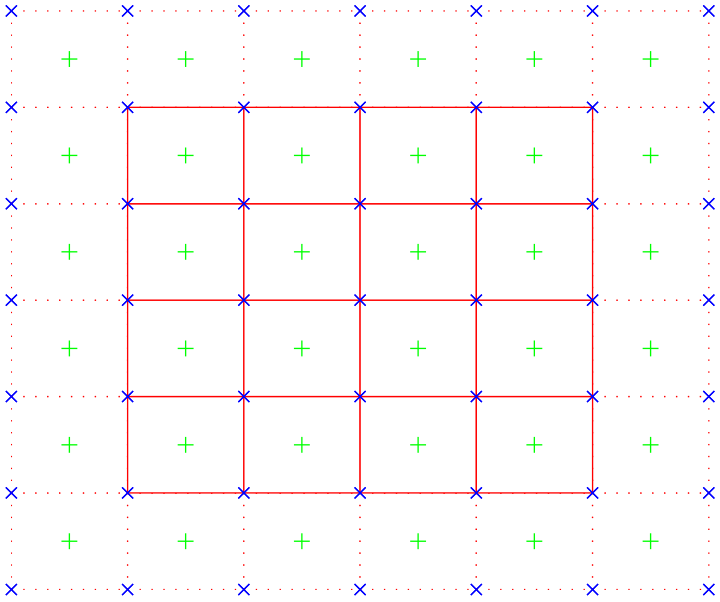

Figure 2.5: Green crosses denote cell centres (where scalars are stored), blue crosses denote cell boundary decomposition (where fluxes are stored), red lines show cell boundaries with the dashed red lines indicating ghost zones, that are used for derivative calculations and boundary conditions but do not reflect a physical solution.

A further advantage of this approach is that it vectorises easily allowing parallelisation (MPI Parallelisation), which is crucial for such heavy computational loads. For parallelised codes it is important to ensure that communication between sub-domains is kept as little as possible, in order to achieve the desired acceleration in code performance. 3D models of stellar atmospheres are massively more computationally demanding than 1D stratified models making optimisation and speed considerations imperative for 3D while relatively minor in 1D.

2.2.1 Artificial viscosity

The numerical stability of the hydrodynamic code makes a degree of artificial smoothing of the solution necessary. This is done by the addition of the viscosity tensor to the equation of motion.

$$\tau_{ij} = \frac{1}{2}\rho(\nu_j \frac{\partial u_i}{\partial x_j} + \nu_i \frac{\partial u_j}{\partial x_i}) \tag{2.19}$$

Artificial diffusion leads to unrealistically high plasma viscosities, which suppress small scale structures, effectively reducing the resolution of the simulation. It is therefore desirable to apply the smoothing only where strictly necessary. Quenched diffusion is a mechanism to keep the artificial viscosity local. The viscosity tensor is scaled with quenching factors which depend on the spatial derivatives of a hydrodynamical variable U and their second numerical derivative Δ^2. The quenching factors q vanish if $\partial U/\partial x$ is smooth and no artificial viscosity is added, but where strong discontinuities occur the effect of the artificial viscosity is amplified. These factors are bounded by the parameter

q_{max}.

$$\frac{\partial U}{\partial x} = \frac{\Delta^2(\frac{\partial U}{\partial x})|}{|\frac{\partial U}{\partial x}| + |\Delta^2 \frac{\partial U}{\partial x}/q_{max}} \tag{2.20}$$

The kinematic viscosities consist of three components corresponding to short wavelength oscillations ν_{wave}, advective transport $\nu_{advection}$ and shocks ν_{shock}. Short wavelength oscillations are not resolved by the numerical grid and therefore propagate with erroneous speeds, producing phase errors in travelling wave groups. A term

$$\nu_{wave} = a_1 \Delta x c_s \tag{2.21}$$

with scaling constant a_1, grid point separation Δx and local sound speed c_s, damps these oscillations. Similarly advective transport of small scale fluctuations causes amplitude deviations that grow with time. These are damped via

$$\nu_{advection} = a_2 \Delta x |\mathbf{u}| \tag{2.22}$$

which scales with both the grid point separation and the total gas velocity u. Finally, shocks form in the compressible gas and create strong discontinuities in the solution. This may be strong enough to destabilise the solver, or the solution could exhibit Gibbs phenomena around the shock (also known as ringing). A diffusion term

$$\nu_{shock} = a_3 (\Delta x)^2 |\nabla \cdot \mathbf{u}|^- \tag{2.23}$$

is introduced in order to resolve the shock, where the minus sign indicates that only gas compression ($\nabla \cdot \mathbf{u} < 0$) is considered.

2.3 Boundary conditions

Boundary conditions are critical to solving any equation modelling a physical system as they dictate the interaction of the domain under consideration with the rest of the Universe. Boundary conditions can dramatically change the results of a simulation and improper boundary conditions may introduce non-physical influences into the simulation.

Simulation domains should encompass a representative portion of the atmosphere large enough to capture the granulation flow in a statistical sense, while balancing considerations of computational cost. For stellar surface convection simulations this typically means of order ten convective cells horizontally, while the vertical extent is governed by optical depth. The simulation must penetrate deeply enough to sample the very optically thick layers where convection dominates and extend out to very low optical depth to ensure that the region of the atmosphere from which the spectrum emerges is adequately modelled.

2.3.1 Horizontal Boundary Conditions

As the modelled portion of the stellar atmosphere is imagined to be only a section of a much larger surface convective flow pattern, periodic boundary conditions, where the outflowing material at one boundary returns at the opposite boundary, are appropriate in the horizontal directions as they preserve the information of the flows across the artificial simulation box boundary, closely mimicking an infinitely extended planar atmosphere. Periodic boundary conditions place implicit constraints on

the grid resolution: the size of the computational cell should be a minimum of double the distance of the interaction potential, to prevent any single cell interacting with more than a single copy of another cell in any direction and that the characteristic size of any structural feature of interest or the scale-length of any critical effect must be smaller than the size of the computational domain. With interpolation and derivatives each having an interaction length of 3 cells either side, current simulations of order 120 grid points in each dimension easily fulfil this criterion. Likewise the physical scale of the computational grid is adjusted for each simulation to ensure the structures are resolved.

2.3.2 Vertical Boundary conditions

In the vertical direction periodic boundary conditions are inappropriate. Instead consideration must be given to the lower boundary which attaches the convection zone to the interior of the star and the upper boundary where the atmosphere extends out into space. For non-periodic boundary conditions, additional layers or ghost zones are added to the computational domain. Ghost zones are layers added to enable the interpolation and derivative expressions to be evaluated at the simulation boundaries, see Figure 2.5. The solutions obtained in the ghost zones are unphysical and should simply be discarded in subsequent analysis. The extent of the ghost zones is determined by the number of nearest neighbours that enter the derivative and interpolation routines, meaning for fifth and sixth order accurate methods the ghost zones should be at least 4 cells thick. The advantage of adding ghost zones, rather than considering spatial operators with spatially dependent coefficients is that for increasing simulation size ghost zones constitute a dwindling fraction of the memory.

2.3.3 The Lower Boundary

The lower boundary lies in the optically thick, convectively unstable region of the star. Lanes of cool dense low entropy gas sink down into the inner convection zone and leave the simulation while hot gas rises and expands adiabatically from below to enter the simulation domain. The lower boundary condition regulates heat flow into the simulation box, while ensuring that mass is conserved in order to retain a quasi-stationary state. The atmospheric density structure is broadly exponential, therefore anti-symmetric logarithmic extrapolation is used to define the densities in the ghost zones as follows:

$$\log \rho(z_{bot} - h) = 2 \log \rho(z_{bot}) - \log \rho(z_{bot} + h) \tag{2.24}$$

where h is the distance from the boundary z_{bot}. The volumetric internal energies will also be dominated by the exponential density stratification, therefore it is more convenient to work with the specific (per unit mass) internal energy, $\epsilon = e/\rho$. The specific energy boundaries are given by anti-symmetric linear extrapolation:

$$\epsilon(z_{bot} - h) = 2\epsilon(z_{bot}) - \epsilon(z_{bot} + h) \tag{2.25}$$

Physically, it is the entropy of the inflowing gas, $S(\epsilon, \rho)$, that must be specified at the lower boundary, to match the entropy of gas in the inner convection zone. A relaxation term with preset constants ϵ_{bot}

and ρ_{bot} regulates the entropy of the inflowing gas.

$$Q_{\rho,incoming}(z_{bot}) = -\frac{\rho(z_{bot} - \rho_{bot})}{\tau_{bot}} \tag{2.26}$$

$$Q_{\epsilon,incoming}(z_{bot}) = -\frac{\epsilon(z_{bot} - \epsilon_{bot})}{\tau_{bot}} \tag{2.27}$$

$$\tag{2.28}$$

where τ_{bot} is a relaxation time constant.

The lower boundary should be open, to allow gas to flow freely in and out of the simulation. The velocities are extrapolated symmetrically to guarantee a null vertical derivative.

$$u_i(z_{bot} - h) = u_i(z_{bot} + h) \qquad \leftrightarrow \qquad \left.\frac{\partial u_i}{\partial z}\right|_{bot} = 0 \qquad i = x, y, z \tag{2.29}$$

However, to reduce drifts in the horizontal plane, the lateral motion of inflows is damped as follows:

$$Q_{u_x,incoming}(z_{bot}) = -\frac{u_x}{\tau_{bot}} \tag{2.30}$$

$$Q_{u_y,incoming}(z_{bot}) = -\frac{u_y}{\tau_{bot}} \tag{2.31}$$

$$\tag{2.32}$$

The stochastic flow in the convection zone excites waves, in particular pressure waves. The boundary conditions are chosen such that they simulate a pressure node at the bottom of the simulation box. Physically, this approximates well the reflection of these pressure waves or 'p-mode' oscillations by the dense stellar interior. The pressure of inflowing material is already fixed as constant via the entropy relaxation conditions, meaning that pressure fluctuations of outflows must be balanced by an inverse adiabatic response. The damping terms are

$$Q_{\rho,outgoing}(z_{bot}) = -\frac{\left(\frac{\partial P}{\partial \rho}\right)_e d\rho + \left(\frac{\partial P}{\partial e}\right)_\rho de}{\left(\frac{\partial P}{\partial \rho}\right)_S} \tag{2.33}$$

$$Q_{\epsilon,incoming}(z_{bot}) = -\frac{P + e}{\rho} Q_{\rho,outgoing}(z_{bot}) \tag{2.34}$$

$$\tag{2.35}$$

where the thermodynamic derivatives are provided by the EOS and the density.

The pressure node regulates mass flow across the boundary thus ensuring that mass in the simulation is conserved. Outflows create low pressure regions which steepen the pressure gradient, causing gas to enter the simulation, while strong inflows act to reduce the gradient. Vertical mass flux therefore, oscillates with a relaxations time set by τ_{bot}.

2.3.4 The Upper Boundary

The upper boundary of the simulation is constructed to ensure the simulation encompasses the whole spectral line forming region, that is extends to very low optical depths. The typical criterion for a

solar model is that the continuum optical depth reaches $\tau_{5000} = 10^{-6}$. The largely exponential density stratification guarantees that the gas densities in this region are extremely low and consequently the mass and internal energy flux across the upper boundary are negligible. Accordingly, the logarithmic density values across the boundary are extrapolated anti-symmetrically.

$$log\rho(z_{top} - h) = 2\log\rho(z_{top}) - \log\rho(z_{top} + h) \tag{2.36}$$

where h is the distance from the boundary, defined by the atmospheric height z_{top}. Internal energies are found by anti-symmetric linear extrapolation, although it is convenient to convert the internal energies per unit volume into quantities per unit mass $\epsilon = e/\rho$ in order to naturally fold in the influence of exponential atmospheric stratification,

$$\epsilon(z_{top} - h) = 2\epsilon(z_{top}) - \epsilon(z_{top} + h) \tag{2.37}$$

Drifting of the mean internal energies at the boundary can be avoided by adding a sink term in the uppermost layer causing the relaxation towards a slowly evolving horizontal average $< \epsilon_{top} >$:

$$Q_\epsilon(z_{top}) = -\frac{\epsilon(z_{top}) - < \epsilon_{top} >}{\tau_{top}}, \tag{2.38}$$

where τ_{top} is a preset relaxation time constant. Physically the atmospheric gas must be free to leave the simulation domain and this is approximated by maintaining constant velocities across the boundary.

$$u_x(z_{top} - h) = u_x(z_{top}) \tag{2.39}$$
$$u_y(z_{top} - h) = u_y(z_{top}) \tag{2.40}$$
$$u_z(z_{top} - h) = u_z(z_{top}) \tag{2.41}$$
$$\tag{2.42}$$

2.3.5 Time Integration

The *stagger* code uses a semi-explicit time integration scheme to deliver numerical approximations to the system of partial differential equations that makes up the hydrodynamical model. Explicit time-stepping methods extrapolate the solution from previous time steps while implicit methods include the new solution as part of the time-integration itself. Implicit methods allow larger time stepping and tend to be more numerically stable, but since they are not bounded by wave speed it is difficult to study wave motion in detail. The importance of wave motion makes explicit methods more appropriate for application to stellar atmospheres.

Stagger employs a version of Hyman (1979) modified to apply to variable time steps. It is a predictor-corrector method which combines explicit prediction with a quasi-implicit correction step. The predictor extrapolates a weighted sum of the previous solution f_{n-1} and the current solution f_n forward in time to calculate the predicted solution at $t_0 + \Delta t$

$$f_{n+1}^{(pred)} = k_1 f_{n-1} + (1 - k_1) f_n + k_2 \frac{\partial f}{\partial t} \tag{2.43}$$

where $k_1 = (\Delta t_{n+\frac{1}{2}} / \Delta t_{n-\frac{1}{2}})^2$ and $k_2 = \Delta t_{n+\frac{1}{2}}(1 + \Delta t_{n+\frac{1}{2}} / \Delta t_{n-\frac{1}{2}})$. The hydrodynamical solver is called to obtain $\frac{\partial f}{\partial t}$ by solving the right-hand sides of equations 2.8, 2.9 and 2.10.

In the corrector step the solution is amended by obtaining the final solution from the weighted sum

$$f_{n+1} = k_3 f_{n-1} + (1 - k_3) f_n + k_4 \frac{\partial f}{\partial t} + k_5 f_{n+1}^{(pred)} \tag{2.44}$$

where $k_3 = 2\frac{1+\Delta t_{n+\frac{1}{2}}/\Delta t_{n-\frac{1}{2}}}{2+3\Delta t_{n+\frac{1}{2}}/\Delta t_{n-\frac{1}{2}}}$, $k_4 = \Delta t_{n+\frac{1}{2}} \frac{1+(\Delta t_{n+\frac{1}{2}})^2/\Delta t_{n-\frac{1}{2}}}{2+3\Delta t_{n+\frac{1}{2}}/\Delta t_{n-\frac{1}{2}}}$ $k_5 = \Delta t_{n+\frac{1}{2}} \frac{1+\Delta t_{n+\frac{1}{2}}/\Delta t_{n-\frac{1}{2}}}{2+3\Delta t_{n+\frac{1}{2}}/\Delta t_{n-\frac{1}{2}}}$. Once again the hydrodynamical solver computes $f_{n+1}^{(pred)}$. The method is semi-implicit as the approximate solution is used to obtain the final solution at $t = t_0 + \Delta t$.

The 3rd order Runge-Kutta method splits the integration into three sub-steps, requiring three evaluations of the hydrodynamical equations to perform the integration. Higher order methods require the evaluation of sub-steps between the main timesteps, but the effective computational load is reduced as a larger timestep may be taken. Higher order methods also produce lower amplitude numerical errors in the solution (Brandenburg 2003).

$$k_1 = f(y_i) \tag{2.45}$$

$$k_2 = f(y_i) + \Delta t(a_{11}\frac{\partial}{\partial t}k_1) \tag{2.46}$$

$$k_3 = f(y_i) + \Delta t(a_{12}\frac{\partial}{\partial t}k_1 + a_{22}\frac{\partial}{\partial t}k_2) \tag{2.47}$$

$$f(y_{i+1}) = f(y_i) + \Delta t(a_{13}\frac{\partial}{\partial t}k_1 + a_{23}\frac{\partial}{\partial t}k_2 + a_{33}\frac{\partial}{\partial t}k_3) \tag{2.48}$$

While the memory load of the Runge-Kutta method is large, requiring four sets of variables to be stored, *stagger* employs the clever reordering scheme of (Williamson 1980), to use a recurrent algorithm storing only two sets of variables.

Stability

In numerical integration, the timestep Δt is subject to restrictions, to guarantee the convergence and physical results. Finite difference schemes, like *stagger* are typically studied under von Neumann stability analysis, which requires that a partial differential equation with a bounded solution also produces a numerical result that is bounded and one for which the amplitude of perturbation of the solution must decay with time for all wave-numbers.

Transport term: The Courant condition, requires that the local speed of numerical propagation of information, must exceed the local physical propagation speed, to ensure causal order in the time evolution of the partial differential equation. In hydrodynamical models this physical speed, u, is set by the sum of the sound speed and the magnitude of the advective velocity.

Diffusion term: The diffusion timestep criterion $\Delta t < \frac{(\Delta x)^2}{2\nu}$ is often more restrictive due to the Δx^2 dependence. Diffusion terms occur in the artificial viscosity tensor of the hydrodynamical solver. The timestep is restricted to ensure numerical stability.

In general, while a strict and consistent stability analysis proves difficult, the time integration is considered stable if the strictest condition is satisfied at all grid-points.

$$\Delta t < C \cdot min\left(\left\{\frac{1}{\mid \Delta \mathbf{U} \mid}\right\}_i, \left\{\frac{\Delta x}{c_s + |\mathbf{U}|_i}\right\}, \left\{\frac{\Delta x^2}{\nu}\right\}\right), \tag{2.49}$$

where $\Delta\mathbf{U}$ denotes the local relative change of variable $\mathbf{U}$, c_S is the local sound speed, $\mathbf{U}$ is the local advection velocity and ν is the artificial diffusion coefficient. The constant C is typically set to $\simeq$ 0.3, depending on the time integration method. *Stagger* dynamically adapts to allow the largest permissible timestep at every timestep to allow rapid simulation when appropriate and the necessary time resolution if required.

2.4 Summary

Convection operates in the envelopes of cool stars, leading to a characteristic inhomogeneous surface pattern, see Figure 2.1. By nature, it is multi-dimensional and dynamic, meaning that a hydrodynamic model is appropriate, Physically, the hydrodynamic equations require thermodynamic data and opacities for radiative transfer to close the system of equations. Together these ingredients provide a powerful tool to study convection in stars.

Chapter 3

3D modelling of cool dwarfs

3.1 Introduction

For cool stars, the interplay of radiative and convective energy transport governs the spectrum emitted from their atmospheres, with layers close to the optical surface having the strongest influence. The complexity of this problem prevents straightforward inversion of the spectrum to find a unique solution for the atmospheric structure; instead the forward problem of modelling the atmosphere, under certain assumptions, is tackled.

Atmospheric modelling in 1D has been remarkably successful in reproducing the main features of the spectrum, despite the restrictive assumptions required (e.g. Gustafsson et al. 1975, 2008; Kurucz 1979; Castelli & Kurucz 2004; Hauschildt et al. 1999). Hydrostatic equilibrium, plane-parallel geometry, flux constancy and local thermodynamic equilibrium (LTE) are all common assumptions made in 1D modelling. Later generations of 1D models have attempted to address critically many of the assumptions, with spherically symmetric models and restricted non-LTE effects considered in some models. With constantly improving observations, it is clear that while broadly and qualitatively understood, more detailed observations require ever more accurate models necessitating the relaxation of these assumptions.

As convection is manifestly 3D and time-dependent, traditional 1D atmospheric models must approximate this in some simplified manner. Typically this is done by invoking mixing-length theory (MLT) (Böhm-Vitense 1958), where free parameters are introduced to characterise the micro- and macroscopic velocity fields and the typical length scale of the induced mixing. Free parameters cannot be derived *ab initio*, and are assumed to be uniform across the star, but may be calibrated from comparisons between synthetic and observed spectra (Fuhrmann et al. 1993; Barklem et al. 2002; Smalley & Kupka 2003). In practice, usually only α_{MLT}, the mixing length (scaled to the local pressure scale height), is calibrated; this is done by investigating its effect in reproducing selected line profiles. Convection is implemented based on a typical length-scale for mixing in the region of the atmosphere that is convectively unstable.

Early 3D simulations already challenge this view of of how convection operates in practice (Nordlund 1982; Nordlund & Dravins 1990; Steffen et al. 1989). Convective simulations show broad slow upflows surrounded by narrow fast-flowing lanes of downflowing material, in contrast to the homogeneous elements assumed in MLT (Stein & Nordlund 1998). Such a morphology of convective

granules leads to the natural explanation of line-asymmetries observed in cool stars (e.g. Dravins 2008). That is that the hot, slow moving upflows dominate the flux due both to the areal filling factor of these flows and the brightness contrast with the cool, entropy-poor downflows (See Figure 3.1). Furthermore, the inclusion of convective overshooting beyond the Schwarzschild instability criterion in 1D modelling has met with only limited success (Castelli et al. 1997) and it introduces further free parameters, while this is naturally included in 3D hydrodynamic modelling.

1D solar structure models, despite their successes, are challenged by helioseismic observations (Rosenthal et al. 1999). It seems that turbulent pressure, naturally included in 3D models and their mean structures, provide better agreement with the observed high frequency p-modes (Rosenthal et al. 1999). Other studies find improvements in the predicted p-mode excitation rates and the photometric granulation-induced micro-variability, when moving from 1D to mean 3D models.

Unfortunately, 3D modelling requires considerably more computational effort, both in terms of raw floating point operations and because of the relaxation phase that requires much more manual input. It is therefore of significant interest to characterise the differences between 1D and 3D modelling in order to determine whether 3D is required for a particular application, as well as to investigate the properties of granulation in detail.

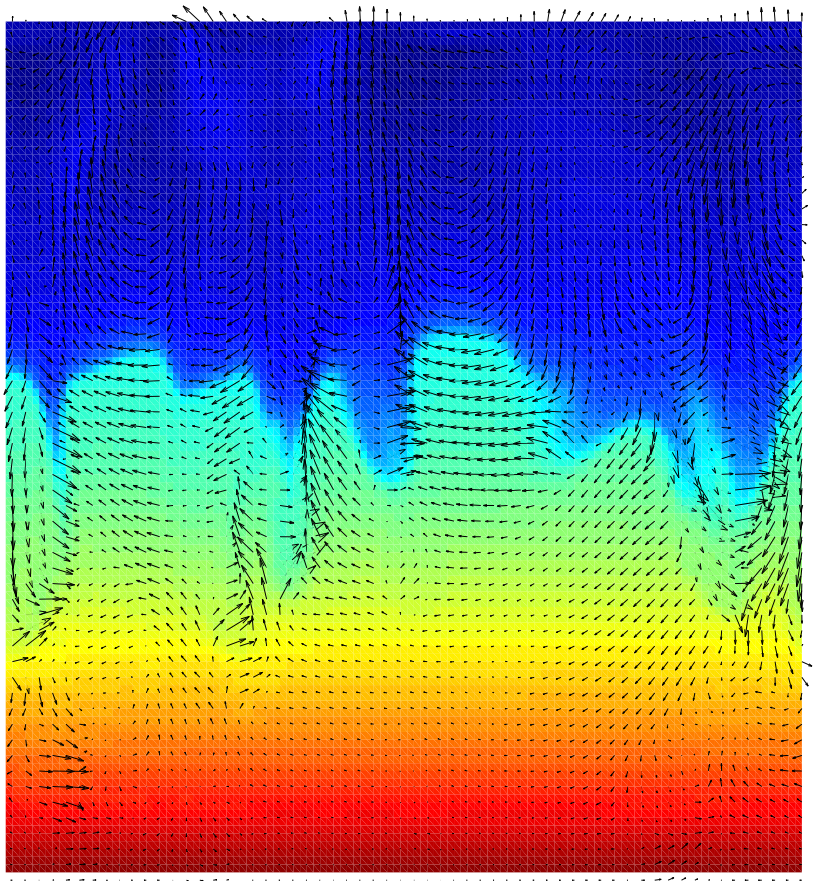

Figure 3.1: A vertical slice of the temperature stratification of a cool dwarf, with the velocity field over-plotted. Red colours denote hot, entropy-rich gas, while blues demark cool, entropy-poor gas. Taken from the T_{eff} = 4500K, log(g)=5.0 and solar metallicity M dwarf simulation.

3.2 Models

The modelling of cool dwarfs was undertaken using the 3D radiative hydrodynamic code, *Stagger*, described in detail in Chapter 2. The code solves the hydrodynamic equations of mass, momentum and energy conservation on an Eulerian staggered mesh and these equations are closed by a realistic equation of state table (EOS) and multi-group binned opacity table (See Chapter 6 for more details). *Stagger* is fully parallelised in MPI, allowing models to be computed efficiently on multiple cores.

The models simulate a 'box-in-a-star'; that is model a representative portion of the stellar atmosphere in the computational domain. This is appropriate for cool dwarfs where the atmosphere is thin compared to the stellar radius but becomes highly questionable for giant or supergiant stars. Vertically, simulations cover several orders of magnitude in optical depth, $10^{-4} < \tau_{Rosseland} < 10^{6}$, while horizontally the box dimensions are adjusted to ensure a minimum of 10 granules are visible.

The equation-of-state table (EOS) is from Mihalas, Hummer and Däppen and considers the 17 most abundant elements Mihalas et al. (1988); Hummer & Mihalas (1988); Trampedach et al. (2006). Computed for solar abundances (Asplund et al. 2009), it stores thermodynamic quantities, along with their derivatives, as a function of density and specific internal energy allowing rapid and accurate interpolation.

The opacity table is ultimately based on VALD-2 and SCAN databases of atomic and molecular lines respectively (Stempels et al. 2001; Jørgensen 1997), with improvements from, among others (Nahar 2004). The opacity table is constructed using the multi-group binning method, where monochromatic opacities are sorted into bins and mean opacity coefficients for these bins computed. These mean opacity coefficients are stored as a function of density, temperature and bin number.

3.2.1 Scaling

While it is possible to set up a 3D simulation *ab initio*, specifying only the boundary conditions and supplying appropriate EOS and opacity tables, consideration of the relaxation timescale means that perturbing an existing relaxed model is significantly more efficient.

Scaling models requires a relaxed 3D simulation and two 1D stratifications, the first with the same atmospheric parameters as the 3D model and the second with the desired parameters of the new model. The 1D models are used to construct scaling ratios of density, pressure and temperature between the models, on a depth-scale specified by the Rosseland optical depth in optically thin regions and a normalised pressure scale below the optical surface. These ratios are used to rescale the 3D datacubes from the hydrodynamic model. Additional variables are scaled using a combination of these ratios and information from the EOS. The geometrical depth scale is then constructed by enforcing quasi-hydrostatic equilibrium on the new pressure and density profiles. In contrast to the horizontal mesh, the vertical depth scale is not equidistant, but approximately evenly distributed on the optical depth scale, meaning features may be resolved efficiently.

For these models, the effective temperature emerges from the simulation; it is not an input. This contrasts with the case in 1D. Instead, the input parameter is the entropy of the gas inflowing via the lower boundary of the simulation. Deep in the convection zone the temperature gradient is adiabatic, as such the entropy of the inflowing gas must match the adiabatic entropy, meaning that, despite their

relative shallowness, these simulations are physically valid. Unfortunately, the relationship between the entropy of the inflowing gas and the resultant effective temperature is not straightforward and the influence of the EOS and the opacities via the radiative transfer equation mean that targeting specific parameters is akin to an art. Ideally, new models are scaled along lines of constant entropy in the temperature surface-gravity plane, meaning that the entropy of the inflowing gas need not be adjusted. However, the parameter space explored here covers new ground in this plane, for which there are no suitable models from which to scale. This means that the models are significantly more unpredictable at first, and take longer to relax. General trends are used to inform the choice of input entropy, but targeting specific values remains haphazard.

For 3D models the input values are then the surface gravity, the metallicity (or more correctly the abundances of the 17 most abundant elements as covered by the EOS table) and the entropy. The entropy is specified in the code as inflowing specific energy and density of the gas at the simulation base. It should be noted that together the inflowing energy and density specify the entropy and map directly to the effective temperature of the simulation.

3.2.2 Relaxation

In one dimension models are considered to have converged on a solution when further iterations do not change the resulting structure beyond some threshold tolerance. 3D simulations are, by nature, dynamic and alternative relaxation criteria are required. Scaling models typically perturbs the solution resulting in a 'kick' of excess energy, which is channelled into pressure wave oscillations (p-modes) in the atmosphere. To remove this excess energy, the period of the dominant (highest amplitude) radial p-mode is determined and the simulation is run with exponential damping in the momentum equation at this frequency. This procedure is repeated for all strong modes present in the system. Next the damping is reduced slowly to prevent further kicks until no damping remains and the natural oscillation mode of the simulation, excited by the stochastic convective motions, is allowed to emerge. The simulations are considered relaxed when the temporal evolution of the effective temperature, T_{eff}, is stable; that is showing no long-term trends and the simulation covers a minimum of ten granules in the horizontal plane. To produce a model run suitable for subsequent analysis, the relaxed simulation is then evolved for a minimum of 7 periods of the fundamental p-mode, which corresponds to roughly 2 convective turnover timescales. Typically, this equates to a few tens of thousands of individual timesteps, of which snapshots are stored at regular intervals $\sim \Delta t_{snap} =< H_P/c_s >_{\tau=2/3}$, where H_P is the local scale pressure height and c_S is the sound speed, resulting in 100-200 snapshots for analysis.

3.3 Results

The models presented here form a sequence in effective temperature at constant gravity, with the gravity corresponding to models of the main sequence. Table 3.1 details the parameters of the models. Effective temperature is calculated from the spatially averaged emergent energy flux F_{rad} and the Stefan-Boltzmann Law, $T_{eff} = [F_{rad}/\sigma]^{1/4}$, where σ is the Stefan-Boltzmann constant. T_{aim} is the targeted effective temperature, as 3D models show significant variation it is reasonable to adopt a a tolerance of $T_{eff} = T_{aim} \pm 10K$. Surface gravity, g, is an input, while $l_{x,y,z}$ are the simulation box

T_{aim} (K)	T_{eff} (K)	g (cms^{-2})	$l_{x,y}$ (Mm)	l_z (Mm)	r_{bot} ($g\,cm^{-2}$)	e_{bot} ($erg\,g^{-1}$)
4500	4502	10^5	1.4	0.79761	1.03041×10^{-4}	6.796×10^{8}
4300	4298	10^5	1.4	0.74594	1.70448×10^{-4}	1.1585×10^{9}
4150	4149	10^5	1.5	0.71645	1.87632×10^{-4}	1.1859×10^{9}
4000	4004	10^5	1.5	0.67949	2.09060×10^{-4}	1.1966×10^{9}
3900	3902	10^5	1.6	0.63616	2.37231×10^{-4}	1.1974×10^{9}
3800	3804	10^5	1.6	0.58943	2.74818×10^{-4}	1.2013×10^{9}

Table 3.1: Table of input parameters for 3D hydrodynamic models. T_{aim} is the targeted effective temperature of the model, while T_{eff} is the emergent effective temperature. The surface gravity,g, corresponds to the main sequence. The simulation box size is defined horizontally by $l_{x,y}$ and vertically by l_z. The entropy of the inflowing gas is specified through the density,r_{bot}, and the energy, e_{bot}, of the gas at the base of the simulation box.

dimensions. The entropy of the inflowing gas at the lower boundary, s_{bot}, is the input parameter that leads to effective temperature, this is fixed by the inflowing gas density,r_{bot} and specific energy e_{bot}. Each model adopts solar metallicity (Asplund et al. 2009).

3.3.1 Emergent Intensity

3D models are distinguished by their inhomogeneous surface features, in contrast to 1D models. Figure 3.2 shows the bolometric emergent intensity in the horizontal plane of all six models. The intensities are normalised to the mean intensity of the simulation and the colourbars illustrate the magnitude of the fluctuations. Dark regions represent cold inter-granular lanes while the hot granules are the bright regions. Due to highly non-linear opacity, in particular the opacity from H^-, radiation from the granules originates significantly higher in the atmosphere than for the cooler inter-granular lanes.

Qualitatively, the granulation patterns in Figure 3.2 are rather self-similar, although the amplitude of the fluctuations increase towards higher effective temperatures. The granules, while irregular in shape, show a distinct brightness pattern, with the centre being brightest and a smooth drop off of intensity towards the cell edges. It is evident that the granules dominate the surface area, with inter-granular lanes remaining narrow and sharply defined. This has important ramifications; such an unequal areal filling factor means that the assumption underlying 1D models, such as mixing-length theory, are quite wrong and furthermore, the inherent motion of the convection pattern results in a blue-shift of the spectral lines compared with equally sized granules and lanes. Towards lower effective temperatures the convective cells become slightly more sharply delineated.

Figure 3.3 shows the same series of models but using the same colourmap for shading, in order to highlight the decreasing intensity contrast between cells and inter-granular lanes with decreasing effective temperature. The colourmap runs from 0.8 to 1.2 in relative intensity. The behaviour of the intensity contrast with effective temperature is to be expected. Intensity from the centre of granules originates in photospheric layers, where intensity is strongly correlated with effective temperature, while inter-granular lanes intensities are governed by the entropy poor, cool gas returning to the stellar interior after having lost its energy in the optically thin region of the atmosphere and therefore

T_{aim} (K)	T_{eff} (K)	ΔI_{rms} (%)
4500	4502	6.30
4300	4298	4.50
4150	4149	4.73
4000	4004	3.66
3900	3902	2.70
3800	3804	2.24

Table 3.2: Table of targeted effective temperature(T_{aim}), simulation resultant effective temperature (T_{eff}) and root-mean-square intensity fluctuations (ΔI_{rms}).

is not as strongly affected by effective temperature.

A more quantitative analysis is facilitated by consideration of the root mean square of the bolometric intensity fluctuations, calculated via

$$\Delta I_{rms} = \left[\frac{\Sigma (I_i - \bar{I})^2}{N \bar{I}^2} \right]^{1/2} \tag{3.1}$$

where $\bar{I}$ is the mean intensity and N is the number of data points.
Table 3.2 shows the root mean square intensity fluctuations expressed as a percentage of the mean intensity. Evidently there is a trend that towards lower effective temperatures the amplitude of the intensity contrast between bright granular cells and dark inter-granular lanes decreases.

For these simulations the computational run is sampled by 200 snapshots, it is therefore possible to calculate this value, ΔI_{rms}, for each snapshot, and consider not only the characteristic scale of fluctuation for each snapshot, but due to the stochastic nature of the convective flow, it is interesting to characterise the stability of this measure. Figure 3.4 shows boxplots for each model giving the mean and distribution properties of the r.m.s. intensity fluctuations. It should be noted that the x-axis is a *label* only and does not scale with the labelled values. The red lines give the mean intensity fluctuations while the blue box encloses a single standard deviation. The black lines denote the extreme values of the time-series and the red plus signs show the locations of statistical outliers.

The clear trend of larger amplitude fluctuation with hotter models, broadly linear, remains evident, but further to this the distributions become wider, with the two hottest models showing statistical outliers. This indicates more chaotic and violent convection in the hotter models. Returning to Figure 3.2 this can be seen qualitatively with cooler models having neater convective patterns than the hotter models.

To illustrate this result in the context of other 3D model results Figure 3.5 shows the mean ΔI_{rms} values from the simulations plotted against the effective temperature, augmented by values from the literature for hotter dwarf stars (Magic et al. 2013) and the stagger code solar model (in red, it has the solar surface gravity of $10^{4.44} cm/s^2$ while all other models have $10^5 cm/s^2$). Evidently the trend continues to still hotter temperatures, although the slope seems to be shallower than for the cool dwarfs.

To further characterise the intensity fluctuations, Figure 3.6 shows the temporally averaged histograms of individual pixel intensities, I, normalised to the model snapshot mean intensity, $\bar{I}$. The histograms clearly show two components, with the peak of lower intensities corresponding to the

cool, dark downdrafts while the stronger peak of higher intensities corresponds to the granules themselves, qualitatively in agreement with expectations. The distribution is asymmetric, becoming more strongly pronounced at lower effective temperature. Results from Magic et al. (2013) show they find the downdrafts to be more strongly peaked than the granules for all models except metal poor ([Fe/H]=-2) dwarfs. The results presented here confirm the findings for the highest temperature model, $T = 4500K$, the only overlapping model in the dataset, but show that this reverses at lower temperatures forming a clear trend of increasingly peaked high-intensity granules with decreasing effective temperature.

Surface inhomogeneity in these objects, as characterised by photometric contrast (Figure 3.3) and intensity fluctuations (Figure 3.5), is significant, but becomes less pronounced with decreasing effective temperature.

3.3.2 Flux Transport

In the atmospheres of cool dwarf stars energy flux is conserved and the total flux emerges from the top of the atmosphere in the form of radiation. Deeper in the atmosphere convective motion propagates energy in addition to radiative flux. In 1D the convective energy flux is derived from the parametrised implementation of convection - typically mixing-length theory. It follows naturally that the flux profile is heavily dependent on the assumptions of the model. Mixing-length theory assumes equally sized upflows and downdrafts which mix the medium on some typical length scale with a characteristic speed in regions classically unstable against convection. Overshooting beyond this region into formally stable layers is not considered. Due to the lack of a self-consistent velocity field in 1D, the individual fluxes contributing to the total flux cannot be resolved, while in 3D these are readily available. Furthermore, convective overshooting beyond the convective zone arises naturally.

3D models conserve the total flux via the conservation of energy. Nordlund et al. (2009) derive a conservation equation with the individual fluxes as follows

$$\frac{\partial}{\partial t}(e + \frac{1}{2}\rho u^2) + \nabla \cdot (e\mathbf{u} + P\mathbf{u} + \frac{1}{2}\rho u^2 \mathbf{u} + \tau_{visc} \cdot \mathbf{u} + F_{rad}) = -\rho \mathbf{g} \cdot \mathbf{u} \tag{3.2}$$

where $e = e_{ion} + e_{diss} + e_{th}$ is the total specific internal energy, composed of the ionisation energy, the molecular dissociation energy and the thermal energy, and $\mathbf{u}$ is the gas velocity. The radiative flux contributes via the first moment of the specific intensity, i_ν integrated over the frequency spectrum

$$F_{rad} = \int_0^\infty \int_{S^2} I_\nu(\hat{\mathbf{n}}_\mathbf{i}, \hat{\mathbf{n}}) d\Omega d\nu \tag{3.3}$$

The radiative flux completely dominates high above the stellar surface, but makes only a small contribution in the dense optically thick layers below the stellar surface. The acoustic energy flux, F_{acous}, results from the compression and expansion of the gas and is given via

$$F_{acous} = P\mathbf{u}. \tag{3.4}$$

Viscous energy transport is given by

$$F_{visc} = \tau_{visc} \cdot \mathbf{u} \tag{3.5}$$

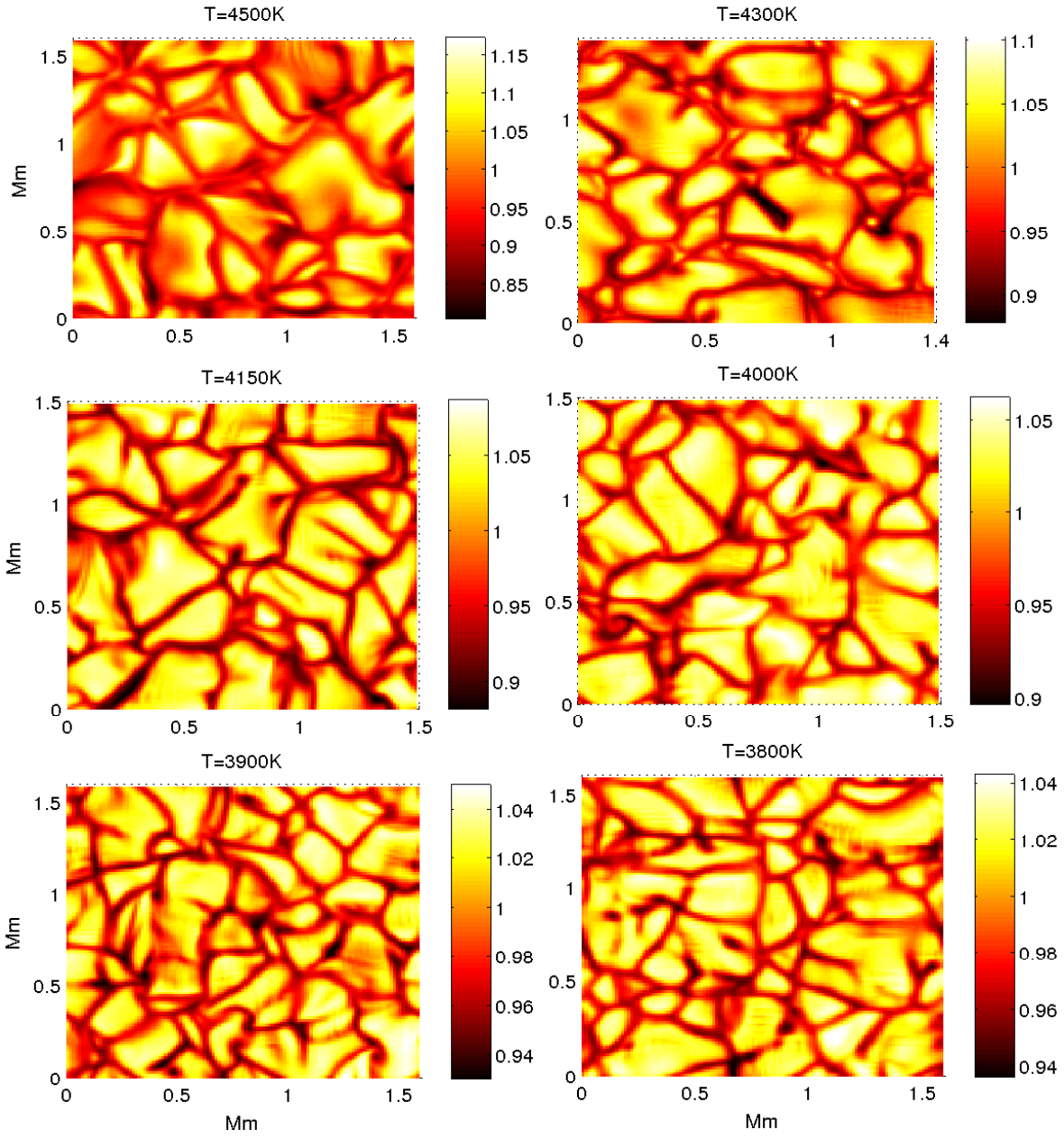

Figure 3.2: Surface emergent intensity plots in the horizontal plane for a series of dwarf models ($g = 10^5 cm/s^2$) with decreasing effective temperature. The horizontal scales are marked in Mm, while the colourbars at the side show the normalised simulation intensity.

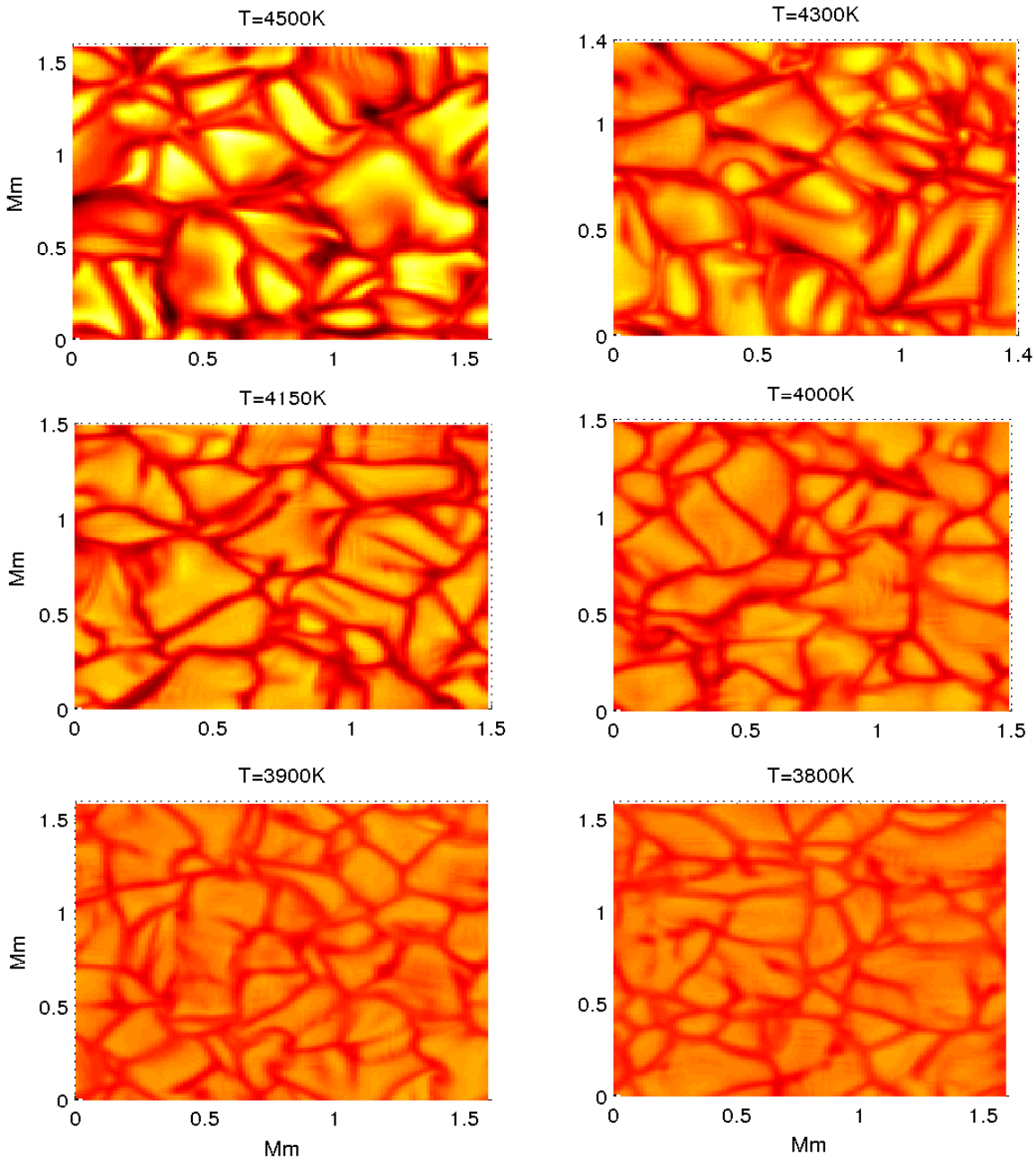

Figure 3.3: As Figure 3.2, but in this figure each simulation uses the same colourmap, to highlight the decrease in contrast with effective temperature.

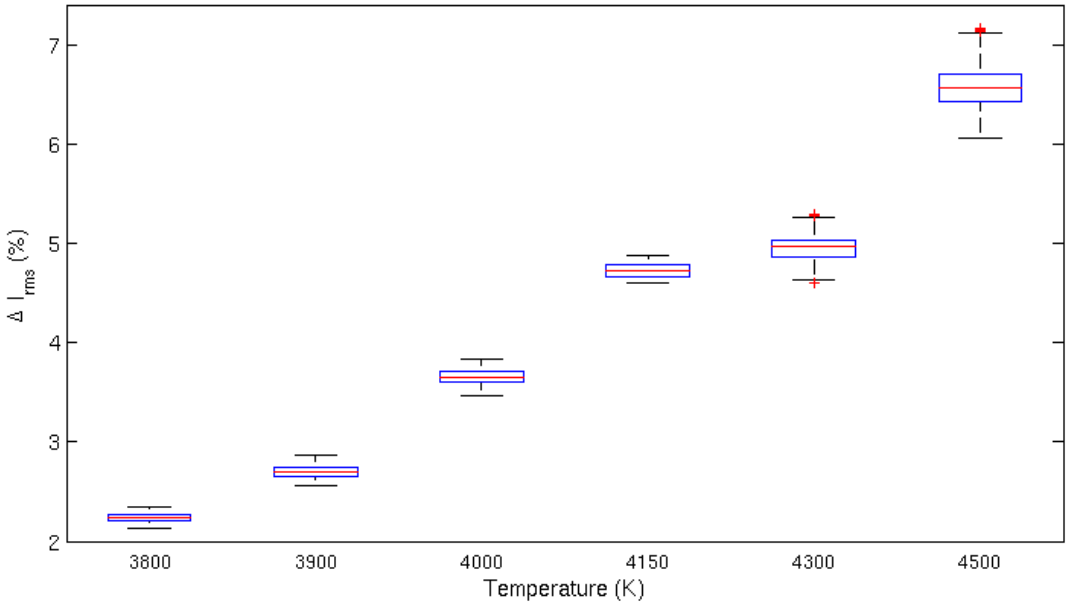

Figure 3.4: Boxplots of the root mean square intensity fluctuations, ΔI_{rms}, expressed as a percentage of the simulation mean intensity based on 200 snapshots of the hydrodynamical models for the six models with effective temperatures, $T_{eff} = 3800 - 4500K$. The red lines denote the mean ΔI_{rms} while the blue box shows the 25th and 75th percentiles of the data. The black whiskers show the extrema of the data that are not considered statistical outliers, while outliers are plotted individually with red crosses. It should be noted that the effective temperatures are labels and not an axis.

and typically contributes little to the total flux. The internal energy flux $F_{internal} = e\mathbf{u}$ is composed of terms that represent the energy stored in ionisation, the internal thermal energy of the gas and the dissociation energy, $e_i = e_{ion} + e_{th} + e_{diss}$.

Since enthalpy density is defined as $h = e + P$, the enthalpy flux consists of the internal energy flux,$F_{internal}$, and the acoustic flux, F_{acous}. Adding the kinetic energy flux

$$F_{kin} = \frac{1}{2}\rho u^2 \mathbf{u} \tag{3.6}$$

to this gives the total convective flux.

Figure 3.7 shows the fractional contribution of the radiative flux to total flux as a function of the Rosseland optical depth, $\tau_{Rosseland}$. The solid lines show the 3D model geometrical average while the dashed lines show the equivalent model from the 1D MARCS package and the colours correspond to the different effective temperatures of the models. As a result of the finite resolution of the MARCS grid of model atmospheres, not every $< 3D >$ model has a corresponding model in 1D. Interpolation of quantities, while possible, is not carried out as it is not suitable for the fluxes and adds nothing constructive to the discussion, although the $< 3D >$ models are retained to form a smoother run of effective temperatures highlighting the parameter dependence of the $< 3D >$ results. In the deep, hot layers corresponding to large optical depths, the contribution of radiative flux to the total is negligible, as convection is the dominant energy transport mode in these layers. The optically thin layers correspond to the outer atmosphere of the star where convection no longer operates and energy is

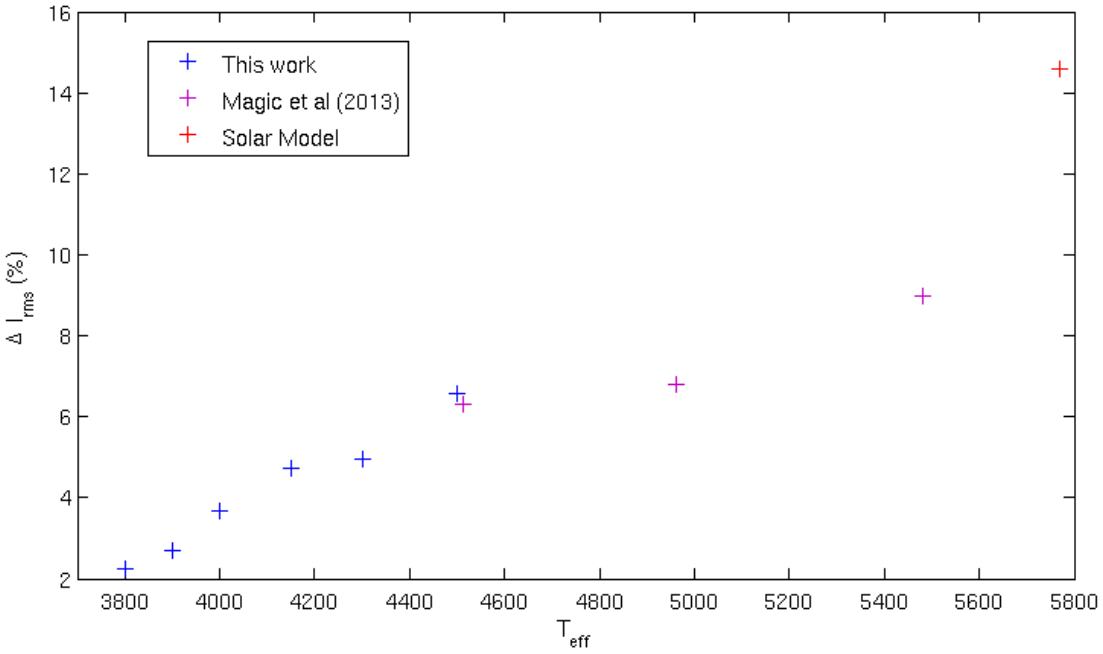

Figure 3.5: Root mean square intensity fluctuations, ΔI_{rms}, with effective temperature. The blue pluses show the models in this work and are augmented by hotter models from Magic et al. (2013) and the *stagger* code solar model is shown for comparison. All models have log(g)=5.0 (dwarf stars), except the solar model with log(g)=4.44 and solar metallicity as defined by Asplund et al. (2009).

transported solely by radiation. It should be noted that the MARCS models are not as extended as the $< 3D >$ hydrodynamical models and cut off at $\tau_{Ross} \simeq 10^2$.

Qualitatively, the models all behave as expected, exhibiting a monotonic smooth transition from convectively to radiatively dominated energy transport. The major difference between the 1D and $< 3D >$ models is that convection, rather than radiation, plays a more significant role out to lower Rosseland optical depths - corresponding to higher geometrical height in the atmosphere. This may be understood in terms of overshooting.

Convective overshooting is the extension of convective motion beyond the bounds of the convectively unstable layers into a region of the atmosphere that is classically stable against convection. Overshooting is caused by the momentum of the convective material at the boundary between stable and unstable layers, which causes it to penetrate the otherwise stable layers beyond.

In the 1D MARCS models radiation supersedes convection in the layers around $\tau_{Rosseland} = 10^1$, while the $< 3D >$ models show that radiation begins to make a contribution in these layers but does not dominate until lower optical depths $\tau_{Rosseland} = 10^0 - 10^1$ and is completely dominant below $\tau_{Rosseland} \simeq 10^{-1}$. Geometrically this covers a relatively thin layer and so has a fairly minor effect on the geometric scale of the atmosphere. Of more significance is the impact of this on the spectrum. In the $< 3D >$ models the continuum formation remain in the convectively dominated part of the atmosphere, while much of the line-formation occurs in a region where convection remains significant, rather than the radiatively dominated region as in 1D models and classical convection theory would suggest. At the very least, this suggests that $< 3D >$ spectral line would be broadened in comparison to their 1D counterparts, as a result of the strong velocity fields still present. Parametrising overshooting for the

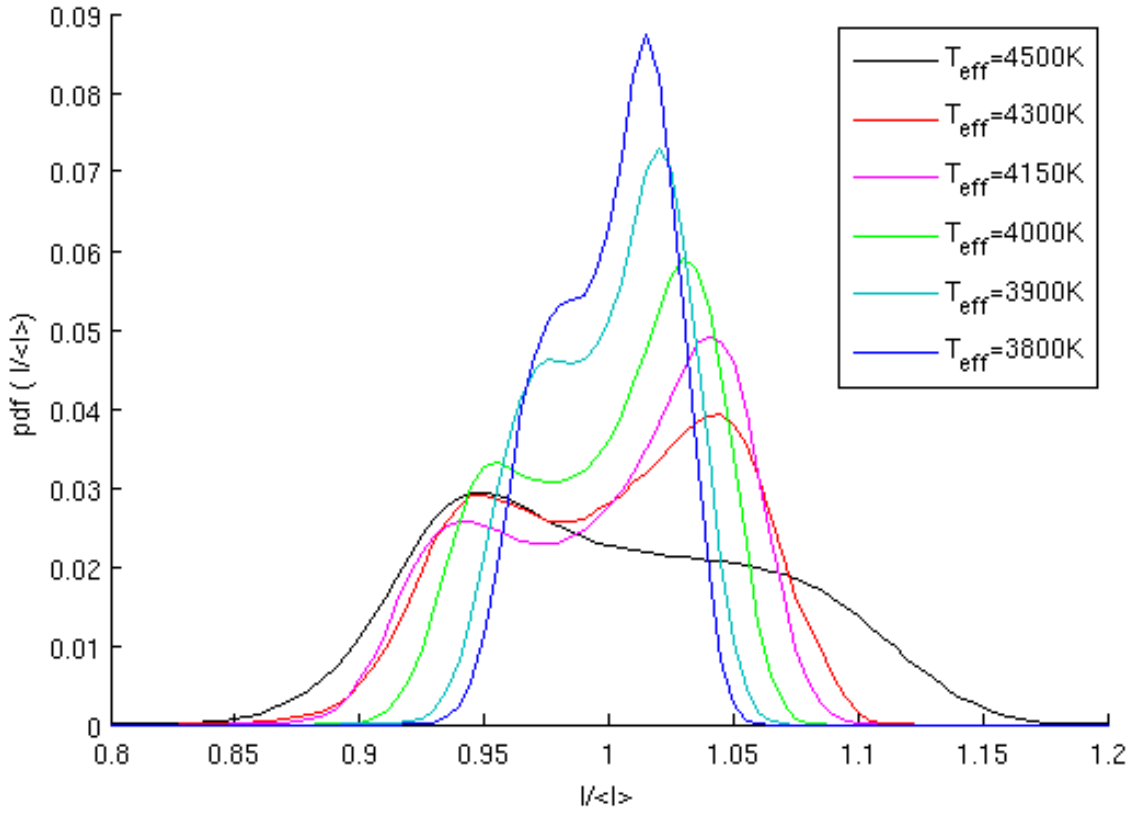

Figure 3.6: Temporally averaged histograms of the bolometric emergent intensity from hydrodynamic simulation of dwarfs stars. The bimodal structure is a result of the asymmetry and strong contrast between upflows and downflows while the increasingly peaked structure for lower effective temperatures is a consequence of the lower contrast for these models.

1D models would produce a shift to the left of the diagrams bringing them closer to the $< 3D >$ result, but tweaking the micro-turbulence makes negligible difference.

The transition between the two regimes, convection dominated to radiation dominated, is far more shallow in 3D, suggesting the MLT prescription causes far too rapid a switchover. The $< 3D >$ results suggest a smoother transition, not such a rapid change of regime. In addition, the $< 3D >$ models show more variation with effective temperature than their equivalent 1D result, with the coolest models having convective motions surviving well into the quite optically thin layers. Again, this points to shortcomings in mixing-length theory for a detailed understanding of atmospheric dynamics, although it remains a useful simplification for standardised calculations that require a rapid convergence.

Figures 3.8, 3.9, 3.10, 3.11, 3.12 and 3.13 show the composition of the total energy flux with optical depth in the atmosphere. As expected radiation dominates completely in the upper atmosphere, while deep in the convective zone, at high optical depth, convection strongly dominates.

Internal energy (purple line) is the largest component of the convective flux (red line), completely dominating the other contributing terms, e.g. F_{visc}, F_{acous}, although at large optical depths the balancing of kinetic energy (green) becomes more significant. The kinetic energy flux is always negative, as while mass is conserved, the convective motions have asymmetric velocities. The hot bright granules

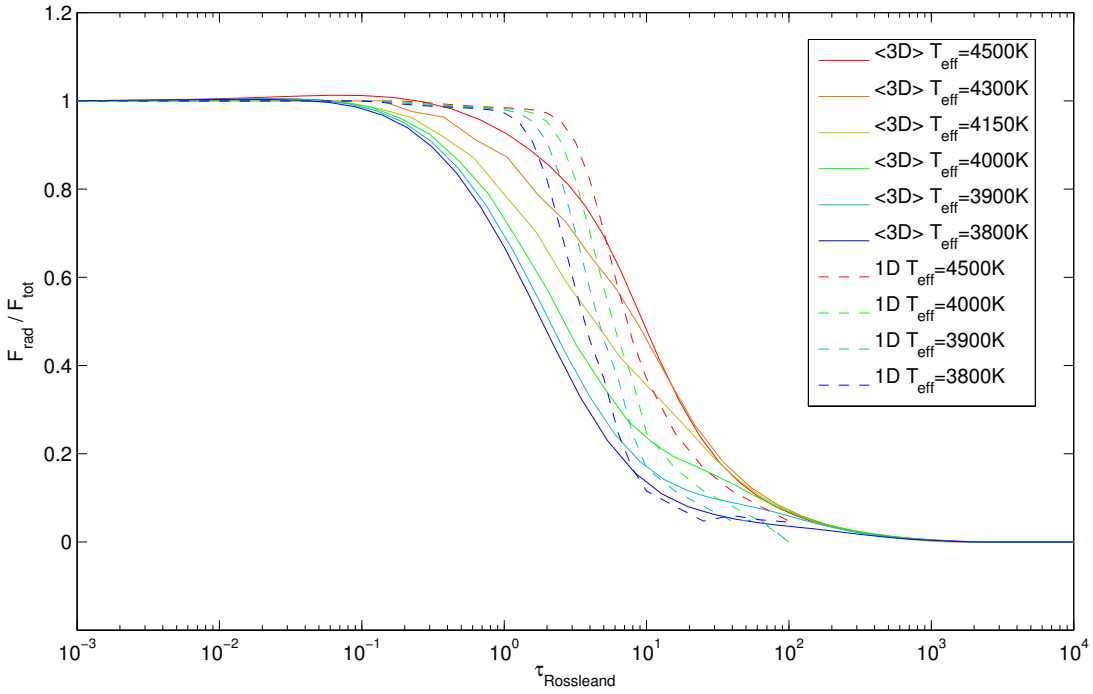

Figure 3.7: The contribution of radiative flux to the total flux, across the atmosphere with the Rosseland optical depth. The solid line models are $< 3D >$ stratifications while the dashed lines show the equivalent model using a 1D model. High Rosseland optical depths correspond with the deep convective part of the stellar envelope while low optical depths characterise the outer atmosphere. Not every $< 3D >$ model has an equivalent 1D counterpart, as the model grid in 1D has finite resolution and interpolation of these quantities is unwise. The photosphere lies around $\tau_{Rosseland} = 1$ and it should be noted that it is here that the maximal differences between the 1D and $< 3D >$ results occur.

are characterised by slow upflows while the cool downdrafts of the inter-granular lanes flow much faster. Contrasting with the symmetric flows in 1D (which would then cancel each other out) this means that the kinetic flux is always downflowing and is balanced by commensurately higher convective flux in order to conserve the total flux. The internal energy is composed of the thermal energy, e_{th}, the energy stored in ionisation, e_{ion} and the energy required for molecular dissociation, e_{diss}, but only e_{th} is monitored separately. In the hottest models, the thermal energy (yellow line) is clearly the dominant component of the internal energy, while in the cooler models it makes a progressively smaller contribution, between $\tau_{Ross} \simeq 10^{-4} - 10^{2}$. It continues to be the major contribution above this for all models.

The acoustic flux (cyan line) contributes significantly in deeper layers, but is largely insignificant in optically thin layers. Its contribution for these models reaches a much larger fraction than has been reported for hotter stars, where the contribution stabilises around the 7% mark (Magic et al. 2013). This might be due to the cooler models having comparatively lower internal energy as the ionisation fraction becomes lower in these stars. The viscous flux (black line) is insignificant for all models reflecting the robustness of the calculation, as the viscosity is largely artificial and added to ensure numerical stability of the system.

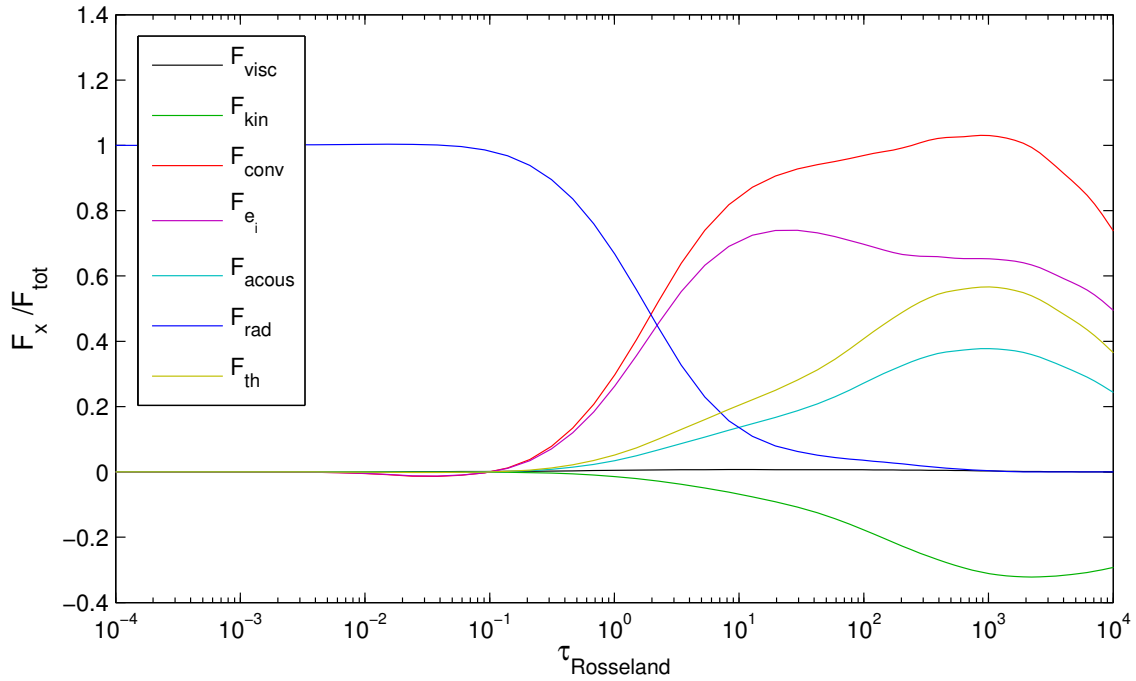

Figure 3.8: The behaviour of the normalised energy fluxes F_x/F_{tot} with Rosseland optical depth in the atmosphere for the $T_{eff} = 3800K$ model. The radiative (blue) and convective (red) fluxes are of principal interest. The major components constituting the convective flux, internal energy (F_{e_i}), thermal (F_{th}), acoustic (F_{acous}) and kinetic (F_{kin}) are also shown. The viscous energy flux (F_{visc}) is also shown, although it contributes negligibly throughout the atmospheric structure.

3.3.3 Atmospheric structure

A 3D model is inhomogeneous by its nature, and while the simplest way to average the resulting datacubes would be to simply average over the horizontal plane, this is not the most physically correct approach. As the quantities we are really interested in ultimately relate to the formation of the spectrum, it is more correct to consider the average over surfaces of constant optical depth (iso-tau). Unfortunately, as quasi-hydrostatic equilibrium is enforced on the physical height scale, this means that iso-tau averages will necessarily exhibit small deviations from conserving exactly the conservation equations and hydrostatic equilibrium.

Figure 3.14 shows the temperature stratification of the atmosphere with optical depth (solid $< 3D >$ dotted 1D). The upper panel shows the temperature dependence with Rosseland optical depth, $\tau_{Rosseland}$, over the whole atmospheric structure - reaching down into the deep convection zone at high optical depth and out to the tenuous outer atmosphere in the very optically thin layers. The lower panel shows the same plot, but zooms in to highlight the crucial layers around the optical surface. As with figure 3.7, the (dotted) MARCS 1D models do not extend as far into the star and cut-off at $\tau_{Rosseland} = 10^2$, and due to the coverage of the MARCS model grid, not every $< 3D >$ model has an equivalent in 1D. The models broadly agree, although the small differences could be significant in terms of spectral line formation. The $< 3D >$ models are significantly cooler than the 1D models in the optically thick layers ($\Delta T \sim 200K$) corresponding to the hot, deep convective region of the atmosphere, but in the optically thin layers the temperature difference between the two is reduced ($\sim 50K$).

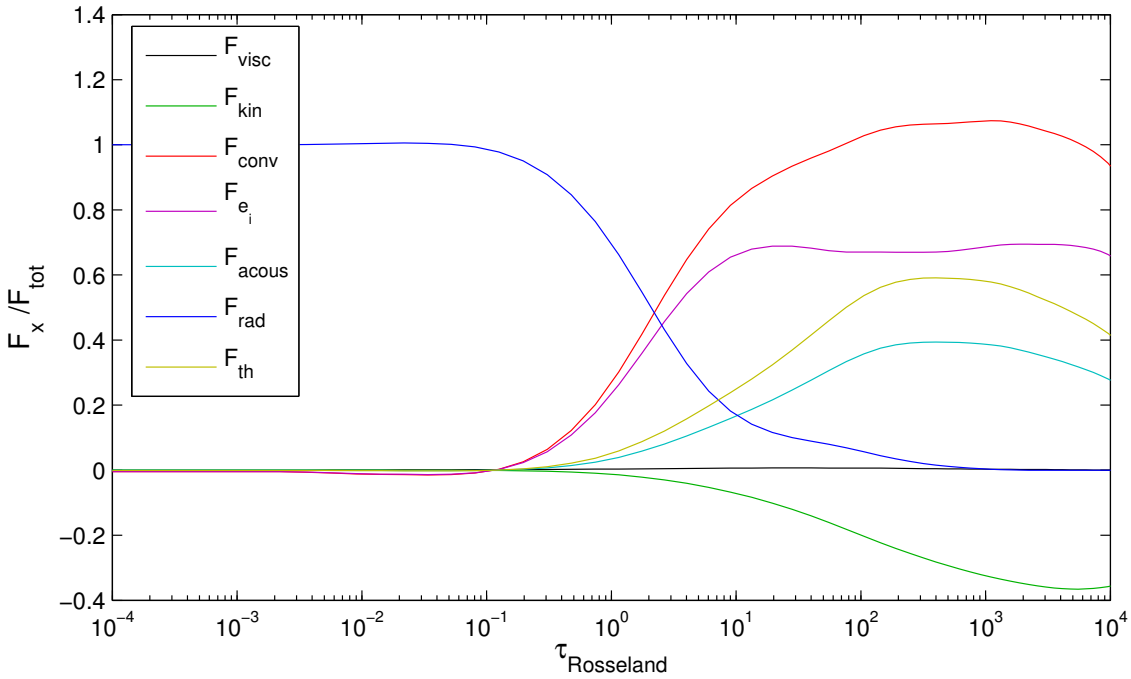

Figure 3.9: As Figure 3.8, but for the $T_{eff} = 3900K$ model.

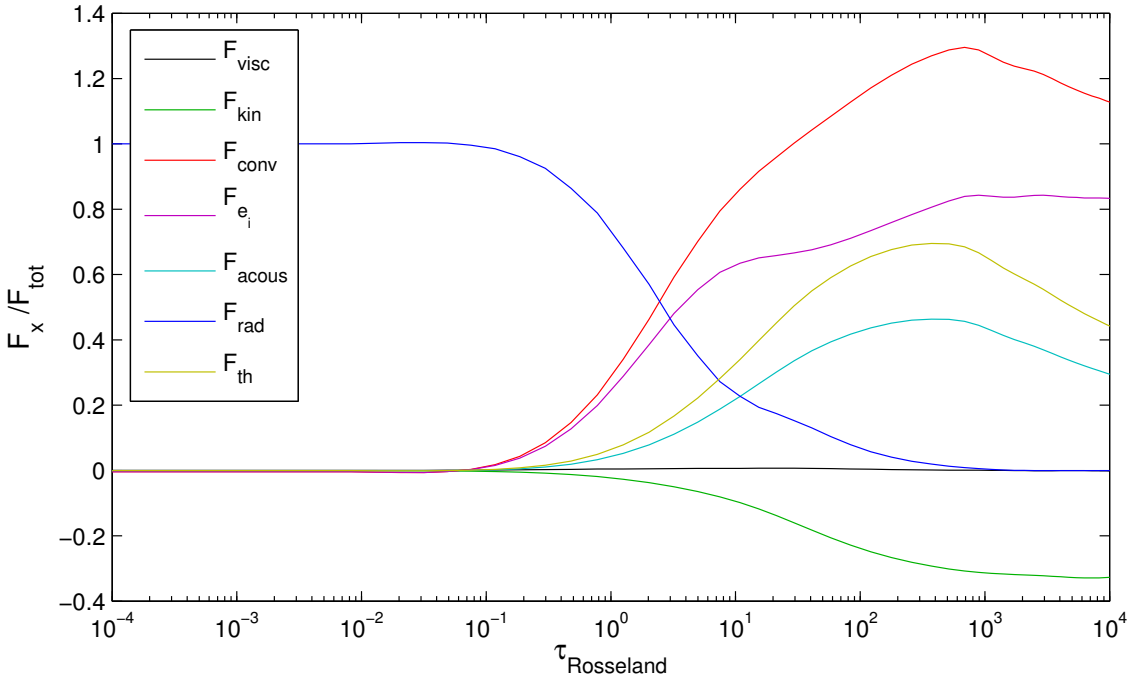

Figure 3.10: As Figure 3.8, but for the $T_{eff} = 4000K$ model.

The (dotted) 1D models are slightly steeper, particularly around the optical surface of $\tau = 1$. The shallower profile of the $< 3D >$ models derives from the flux profiles in the previous figures. The 3D models transport energy in the region both convectively and radiatively. Radiative transport is

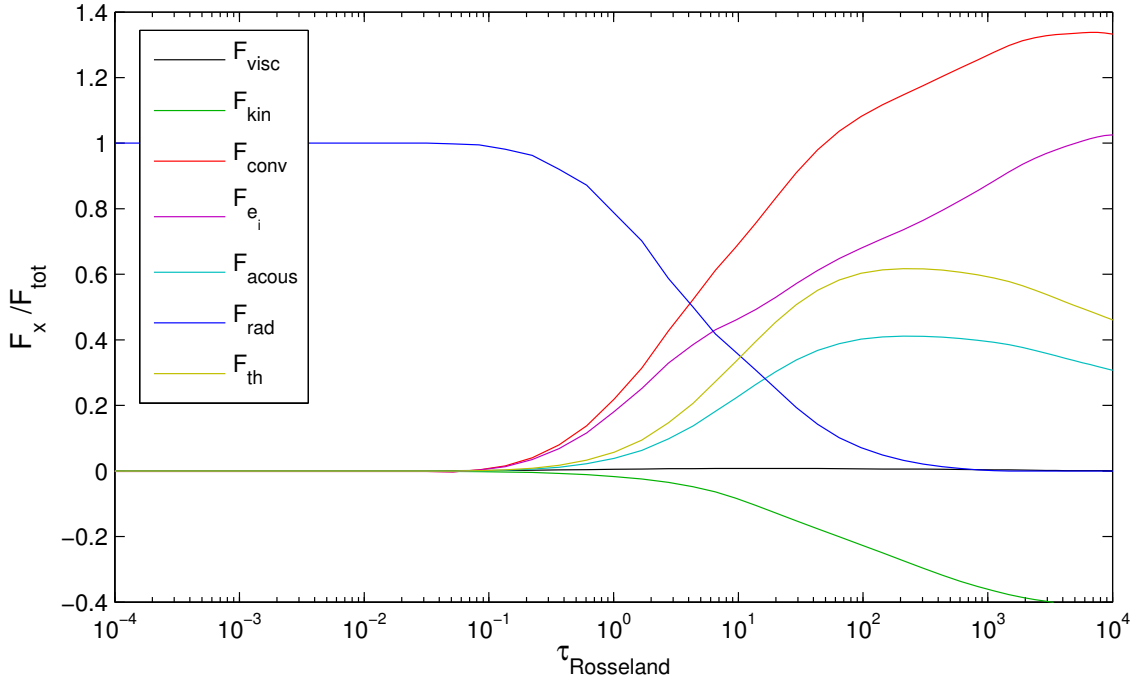

Figure 3.11: As Figure 3.8, but for the $T_{eff} = 4150K$ model.

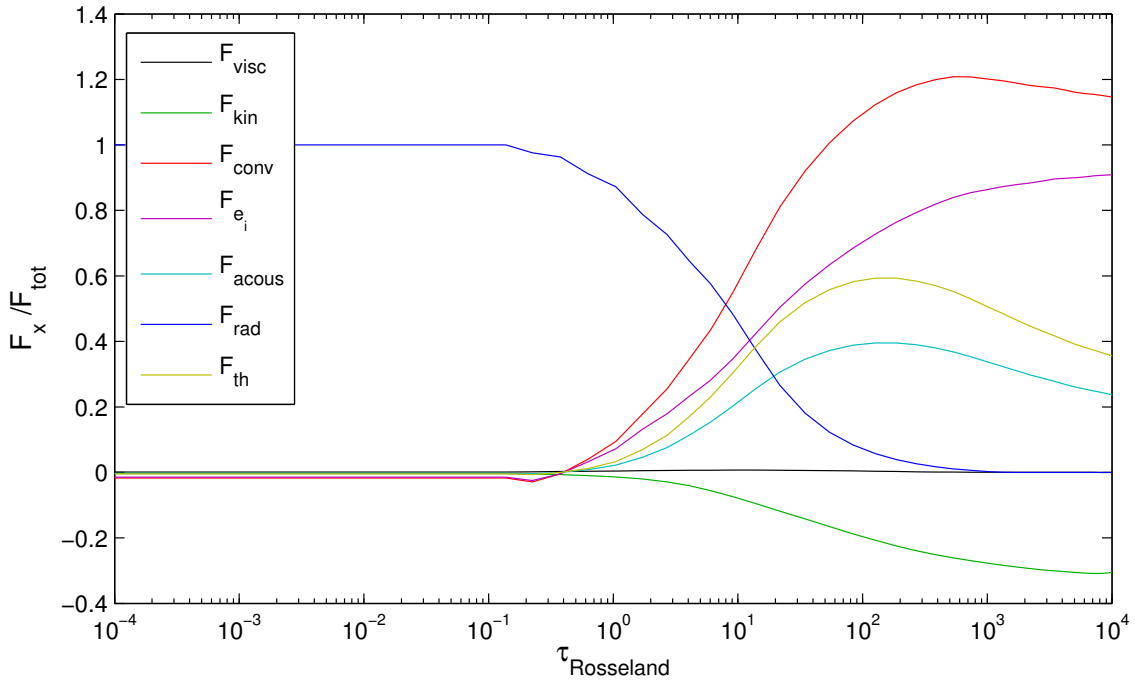

Figure 3.12: As Figure 3.8, but for the $T_{eff} = 4300K$ model.

governed by the gradient of the temperature profile, therefore to transport the same energy without a significant contribution from convective overshooting requires a steeper temperature profile from the 1D model. Again while the differences are not dramatic they are, though small, significant.

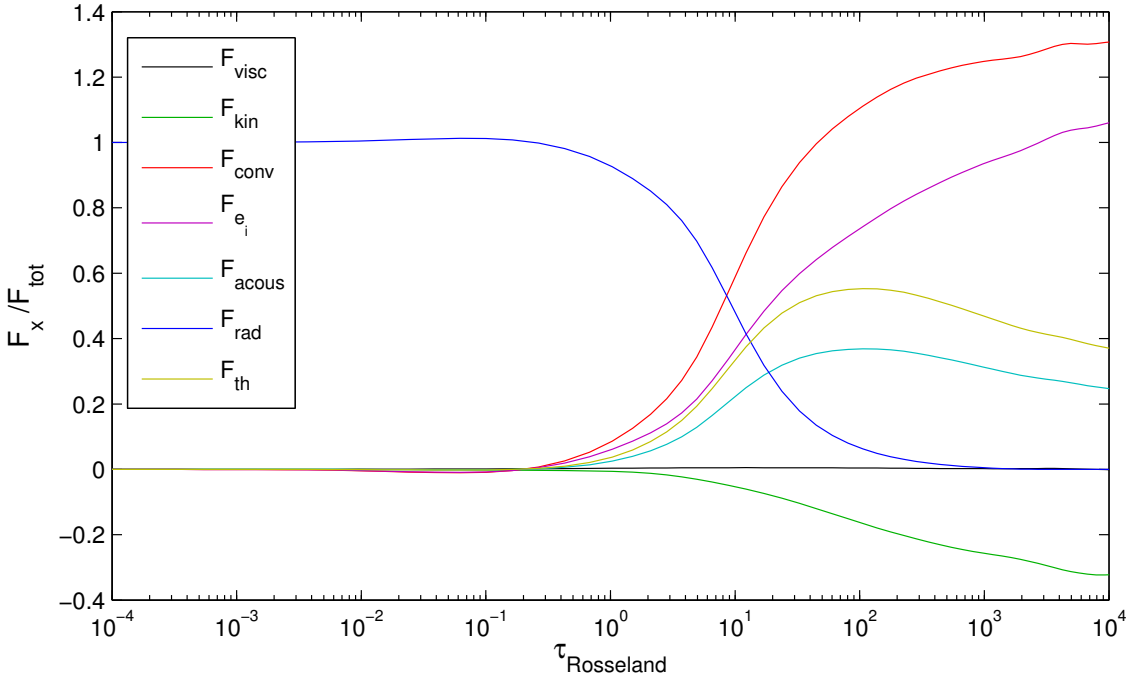

Figure 3.13: As Figure 3.8, but for the $T_{eff} = 4500K$ model.

Figure 3.15 shows the atmospheric pressure stratification with Rosseland optical depth. The pressures for the $< 3D >$ (solid) models are systematically lower than in the equivalent 1D (dotted) models. While the $< 3D >$ models show reduced pressure compared to 1D the trends across the range of Rosseland optical depth remain very similar and the trend with effective temperature seems unchanged.

Figure 3.16 shows the density stratification with Rosseland optical depth. Once again the upper panel shows the full extent of the atmosphere, while the lower panel highlights the most interesting layers around optical depth unity. Broadly, the (dotted) 1D models show systematically higher densities than the $< 3D >$ (solid) models. Over the photosphere (lower panel), the $< 3D >$ models have lower densities and, furthermore, across the range of effective temperatures the density offset seems to be almost constant. Lower densities are to be expected for the $< 3D >$ models as, although the cooler temperatures would be expected to lead to higher densities, the lower pressures have a far stronger influence on the density, through the equation-of-state, see Figure 4.3. Figure 3.17 shows the turbulent pressure with Rosseland opacity, for lines representing models of different effective temperatures.The figure shows that turbulent pressures are large in the optically thick layers ($\tau_{Rosseland} > 1$) and decline towards the optically thin layers after peaking around $\tau_{Rosseland} = 10^3$. Of note, is that while the turbulent pressure declines in the optically thin layers, it does not do so very dramatically, meaning that the turbulent pressure remains sizable even around $\tau_{Rosseland} = 10^{-2}$. This reflects the fundamental difference between the 1D and $< 3D >$ models, as the dynamics of the system in $< 3D >$ result in a contribution from turbulent pressure at all optical depths. While models in 1D could calculate a turbulent pressure contribution from the convective velocity given by mixing-length theory, this is not included self-consistently and would not extend beyond the limits of classical stability into the overshooting region.

With effective temperature, the turbulent pressures are smaller, with pressures declining in the op-

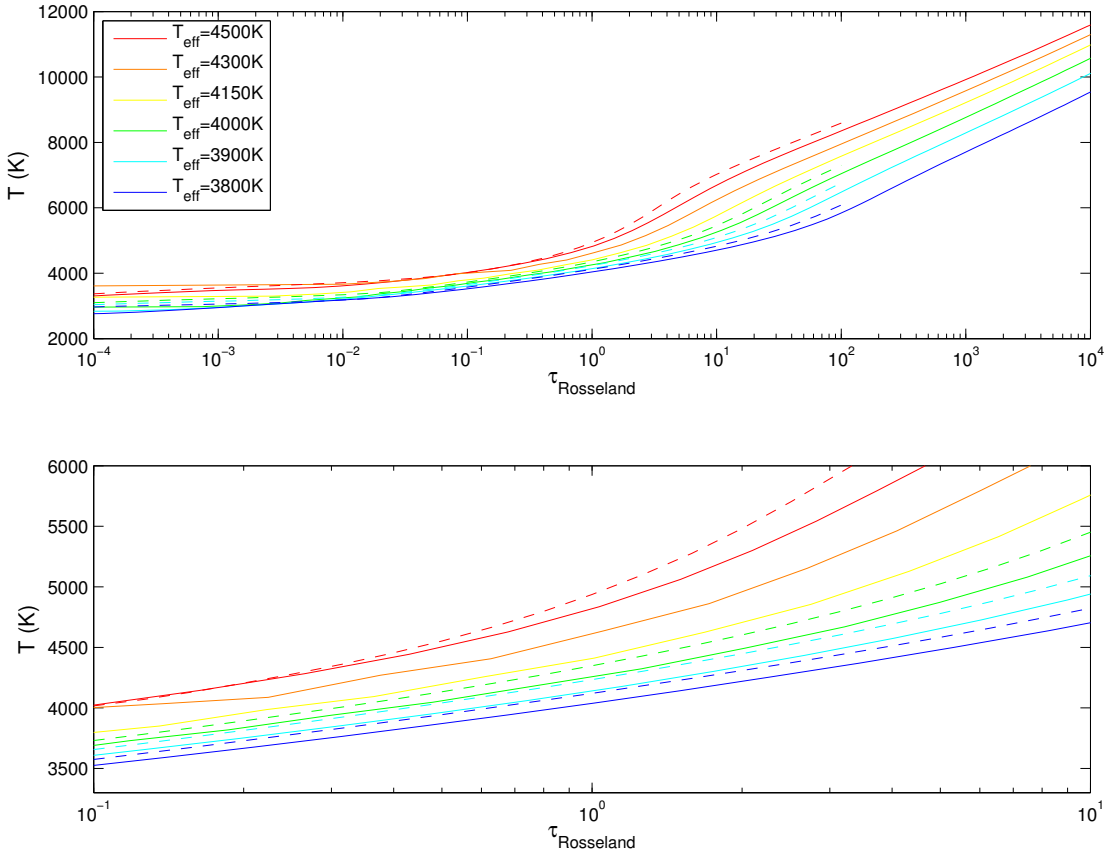

Figure 3.14: The local gas temperature stratification with Rosseland optical depth over the photosphere. The solid lines show the $< 3D >$ stratifications averaged over constant optical depth, while the dashed lines show the 1D models with the same input parameters. It should be noted that the 1D models do not include the convection zone and are therefore much shallower, cutting off at $\tau_{Rossland} = 100$, reflecting the end of the computational domain only. The upper panel shows the full atmospheric structure, while the lower panel zooms in to show the critical layers around the optical surface of the star. Not every $< 3D >$ model has an equivalent 1D model, as the 1D model grid has finite resolution.

tically thin region most steeply in cooler models. This reflects the neater, less violent convection commented on for the surface intensities in Section 3.3.1.

Normalising the turbulent pressure to the total pressure, in Figure 3.18, allows the contribution to the total pressure to be considered. Again, turbulent pressure is most important in the hottest models, becoming less so for decreasing effective temperature. The peak contribution of the turbulent to the total pressure occurs at $\sim$ 3.5% for the hottest model, and only a few percent for the cooler models.The location of the peak contribution shifts noticeably from the optically thick layers for hot models to the optical surface for the coolest. This means that although the overall effect is smaller for cooler models, its peak occurs nearer the line-forming regions, which may have consequences for the spectral synthesis. One final point to note is that turbulent pressure continues to contribute $O(1\%)$ of the pressure throughout the line-forming layers to the very optically thin atmosphere.

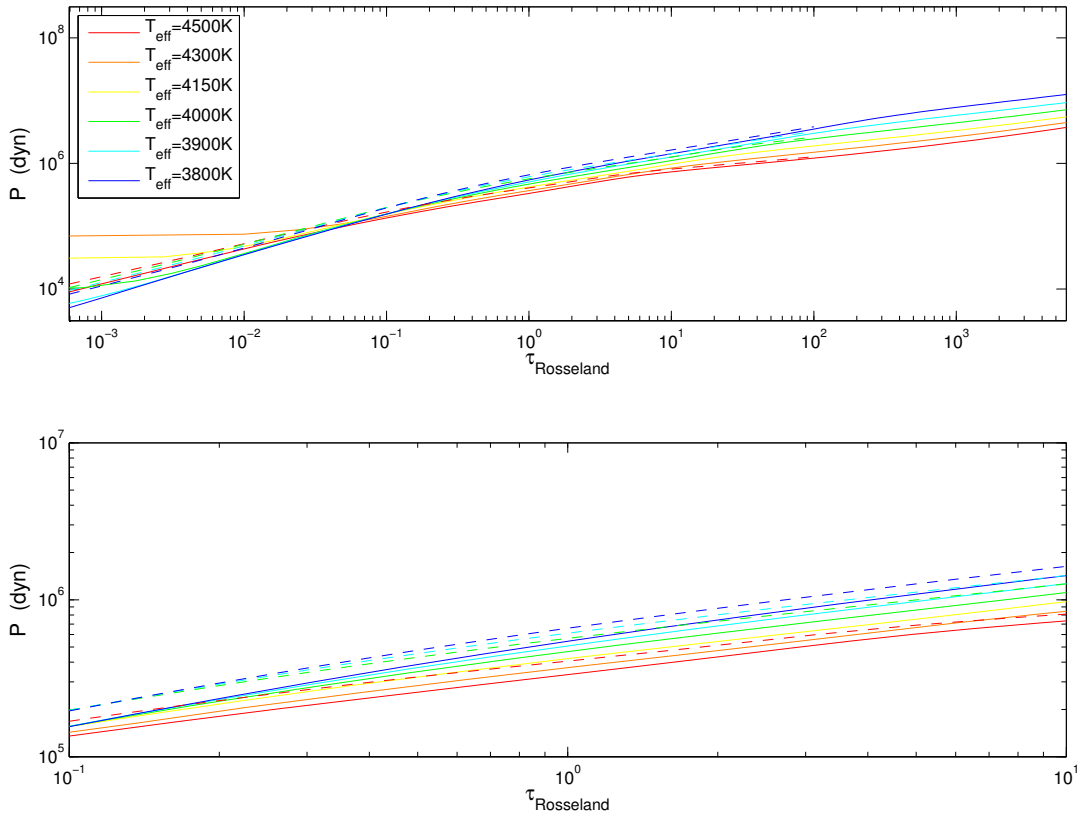

Figure 3.15: The pressure stratification with Rosseland optical depth over the photosphere. The solid lines show the $< 3D >$ stratifications averaged over constant optical depth, while the dashed lines show the 1D models with the same input parameters. 1D models do not include the convection zone and therefore do not extend so deep, cutting off at $\tau_{Rossland} = 100$. The upper panel shows the full atmospheric structure, while the lower panel zooms in to show the critical layers around the optical surface of the star.

Figure 3.19 shows the convective velocities with Rosseland optical depth. The convective velocities remain significant out well beyond classical stability. Unsurprisingly, given the definition of turbulent pressure, the convective velocities show very similar trends to the turbulent pressure, with hotter models producing faster mixing velocities and the peak velocities in cooler models moving towards the optical surface. Of interest here is the values of the convective velocities, that are of order $\sim 0.5 km/s$. This is significant and measurable in analysis of spectra. Furthermore, the convective velocity evolves over the atmospheric structure, meaning that peak velocity is $\sim 1.5 - 2$ times the velocity in the optically thin layers. Again, as this would be a measurable difference, with lines formed at different heights showing the signature of different velocity fields. The magnitude of these fields and their shape across the atmospheric structure is a powerful test of these atmosphere models, but one which would need quality high-resolution spectroscopy to be carried out.

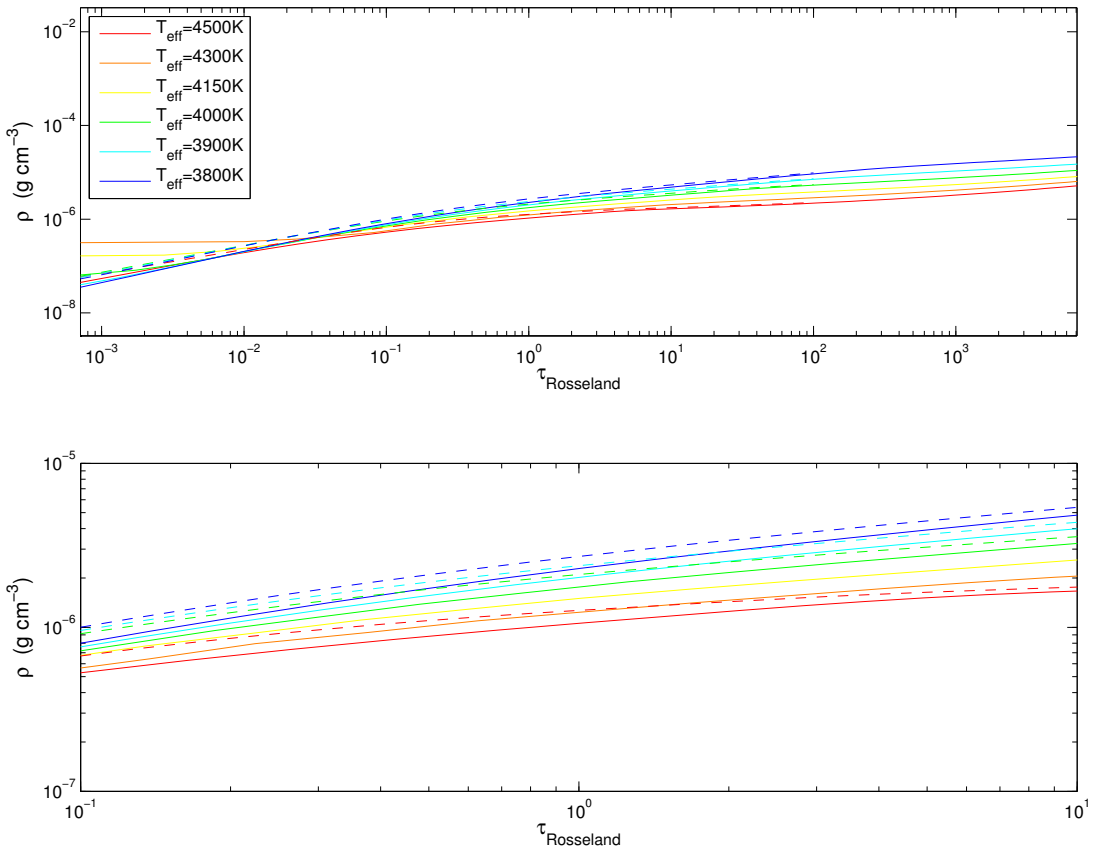

Figure 3.16: The density stratification with Rosseland optical depth over the photosphere. $< 3D >$ stratifications (solid) are averaged over constant optical depth, while 1D models have the same stellar parameters as the 3D models. The upper panel shows the full model, while the lower panel zooms in to show the critical layers around the optical surface of the star.

3.3.4 Spectra

Synthetic spectra, where continuum and line flux profiles are calculated by performing radiative transfer through a model atmosphere, are extremely useful in testing the validity of models atmospheres. By comparing observed stellar spectra to those created using synthetic spectral synthesis, key assumptions may be tested and model parameters varied, as well as allowing the measurement of physical quantities such as chemical composition, velocity fields and the determination of stellar parameters.

Spectral lines form at very different height in the stellar atmosphere, meaning different spectral lines sample physical conditions across the atmospheric structure. Late-type stars have a convection zone forming their lower boundary, resulting in an inhomogeneous medium with strong flow fields that affect the line profile (e.g. Nordlund et al. 2009). Calculating line profiles constitutes a whole field in itself as, in principle, it is a non-local problem depending not only on local atmospheric conditions, but coupled with long-range atmospheric conditions through the radiation field. Excluding long-range interactions by assuming local thermodynamic equilibrium (LTE) means a tremendous simplification

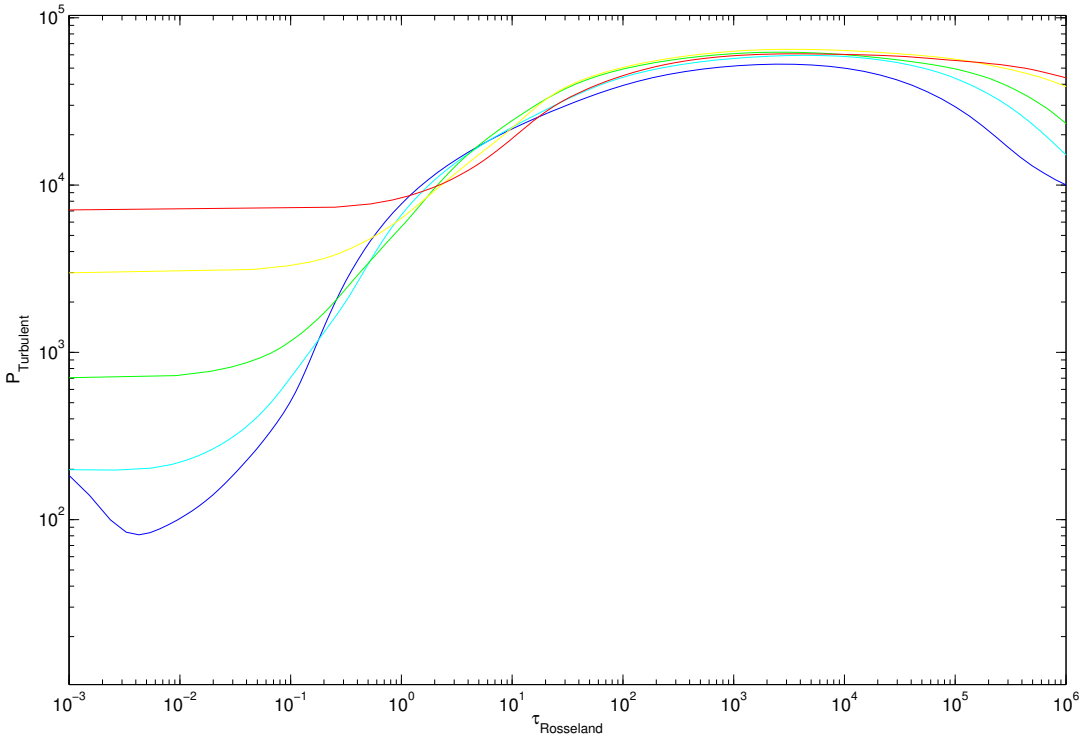

Figure 3.17: Turbulent pressure (dyn/cm^2) with Rosseland optical depth in dwarf stars for a series of effective temperatures. The solid lines show $< 3D >$ models where quantities are averaged over surfaces on constant optical depth, rather than geometric depth in the atmosphere. Of particular note is the continued component of turbulent pressure out into the very optically thin layers, which is neglected in hydrostatic models.

of line formation calculations and therefore is commonly adopted. Unfortunately, it is rarely a good approximation. Equally, 3D line formation studies are becoming feasible (e.g. Collet et al. 2007; Behara et al. 2010) but are still complex and computationally costly. These studies show that the temperature stratification and inhomogeneities have an important effect on line formation for metal-poor stars. Instead 1D LTE studies are common and relatively straightforward, and adopted here to give a handle on the mean structural differences between $< 3D >$ and 1D models.

While binned radiative transfer under the multi-group approximation is sufficient for the hydrodynamical model, a more detailed post-processing treatment is necessary for this application.

Synthetic spectra in red and near-infrared are calculated for six models, three mean 3D stratifications and their equivalent counterparts modelled in 1D. The spectra cover the range 6000Å to 8000Å in wavelength, with $\Delta\lambda \sim 0.062$Å, surface gravity $g = 10^5 cms^{-2}$and solar abundances.

Figure 3.20 shows the spectrum over the full spectral window for the $T_{eff} = 3800K$ models. The upper panel overplots the red 1D model with the mean 3D model in blue. The two lower panels show the 1D (red) and $< 3D >$ (blue) spectra respectively.

The two spectra are broadly very similar at this level, as it to be excepted, as the differences in their atmospheric structure are comparatively moderate and opacities would not be expected to very so

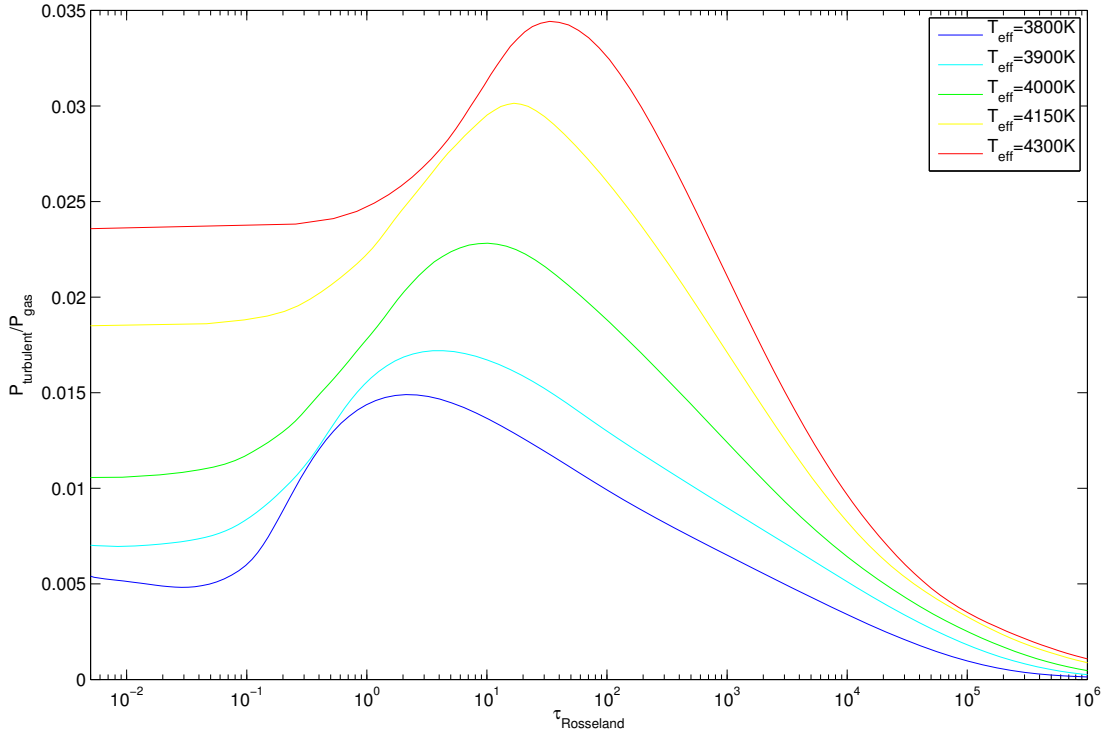

Figure 3.18: Ratio of turbulent pressure to gas pressure with Rosseland optical depth. The models are for dwarf stars, log(g)=5,0, with solar metallicity and the 3D datacubes are averaged over surfaces of constant optical depth.

dramatically over these differences in temperature and pressure. The only real difference that can be seen at this level is that the line centres for the 1D model extend below those for the mean 3D model. This is a result of the smearing out of the line by the implicit velocity fields in the mean 3D model, broadening the line centre, while the 1D model does not take account of these fields in any way and therefore the $< 3D >$ model shows a more accurate representation of the atmosphere, without additional free parameters.

Figure 3.21 shows a restricted section of the spectrum at the beginning of the wavelength range, where the individual line profiles begin to become more evident. At this point, it is clear that the continua are very close, but the line cores are quite different. In order to look in more detail at the flux across the line profile it is necessary to consider a particular line.

Figure 3.22 shows the line profile of a neutral Calcium line, Ca I at 6122Å. It is a strong line with broad wings. As expected the core of the 1D model is significantly deeper than the $< 3D >$ line core, but also evident is the marginally wider wings in the lower portion of the line profile. If the same line, with and without broadening, was considered, it would be expected that the broadened line would have wider wings, thus conserving flux over the whole line profile. However, the wider wings in the 1D models suggests that the line in the $3D$ model is slightly weaker than in the 1D model. Were this work considering abundance determination, this would translate to a lower population of CaI absorbers in the mean 3D atmosphere, compared to the 1D case. Qualitatively, this is in agreement with the downward revision of the solar metallicity when considered with 3D models. The next figure,

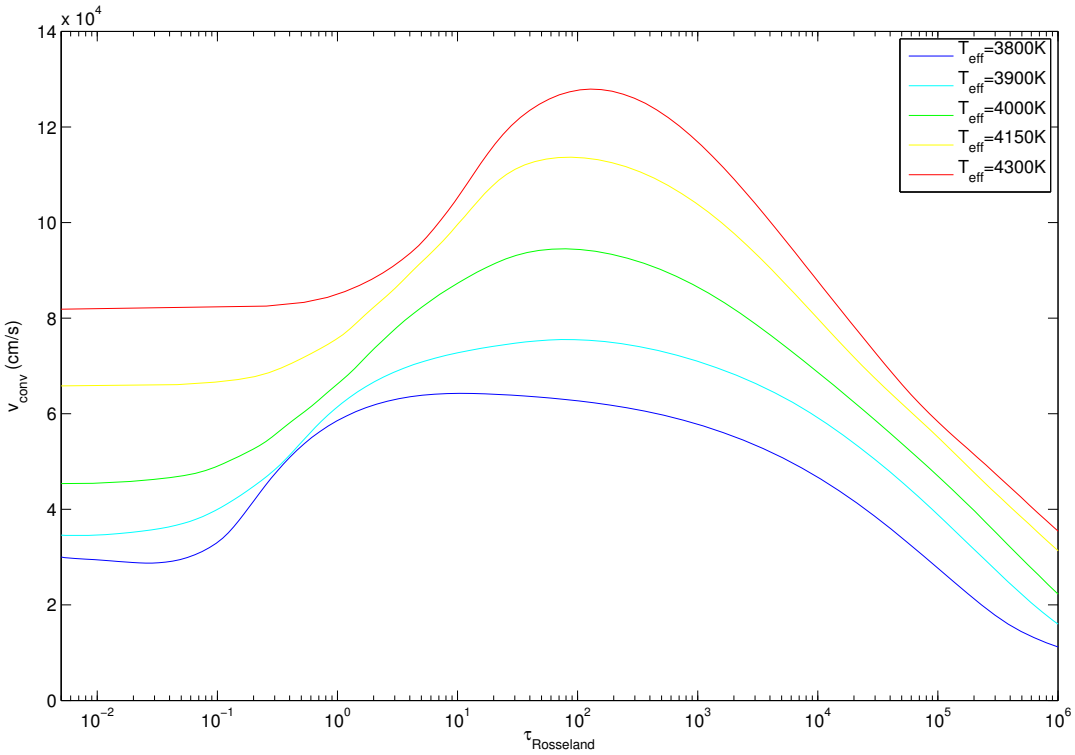

Figure 3.19: The convective velocity of the gas with Rosseland optical depth. Of note is that the convective velocities remain sizable out to very low optical depths.

Figure 3.23, shows the H_α line at 6562Å. This line is much weaker but conforms to the pattern of the strong CaI line, in that the line core is deeper in 1D, where the wings are also slightly wider. Finally, Figure 3.24 shows a molecular line of TiO. Once again, the 1D spectrum has a systematically deeper line core and a wider line profile throughout the line, including the blend at 6358.8nm, compared to the $< 3D >$ model.

Figures 3.25, 3.26, 3.27, 3.28 and 3.29 show the equivalent plots for the $T_{eff} = 3900K$ model. The hotter model shows shallower line cores in general than either the 1D and $< 3D >$ cooler models. Concentrating on the CaI line, Figure 3.27, the line core is $\sim 5\%$ shallower, while the wings are narrower (and $\sim 2\%$ shallower) over most of the profile. In between, the profiles are closer, therefore the wings and core are fairly sensitive temperature indicators, but near the core is comparatively insensitive. Figure 3.28 shows a poorer correspondence between the 1D and $< 3D >$ models, than for the cooler model in Figure 3.23. The line itself is deeper and still follows the general trend of having a shallower line core and narrower wings in $< 3D >$. With effective temperature, this line backs the trend of shallower lines, becoming deeper from $T_{eff} = 3800K$ to $T_{eff} = 3900K$. It should be noted that this is a weak line and therefore samples a different part of the atmosphere to the stronger lines considered in the other plots. The line at 6358.7nm shows little variation with effective temperature, compared to the $T_{eff} = 3800K$ model, with the line core being only $\sim 1\%$ shallower. Marginally deeper line cores and wider wings are found for 1D models compared to the $< 3D >$, but this is not a good line to probe the differences in detail around this temperature.

Figures 3.30, 3.31, 3.32, 3.33 and 3.34 show the same again, but for $T_{eff} = 4000K$. The $T_{eff} =$

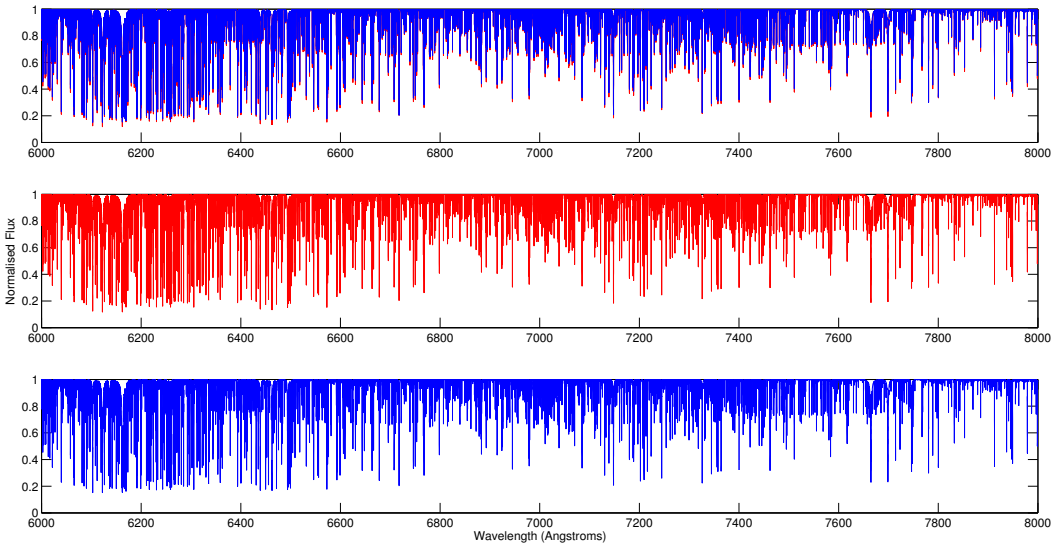

Figure 3.20: Emergent flux with wavelength, normalised to the continuum for 1D (red) and $< 3D >$ (blue) for the $T_{eff} = 3800K$ model defined in Table 3.1. The wavelength coverage is λ =6000Å-8000Å covering the red and near-infrared. The upper panel shows the 1D and $< 3D >$ models overplotted, the middle panel the 1D model alone and the lower panel shows the $< 3D >$ model.

$4000K$ model yields shallower line cores, in general, than both the cooler models, with a stronger difference between $T_{eff} = 3900K$ -$T_{eff} = 4000K$ than $T_{eff} = 3800K$ - $T_{eff} = 3900K$. Moving

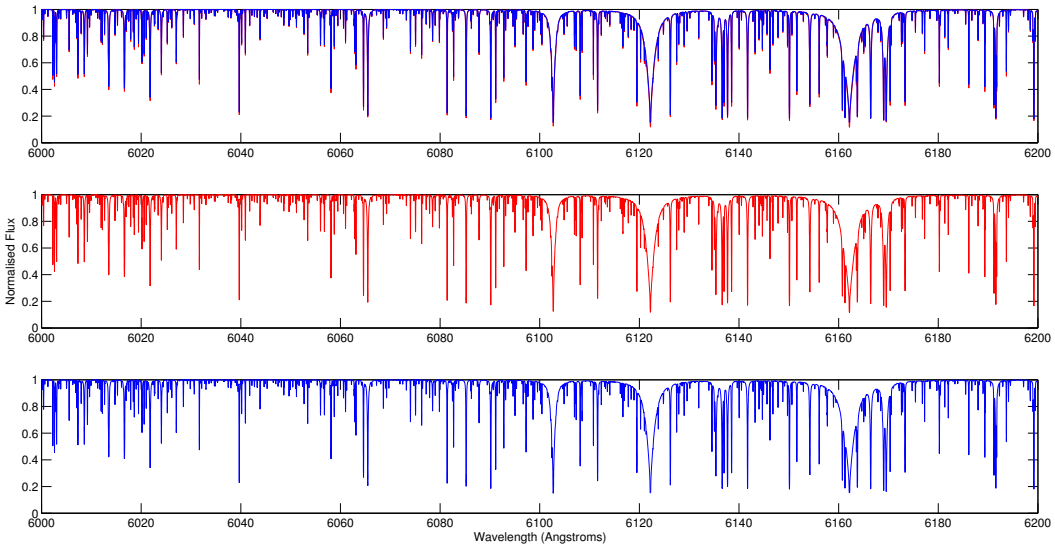

Figure 3.21: Emergent flux with wavelength, normalised to the continuum for 1D (red) and $< 3D >$ (blue) for the $T_{eff} = 3800K$ model defined in Table 3.1. The wavelength coverage is λ =6000Å-8000Å covering the red and near-infrared. The upper panel shows the 1D and $< 3D >$ models overplotted, the middle panel the 1D model alone and the lower panel shows the $< 3D >$ model.

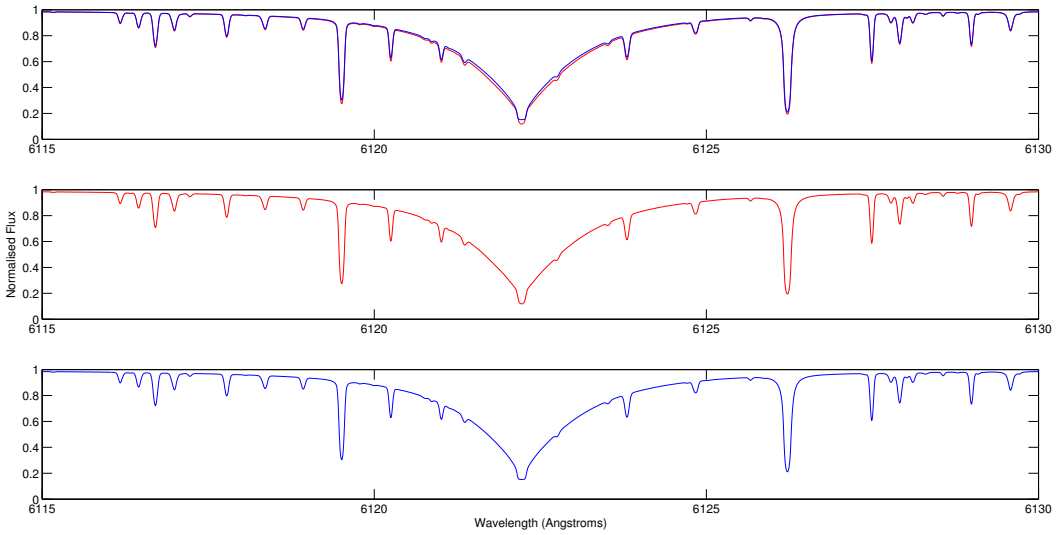

Figure 3.22: Emergent flux profile of the CaI line at 6122Å for the $T_{eff} = 3800K$. Again the upper panel shows the 1D and $< 3D >$ models overplotted, the middle panel the 1D model alone and the lower panel shows the $< 3D >$ model.

to consider individual spectral lines, the CaI line in Figure 3.32, shows a significantly shallower profile and narrowed wings compared to the $T_{eff} = 3900K$ model. The core is around $\sim 10 - 15\%$ shallower, while the wings are typically $\sim 2 - 3\%$ narrower in the hotter model. Compared to the $< 3D >$ model, the 1D model is deeper and has wider wings again showing that the $< 3D >$ result mimics the properties of a warmer 1D model. Figure 3.33 again backs the general trend with effective temperature, by being $\sim 5\%$ deeper in the core than the cooler model. Compared to the 1D model the $< 3D >$ model still shows a weaker line, meaning that this is a systematic effect between 1D and $< 3D >$ not merely the result of slightly different height sensitivity of the line. The TiO line in Figure 3.34 changes considerably with effective temperature, resulting in a line core that is $\sim 8 - 10\%$ shallower than the model only 100K cooler. While the core for this line shows a marked difference, the wings correspond fairly closely being only $\sim 1\%$ narrower. Comparing 1D and $< 3D >$ the general trend of deeper and wider 1D profiles is continued and can be seen quite clearly.

Quantitative spectral analysis will find that different parts and lines of the spectrum are more or less sensitive to the differences between 1D and $< 3D >$, as a result of lines forming at different heights in the atmosphere and sampling the local atmospheric conditions there. However, one of the important successes of 1D models is providing a simple and consistent description of the whole atmosphere from only a few input parameters. In general, mean 3D models exhibit systematically shallower line cores and narrower spectral line profiles than their equivalent 1D models. Consequently, a 1D model fit to the same observed spectrum as a $< 3D >$ model will be warmer. In an attempt to roughly quantify this Figures 3.35, 3.36, 3.37, 3.38 and 3.39 show lines for three 1D models of differing effective temperatures, $T_{eff} = 3800K$ (blue), $T_{eff} = 3900K$ (green) and $T_{eff} = 4000K$(magenta). A $< 3D >$ model (black) with effective temperature $T_{eff} = 3900K$ is superimposed. Were there no differences between 1D and $< 3D >$ the black and green lines would coincide exactly. Green lines can be seen in several places in both Figure 3.35 and Figure 3.36. The Calcium line, see Figure 3.37, shows a substantially shallower line depth for the $< 3D >$ model compared to each of the 1D spectra,

while in the wings the $< 3D >$ model lies between the model of the same effective temperature and the model 100K hotter. To force correspondence between the two in the wings, a 1D model that is around 50K hotter than the $< 3D >$ would be required. Conversely, for the H_α line, see Figure 3.38, forcing the two to coincide would require a 1D model 30-50K cooler than the $< 3D >$ spectrum. Finally, the line at 6358.7nm, see Figure 3.39, lies both shallower and narrower than all 3 models in 1D and would require a model around 150-200K warmer than the effective temperature of the $< 3D >$ model. As a result, while general trends may be found the height sensitive nature of line-formation requires that the differences between 1D and $< 3D >$ models are accounted for across the full atmospheric structure.

3.4 Summary

3D hydrodynamic modelling is a powerful tool to investigate the real physics behind the atmospheric structure of late-type stars. In these objects convection dominates in the sub-surface layers governing the temperature stratification, dynamics, horizontal surface pattern and influencing strongly spectral line formation.

Examining for the first time cool dwarfs below $T_{eff} = 4500K$, convection determines the horizontal inhomogeneity. Consisting of cool downdrafts and hot upflows the convection pattern shows that hot

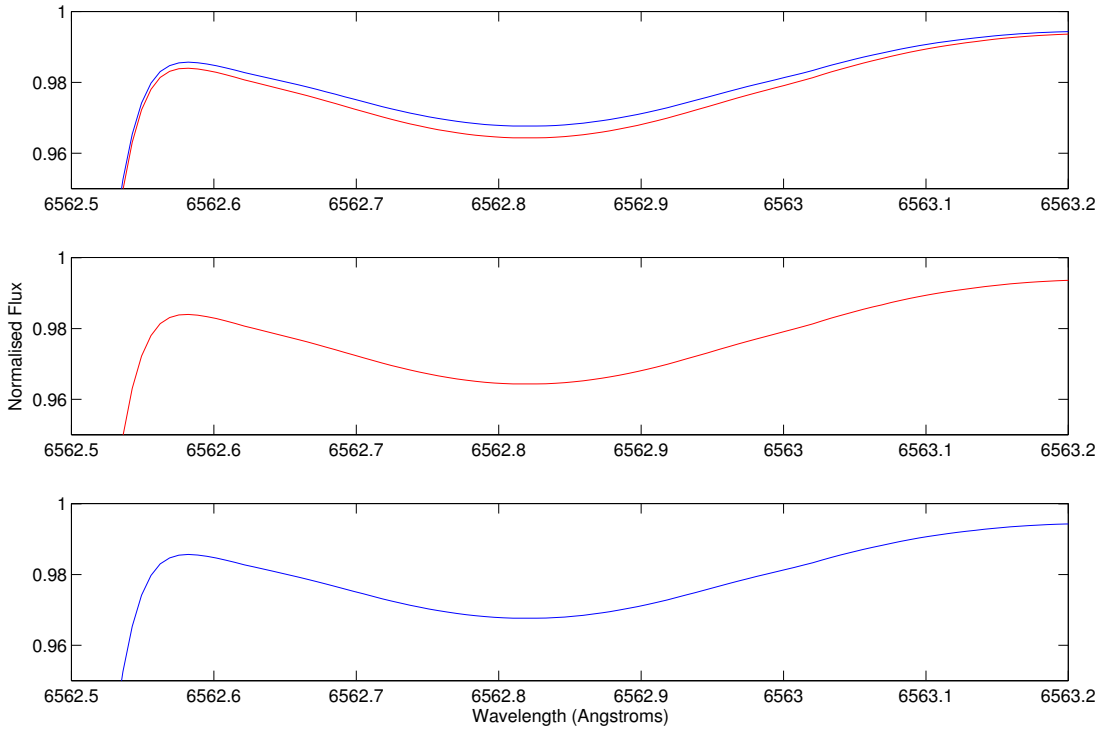

Figure 3.23: Emergent flux profile of the weak line H_α at 6562Å for the $T_{eff} = 3800K$. Upper panel is the 1D and $< 3D >$ models overplotted, the middle panel the 1D model and the lower panel the $< 3D >$ model.

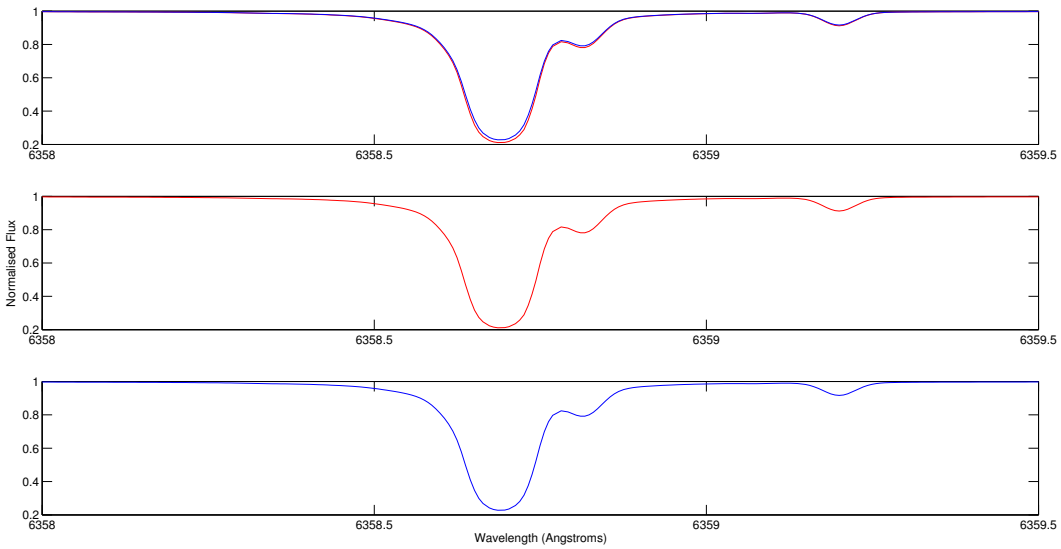

Figure 3.24: Emergent flux profile of a TiO molecular line at 6358.7Å for the $T_{eff} = 3800K$. Again the upper panel shows the 1D and $< 3D >$ models overplotted, the middle panel the 1D model alone and the lower panel shows the $< 3D >$ model.

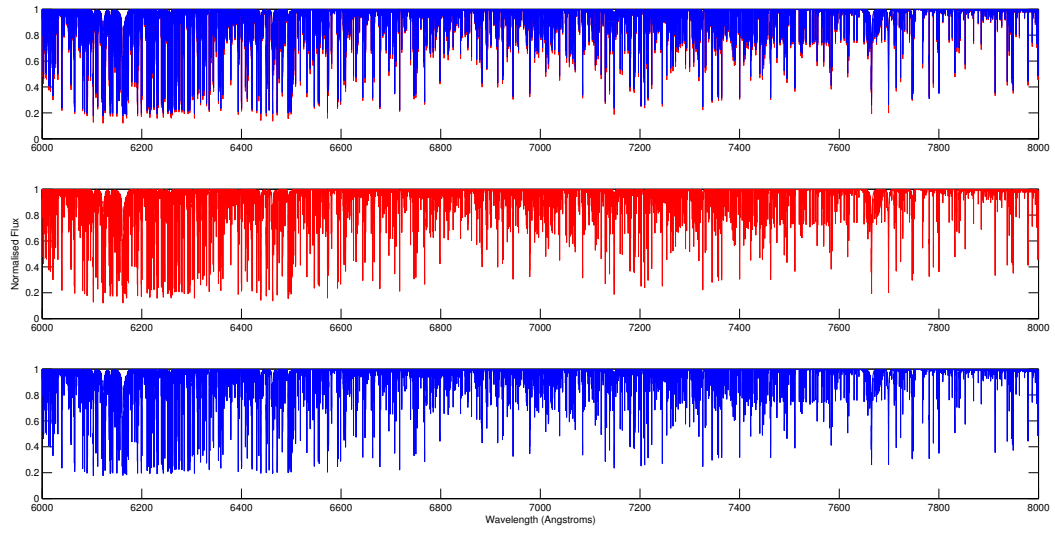

Figure 3.25: As Figure 3.20 but for an effective temperature of $T_{eff} = 3900K$.

convective cells dominate the surface area, with intergranular lanes being far more tightly entrained. Moving to cooler temperatures, the convection pattern becomes far more regular with both lane and granule intensity distributions becoming far more peaked. Simultaneously, the root-mean-square intensity fluctuations are decreasing in amplitude towards cooler temperatures. The overall effect is a neatening of the horizontal surface pattern for cooler spectral types.

Energy transport in the atmosphere may be studied in more detail with 3D hydrodynamic models. In particular, the true convective flux resulting from the dynamical nature of the atmosphere is com-

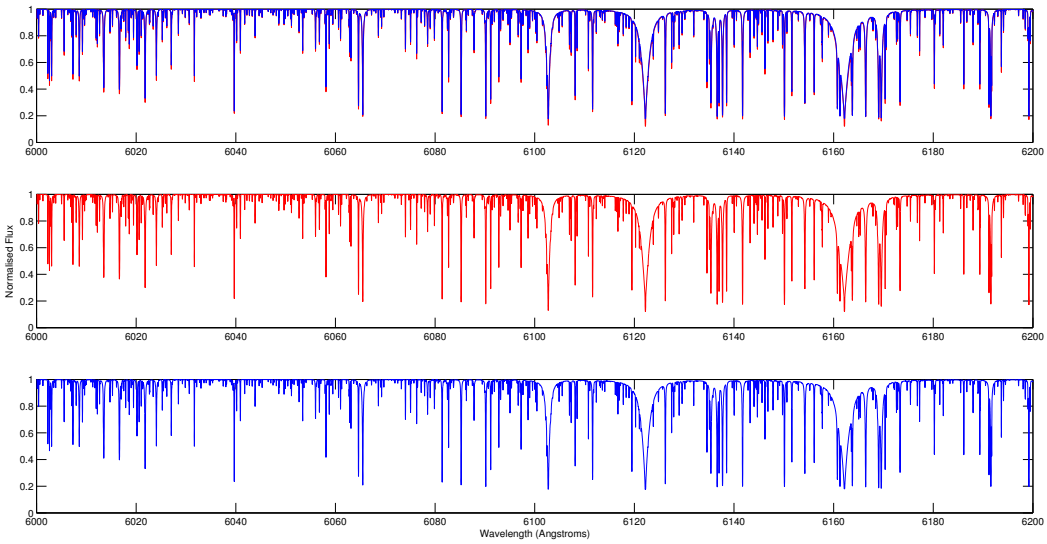

Figure 3.26: As Figure 3.21 but for an effective temperature of $T_{eff} = 3900K$.

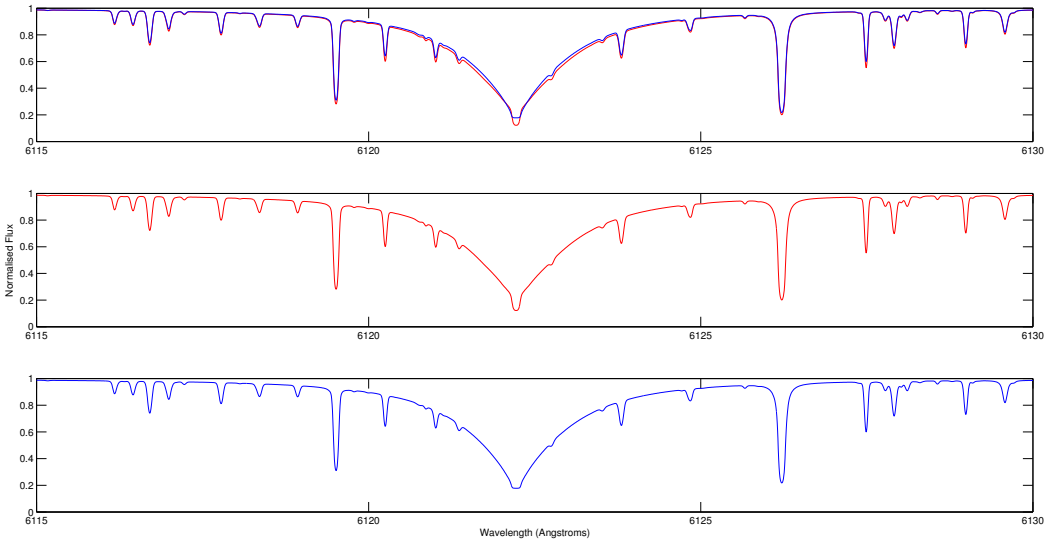

Figure 3.27: As Figure 3.22 but for an effective temperature of $T_{eff} = 3900K$.

puted, and shows that the transition from the convectively dominated sub-surface layers to the radiatively dominated outer atmosphere is considerably less sharp than 1D hydrostatic models suggest. Importantly, the hydrodynamical models show that convective energy flux continues to contribute significantly to the energy budget out into the line-forming region of the atmosphere - and this has important consequences for spectral synthesis models. Furthermore, in dynamic models the energy flux and its contributions may be examined across the atmosphere, showing that internal modes of energy, like ionisation, are critically important in energy transport in the deep atmospheric layers.

Convection also influences the structure of the atmosphere itself. As energy may be transported

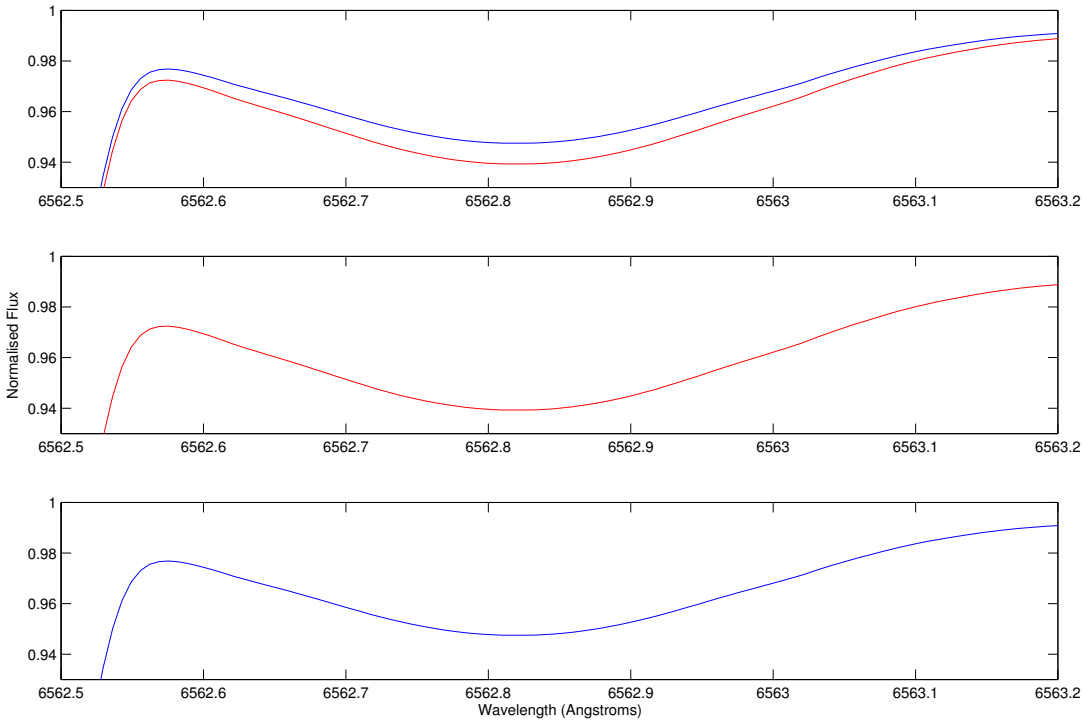

Figure 3.28: As Figure 3.23 but for an effective temperature of $T_{eff} = 3900K$.

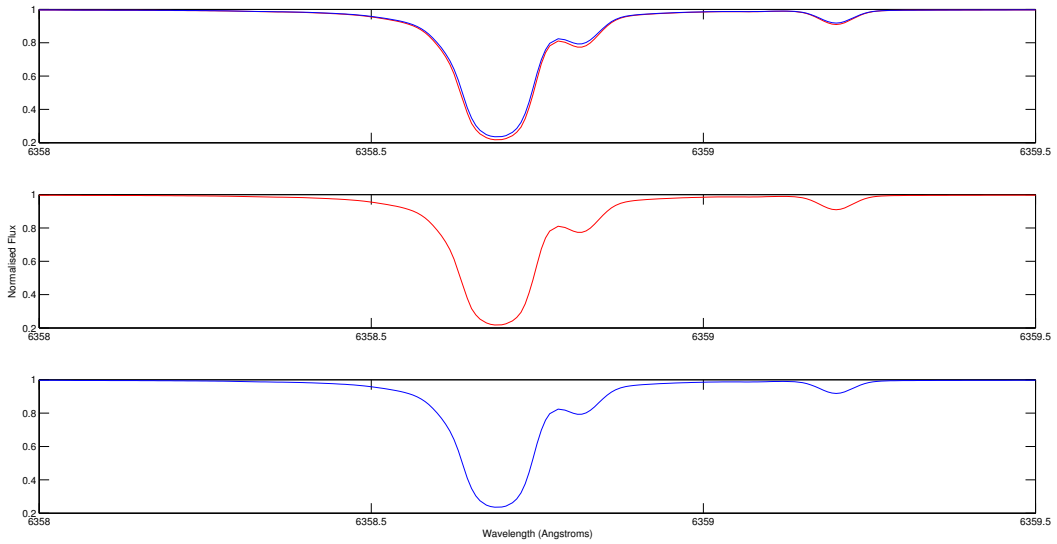

Figure 3.29: As Figure 3.24 but for an effective temperature of $T_{eff} = 3900K$.

convectively, as well as radiatively, in the optically thin layers, the atmospheric temperature gradient is shallower and, in general cooler, than in an equivalent 1D model. In addition, turbulent pressure contributes to the local condition for the dynamic models while it is absent from static structures.

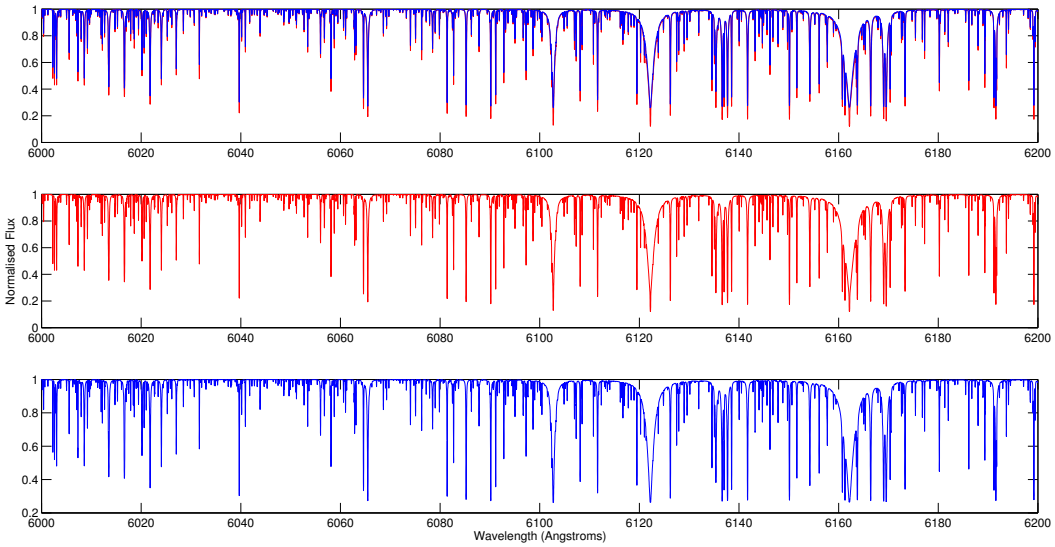

Figure 3.30: As Figure 3.20 but for an effective temperature of $T_{eff} = 4000K$.

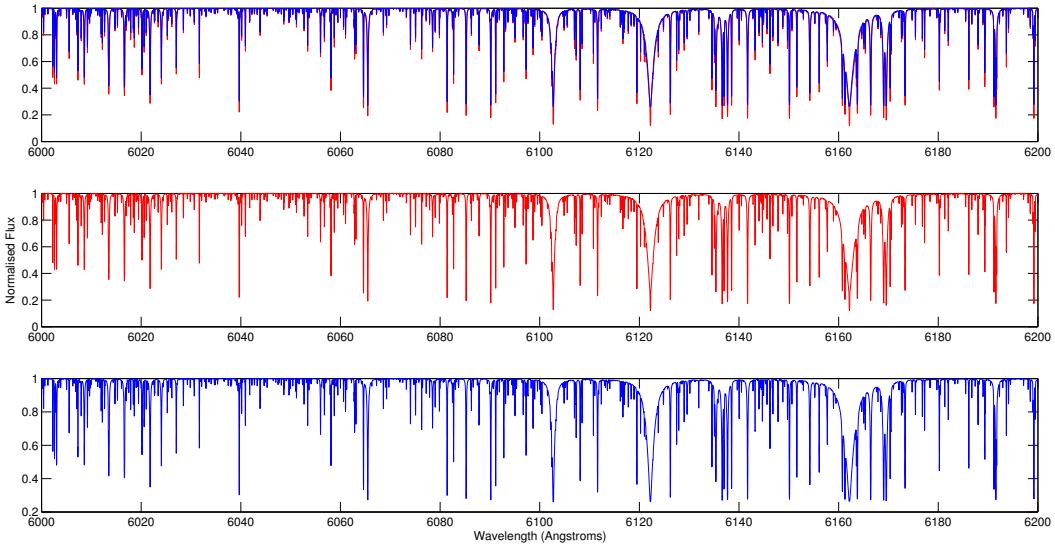

Figure 3.31: As Figure 3.21 but for an effective temperature of $T_{eff} = 4000K$.

Finally, the convective velocities in the dynamic models continue to be significant throughout the line-forming region in the dynamic model, which will have important ramifications in the shifting and broadening of spectral lines.

Comparisons of spectral synthesis performed on 1D and $< 3D >$ stratifications show important differences. Line cores are systematically deeper in 1D, due to the omission of atmospheric velocity fields broadening the line, while models of the same effective temperature show that 1D models also have wider wings for most lines, leading to a systematic overestimation of abundances in studies using these 1D models. Finally, the height-dependent formation of spectral lines makes it impossible to

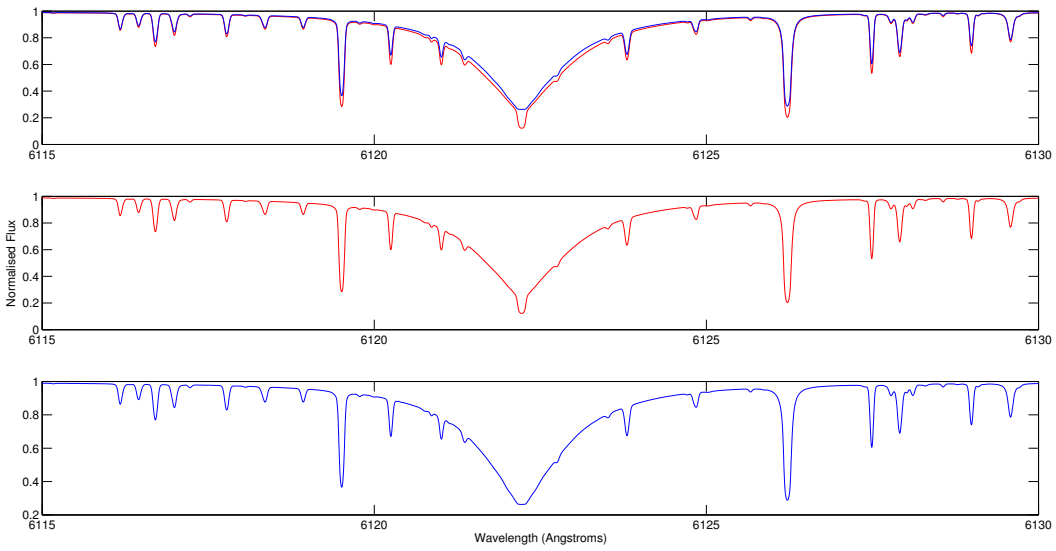

Figure 3.32: As Figure 3.22 but for an effective temperature of $T_{eff} = 4000K$.

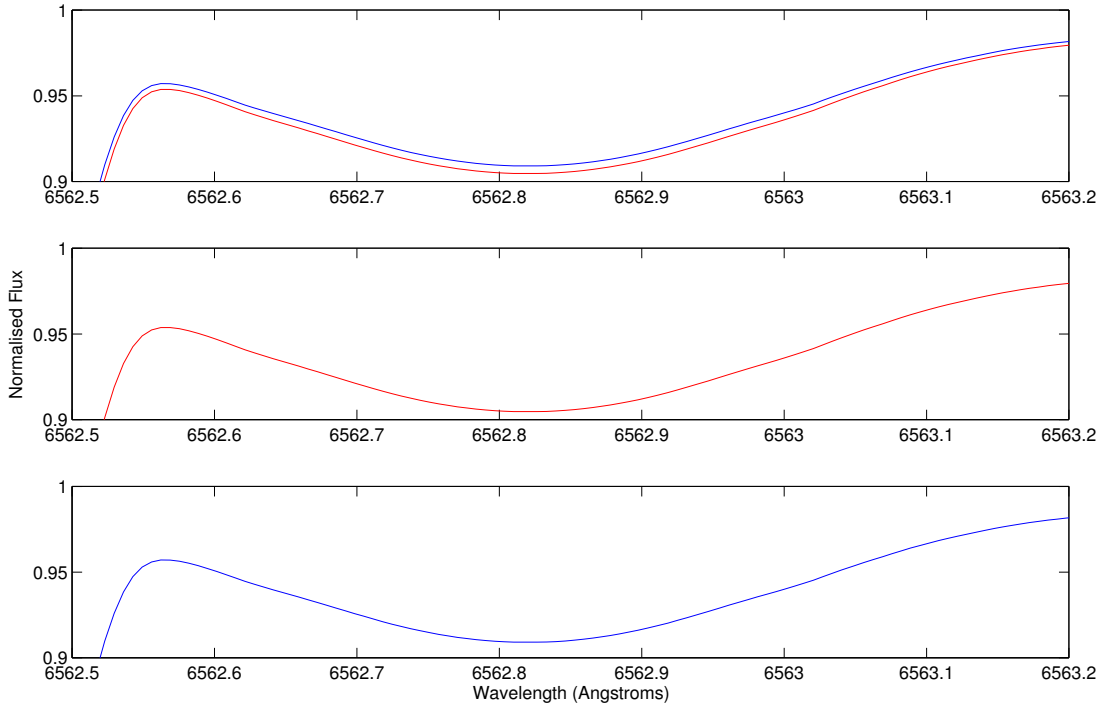

Figure 3.33: As Figure 3.23 but for an effective temperature of $T_{eff} = 4000K$.

easily adjust the 1D model using an simple offset. Instead, to correct the 1D model would require applying a height-dependent correction derived from the mean 3D atmospheric structure and at this point the 1D model is obsolete anyway.

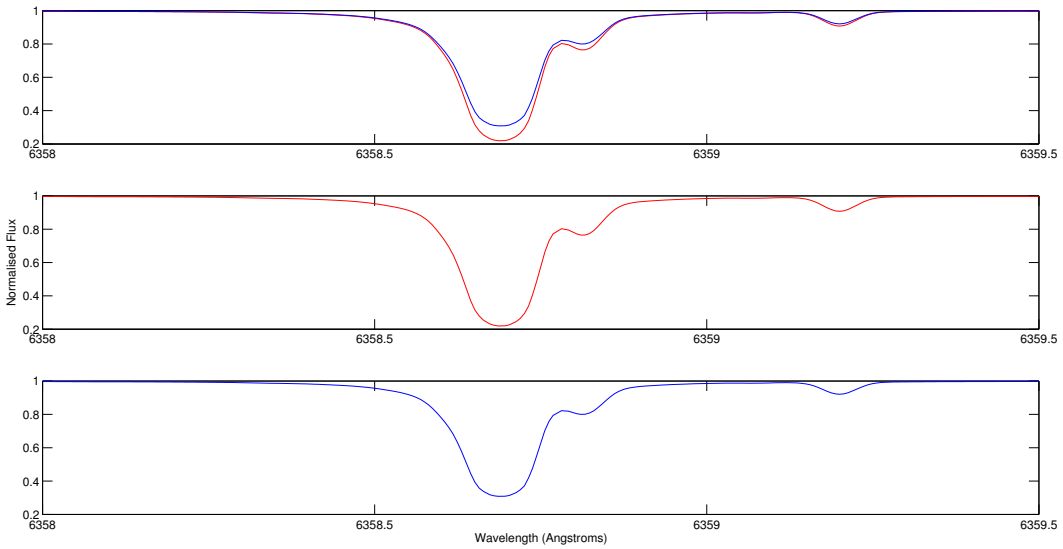

Figure 3.34: As Figure 3.24 but for an effective temperature of $T_{eff} = 4000K$.

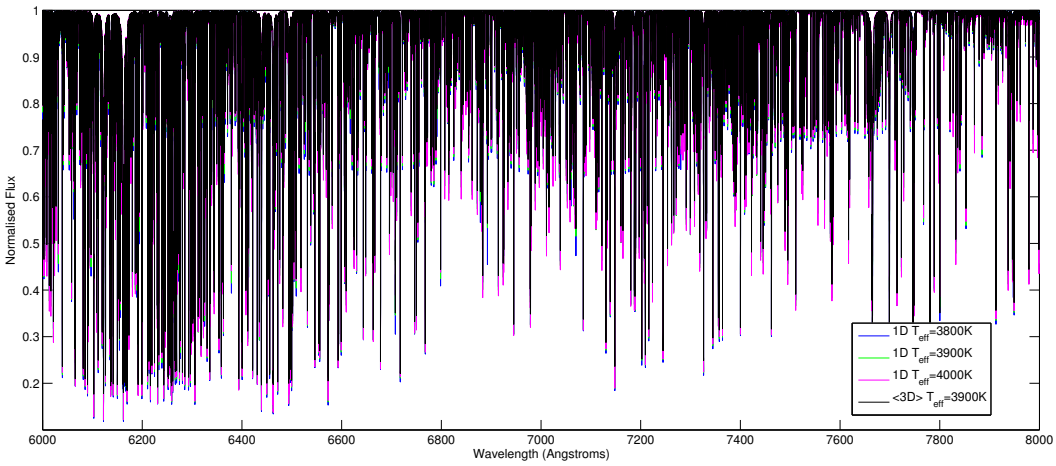

Figure 3.35: Emergent flux in the red and near infrared (6000 Å to 8000 Å normalised to the continuum. Three 1D models are shown with $T_{eff} = 3800K$ (blue line), $T_{eff} = 3900K$ (green line) and $T_{eff} = 4000K$ (red line). The black line overplotted shows the spectrum from the mean 3D structure for $T_{eff} = 3900K$.

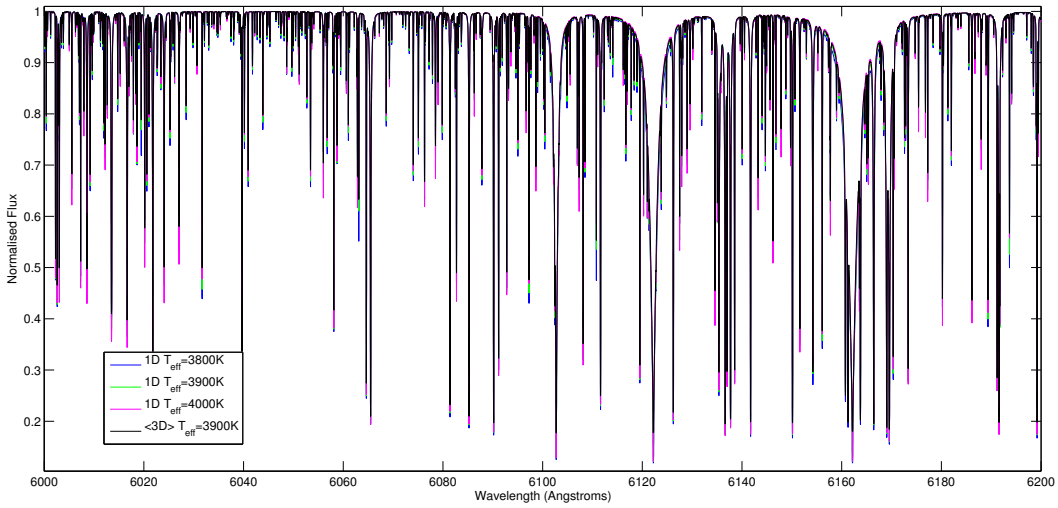

Figure 3.36: As Figure 3.35 but restricted to the range 6000Å - 6200Å to allow a clearer comparison.

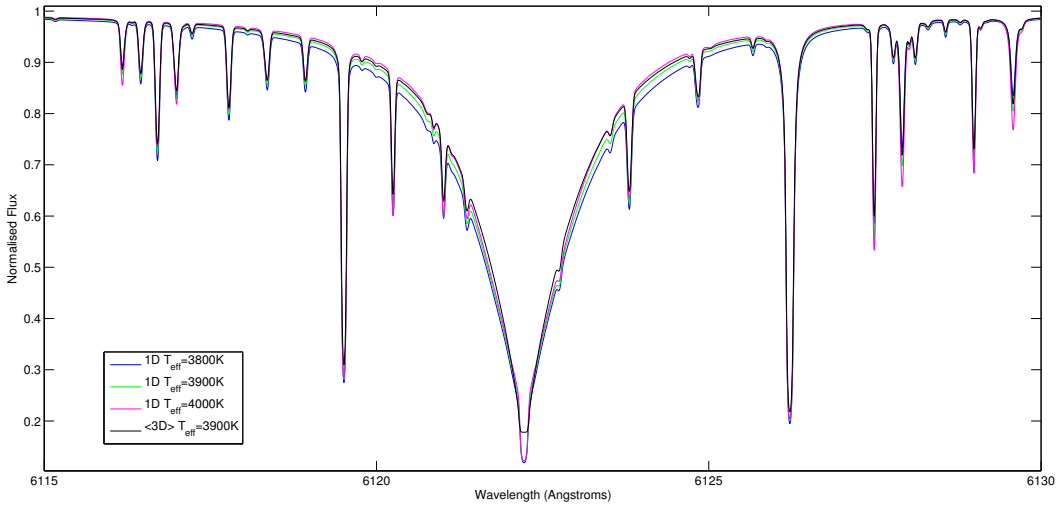

Figure 3.37: As Figure 3.35 but with wavelength coverage appropriate for considering the CaI neutral calcium line at 6122Å.

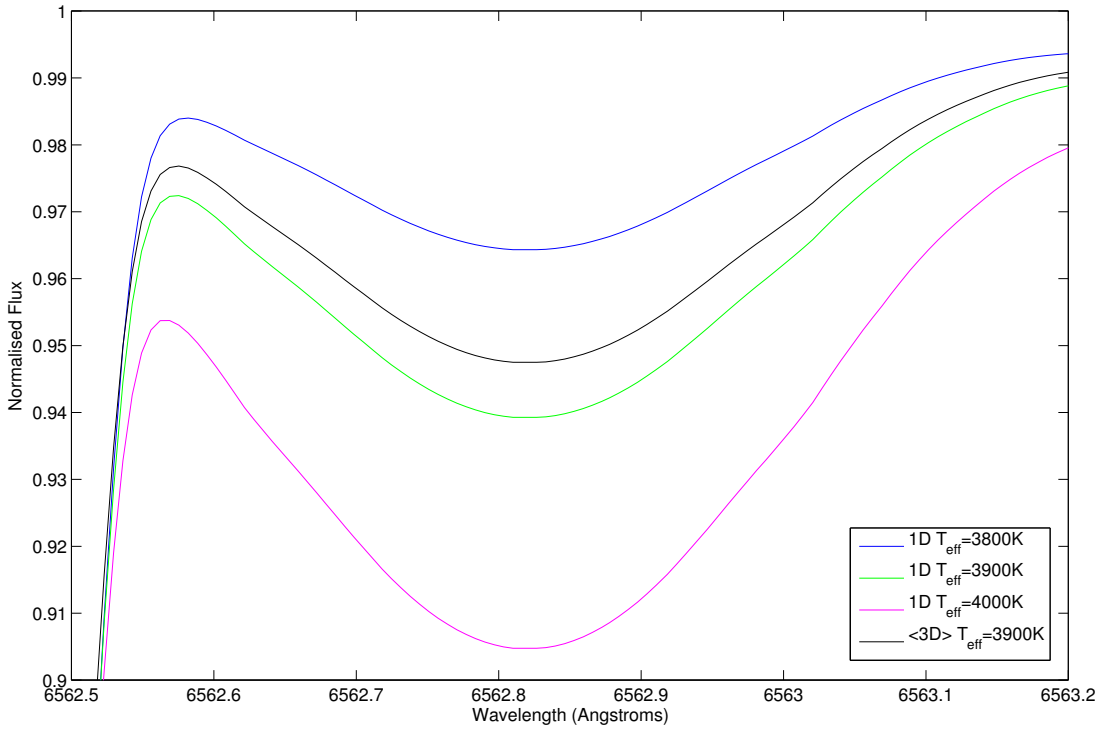

Figure 3.38: As Figure 3.35 but restricted to consider the H_α line at 6562.8Å.

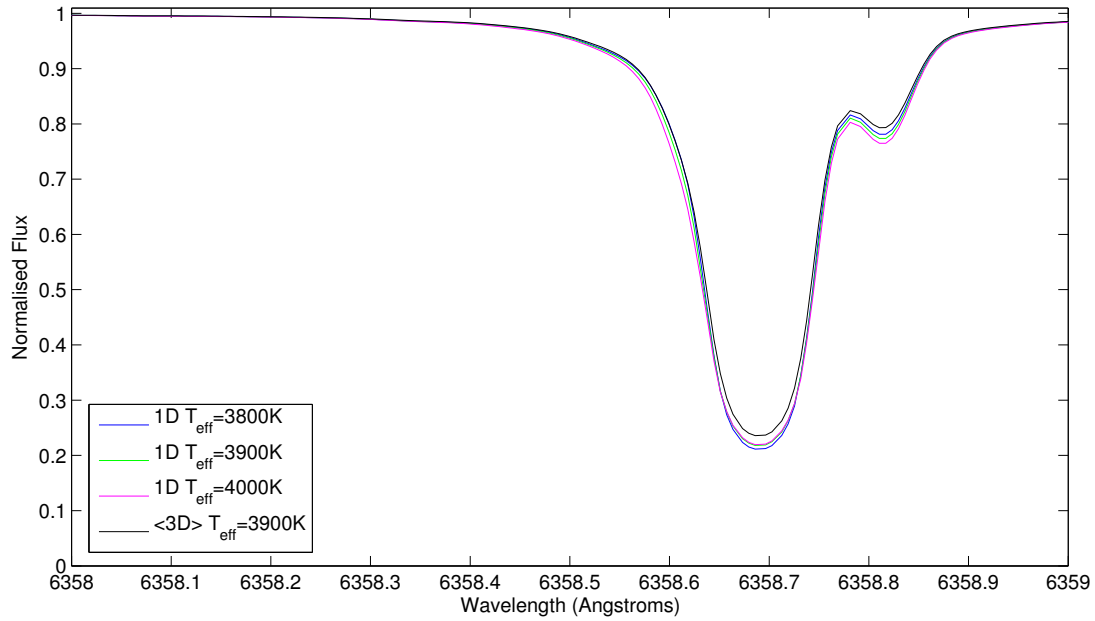

Figure 3.39: As Figure 3.35 but restricted to consider the molecular TiO line at 6358.7Å.

Chapter 4

Equation-of-state and opacities

4.1 Equation-of-state

The Equation-of-state (EOS) in an atmosphere model is required to close the system of hydrodynamic equations and to provide, quickly and easily, thermodynamic quantities. The construction of an EOS must be tackled with reference to the physical regime under consideration and reflect appropriate assumptions for the intended results. While a 'perfect gas' law may be appropriate for many laboratory based experiments, the ideal regime (which may incorporate ionisation, internal degrees of freedom, radiation and Fermi-Dirac electrons interacting with infinitesimal range) is more appropriate for hot stars. For solar-like stars this proves inadequate as the neglect of finite range interactions leaves around a quarter of the plasma unionised, while consideration of the size of neutral atoms forces this figure to be less than 7%.

More detailed equations of state, that incorporate non-ideal effects, tend to be based on the chemical or physical picture. The physical picture considers a grand canonical ensemble of electrons and nuclei interacting through the Coulomb potential. The physical picture is formulated in terms of density and activity expansions, which are cumbersome and additionally, the problem converges only slowly, limiting the range of validity.

The chemical picture is predicated on the principle of free-energy minimisation and the use of approximate statistical mechanical models (e.g. non-relativistic electron gas, Debye-Hueckel theory for ionic species, quantum mechanical models of atoms in perturbed fields, hard-core atoms to simulate pressure ionisation via configurational terms etc). From these models a macroscopic free-energy is constructed as a function of temperature, volume and particle numbers $N_1, ..., N_m$ of the m molecules, atoms and ions (Trampedach et al. 2006). The energy is minimised, at a given temperature and volume, subject to stoichiometric constraints connecting the particles through ionisations and dissociations. The solution yields not only the equilibrium concentrations, but through the free energy and its derivatives, also the equation of state and thermodynamic quantities.

Consistency is automatically guaranteed through the satisfying of Maxwell's equations. The principal advantages of this method over the physical picture are that complicated plasmas composed of realistic abundance patterns may be computed due to rapid convergence and that numerically smooth thermodynamic quantities can be obtained.

The Mihalas-Hummer-Däppen EOS is non-ideal and based on the chemical picture of equilibrium between a set of predefined molecules, atoms and ions (Trampedach et al. 2006; Hummer & Mihalas 1988; Mihalas et al. 1988). Developed for the international Opacity Project (Seaton 1995; Berrington 1995) a leading opacity calculation collaboration of recent years, it has garnered some success in modelling the solar atmosphere (Trampedach et al. 2006). The Opacity Project, and therefore the MHD EOS, restricts itself to the case of stellar envelopes, rather than interiors, where the density is sufficiently low that the concept of atoms remains valid. Optimised for studying the solar atmosphere, it considers the 17 most abundant elements and the formation of H_2 and H_2^+. The abundances used are from Asplund et al. (2009). The MHD EOS has been well tested (Trampedach et al. 2006; Di Mauro et al. 2002) and shows closer agreement with constraints from helioseismology in the outer 20Mm (0.97 $R_\odot$) than the OPAL EOS, another highly successful EOS used for the solar model.

One may define a coupling parameter Γ as the ratio of average potential binding energy over the mean kinetic energy

$$\Gamma = \frac{q^2}{k_B T < r >} \tag{4.1}$$

where q is the charge of the ion, k_B is Boltzmann's constant, T is the temperature of the plasma and $< r >$ is the mean particle separation. $\Gamma >> 1$ implies strongly coupled plasma, as for white dwarfs while $\Gamma << 1$ defines the weakly coupled regime that occurs in stars more massive than the Sun. In the Sun, the plasma is only weakly to moderately coupled, but lower thermal energies in cooler dwarfs mean these stars will become progressively more strongly coupled towards brown dwarfs and sub-stellar objects. Furthermore, molecules become increasingly important in these atmospheres, with carbon monoxide (CO), ammonia (NH_3), water (H_2O) and methane (CH_4) all playing a strong role. Consequently, the EOS must reflect the formation of this suite of molecules. Reflecting the importance of molecular formation for cool atmospheres a number of groups have published chemical equilibrium calculations including (Burrows & Sharp 1999; Allard et al. 2001; Fegley & Lodders 1996; Lodders & Fegley 2002; Saumon et al. 2003; Visscher et al. 2006; Troyer et al. 2007; Visscher et al. 2010). As we move to these cooler, denser, more degenerate stars like ultracool dwarfs the coupling becomes stronger necessitating an even more detailed treatment of the EOS.

ACES (astrophysical chemical equilibrium solver) is a robust chemical equilibrium algorithm developed by Barman IN PREP and integrated into the PHOENIX model atmosphere code. Based on the method of Smith & Missen (1982), it too follows the chemical picture and solves chemical equilibrium for over 4000 species including new experimental and theoretical thermodynamical data for 839 species (84 elements, 289 ions, 249 molecules, 217 condensates) (Husser et al. 2013). It is well tested from 100K to 100,000K for a broad range of pressures and compositions. This work is restricted to solar composition as defined by Asplund et al. (2009) in order to facilitate lucid comparison.

In principle, the EOS should reflect the time and space dependent element abundances for the chemical equilibrium calculation. In particular, molecule formation and dust formation are directly competing processes, with the hysteresis type behaviour of dust affecting effective abundances in a non-equilibrium way. However, in the restricted model of dust present in Chapter 6, dust formation affects only two elements, titanium (Ti) and oxygen (O). Titanium is an extreme minority species, ($\sim 10^{-7}$), and has a negligible effect on the EOS, while oxygen is so abundant that even were the maximum possible volume of dust to form, this would make only a very small difference to the overall oxygen abundance, therefore this effect may be safely neglected. Even considering an enlarged chemical network, the oxygen abundance remains stable despite the dominant role of oxygen in the formation and composition of condensates (Witte et al. 2009). It should be noted that while minority elements have

little impact on the EOS, this is categorically not the case for the opacities, where minority species and their molecules play a crucial role. Neglecting the temporal and spatial effective abundance deviations from equilibrium allows the EOS parameter space to be condensed and the EOS may then to be stored as a table based on two state variables.

4.1.1 Equation of State Table

In order to model objects with significant molecular formation, it is necessary to move from the MHD EOS to an EOS which takes account of these species. While other suitable EOSs exist, ACES has been rigorously tested for temperatures between 100K and 100,000K making it an ideal selection.

The ACES EOS provided by Hauschildt, Barman and the PHOENIX collaboration consists of data structure which holds thermodynamic variables on regularly gridded planes in temperature and gas pressure. The variables are density, specific energy and specific entropy. The hydrodynamic code *stagger* uses an EOS based on regularly gridded density and specific energy of the plasma. The two datasets have differing footprints in the temperature and gas pressure plane, but are overlapping. The conversion from one format to another is performed in a two step process. First, the regular grid of desired density and specific energy values is inverted by triangulation to find the corresponding coordinates in the temperature and gas pressure plane. Secondly, on this inverted grid, linear logarithmic interpolation is performed to give the thermodynamic variables, including temperature and gas pressure. Tests were performed to consider more sophisticated interpolation and the results were not significantly different, but for stability reasons the linear interpolation was preferred. The corresponding derivatives with respect to specific energy and density are then found numerically.

Special care must be taken as the ACES and MHD energies are not calculated consistently. Indeed, the ACES specific energies become negative for low temperature gas - this is due to a different zero point. The zero point of the ACES data is refixed by considering the absolute value of the energy in the MHD EOS at a specific temperature and gas pressure (which is also checked against the density). As the hydrodynamic code only ever uses energy differences, therefore the definition of the zero point should not be critical.

The final EOS table is a 4-dimensional structure with six quantities ($P_{gas}, T, n_e, \kappa_P, \kappa_R, \kappa_{500}$) and their corresponding derivatives held as planes on a regular density and specific energy grid. The table comes with a header which specifies the size, units and limits of the table as well as some auxiliary information about the compilation of the table.

Figure 4.1 shows a contour plot of the temperature of the two equations of state on the temperature - gas-pressure plane. The grey shaded area marks the footprint of the MHD EOS in the rectangular ACES data. The MHD EOS data have been inverted onto the temperature - gas-pressure plane, critically without requiring interpolation. The colour-bar defines the shading on a logarithmic scale of the temperature. Naturally, the contours follow straight horizontal lines and the two sets of contours coincide. Of note, is the larger parameter space coverage of the ACES data, particularly at lower temperatures than are covered by the MHD EOS.

Figure 4.2 is rather similar, but shows the contours of the gas pressure. Again the colour-bar defines the shading on a logarithmic scale, but this time of the gas pressure. By definition, the contours again coincide. The ACES data, compared to the MHD, provides the full range of pressures at low temperature ($T \lesssim 1000K$) and covers the high pressure range at moderate to high temperature ($T \simeq$

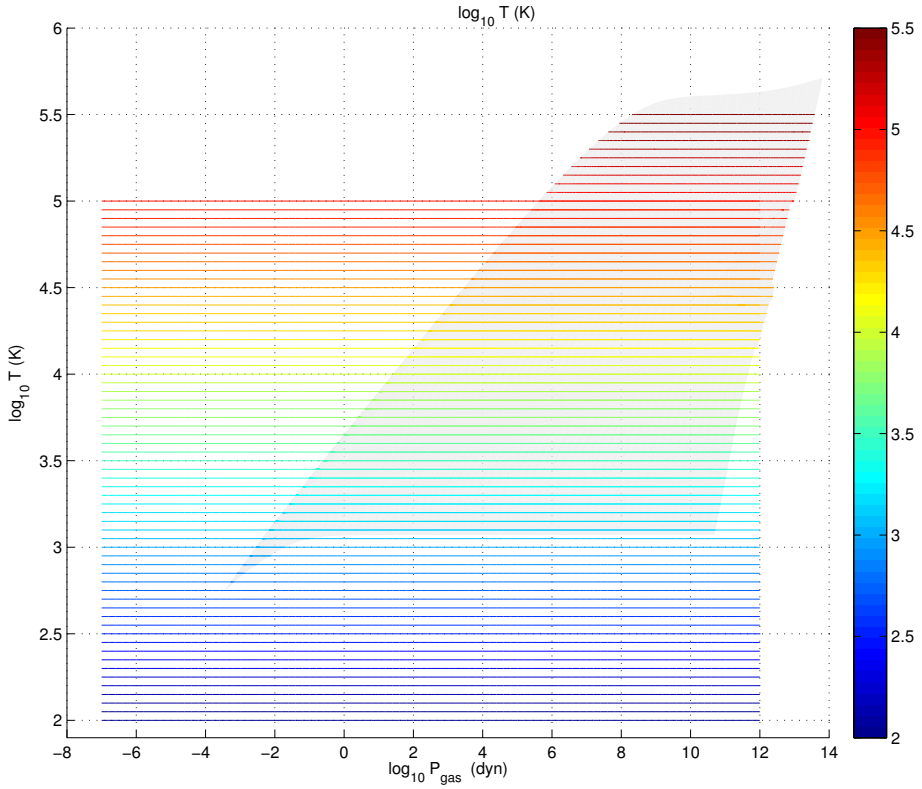

Figure 4.1: Temperature contour plot of the MHD and ACES equations-of-state in the temperature - gas pressure plane. The colourbar shows the base 10 logarithm of the temperature. The grey shaded area shows the parameter space coverage on the MHD data, while the ACES data is rectangular in this plane.

$10^3 - 10^4$K). The extra coverage of low pressure at high temperature is unlikely to be significant for the current models being calculated. Such a region is likely to be more significant where chromospheres are considered. While interesting, chromospheres are beyond the scope of this work.

Figure 4.3 shows the density contours on the temperature - gas-pressure plane. The colour-bar defines the scale of base 10 logarithmic density. It is obvious by inspection that at high temperatures the contours of the two datasets, while not coinciding precisely, are very close. This is encouraging. Deviations occur along the high temperature edge of the MHD data (grey shaded). The contour lines here of the MHD data bunch up towards the edge of the dataset, this reflects deficiencies of the data at the very edge of the table.

A clear feature of the data begins at low gas pressure and temperature $\sim 10^3$K and $\sim 10^{3.5}$K. The two lines that begin here migrate to higher temperatures with pressure, but the features agree well in both datasets. Physically this corresponds to the absorption edges of hydrogen and helium. The other strong feature visible is at high pressure and temperature $\sim 10^{4.5}$K. This feature again is broadly consistent in the two datasets, although it occurs at high enough temperature as to make it unlikely to be encountered in simulations of the convection zone of cool dwarfs.

Figure 4.4 shows the specific energy contours on the temperature - gas-pressure plane. The specific

energy and density are important as major deviations between the datasets would be problematic in recasting the ACES data into the MHD format for incorporation into the stagger code. Fortunately, this does not seem to be a problem. Again the MHD data, defined by the grey shaded area, shows some evidence of edge effects. Except this, the contours match well in their values and spacings. In particular, bunched contours at the ionisation edges and very sparsely populated in between. At the highest pressure and temperature $\sim 10^3 - 10^{3.5}$K, there is a feature in the ACES data only. This may be physical, but as the MHD EOS does not extend to here it is impossible to say if this feature would be seen in MHD.

Figure 4.5 shows the logarithmically spaced contours of the gas pressure in the density - specific energy plane, for the two datasets. The labels for the datasets change at this point, as the EOSs require input from the opacity data, therefore the dataset labels refer to the source of the opacity data. The MARCS opacity data is used by the MHD EOS (e.g. Gustafsson et al. 1975, 2008), while the ACES EOS uses opacity data from the PHOENIX collaboration (e.g. Husser et al. 2013; Barman in prep.). MARCS-MHD and PHOENIX-ACES agree remarkably well, although there are deviations at low density with specific internal energies. The PHOENIX-ACES gas pressure is lower compared to the MARCS-MHD data, this is likely to reflect the additional species considered in the PHOENIX-ACES package, meaning that low density low pressure gas is likely to form and retain molecules, not considered in MHD-MARCS.

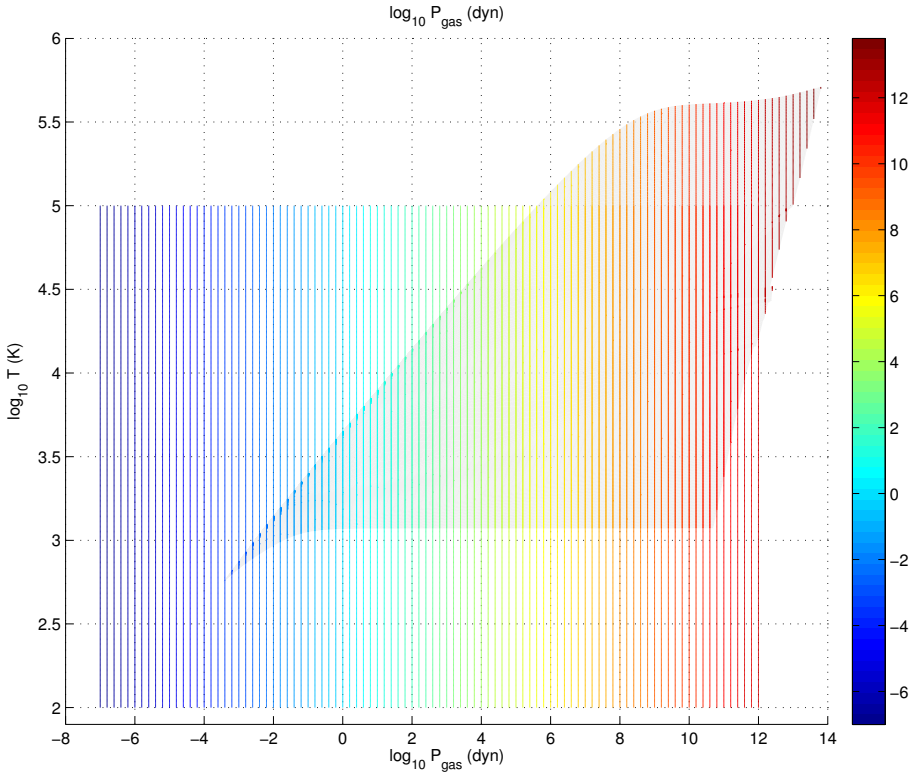

Figure 4.2: Gas pressure contour plot of the MHD and ACES equations-of-state in the temperature - gas pressure plane. The grey area shows the MHD data footprint, while the ACES data is rectangular. The colourbar reflects the logarithmic (base 10) gas pressure.

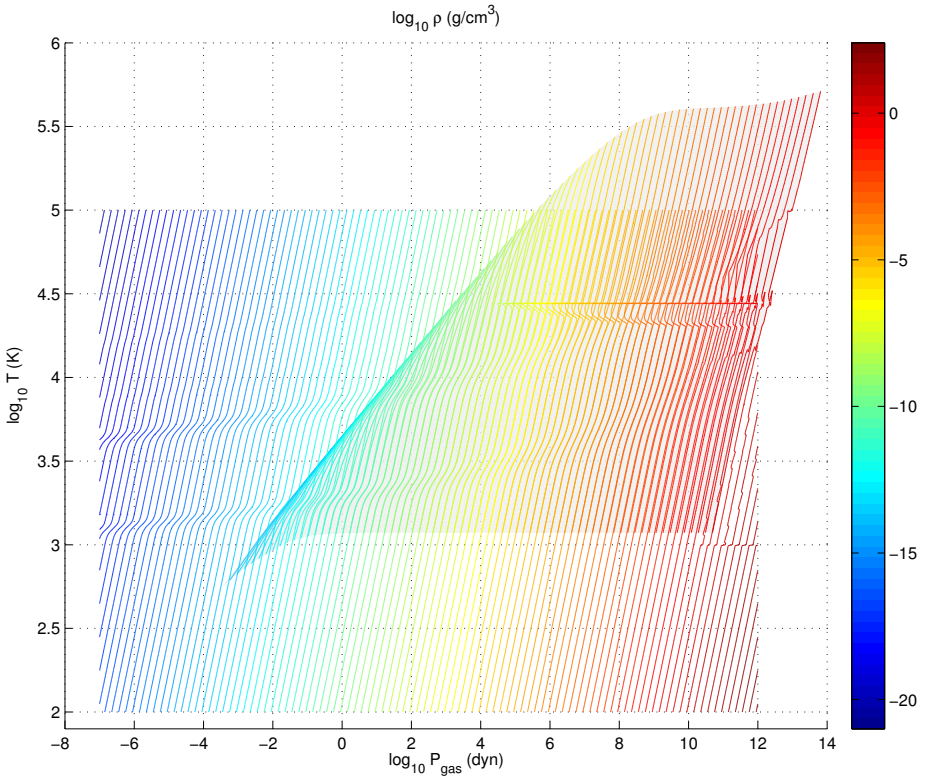

Figure 4.3: Density contour plot of the MHD and ACES equations-of-state in the temperature - gas pressure plane. The MHD parameter space is highlighted in grey. The bunched contours at the left-hand side of the MHD data are merely an artifact of the edge of the MHD table.

Figure 4.6 shows the logarithmic temperature contours also in the density - specific energy plane. The two datasets agree very well at all but the lowest densities. Low densities correspond to the outermost edges of the atmospheres of these stars and such low densities are not yet encountered by the models produced thus far. The deviations present at high specific-energies are not physical (where the dotted PHOENIX-ACES contours become practically vertical), but instead are merely an artifact of the edge of the PHOENIX-ACES data. The PHOENIX-ACES data extends only as far as $e_{sp} \simeq 10^{13.5} erg/g$. The green contour defining $T = 10^4.2K$ is rather blurred in the PHOENIX-ACES data. This is due to a shallow gradient in this region, which magnifies the interpolation errors; in reality, this is a very minor effect.

Figure 4.7 shows the contours of the Planck mean absorption coefficient, logarithmically spaced, on the density - specific energy plane. The Planck mean absorption coefficient is defined as a straight weighted mean opacity, weighted by the blackbody intensity (Planck) function. It is suitable mean opacity measure for optically thin media. The two datasets show close agreement at low energies, $e_{sp} \lesssim 10^{12.5} erg/g$, for all temperatures. At higher energies, the PHOENIX opacities are lower, with the broad trends following in both datasets, but the depth of the dip in the contour lines being shallower for the PHOENIX data. As the two means are calculated from different opacity data, this implies that the PHOENIX spectral line opacities are systematically lower than those in the MARCS data (See further discussion in section 4.2), although the effect is not very large and is likely to be largely explained by the small differences in the ambient conditions the different EOSs define.

Figure 4.8 shows the contours of the Rosseland mean absorption coefficient or opacity on the density - specific energy plane. The Rosseland mean absorption coefficient is formed by an harmonic mean of the opacities weighted by the temperature derivative of the Planck function, $\frac{dB_\nu}{dT}$. It is appropriate for optically thick conditions. The Rosseland mean opacities agree well for low energies. At higher energies, the MARCS opacities are higher, as with the Planck mean opacity - suggesting that the difference comes from the intrinsic differences in raw opacity data and that the PHOENIX data is systematically lower than the MARCS. The differences are small and easily explained by the slight differences in physical environment described by the respective EOSs.

Figure 4.9 shows the contours of the monochromatic opacity at a wavelength of 500nm. The two datasets agree fairly well at higher energies, but the PHOENIX data shows significantly lower opacities at low energy. This could be an artifact of the different resolution of the two datasets.

It should be noted that all the absorption coefficients show some evidence of blurring or erratic contours at the sharp turning of contour lines in the PHOENIX-ACES data. This is just an artifact of the interpolation, and has a small effect overall. Other interpolation schemes were tried but the sophistication of the schemes is unnecessary and the robust nature of the simple linear scheme on the logarithmic quantities is preferable.

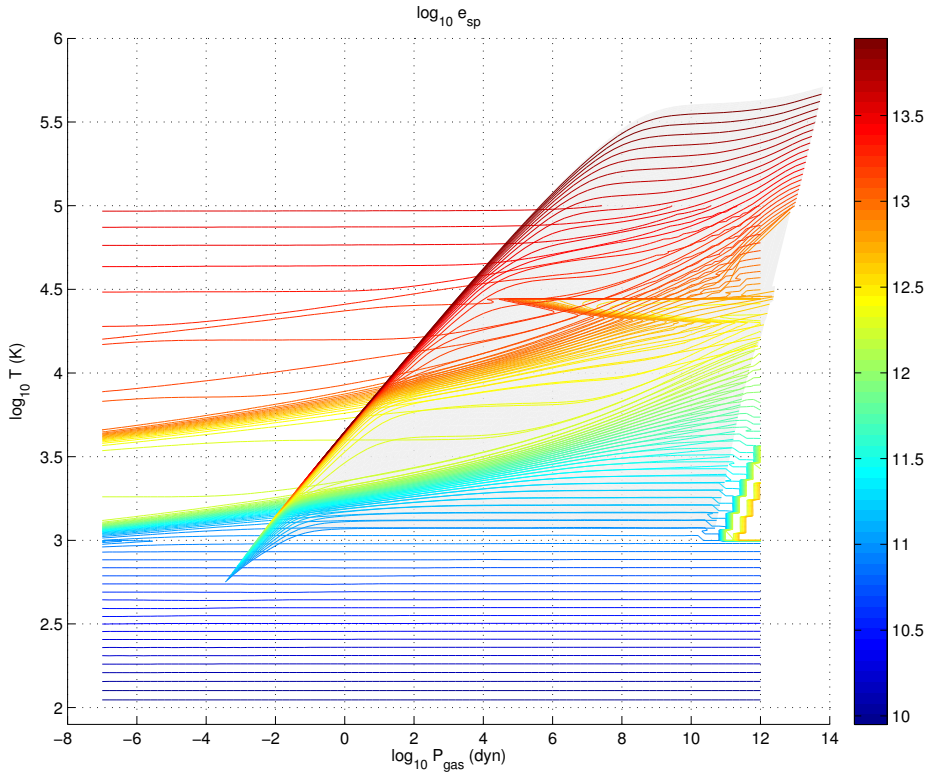

Figure 4.4: Specific energy contour plot of the MHD and ACES equations-of-state in the temperature - gas pressure plane. The bunched contours at the left-hand side of the MHD data are merely an artifact of the MHD table limits.

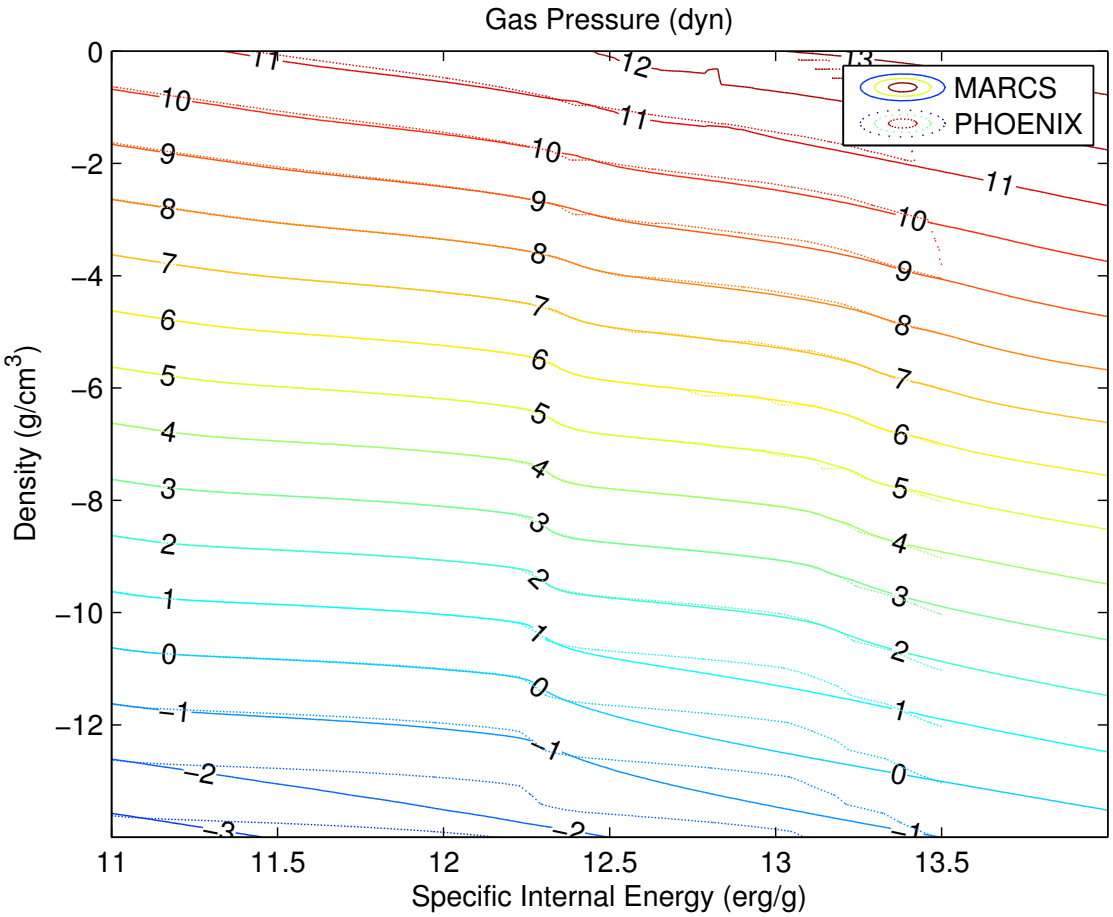

Figure 4.5: Gas pressure contour plot on the density - specific energy plane. The solid lines show the MARCS-MHD data, while the PHOENIX-ACES data contours are dotted. It should be noted that the PHOENIX-ACES data extends only to $\log_{10} e_{sp}$=13.5. The contours are labelled with the $log_{10} P_{Gas}$.

4.2 Radiative Transfer

The equation of radiative transfer may be solved analytically only in extremely simplified cases. In general, a numerical treatment is required due to the plethora of spectral lines and absorption edges that govern the opacity. It is convenient to recast the equation of radiative transfer in terms of optical depth, τ_ν. Optical depth is defined as

$$\tau_\nu = -log_e(\frac{I}{I_o}) = \int_0^s \rho\kappa_\nu ds \tag{4.2}$$

and expresses the removal of intensity from a beam due to scattering and absorption on its path through a medium, where τ_ν is the monochromatic optical depth at frequency ν, I is the intensity after traversing the medium and I_0 is the incident intensity. The optical depth is typically calculated by integrating the density, ρ and the absorption coefficient or opacity, κ_ν, along the path, s. The quantity $\chi_\nu = \rho\kappa_\nu$ is used in some texts for convenience. Optical depth is dimensionless and the transition from diffusive radiative transfer to photon free-streaming is described by it. The equation of radiative

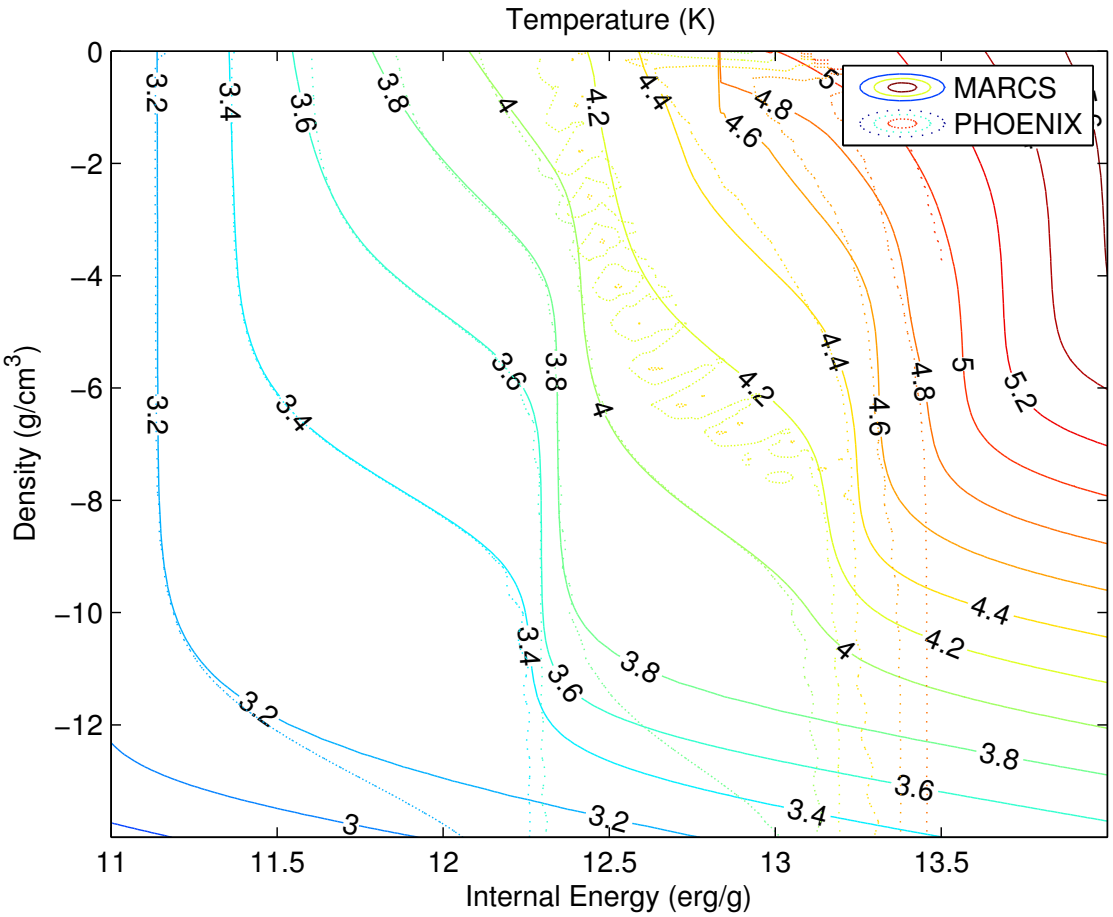

Figure 4.6: Temperature contour plot on the density - specific energy plane. The solid lines show the MARCS-MHD data, while the PHOENIX-ACES data contours are dotted. It should be noted that the PHOENIX-ACES data extends only to $\log_{10} e_{sp}$=13.5, and so the dotted lines behave unphysically here. The contours are labelled with the $log_{10} T$.

transfer then becomes

$$\frac{dI_\nu}{d\tau_\nu} = (S_\nu - I_\nu) \tag{4.3}$$

where S_ν is the source function and I_ν is the monochromatic intensity, with the formal solution

$$I_\nu(\tau_\nu) = I_\nu(\tau_{u,\nu}) e^{-(\tau_\nu - \tau_{u,\nu})} + \int_{\tau_{u,\nu}}^{\tau_\nu} S_\nu(t) e^{t-\tau_\nu} dt \tag{4.4}$$

where the first term describes the attenuation of the incident specific intensity along the ray, while the second accounts for the contribution to the intensity from the source function. The hydrodynamic equations require the radiative heating, Q_{rad}, in every cell at every timestep, which in turn requires the solution of the radiative transfer equation. The heating rate is the wavelength integral of the flux divergence, alternatively calculated via the monochromatic opacity, κ_ν, and the difference of the mean intensity, J_ν and the source function, S_ν.

$$Q_{rad} = -\int_\nu \nabla \times F_\nu d\nu = 4\pi\rho \int_\nu \chi_\nu (J_\nu - S_\nu) d\nu \tag{4.5}$$

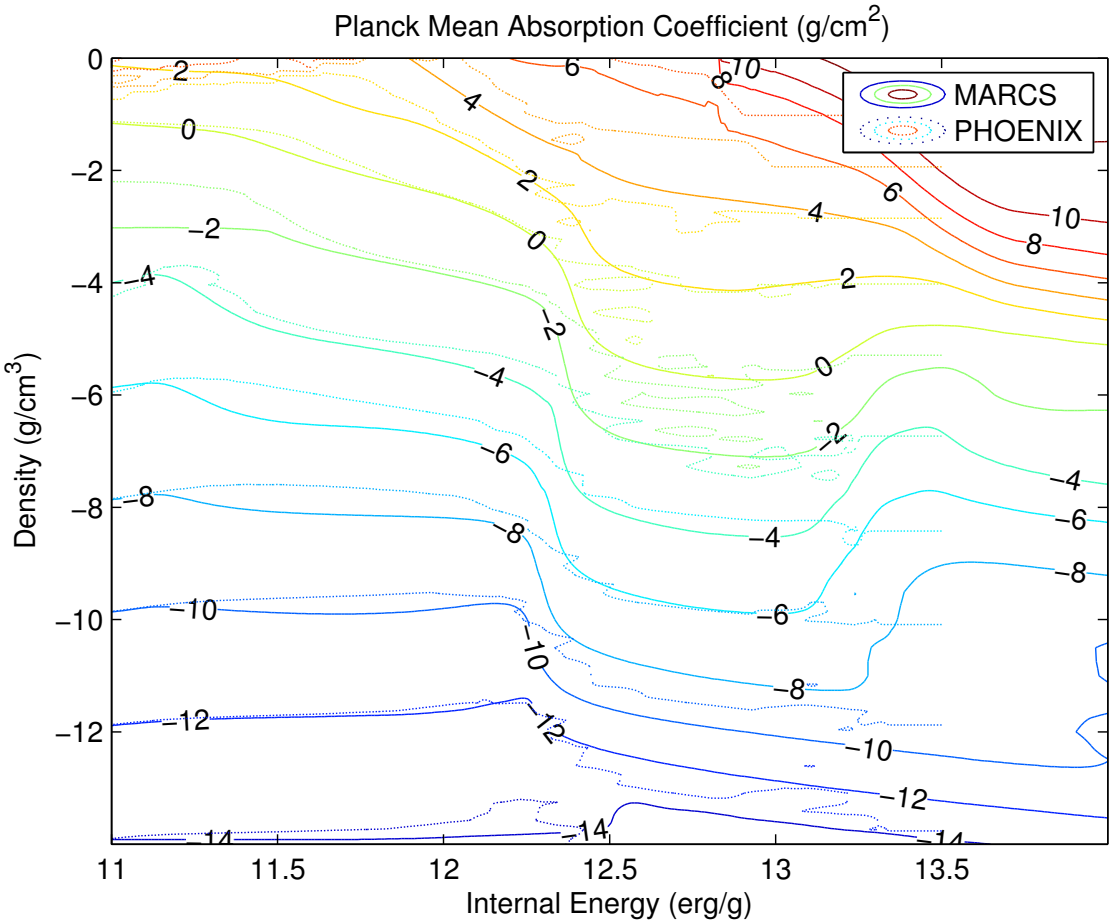

Figure 4.7: Planck mean absorption coefficient contour plot on the density - specific energy plane. The solid lines show the MARCS-MHD data, while the PHOENIX-ACES data contours are dotted. It should be noted that the PHOENIX-ACES data extends only to $\log_{10} e_{sp}$=13.5. The contours are labelled with the $log_{10}\kappa_{Planck}$.

Solving this involves an integral over frequency (or equivalently wavelength if the equations are formed in that way). In 1D models, the equation of radiative transfer is solved for $10^5 - 10^6$ frequency points, although for more detailed applications Vögler (2004) suggest that as many as 10^7 are required. The wavelength points are selected through statistical sampling (known as opacity sampling) and provide an excellent approximation of the spectrum (Peytremann 1974). In the lower atmosphere where absorbers are sufficiently well spread, this captures the continuum absorbers and the line blanketing without bias.

Tackling a problem of this magnitude in 3D is infeasible even with current supercomputers. A common approach is to invoke the Gray approximation to collapse the integral over frequency. The grey approximation, the assumption that the absorption coefficient κ_ν is independent of frequency, offers a radical simplification. The Rosseland mean opacity is appropriate in optically thick regions of the atmosphere where the photon mean free path is short leading to a well thermalised radiation field and diffusive radiative transfer.

$$\frac{1}{\kappa_{Ross}} = \frac{\int_0^\infty \frac{1}{\kappa_\nu}\frac{dB_\nu}{dT}d\nu}{\int_0^\infty \frac{dB_\nu}{dT}d\nu} \tag{4.6}$$

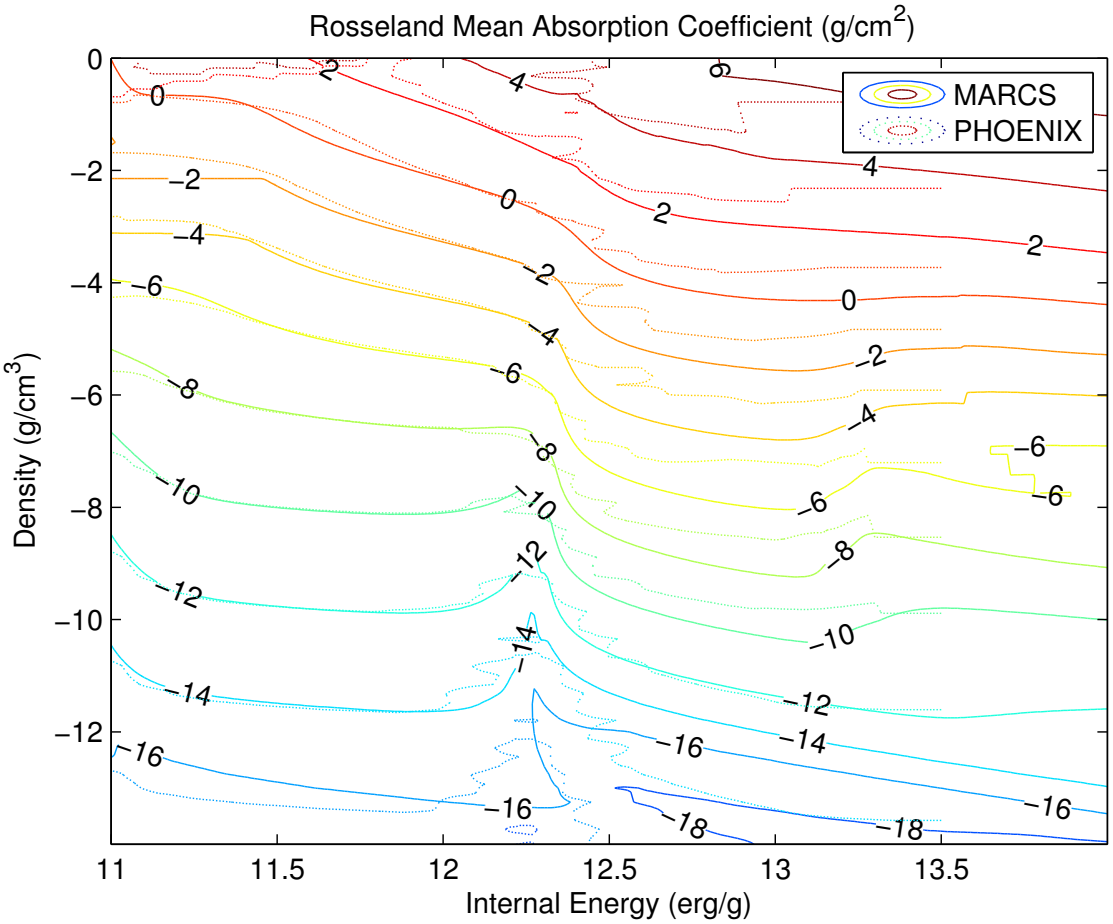

Figure 4.8: Rosseland mean absorption coefficient contour plot on the density - specific energy plane. The solid lines show the MARCS-MHD data, while the PHOENIX-ACES data contours are dotted. It should be noted that the PHOENIX-ACES data extends only to $\log_{10} e_{sp}$=13.5. The contours are labelled with the $log_{10}\kappa_{Rosseland}$.

It is formed by an harmonic mean of the monochromatic opacities, κ_ν, weighted over the temperature derivative of the Planck function, $\frac{dB_\nu}{dT}$. The Rosseland opacity describes well the mean opacity in the optically thick regime, where the radiation field is well described by the Planck function, B_ν, but fails in regions of low optical depth where spectral lines, rather than thermal blackbody emission dominate. The Planck mean opacity provides an alternative appropriate to optically thin layers and is calculated by a straight mean of the opacities weighted by the Planck function, B_ν.

$$\kappa_{Planck} = \frac{\int_0^\infty \kappa_\nu B_\nu d\nu}{\int_0^\infty B_\nu d\nu} \tag{4.7}$$

Unfortunately, a truly grey approach is too crude to describe the radiative transfer over the whole atmosphere.

More sophisticated approaches, without having to resort to calculating the full frequency integral, include opacity distribution functions (ODFs) and opacity binning. Opacity distribution functions (ODFs) divide the frequency spectrum into discrete intervals $\Delta\nu_i \simeq 10^2 - 10^3$ and replace the detailed

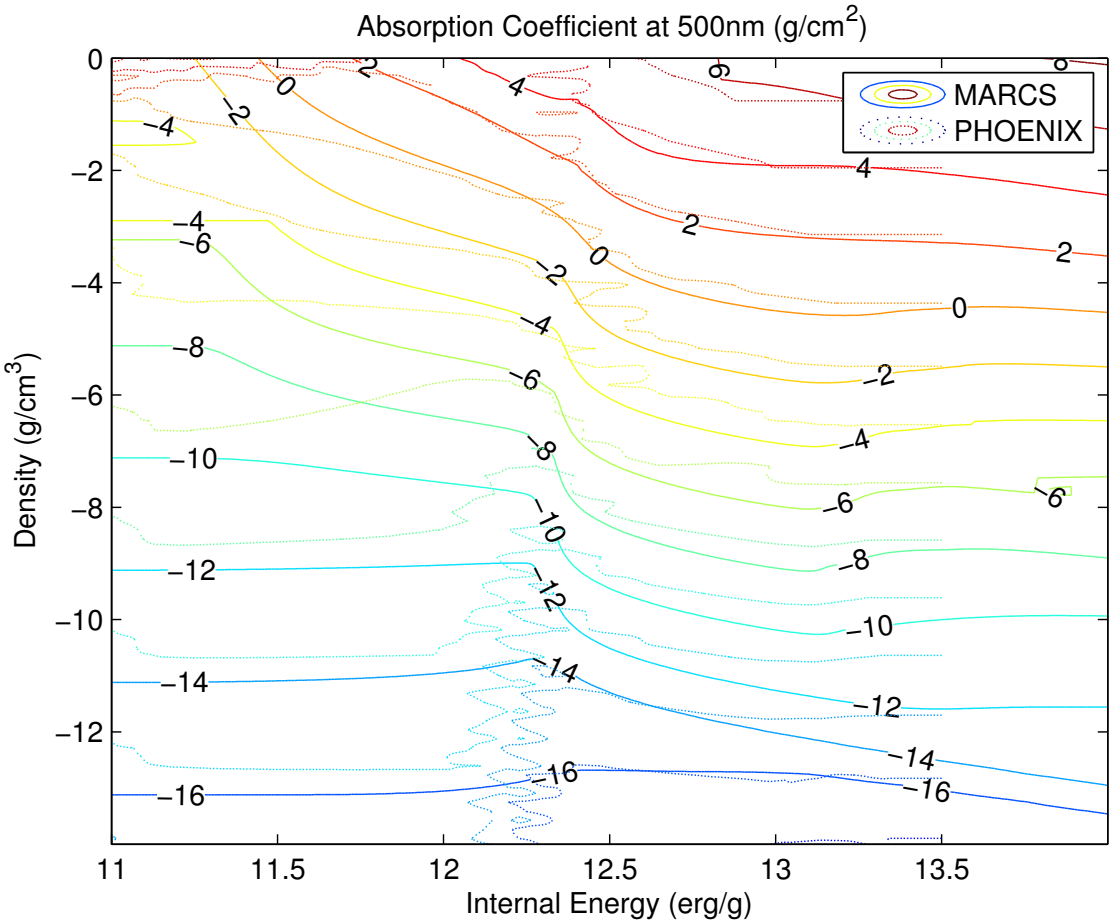

Figure 4.9: Monochromatic absorption coefficient at 500nm contour plot on the density - specific energy plane. The solid lines show the MARCS-MHD data, while the PHOENIX-ACES data contours are dotted. It should be noted that the PHOENIX-ACES data extends only to $\log_{10} e_{sp}$=13.5. The contours are labelled with the $log_{10}\kappa_{\nu=500nm}$.

line opacities within each bin with a smooth distribution function (Strom & Kurucz 1966; Mihalas 1967), often just a mean or weighted mean value. ODFs have been relatively successful in calculations of static model atmospheres (e.g. Gustafsson et al. 1975), although velocity gradients in 3D RHD simulations may introduce larger errors (Vögler 2004). ODFs produce an efficiency saving that depends on their frequency resolution, $\Delta\nu_i$.

A more dramatic computational saving may be achieved using the more sophisticated strategy of the multi-group binning method (Nordlund 1982; Ludwig 1992; Ludwig et al. 1994; Skartlien 2000; Vögler 2004). In this approach frequency points are assigned to one of $\sim 4-12$ bins, where bin membership is defined not by frequency, but opacity strength (Skartlien 2000). By reducing the computational load of the integration from $O(10^7)$ to $O(10^1)$, this represents the most dramatic acceleration of the code, greater than ODFs which still require $O(10^3)$ computational per evaluation of radiative transfer. As a result the multi-group method has been favoured by many groups working on the computationally intensive 2D/3D RHD/MHD models (e.g. Vögler et al. 2005; Freytag et al. 2010; Gudiksen et al. 2011; Magic et al. 2013).

4.2.1 Multi-group method

In the multi-group method frequencies are sorted by opacity strength into a small number of bins (Nordlund 1982). As opacity strength is discontinuous in frequency, bins are discontinuous also (see Figure 4.10)

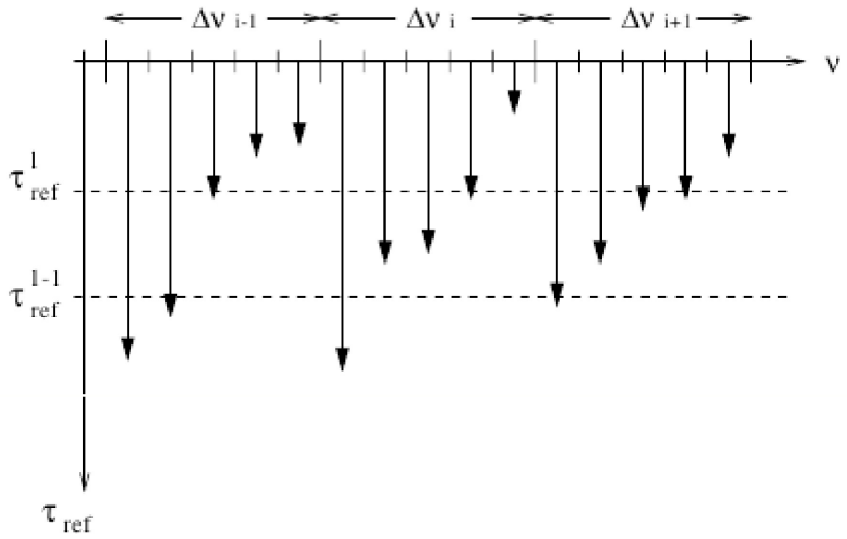

Figure 4.10: Schematic illustration of the τ-sorting procedure using opacity distribution functions. Within each opacity distribution function interval, $\Delta\nu_i$, the opacity distribution function steps, $\Delta\nu_{ij}$ are sorted into frequency bins, Ω_i, depending on the height where the monochromatic optical depth unity is reached (bold arrows). Adapted from Vögler et al. (2004).

This means continuum opacities and lines of differing strength are allocated to separate bins and each bin is then represented by a single bin-averaged opacity. Utilising the bin-averaged opacity the equation of radiative transfer may be recast as follows

$$\frac{dI_i}{ds} = -\int_{\Omega_i} \kappa_\nu \rho (I_\nu - S_\nu) \simeq -\bar{\kappa}_i \rho \left(\int_{\Omega_i} I_\nu d\nu - \int_{\Omega_i} B_\nu d\nu \right) \tag{4.8}$$

effectively allowing much of the frequency integration to be performed *before* the integration along the ray path, meaning this equation need only be solved a single time for each bin. Strictly, this is only valid if κ_ν is constant over the whole bin, that is the τ_ν scales and therefore depth-dependence of κ_ν are the same, or nearly so, for the member frequencies of a single bin.

Clearly an appropriate criterion for assigning frequencies to their respective bins is required and should have the effect of grouping together opacities of the same order of magnitude and similar dependence with atmospheric depth. κ-sorting is a simple choice, which uses a fixed atmospheric height, z_0, and then sorts frequencies based on the spectral shape of $\kappa_\nu(z_0)$, with threshold values dividing the opacities into bins. A reasonable choice for z_0 is the height at which the continuum at 500nm forms, as $\tau_{500nm}(z_0) \simeq 1$. However, in optically thick regions this is a poor method as opacity values that are optically thick at z_0 have no impact on the energy exchange.

Instead, the radiation table code employs so-called τ-sorting (Ludwig 1992; Vögler 2004), which has the advantage that all opacities between $\tau_\nu = 0$ and $\tau_\nu = 1$ contribute, that is the τ_ν-scales around

$0 < \tau_\nu \leq 1$ are similar in precisely the region where a non-grey description of radiative transfer is critical. τ-sorting requires a 1D reference atmosphere upon which $\kappa_\nu \rho$ is integrated along the z-direction at every frequency to determine the geometrical height corresponding to $\tau_\nu = 1$. A 1D static model can be used for this purpose without introducing significant inconsistencies, but in this work a 1D model was used initially then replaced by the mean 3D stratification in subsequent runs. Bin specifications and thresholds are chosen against a reference optical depth scale, Rosseland opacity in this case. A frequency, ν, is assigned to a bin, Ω_i if $\tau_\nu = 1$ is reached in the interval of Rosseland optical depth.

$$\nu \in \Omega_i \quad \text{if} \tau^i_{Ross} \geq \tau^i_{Ross}(\tau_\nu = 1) \geq \tau^{i+1}_{Ross} \tag{4.9}$$

The Rosseland optical depth requires the Rosseland mean opacity, κ_{Ross}.

$$\tau_{Ross} = \int_s \rho \kappa_{Ross} ds \tag{4.10}$$

The bin mean opacity choice depends on the physical regime in question. In hot, dense, deep layers the atmosphere is optically thick and therefore the photon mean free path is short, leading to many thermalising collisions meaning the Rosseland mean opacity provides an adequate description of the opacity for all wavelengths.

$$\kappa_{Ross} = \frac{\int \kappa_\lambda \frac{dB_\lambda}{ds} d\lambda}{\int \frac{dB_\lambda}{ds} d\lambda} \tag{4.11}$$

In the optically thin regime a Rosseland description is no longer sufficient to describe the height dependent line blanketing above the surface. In these layers the atmosphere is sensitive to the radiation field and atomic and molecular opacities become important wavelength dependent opacity sources. In this regime a Planck-like mean opacity is used. Composed of a straight mean of the mean intensity, J, weighted monochromatic opacities, it is appropriate in the optically thin regime.

$$\kappa^J = \frac{\int \kappa_\lambda J_\lambda d\lambda}{\int J_\lambda d\lambda} \tag{4.12}$$

The above depends on the radiation field so we make the assumption that we can use the result from the 1D radiative transfer. This means

$$\kappa^J \simeq \kappa^{J,1D} \tag{4.13}$$

The transition between the two is handled by an exponential bridging function of the two averages, which generates a smooth steep transition

$$\kappa_i = e^{-2\tau_{Ross}} \kappa_{J,i} + (1 - e^{-2\tau_{Ross}}) \kappa_{Ross} \tag{4.14}$$

Radiative transfer proceeds under local-thermodynamic equilibrium (LTE) i.e. the monochromatic source function S_ν is the Planck function at the local gas temperature. While non-LTE studies are common in 1D (e.g. Mashonkina et al. 2007, 2008; Bergemann & Gehren 2008; Bergemann et al. 2010; Bergemann & Cescutti 2010; Bergemann et al. 2011, 2012a) for detailed spectral line analysis there exist studies of non-LTE effects in 1D atmosphere models but true 3D non-LTE investigations are outwith the capacity of current hardware. Collet et al. (2011a) studied the effects of scattering. LTE is a convenient assumption which eases the computational load (Hayek et al. 2010; Hayek 2010),

but seems to be justified in the small parameter space they studied, with the caveat that the contribution of scattering to the extinction should be *excluded* in the calculation of free-streaming mean opacities,$\kappa_{J,i}$ as this leads to an overestimate of heating rates in the optically thin layers, resulting in an erroneous atmospheric structure. To exclude the possibility that scattering has significant influence in the regime of ultracool dwarfs would require further study.

4.2.2 Opacites

By default, the stagger code uses a similar opacity package to that detailed by Gustafsson et al. (2008), which based on the VALD-2 database (Stempels et al. 2001) of atomic lines and for molecular line, the SCAN-base (Jørgensen 1997). This is augmented by bound-free data from the Opacity Project and the Iron Project (Hayek et al. 2010). For 3D models it is necessary to include the second ionisation stage of many metals as the deeper extension of the models compared to the 1D mean that these hotter conditions are reached.

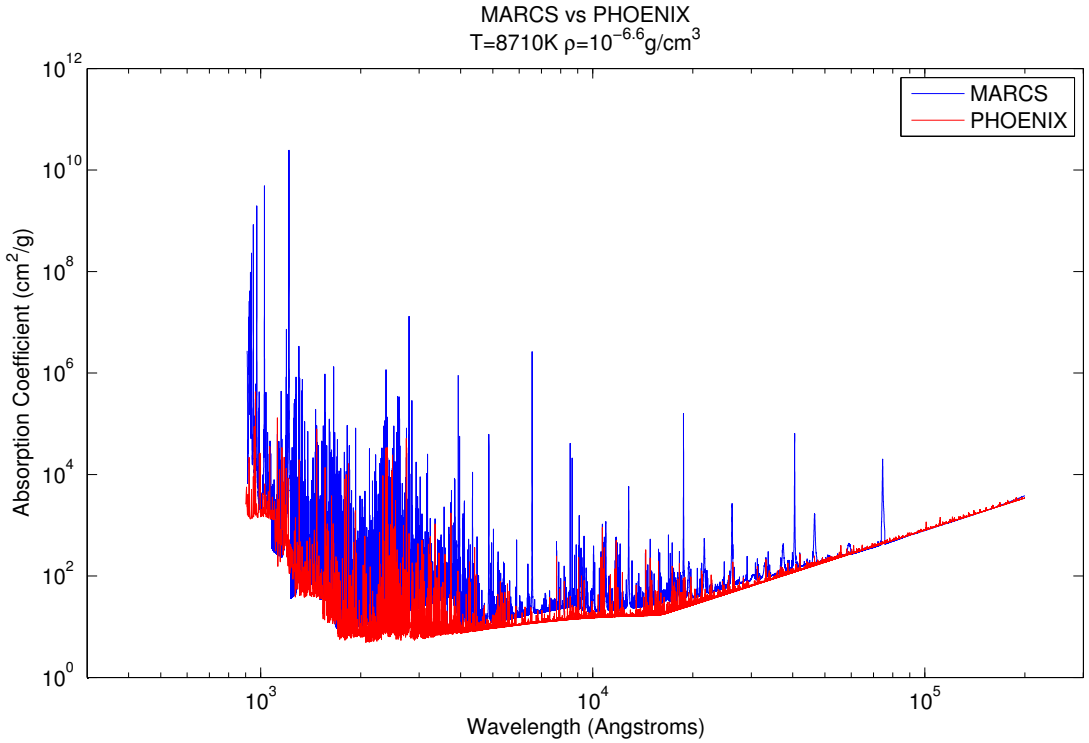

Figure 4.11: Monochromatic absorption coefficients with wavelength for the MARCS (blue) and PHOENIX (red) opacity packages. The atmospheric conditions are T=8170K and $\rho = 10^{-6.6} g/cm^3$ with solar metallicity. These conditions correspond to the optically thick part of the mean solar model.

The opacity data from the PHOENIX collaboration consists of over 550 million atomic and molecular lines. Originally based on data from Kurucz (Kurucz 1993a,c,b), it is continuously augmented and updated as new data becomes available. In particular, the PHOENIX opacities are updated and tested for modelling M dwarfs - a regime much cooler than solar-like stars and thus requiring a whole suite of molecular data that may be safely neglected for hotter stars.

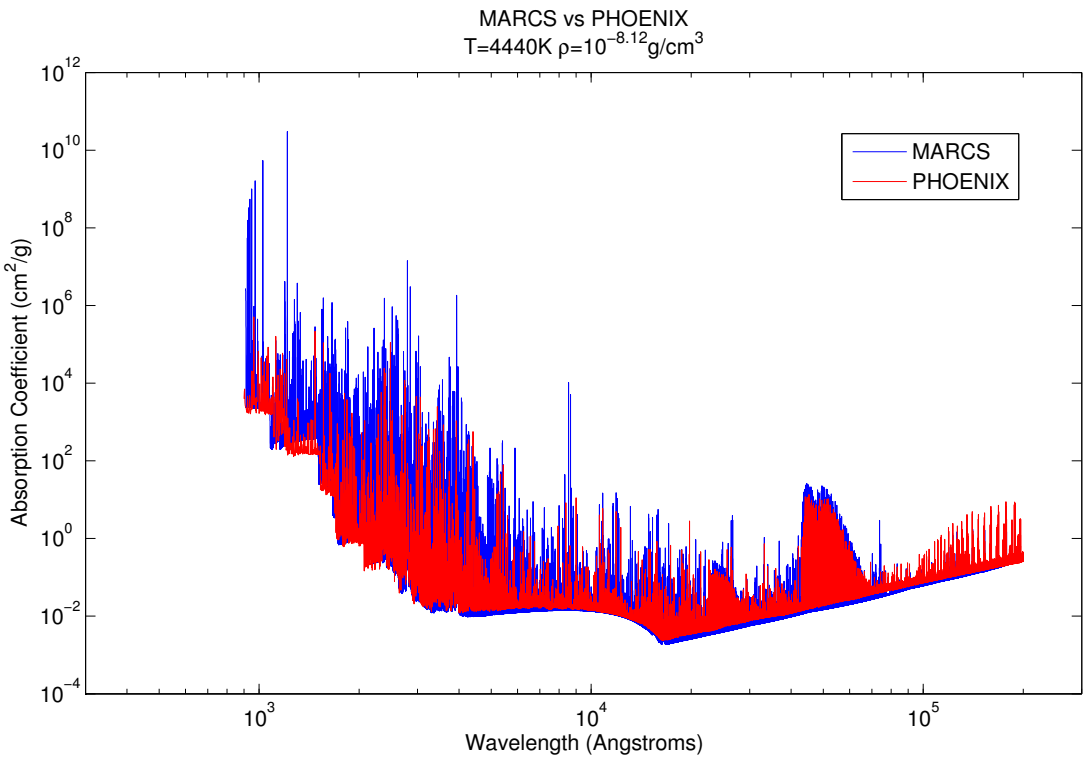

Figure 4.12: Monochromatic absorption coefficients with wavelength for the MARCS (blue) and PHOENIX (red) opacity packages. The atmospheric conditions are T=4440K and $\rho = 10^{-8.12} g/cm^3$ with solar metallicity. These conditions correspond to the optically thin part of the mean solar model.

Figure 4.11 shows a comparison of the monochromatic absorption coefficients of both the MARCS and PHOENIX packages for atmospheric conditions T=8170K and $\rho = 10^{-6.6} g/cm^3$. These conditions correspond to the optically thick part of the mean solar model ($T_{eff} = 5777K, g = 10^{4.44} m/s^2$, [Fe/H]=0.00).

The two datasets trace out similar features and in general agree well across the wavelength spectrum. The MARCS data is sampled at constant spectral resolution, $\Delta\lambda/\lambda = constant$, meaning it is more closely sampled in wavelength in the UV than in the infrared. In contrast, the PHOENIX absorption coefficients are sampled at regular wavelength intervals meaning that the red end of the spectrum is significantly more sampled than the blue.

One manifestation of this is that spectral line opacities will be far more peaked in the MARCS data, particularly at the blue end of the spectrum. While the PHOENIX spectral resolution means that, even for the same (or more realistically very similar data), the PHOENIX peaks will be significantly lower as they are 'smeared out' in comparison. This can be seen clearly in figure 4.11, with MARCS peaks outstripping PHOENIX at short wavelengths, while correspondence between the peak heights is much improved at longer wavelengths.

The PHOENIX data seem to be slightly, but systematically lower than the MARCS, not only in the peaks corresponding to the spectral lines, but also in the continuum. This is most noticeable around 10^4 Angstroms. This is a real effect, apparent also in the mean opacities 4.7 and 4.8 earlier, and is caused by the differences in adopted line lists and assumptions inherent in compiling these tables. A more detailed examination of these differences is desirable, but the impact on the physical and spectra

of these objects is minor, and such a study is beyond the scope of this work. It is important to note that these differences are small and of order of the inherent scatter of values obtained by groups with differing methodologies.

Figure 4.12 shows the same comparison, but from an optically thin region of the mean solar structure, $T = 4440K, \rho = 10^{-8.12} g/cm^3$. In this important, optically thin, region the continua of the two datasets corresponds very closely, reflecting the very similar results obtained for the solar model. Evidence of the more peaked data in the MARCS dataset remains clear.

4.2.3 Opacity Table

The binned opacity table is calculated from the monochromatic opacities measured against a mean temperature and density stratification. Using the result of the radiative transfer performed on this mean model, the stratification is refined to a new depth scale to ensure adequate resolution over the line forming region. The opacities for this new stratification are calculated and the individual wavelengths binned based on the results of the new integration of opacity over the structure, which finds the monochromatic opacity at continuum forming . The mean opacities are then calculated from this partitioning of the opacities into bins. The final table consists of a header holding auxiliary data about the table size, table boundaries, input assumptions and units, followed by the 4-dimensional table containing slices in the temperature-density plane of the bin opacity normalised to the Rosseland opacity, the photon destruction probability multiplied by the mean intensity and the photon destruction probability multiplied by the Planck function, for each opacity bin.

4.3 Validation

In order to justify the use of opacity binning, the approximation must reproduce the heating (and cooling) rates, Q_{rad}. Using the mean solar model ($T_{eff} = 5777K, g = 10^{4.44} cm/s^2, [Fe/H] = 0.00$), as a reference the monochromatic and bin heating rates for each atmospheric height are calculated 4.5 and compared. The magnitude of the heating rate is largest around the optical surface, see Magic et al. (2013) Figure 4, where they use the same test for their binning and find close correspondence. To judge the efficacy of the chosen bins the maximum difference between the monochromatic and binned solution is computed,

$$max(dQ_{rad}) = \frac{max(dQ_{rad,bin} - dQ_{rad,\lambda})}{max(dQ_{rad,\lambda})} \tag{4.15}$$

where the radiative heating subscripts refer to the binned and monochromatic solution respectively. The result is very sensitively dependent on the bin locations and boundaries, showing a highly nonlinear response making optimisation difficult. To facilitate a clear comparison between the two datasets, the bin locations and boundaries for both are kept identical, being optimised for the MARCS dataset, which shows the larger difference between the binned and monochromatic solutions. Magic et al. (2013) used a solar model with max(dQ_{rad})=2.78% for 12 bins (MARCS data), that has finer resolution in wavelength, while this work splits the opacity strength with three divisions and the wavelength range with four, in order to make a rectangular grid. The resulting performance improved slightly for

the MARCS data, with max(dQ_{rad})=2.36%, while the PHOENIX dataset reproduces the monochromatic solution more accurately with max(dQ_{rad})=1.17%. For comparison, over the grid of models Magic et al. (2013) find an average value of max(dQ_{rad})=2.38%.

The Rosseland opacity at monochromatic depth unity is used as the criterion for binning, see Figure 4.13. The Rosseland opacity shows the same characteristic 'L'-shape as the raw opacities, with the blue end of the spectrum exhibiting a far wider range of opacity strength than the red. As with the monochromatic opacities, the MARCS data shows higher peaks and more rapid variation, particularly in the blue and UV, due to finer resolution. This leads to differences in bin assignment, see Figure 4.14. The strongest differences in bin assignment between the MARCS and PHOENIX opacity data sets occur for the high opacity strength bins (3, 8, 12), and this will result in a different splitting of the integration making direct comparison of the individual bin properties between the two datasets highly dangerous. Figures 4.15 and 4.16 show the opacity strength with wavelength, with colour-coding corresponding to assigned bin number. The striking difference between these plots concerns the resolution of the data. The MARCS opacity is heavily more populous than PHOENIX in the ultraviolet, while the opposite is true at the reddest end. This leads to dramatically different bin populations for the two datasets, while the reddest PHOENIX data reaches the strongest opacity bin, but the MARCS opacities in this region just fall short. As a result the individual bin mean opacities are not directly comparable, as they represent a different discretisation of the integral. Using a single bin is to the grey approximation and does allow a direct comparison between the two opacity sources, see Figure 4.17. Figure 4.17 shows an example of a high-density slice through the single bin mean opacity. The two datasets broadly agree, but the MARCS model shows evidence of finer

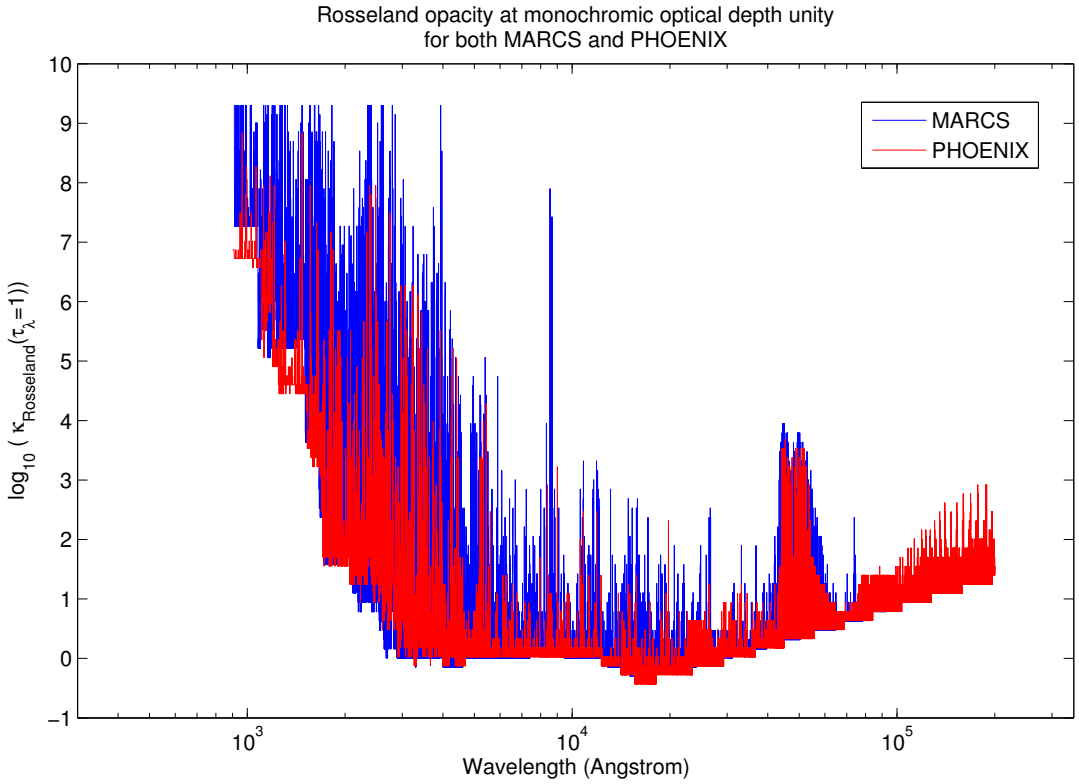

Figure 4.13: Rosseland opacity at monochromatic optical depth unity with wavelength for MARCS (blue) and PHOENIX (red) opacity packages.

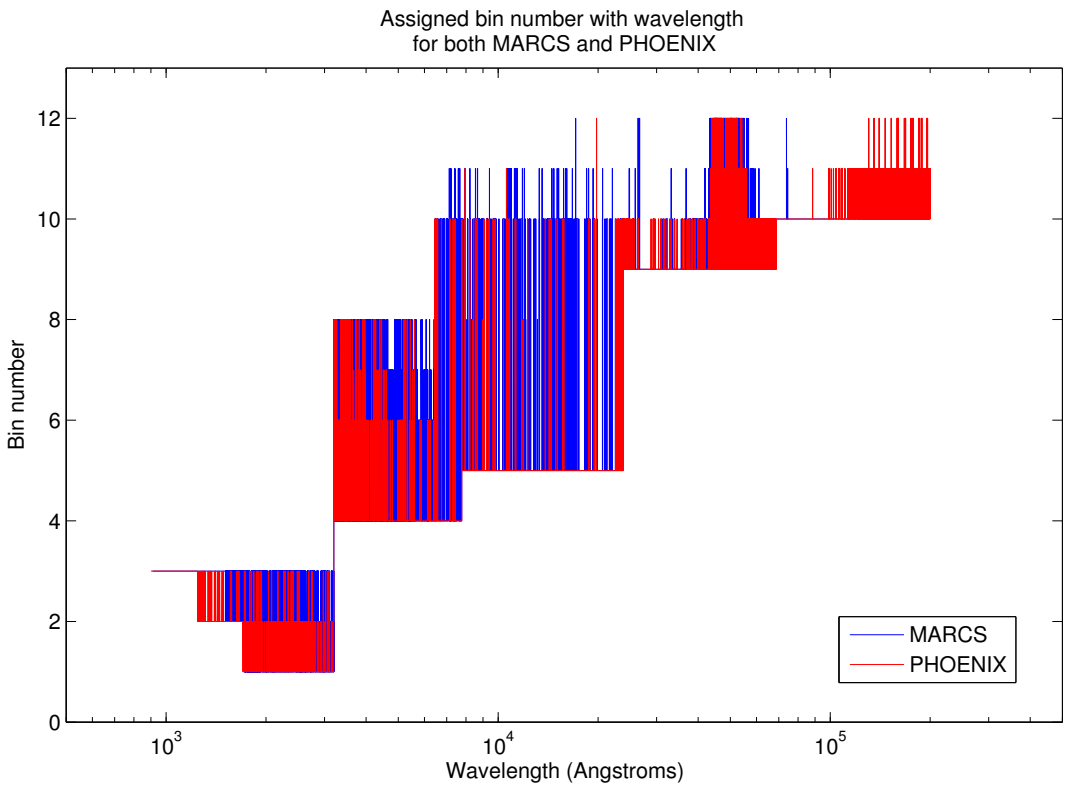

Figure 4.14: Bin assignment with wavelength for MARCS (blue) and PHOENIX (red) opacity packages.

structure, and more rapid transitions. Disentangling the combined effects of resolution, assumptions and fundamental differences in the computation and measurement of the two opacity sets is beyond this work, but the finer structure of the MARCS data may be simply due to the resolution in the respective dimensions as the gas pressure resolution of the MARCS data is around $\sim 25\%$ finer than the PHOENIX.

4.4 Summary

Modelling of stellar atmospheres relies on physical input data - most crucially the equation-of-state and opacity data, which close the system of hydrodynamic equations. It is critically important to use accurate and appropriate data. As the modelling of late-type stars moves down the main sequence to cooler dwarfs, brown dwarfs and even planets, the effects of molecules and dust condensate species become increasingly important. For this reason a move from the Opacity Project based MARCS opacities and MHD equation-of-state to the PHOENIX opacities and ACES equation-of-state is required. The interdependency of opacities and the equation-of-state mean that the two must be treated pairwise, as alone they would produce erroneous results. I have shown that for solar models, the two datasets produce similar results, but demonstrated the great detail of the PHOENIX-MARCS package at cooler temperatures and at the red end of the spectrum, where the majority of molecular lines lie.

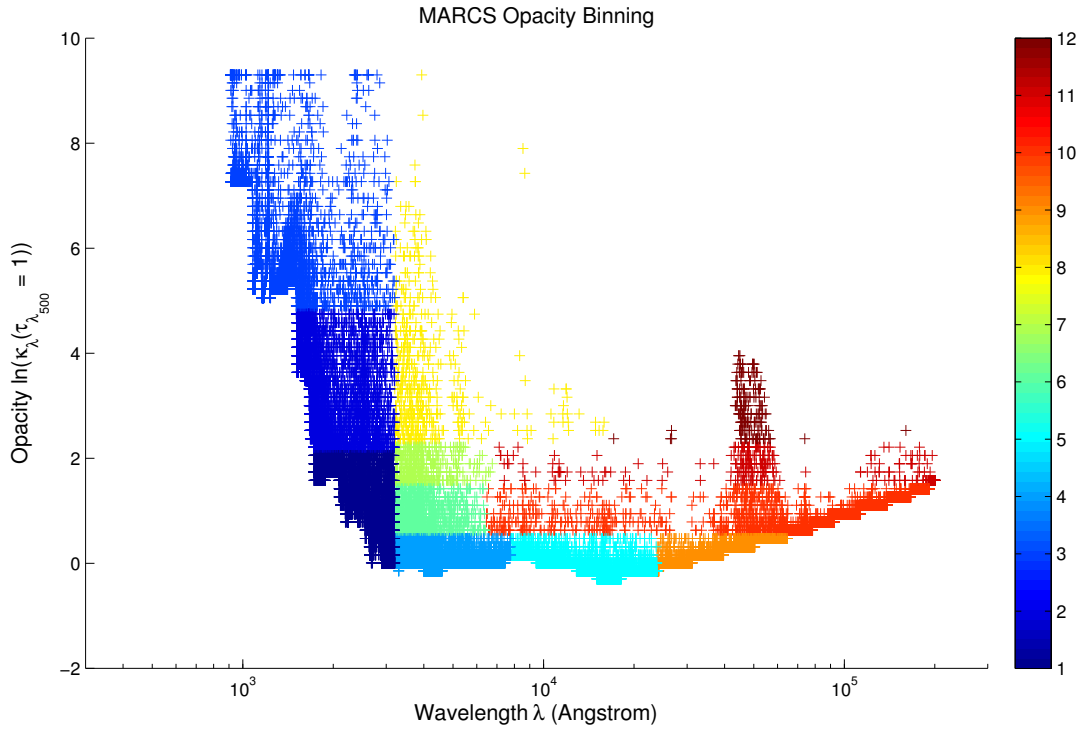

Figure 4.15: Absorption coefficient at monochromatic optical depth unity with wavelength for the MARCS opacity package. The colours correspond to the assigned bin number under the multi-group scheme.

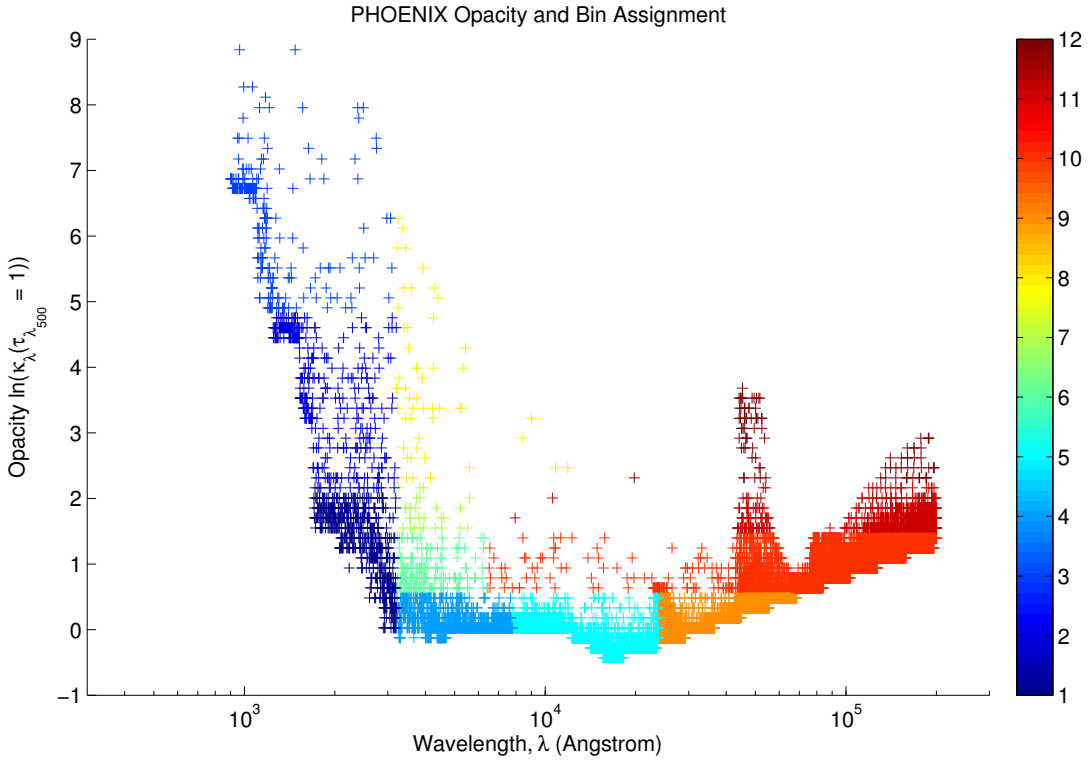

Figure 4.16: Absorption coefficient at monochromatic optical depth unity with wavelength for the PHOENIX opacity package. The colours correspond to the assigned bin number under the multi-group scheme.

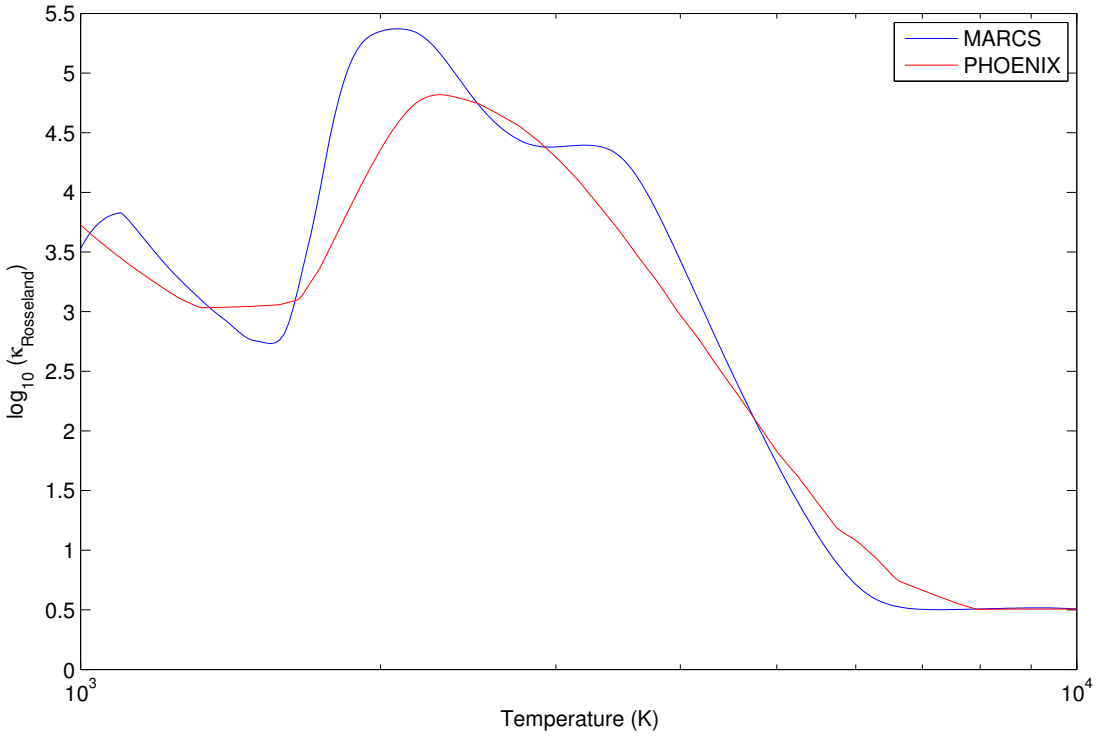

Figure 4.17: The Rosseland mean opacity calculated from the monochromatic opacities for MARCS (blue) and PHOENIX (red) opacity packages with gas temperature.

Chapter 5

Ultracool Stellar Atmospheres

5.1 Introduction

Modelling the coolest stellar and substellar atmospheres is complicated by the formation of molecules and condensates (dust), in addition to the gas problem solved for hotter stars. Spanning stars with convective envelopes and radiative cores to fully convective objects (Hayashi 1961; Kumar 1963b,a), convection plays the dominant role in their atmospheres. As discussed in Chapter 3, approximate one-dimensional models of convection prove inadequate to describe the feedback of the convection onto the atmospheric structure. Convection is manifestly 3D, and cannot operate in one dimension, instead an approximate model must be employed . Similarly, dust (condensate) formation may only proceed in multiple dimensions and even parametrisations of dust in stellar atmospheres require the ad hoc inclusion of mixing in order to achieve a stationary solution (Helling et al. 2008), in line with observations.

Cool stars form a sequence on the right-hand side of the Hertzsprung-Russell diagram, see Figure 5.1, covering stellar types F, G, K, and M in the standard Harvard classification system. With masses below $\sim 1.4 M_{\odot}$, cool stars constitute the cool, dim end of the main sequence. More particularly, ultracool dwarfs span low-mass stars through brown dwarfs to large 'gas-giant' extra-solar planets.

While the existence of such cool dwarfs was predicted by Kumar (1963a,b) who outlined the key properties of these 'black' stars, the first brown dwarf was not discovered until 1995 (Rebolo et al. 1995). Shortly after, Nakajima et al. (1995) discovered Gliese 229b and the discovery of many other objects followed closely behind. This led to the definition of two new spectral classes, L and T, that extend the Harvard system beyond M at the cool end of the main sequence. Although these objects never fuse hydrogen, and therefore never join the main sequence, they form a pseudo- main sequence.

Gas physics has been remarkably successful in describing the atmospheres of stars. Atomic nuclei and electrons seek to minimise their internal energy, by forming first ions, then neutral atoms and molecules. The radiation field and thermal energy counteract this and the resulting equilibrium can be used to understand the diversity of stars across the Hertzsprung-Russell diagram.

Hot stars are also extremely luminous, meaning that the thermal energy and radiation field are stronger than the binding energy of orbital electrons, resulting in a highly ionised gas. Moving along the main

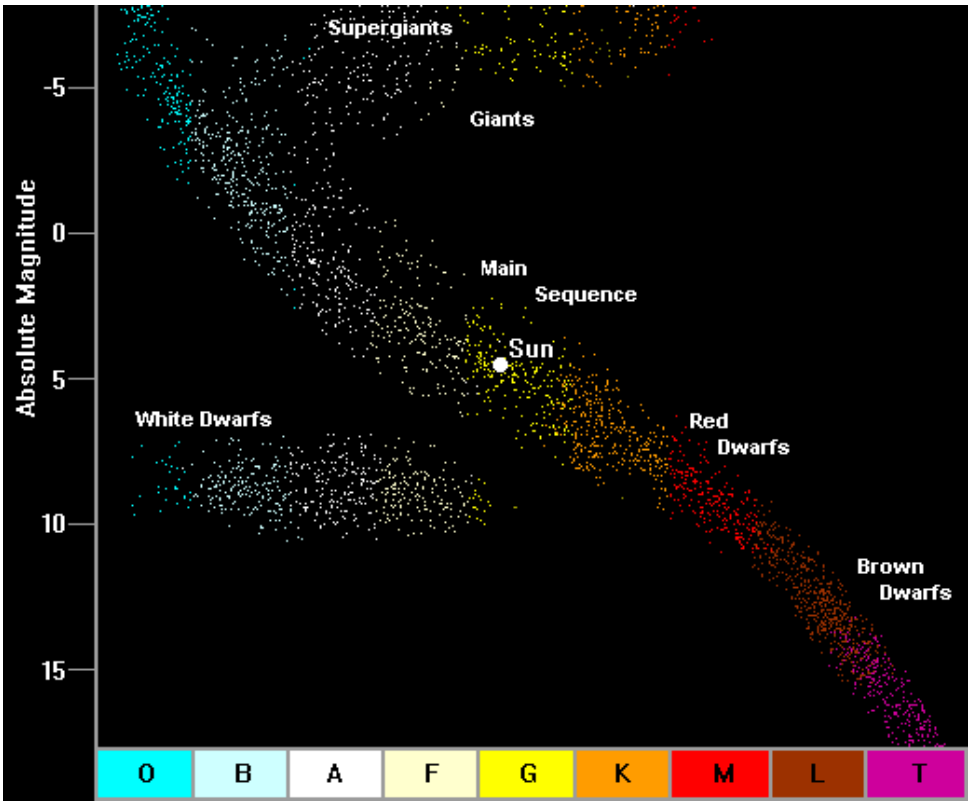

Figure 5.1: A Hertzsprung-Russell diagram of absolute magnitude with spectral type. Ultracool dwarfs form classes M, L and T to the bottom right of the figure. M dwarfs constitute the cool end of the red dwarfs on the main sequence, while brown dwarfs are sub-stellar but form a pseudo-main sequence for cool, dim objects. Courtesy of https://www.uwgb.edu/dutchs/AstronNotes/spectra.htm.

sequence to cooler effective temperatures and higher densities results in an increased rate of stable recombination, meaning lower degrees of ionisation, then neutral atoms and molecules at low temperatures, see Figure 5.2. Spectral classes O-K are well described by partially ionised gas physics and mainly single-species diatomic molecular formation, but for cooler spectral classes a wider problem must be solved.

At very cool temperatures, more complex molecules form and the high opacity of these molecules dominate the spectral appearance of these objects (Leggett et al. 1999; Kirkpatrick et al. 1999a; Burrows et al. 1997). In still cooler atmospheres these molecules bond together forming macro-molecules that will relax into a lattice structure, forming islands of condensates or dust.

The challenge in modelling ultracool dwarfs is to include the complex chemical network of molecular and condensate formation, including the detailed opacities, into the framework of stellar atmosphere models. The problem of dust covers such a large dynamic range, from the molecular collisions to convective motions that couple the whole atmosphere and mix the medium to enable dust formation, that a true molecular dynamics approach is simply intractable. Instead, one must consider statistical models of nucleation, reaction rates etc in order to capture the essence of the problem.

As they span the transition from star to planet, the term ultracool dwarf has the advantage of not distinguishing objects based on their formation history, which is difficult to determine observationally.

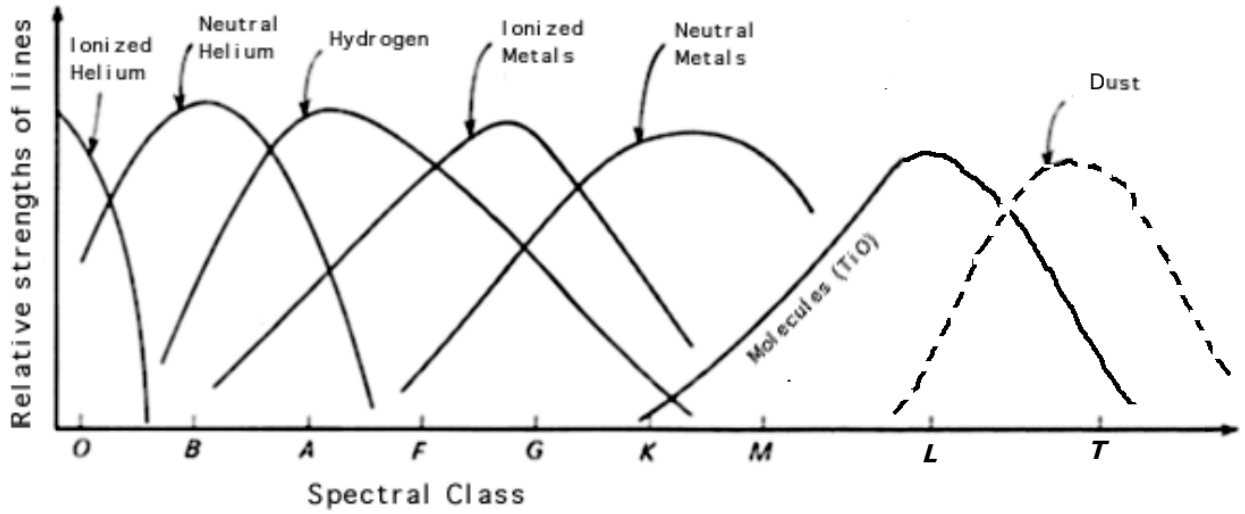

Figure 5.2: Relative line strength with spectral class for O, B, A, F, G, K, M, L and T stars. From left to right (hot to cool) this figure shows that ionisation wanes in importance, while neutral atoms, molecules and dust become increasingly dominant. Adapted from http://www.star.ucl.ac.uk

5.1.1 Formation

Stars form by the collapse and fragmentation of gas clouds (Jeans 1902). Upon stabilising themselves against this collapse by hydrogen burning in their core, stars join the main sequence. Brown dwarfs never fully stabilise themselves by hydrogen burning, although deuterium, tritium and lithium burning may occur (Chabrier et al. 2005). The lack of a stable fusion zone yielding the energy to counteract gravitational collapse defines a sub-stellar object or brown dwarf. Instead the gravitational collapse of these objects is halted by electron degeneracy pressure (Hayashi & Nakano 1963), although they will contract and cool over time (Chabrier et al. 2000). Brown dwarfs form a pseudo- main sequence, and constitute the low-mass tail of objects created by the gravitational collapse of a gas cloud. In contrast, planets form inside proto-planetary disk around a young parent star. Keplerian shearing (e.g. Wuchterl 2004) prevents a straightforward collapse, which proceeds instead by the aggregation of heavier elements into dust and then planetesimals (Blum & Wurm 2008). The light elements are removed by the stellar radiation or scattered by collisions (Chabrier et al. 2005). As a result, the chemical composition of a planet is markedly different to that of a star or brown dwarf.

5.1.2 Spectral Class

Brown dwarfs cover a mass range of $\sim 60 M_{Jupiter}$−few $M_{Jupiter}$, meaning that there is an overlap with the largest observed extra-solar planets (e.g. Johnson et al. 2009). Effective temperature of planets and brown dwarfs also overlap, with cooling for brown dwarfs and irradiation for planets further complicating things, meaning that a spectral type can no longer be attributed to a unique effective temperature (Kirkpatrick 2005; Golimowski et al. 2004).

Molecular species in ultracool dwarfs cause the spectra to deviate strongly from a blackbody, see Figure 2.3, in various spectral bands (Leggett et al. 1999; Kirkpatrick et al. 1999a; Burrows et al. 1997). Obtaining complete opacity data is both critical and has been a major challenge for the field

Spectral Type	T_{eff}	Prototype
L0	2200	2MASP J035+2540
L2	2000	Kelu-1
L4	1800	2MASS J1155+2307
L6	1600	2MASS J0860+1057
L8	1400	2MASS J1632+1904

Table 5.1: Spectral type with effective temperature, including a prototype objects for each spectral class. Adapted from Allard et al. (1997)

(Burrows et al. 2001). In addition, brown dwarf chemistry is complicated by the condensation of gas into liquid or solid phase dust, as naturally occurs at low temperatures. While the spectral appearance of dust-hosting atmospheres may be expected to evolve significantly over the 3000K range of effective temperature that these objects span, due solely to the gas properties, chemistry plays a key role in these atmospheres and introduces molecular formation and dust formation both of which alter the spectrum dramatically.

5.1.3 L and T - Brown Dwarfs

The new spectral classes beyond M dwarfs, L and T, were defined because the spectral changes occurring over this range are significant and inserted following at the cooler end of the main sequence. Temperature is the major factor that drives spectral variations in $O-M$ stars and is also important for later-type objects, but there is a degeneracy that occurs for very cool temperatures (Golimowski et al. 2004).

Spectroscopically, L dwarfs are characterised by the weakening of metal oxide bands such as titanium oxide (TiO) and vanadium oxide (VO), to be replaced by metal hydride and prominent neutral alkali metals. This may be explained by the titanium (Ti) and vanadium (V) bearing compounds condensing to form dust thus leaving the atmosphere depleted in metal oxides with a consequent reduction in opacity for these compounds. Table 5.1 gives the spectral classification with effective temperatures from early to late L dwarfs, including a prototype star defining this class (Allard et al. 1997). Figure 5.3 shows the normalised flux (plus a constant) with wavelength in the red and infrared (Kirkpatrick et al. 1999b). The left-hand panel shows a late M dwarf, where the annotations clearly pick out the metal oxide features. Below this the spectrum of an early L dwarf shows that metal oxide features may still be identified, although other features including metal hydrides are also prominent and the metal oxides are no longer the defining property. Finally the late type L dwarf shows no clear signs of metal oxides in this region of the spectrum. The right-hand panel shows the evolution of observed flux from M7 to L8. The metal oxide features below $\sim$ 8000Å clearly wane while the infrared becomes increasingly busy with spectral lines. Evidently, this implies that any successful modelling of these objects requires complete and accurate molecular line and dust opacities (Burrows et al. 2001; Marley et al. 2002; Burrows et al. 2011). In L dwarfs the dust forms and is retained in the photosphere leading to optically thick cloud layers, that smooth out spectral features (Jones & Tsuji 1997).

T dwarfs are characterised by the unambiguous detection of methane, CH_4, which becomes the dominant carbon bearing molecule at around $1300-1400K$ (Burgasser et al. 2003). Figure 5.4 shows the near infrared spectral standards for T dwarfs, while the right-hand panel shows the near-infrared

Figure 5.3: From Kirkpatrick et al. (1999a): Normalised flux of M and L dwarfs between 6000Å and 10,000Å. Left panel - Enlarged spectra of a late-M, early- to mid-L, and late-L dwarf. Prominent features are marked. Note the absence of oxide absorption in the L dwarfs along with the dominance of alkali lines and hydride bands. Names for the 2MASS objects have been abbreviated. Right-panel - L-dwarf spectral sequence. A subset of the Keck LRIS data from Kirkpatrick et al. (1999a), but showing only one spectrum for each subclass from L0 through L8. Also shown for comparison is the Oppenheimer et al. (1998) spectrum of Gl 229B and three late-M dwarfs, also taken with LRIS on Keck.

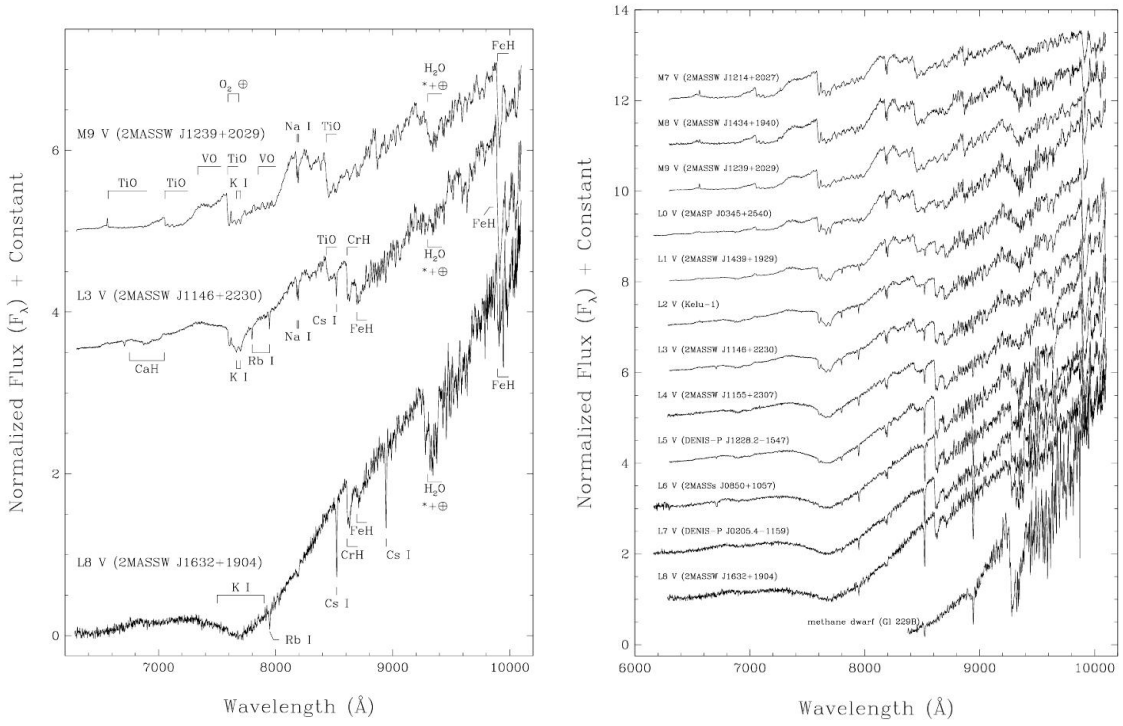

spectra for objects in these classes, from Geballe et al. (2002). Due to their cooler temperatures the cloud decks of T dwarfs are thought to reside below their photospheres (Tsuji et al. 1996b) (as the cloud deck lower boundary is always near the condensation temperature of dust, T_{cond}). Observations appear to confirm this as T dwarf spectra are best fit by models which account for dust as an element sink but not as a source of opacity in the atmosphere. The transition between the two is more problematic with no models adequately reproducing observations in this range. Characterised by a progressive reddening in the near-infrared $J - K_S$ colour throughout most of the L dwarfs, due to an increase in photospheric dust opacity, the transition is marked by an abrupt blue-ward shift of ~ 2 magnitudes in the $J - K_S$ colour, while the J-band magnitude brightens by up to a magnitude (Vrba et al. 2004; Zapatero Osorio et al. 2007; Faherty et al. 2012). Figure 5.5 shows the near-infrared colour-magnitude diagram for M (black squares), L (red squares) and T (green circles) dwarfs. The M dwarfs are well fit by the dusty model (magenta line), the early L dwarfs are well fit by the cloudy models (right thin black line) and the late T dwarfs show agreement with the clear, cloud-free, models (left thin black line). Evidently between the early L dwarfs and the late T dwarfs there are a number of objects that are poorly fit by any of the dusty, cloudy or clear models. Observationally the transition $L7 - T3$ needs a second parameter to break the degeneracy in effective temperature, see Figure 5.6 (Golimowski et al. 2004). This degeneracy also exists in the absolute magnitudes in the M and L

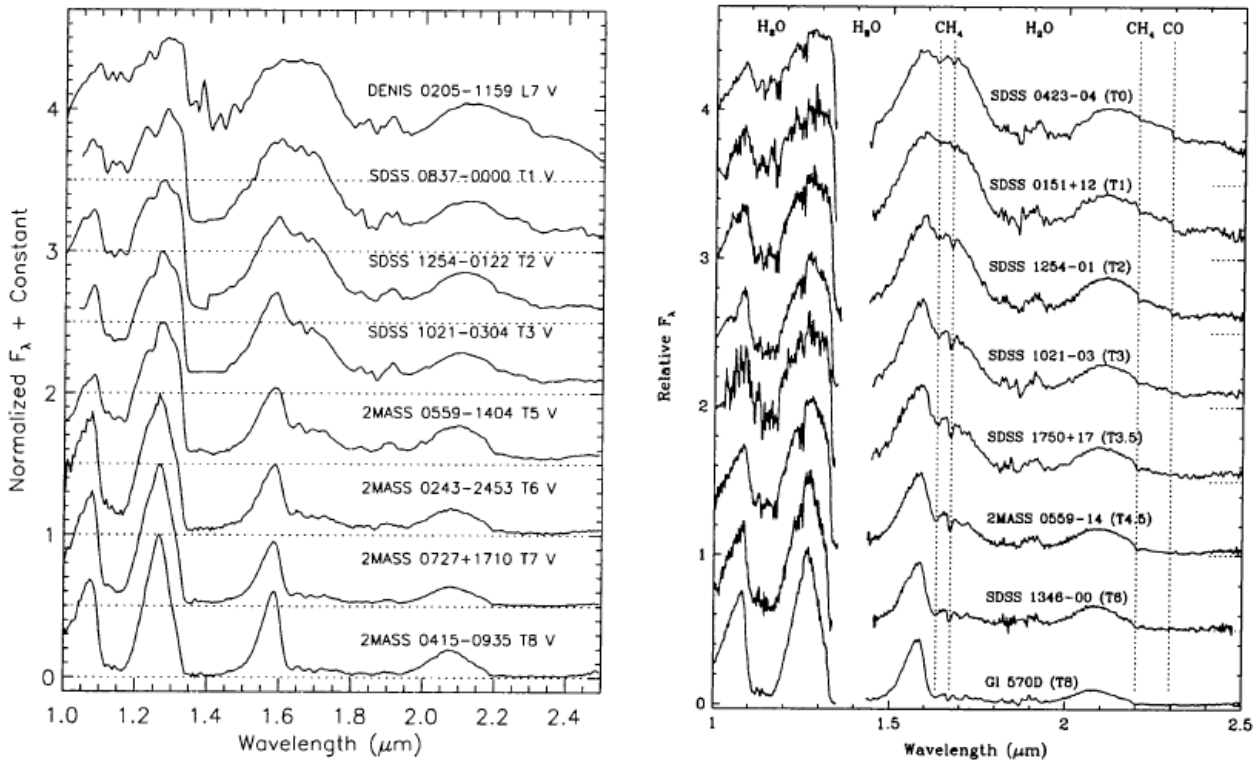

Figure 5.4: Taken from Burgasser et al. (2002a). Plot of 1-2.5μm spectra of T dwarfs observed using the Keck I NIRC instrument. Spectra are normalised at their J-band peaks, offset by a constant (dotted lines), and ordered by increasing 1.15 and 1.6 μm absorption. Major H_2O, CH_4, CO, and FeH absorption bands are indicated, as are lines of K I (1.169, 1.177, 1.243, and 1.252μm and the region of strongest CIA H_2 absorption. The L dwarfs 2MASS 0920+3517(L6.5 V) and 2MASS 0825+2115 (L7.5 V) are shown for comparison.

bands, see Figure 5.7. All modelling attempts thus far have failed to reproduce the abruptness/sharpness of the transition (Ackerman & Marley 2001; Allard et al. 2003; Burrows et al. 2006; Saumon & Marley 2008). A couple of possible scenarios have been suggested, but consensus is still elusive and no systematic study has been performed (Radigan et al. 2012).

The first suggestion is that dust growth becomes suddenly and drastically more efficient, leading to very large dust grains that cannot be sustained by the surrounding atmosphere and precipitate or gravitationally settle rapidly, leading to the sudden collapse of the cloud base below the photosphere(Knapp et al. 2004). This scenario naturally produces a sharp transition but with no physical mechanism suggested that produces the jump in growth efficiency this is a rather ad-hoc solution.

Alternatively, if the cloud deck were to develop holes whose filling factor increases across the L-T transition until the atmosphere is completely clear, this would reproduce the rapid blue-ward shift observed on the colour magnitude diagram (Ackerman & Marley 2001; Burgasser et al. 2002b). To give credence to this theory it has been shown that the L-T transition may be qualitatively reproduced by linearly combining the cloudy L 1D models and cloud-free 1D T models (Burgasser et al. 2002b). Physically this approach is flawed, as cloudy atmospheres provide a large opacity wall with their cloud deck and consequently radiation is trapped behind, leading to a warming of the underlying atmosphere, therefore the two atmospheric temperature structures are incompatible. A rigorous test of

Figure 5.5: Adapted from Burgasser et al. (2002b).Near-infrared colour-magnitude diagram of M, L, and T dwarfs. The absolute J magnitudes and J-Ks infrared colours are shown for a sample of M (black squares), L (red squares), and T (green circles) dwarfs with known parallaxes. The positions of 2MASS J0559-1404 and SDSS J1254-0122 are indicated. The predicted colours and magnitudes for the dusty (magenta line), clear (left thin black line), and cloudy (right thin black line; frain = 3) atmosphere models are plotted as a function of T_{eff} at constant gravity, g = 10^5 cm s^{-2} (typical for very low mass main-sequence stars and evolved brown dwarfs). Connecting the cloudy and clear tracks are the predicted fluxes for our partly cloudy models at T_{eff} = 800, 1000, 1200, 1400, 1600, and 1800 K. The blue squares indicate the cloud coverage fraction in steps of 20%. The apparent evolutionary track of brown dwarfs based on the empirical data is indicated by the thickened line, which crosses from the cloudy to clear track at Teff ≃ 1200 K.

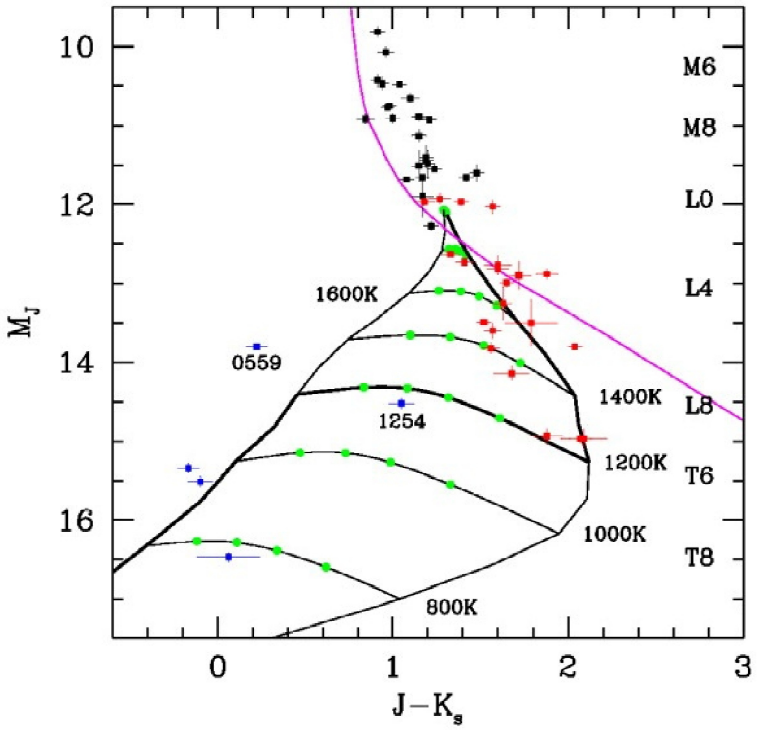

this theory would require a more detailed, multi-dimensional approach. One problem with this idea is that clouds are expected to thicken from L dwarfs to T dwarfs, due to the increasing number of condensible species at cooler temperatures. However, this model would produce azimuthal asymmetry in the photosphere, leading to photometric variability on rotational timescales.

Neither scenario has been modelled in detail as a physical process (Radigan et al. 2012). Instead, they represent requirements to reproduce the observations. Cloud fragmentation has the advantage that it makes testable predictions as fragmentation with azimuthal asymmetry will result in variability on rotational timescales.

5.1.4 Variability in Brown Dwarfs

The L spectral sequence is characterised by the thickening of the dust cloud deck, the L/T transition ($\sim L7 - T4$) by a significant drop-off in opacity at near constant effective temperature (Golimowski

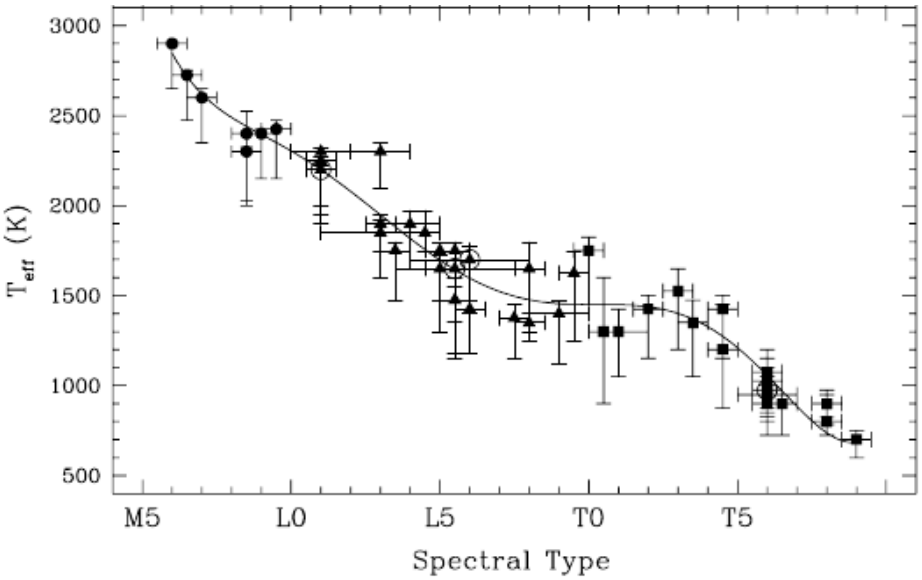

Figure 5.6: From Golimowski et al. (2004). Effective temperature, T_{eff}, with spectral type for ultracool dwarfs -M dwarfs (circles), L dwarfs (triangles), and T dwarfs (squares). The curve is a sixth-order polynomial fit to the weighted data except those representing known close-binary systems (encircled points). The degeneracy in effective temperature over the L-T transition is clear.

et al. 2004; Stephens et al. 2009), and the later T dwarfs by a cloud deck sunken below the photosphere (Tsuji et al. 1996a) leaving a clear atmosphere.

Early searches for variability in these objects mainly targeted late M and early L dwarfs, as the drop-off in optical flux for later objects made observation problematic (Bailer-Jones & Mundt 2001; Gelino et al. 2002; Koen 2003; Koen et al. 2004; Koen 2004; Koen et al. 2005; Koen 2005). In $\sim$ 30% of these early type objects, variability in the I-band is detected, with a peak-to-peak amplitude of a few percent. Unfortunately, magnetic activity in these stars makes the interpretation of this variability ambiguous as to whether it is due to modulation caused by cool magnetic spots or dust clouds or both.

The atmospheres of later L dwarfs and T dwarfs are increasingly neutral, rendering cool magnetic spots significantly less likely (Gelino et al. 2002; Mohanty et al. 2002), meaning the interpretation of variability in these objects is also less ambiguous. Coupled with a move to the infrared, to exploit the higher fluxes, this makes studying transition objects more feasible.

In contrast with the optical, infrared variability in ultracool dwarfs seems to be rare (Enoch et al. 2003; Koen 2004, 2005; Goldman et al. 2008; Morales-Calderón et al. 2006). More recent results from high precision monitoring provide evidence of lower amplitude (10-50 mmag) variability (Clarke et al. 2008; Artigau et al. 2009). Most recently, Radigan et al. (2012) monitored a transition T1.5 dwarf, finding persistent, high-amplitude ($\sim$ 26%) variability in the J-band. The variability is persistent on rotational timescales and shows a slow evolution over a timescale of days - consistent with the evolution of dust cloud features.

Variability in L-T transition objects provides a powerful diagnostic to discriminate between models of different physical processes causing the rapid transition in this region.

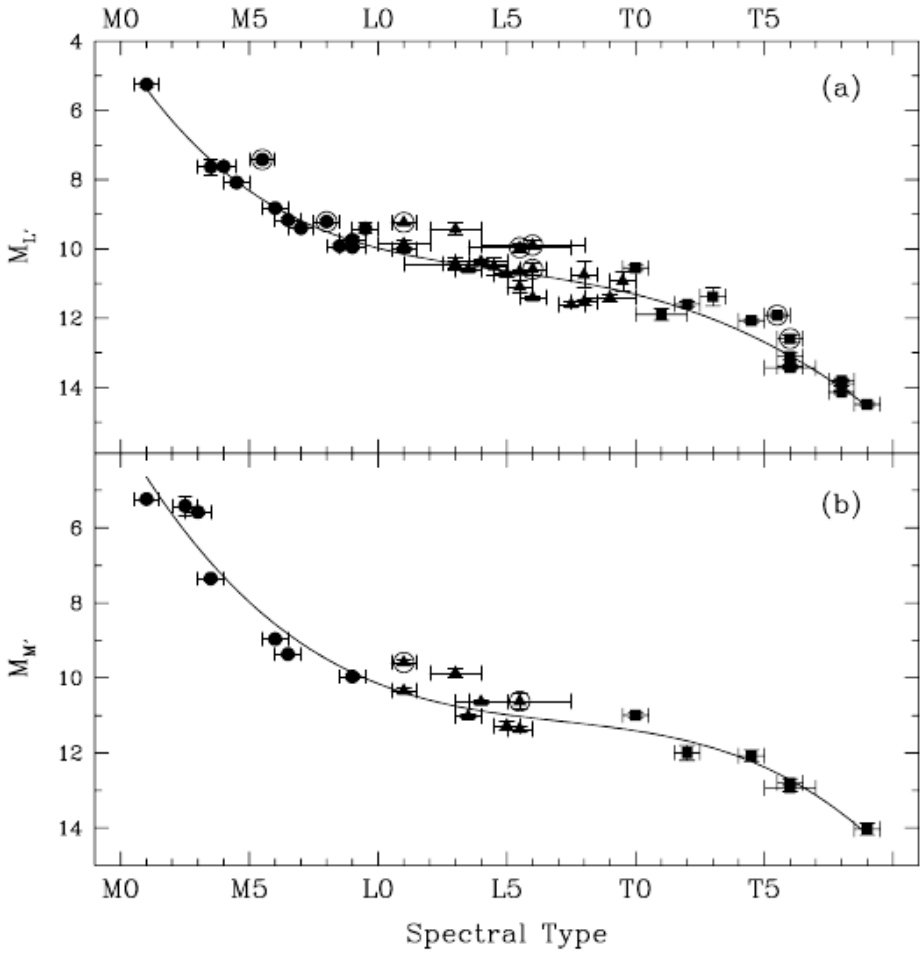

Figure 5.7: From Golimowski et al. (2004). Diagrams of (a) M_L and (b) M_M vs. spectral type for M (circles), L (triangles), and T (squares) dwarfs. All data are based on the MKO photometric system. Diagram (b) is supplemented with MKO M0 measurements reported by Reid & Cruz (2002) for Gl 811.1 (M2.5; G02), Gl 752A (M3; Kirkpatrick et al. (1991)), and Gl 643 (M3.5; Geballe et al. (2002)). The weighted means of the parallaxes of these M dwarfs measured by Yale Observatory (van Altena et al. 1995) and ESA (1997) are, respectively, 55.81± 6.27, 171.01±0.62, and 158.28±3.45 mas. The curves are (a) fourth-order and (b) third-order polynomial fits to the unweighted data except those representing known close-binary systems (encircled points). The degeneracy in absolute magnitude in both bands with effective temperature coincides with the transition from L to T dwarfs.

5.2 Comparison of dust models

The problem of dust in cool dwarf atmospheres has been tackled by a number of groups, under a myriad of assumptions and, for clarity, the foremost of these are detailed below.

Modelling dust multi-dimensionally places strong constraints on the dust model that may be implemented, while other considerations of micro-physics and model assumptions restrict the field further. Ultimately, it is important to find a workable compromise between the accuracy of the physical model and a tractable implementation.

5.2.1 Cooper et al

By consideration of the characteristic timescales on which the important physical processes operate (Rossow 1978), the model of Cooper et al. (2003) determines the most probable particle size of dust grains in a cloud at each vertical pressure level. Intended to offer a simple prescription for estimating cloud opacity in sub-stellar objects, it deliberately omits the intricacies of inhomogeneity, advection in the horizontal plane and time dependence in the solution, to create a simple model that can be easily coupled to spectral synthesis models.

It employs the chemical equilibrium calculations of Burrows & Sharp (1999) and the intersection of the dust species partial pressure curve with its saturation vapour pressure curve to determine the cloud base in the atmosphere. The modal size of the dust grains at each pressure level in the atmosphere are then found by growing embryonic seed particles (∼1nm) until the competing physical growth processes are balanced by the particle sedimentation. The micro-physical processes operating are characterised by a single-valued timescale that expresses their relative importance. The timescales are computed from the expressions given in Rossow (1978) which considers various physical regimes based on classical or kinetic cloud particle interaction and turbulent or laminar flow, as described by the Knudsen and Reynolds numbers respectively.

The model runs separately for each condensible (dust) species, effectively decoupling the dust chemistry from the gas chemistry excluding the possibility of core-mantle composite grains and the blocking of dust species formation by element depletion. The dust materials considered are forsterite ($MgSO_3$), iron (Fe), gehlenite ($Ca_2Al[AlSiO_7]$) and water (H_2O); these choices reflect that the study was of very cool objects with effective temperatures down to ∼ 600K and the assumption that there exist abundant condensates, e.g. corundum (Al_2O_3), that can serve as nucleation sites for the growth of dust species that do not exist in the gas phase. Consequently, while Cooper et al. (2003) acknowledge that dust will only form in a clean atmosphere from supersaturated gas, they chose the required supersaturation as a free parameter and set it to (very low) 1%. Equally, once seed particles are available virtually all condensible atoms become sequestered into dust, making the assumption of no blocking dangerous.

The resultant stellar structures may then be coupled with a stellar atmosphere code, in this case TLUSTY (Hubeny 1988; Hubeny & Lanz 1995). Convergence problems forced some simplifications of the results: a cloud cut-off after one pressure scale height and the assumption of a single constant modal particle radius throughout the cloud. It is to be noted that such simplistic coupling is not physically correct as one would expect strong radiative feedback to affect the thermal structure of the atmosphere significantly. Back-warming or the Greenhouse Effect, familiar from the Earth and Venus, means the additional cloud opacity will trap heat compared to a cloud free atmosphere and this heat will strongly influence the dust cloud itself. Cooper et al. (2003) find discrepancies caused by this effect to be of the order of several hundred Kelvin; clearly highly significant in such cool objects.

Results confirm the findings of other groups (Lunine et al. 1989; Ackerman & Marley 2001), that a single particle size distribution is insufficient to model these clouds as particle size is strongly dependent on a number of physical parameters, including gas temperature, effective temperature, gravity and height in cloud deck. Interestingly, Cooper et al. (2003) find that the presence of the cloud creates gradients in some structures that are strong enough to form a secondary convection zone. A second convection zone has important implications for the dust grain sizes as convective

mixing would allow particles to be sustained in the atmosphere for longer, implying larger grain radii. Indeed, the results find grain sizes between 2-300 μm, much larger than those assumed by Tsuji et al. (1996b) under a stationary solution argument. Evidently, dust causes very strong coupling between the atmospheric thermal structure and the radiative transfer, which is to be expected as dust is a strong absorber of radiation.

5.2.2 Marley, Ackerman et al

Marley, Ackerman and collaborators follow a planetary approach to modelling clouds in brown dwarfs and extrasolar giant planets. They present a model based on balancing turbulent mixing and precipitation to find the modal particle size of the dust. In convectively unstable regions, the convective heat flux is used to determine the mixing, while in radiative regions the atmosphere is mixed by a minimum eddy diffusion coefficient, prescribed by buoyancy wave breaking. Precipitation velocities are calculated for viscous flow around rigid spheres, corrected for gas kinetic effects by a slip factor. The model considers iron (Fe), enstatite ($MgSO_3$) and water (H_2O). Iron is a key temperature regulating species, while enstatite is considered in place of a multitude of silicate species and water is considered as it represents a major opacity source in the coolest objects.

The lower boundary of the dust cloud is well defined as where the partial pressure of the condensate exceeds its saturation vapour pressure. The vertical extent of the dust cloud is then governed by the free parameter f_{rain}, which describes the efficiency of precipitation or sedimentation. Larger values of f_{rain} correspond to more efficient precipitation of dust, implying a thinner cloud deck. The efficiency parameter is rigorously defined as:

$$f_{rain} = \frac{\int_0^\infty v_f \frac{dm}{dr} dr}{\epsilon \rho_a w^* q_c} \tag{5.1}$$

where w^* is the convective velocity scale, v_f is the terminal fall velocity of the dust under viscous flow, $\frac{dm}{dr}$ is the particle growth or evaporation rate, ϵ is the ratio of dust to atmospheric molecular weights, ρ_a is the atmospheric density and q_c is the condensate mole fraction.

The physical meaning of f_{rain} is less clear cut, as it encompasses a multitude of unresolved dynamical and micro-physical processes not considered explicitly in the models, such as the abundance of condensation nuclei and any horizontal inhomogeneity. Together the parameter f_{rain} and the turbulent mixing profile govern the dust structure of the atmosphere.

The chemistry is computed from the interior outwards and removes primary condensates into cloud layers, consequently secondary condensates predicted from pure chemical equilibrium are excluded. Marley et al argue that such secondary condensates are inhibited in Jupiter, and as such are likely to be suppressed in T dwarfs.

The temperature profiles are calculated for cloud-free atmospheres (Marley 2000), therefore the cloud feedback onto the atmospheric structure is omitted. Despite this, it is evident that for cool objects $T_{eff} < 2500K$ dust clouds are an important, if not dominant, opacity source.

Ackerman & Marley (2001) find large cloud particles, $40 - 80\mu m$, forming thin cloud decks in the photosphere. The results agree qualitatively with early L- and late T- dwarfs. These models were used in an early study to discuss the feasibility of cloud disruption as an explanation for the L-T transition (Burgasser et al. 2002b). As can be seen in Figure 5.8, cloud disruption as represented by a linear

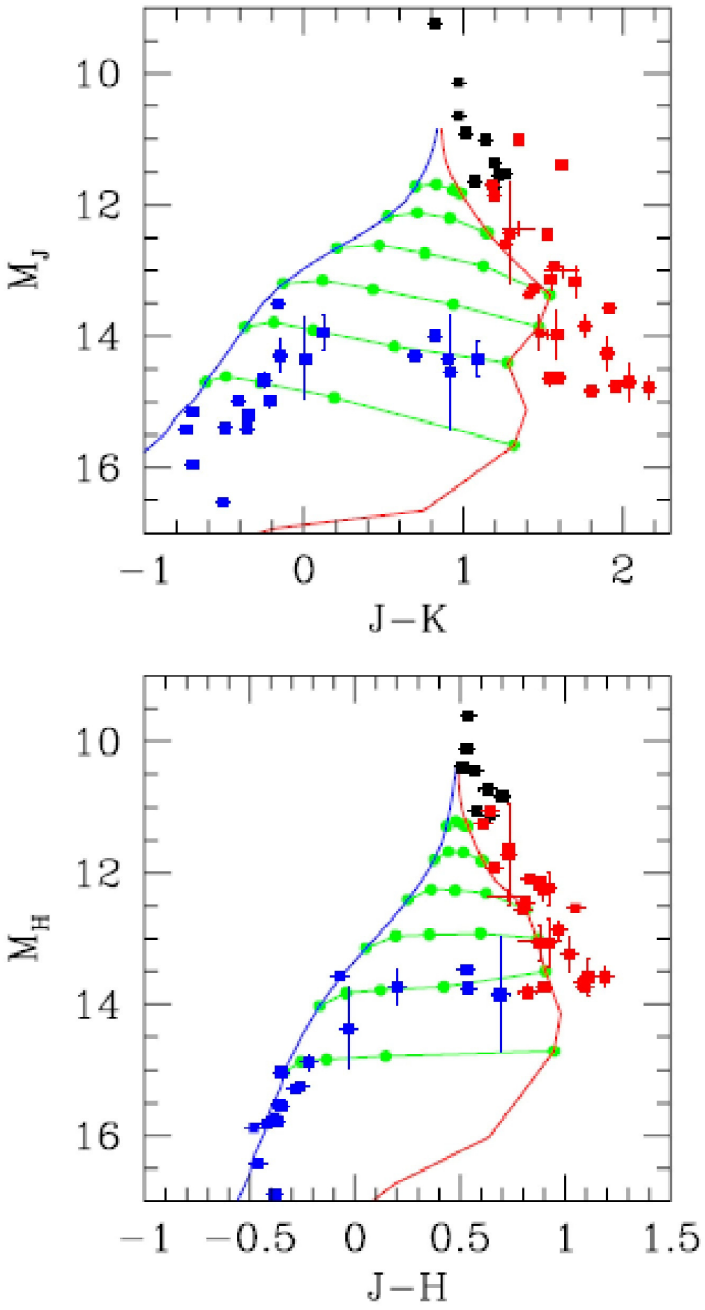

Figure 5.8: Near-infrared model colourmagnitude diagrams (MKO system). Red and blue lines, respectively, show model colours for cloudy sequence with f_{rain} = 2 and cloudless models (both log g = 5). Horizontal green lines connect partly cloudy model colours with T_{eff} = 10002000 K in steps of 200 K (from bottom to top). Partly cloudy models (green dots) are for cloud-free fractions h of 0, 0.25, 0.5, 0.75, and 1, from right to left. Square symbols show field dwarfs with M dwarfs in black, L dwarfs in red, and T dwarfs in blue. The photometry is primarily from Leggett et al. (2002) and Knapp et al. (2004). Additional sources are given in Saumon & Marley (2008).

combination of cloudy and cloud-free models looks promising, but the assumptions underlying these models, along with the sensitivity of dust to atmospheric conditions means that we should be wary of

reading too much into these results.

More recently, the model has been updated to consider cloudy and cloudless models on a single consistent global temperature-pressure profile (Marley et al. 2010). These models consider two adjacent sub-columns of the atmosphere, which share a thermal profile, but differ in their cloud profiles. The free parameter, h, (in addition to f_{rain}) is set to be the fractional coverage of the cloud-free column. The total flux is then calculated and used to determine the radiative-convective equilibrium. The cloud profile and atmospheric chemistry are solved iteratively until converged meaning the final thermal, chemical and cloud profiles are consistent.

Results for near infrared colours are promising and show that by adjusting the two free parameters a reasonable fit can be found. However, as increasing f_{rain} and cloudiness across the L-T transition both reproduce the near infrared colours across the L-T transition, careful consideration must be made of the degeneracies involved. Fractional cloud coverage has a discernible effect on the near infrared spectrum, and this may prove useful, but the differences are subtle and around the level of differences between modelling efforts. A truly patchy cloud model will, therefore, require the next generation of models to consider this problem multi-dimensionally.

5.2.3 Tsuji et al

The model of Tsuji et al approaches the problem from the stellar perspective (Tsuji et al. 1996a). The high density in cool dwarf atmospheres ensures that conditions remain close to thermodynamic equilibrium, justifying the assumption of LTE and chemical equilibrium approach for both the molecules and dust (Tsuji 2002). Tsuji considers that dust will form readily as soon as the ambient temperature falls below the condensation temperature of the dust, T_{cond}, for that dust species. If the formed dust is stable, then it continues to grow until the dust grains reach a size, r_{crit}, where the grains are too large to be supported by the surrounding atmosphere and precipitate out below the dust cloud into deeper hotter layers where they are destroyed (Tsuji 2002). Unstable dust, in contrast, exists in detailed balance, with an equilibrium between formation and destruction. In practise this limits the size of the dust grains, $r_{gr} < r_{crit}$. Consequently, Tsuji et al assume that dust grains never grow larger than $0.01\mu m$ (Tsuji et al. 1996a). (The dust grains are also assumed to be spherical and composed of a single dust material.) In turn, this assumption allows a significant simplification of the radiative transfer, as such small particles result in an opacity that is almost independent of grain size (Tsuji 2002).

Three dust species are considered as a proxy for the full dust chemistry: corundum Al_2O_3, considered as the high temperature condensate. The first (highest temperature) condensate is the most pivotal as it determines the basic structure of the photosphere. Next they consider iron Fe, as it plays a key thermostat role in the atmosphere and finally enstatite $MgSO_3$, which is a low temperature condensate and is considered as representative of the multitude of silicate compounds (Tsuji 2002).

In this model true grain sizes are unimportant as the opacity is independent of grain size and depends only on the column density of dust in the atmosphere. As it is assumed that dust forms readily where it is thermodynamically favoured, column density measures the thickness of the cloud layer. If the cloud can only support grains smaller than some critical radius r_{crit}, then this corresponds to some critical temperature in the atmosphere, T_{crit}, below which grains grow larger than r_{crit} and precipitate rapidly below the cloud deck. Dust exists only in a cloud between $T_{crit} < T < T_{cond}$. While the condensation temperature T_{cond} is well defined by thermochemistry, T_{crit} is not and is treated as a free

parameter in the models (Tsuji 2002).

The dust model is coupled with 1D non-gray radiative-convective model photospheres under the usual assumptions of hydrostatic and radiative equilibria. In areas of the model that were found to be convectively unstable under radiative equilibrium, local mixing length theory was applied to mix the medium. This is solved iteratively to satisfy

$$\pi F_{rad} + \pi F_{conv} = \sigma T_{eff}^4 \tag{5.2}$$

where F_{rad} is the radiative flux, F_{conv} is the convective flux, T_{eff} is the effective temperature and σ is the Stefan-Boltzmann constant. However, the coupling between the local LMLT and the non-local radiative transfer means that this equation is difficult to satisfy exactly, typically there is a discrepancy of a few percent (Tsuji 2002).

This forms a semi-empirical model of dust formation in the static atmospheres of cool dwarfs. The free parameter, T_{crit}, governs the thickness of the cloud, or more correctly the cloud column density, and as such this significantly affects the infrared colours and spectra of these objects. Early models calibrated T_{crit} for L dwarfs (and found $T_{crit} \sim 1800K$) and used this value throughout the spectral sequence (Tsuji 2002). While this appeared to reproduce satisfactorily the colour magnitude diagrams from L to T dwarfs (Tsuji & Nakajima 2003) and spectra (Tsuji et al. 2004; Nakajima et al. 2004), more recent observations show that infrared colours exhibit a large variation when plotted against effective temperatures derived from bolometric fluxes (Leggett et al. 2002; Golimowski et al. 2004) and parallaxes (Vrba et al. 2004). The variation cannot be explained by the effect of gravity or metallicity (Tsuji et al. 2004; Tsuji 2005b). This implies that T_{crit} varies not only across the spectral sequence from L to T (Tsuji 2005a) , but that is it not even constant at the same effective temperature.

While this model has some success in reproducing the properties of early L dwarfs and late T dwarfs, it fails in its predictive power as T_{crit} seems to be ill-defined. Furthermore, Tsuji et al consider convective overshooting only qualitatively arguing it is too weak to mix considerable gas volumes in high, cool layers and although they find the presence of dust creates regions that are unstable against convection, they do not revisit the assumption that grains may only exist in detailed balance. Finally, this model assumes efficient nucleation, while nucleation is the key bottleneck in the dust formation cycle and in these atmospheres there is no reason to assume that seed particles exist already.

5.2.4 Allard Model

Tackling the problem of dust in ultracool dwarf atmospheres by analogy with terrestrial cloud formation, Allard et al consider the timescale arguments of Rossow (1978). Drawing together work from terrestrial meteorology and the planetary community, Rossow (1978) presents a model based on the restricted parameter space of cloud dust grain size, composition, number density and atmospheric structure.

Allard et al calculate chemical equilibrium via the minimisation of functional errors of charge conservation, element conservation, the Saha equation and the mass-action law. Expanded to include a complete series of over 1000 liquid and crystal species, the chemical equilibrium system computes the equilibrium pressures which are then compared to the pressure from the Guldberg law of mass action to find the abundance of the condensed species. The chemical equilibrium complex is solved iteratively until the solution is converged and therefore the depletion of refractory elements from the gas phase is accounted for self-consistently.

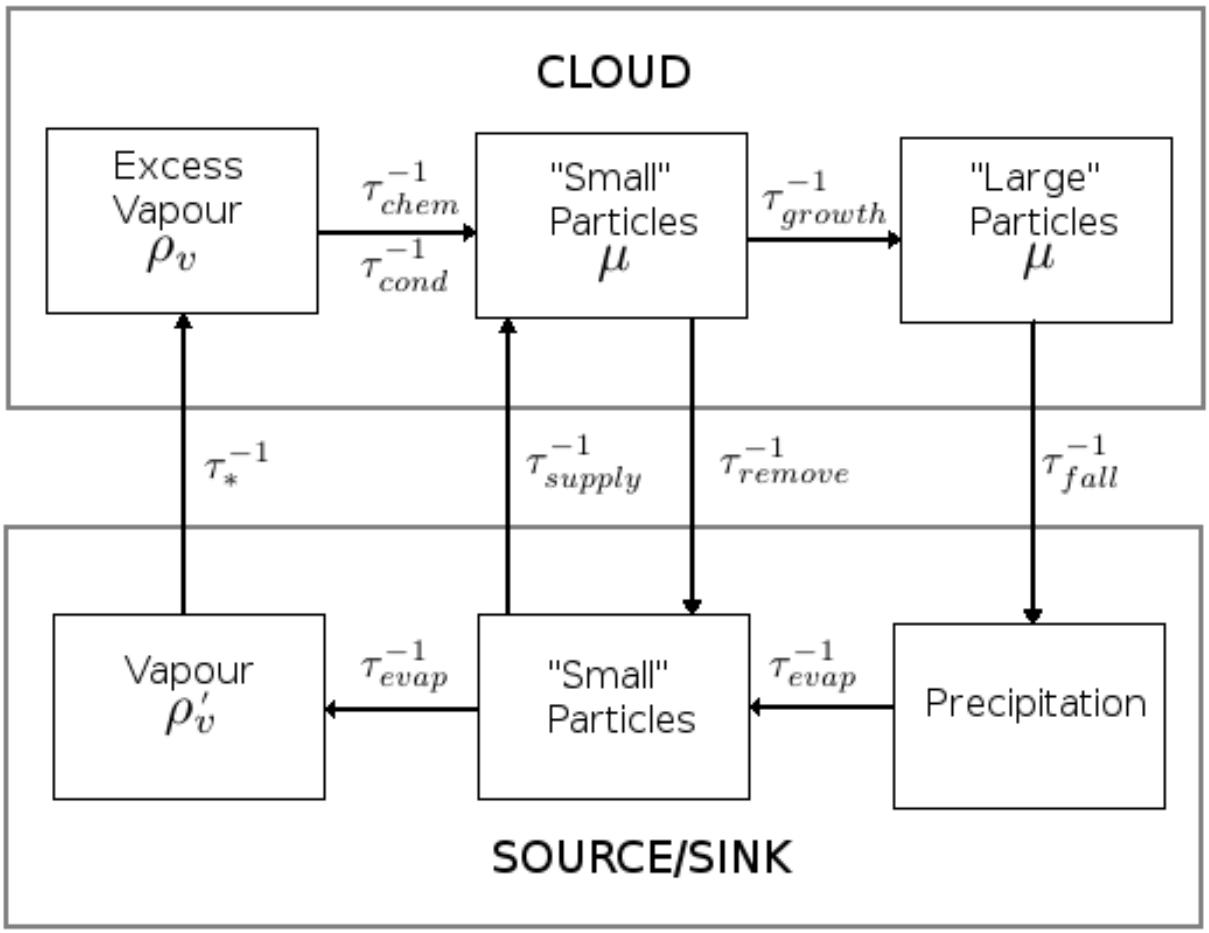

Figure 5.9: Figure from Rossow (1978) showing the schematic dust model diagram. Competing micro-physical processes are characterised by timescales, representing the collisional growth rate, τ_{growth}, the mixing by winds, τ_{supply}, the sedimentation of dust particles, τ_{fall}, removal of dust by winds, τ_{growth}, the nucleation timescale, τ_{chem}, the evaporation timescale, τ_{evap}, the timescale for vapour condensation, τ_{cond} and the cooling timescale of the cloud, τ_*

Assuming efficient nucleation and spherical, chemically homogeneous grains, the dust grain radii are derived from balancing the characteristic timescales for atmospheric mixing, condensation and sedimentation (Rossow 1978; Allard et al. 2001; Reiners et al. 2007), see Figure 5.9. As dust forms in the region of the atmosphere stable against convection, the mixing considered is convective overshooting as prescribed by Ludwig et al. (2002). The dust cloud structure is calculated on a fixed optical depth grid, assuming no dust opacity contribution, but radiative transfer is applied to the resulting thermal structure and this process is iterated until the model converges. In this way, inconsistencies between the radiative transfer and thermal structure are purged.

Integrated into the PHOENIX 1D atmosphere code, the dust model considers only chemically homogeneous or pure grains, excluding the possibility of core-mantle dust grain growth, which would lead to larger grains, and nucleation sites for growth reactions are assumed to be plentiful. The mixing, while calibrated on hydrodynamic models (Ludwig et al. 2002), is extrapolated from hotter stars and the properties of the gas flow at lower temperatures could be significantly different.

5.2.5 Freytag Model

Using the multi-dimensional radiative hydrodynamic code CO^5BOLD, Freytag et al model a single dust field and a single gas monomer field in addition to the usual fields associated with gas hydrodynamics. Nucleation is not modelled, instead nucleation seed particles are assumed to constitute a constant fraction in relation to the monomer field. In practice, this implies a maximum dust radius, which is set by Freytag et al to $1\mu m$. Forsterite was chosen as the dust species as it forms at relatively high temperatures. Condensation and evaporation are modelled as in (Loidl et al. 1999; Höfner et al. 2003; Gail & Sedlmayr 1988).

The equation of state from CO^5BOLD considers only the formation of molecular hydrogen, not other molecular species. The gas phase opacities are generated from the monochromatic opacity tables using modified abundances that reflect the removal of refractory elements that would be locked in dust under chemical equilibrium. Dust opacity is parametrised under the large particle limit and the total opacity is found by co-adding the dust and gas contributions in a spectrally binned radiative transfer scheme. The disparate timescales for the dust and the radiative transfer along with heavy computational cost of the radiative transfer mean that the hydrodynamical problem was solved 6 times for each call to the radiative transfer model - increasing the efficiency of the simulation.

Freytag et al consider a series of 2D radiative hydrodynamical models, and find numerical stability issues with, the physically more correct, open upper and lower boundary conditions, requiring both closed boundaries and strong damping. They find that dust clouds form readily with material mixed through the atmosphere by gravity waves. While they do not report findings on the grain sizes of the dust particles, perhaps as these are strongly influenced by the assumptions noted above, the large gradients caused by the presence of the dust cloud deck do cause a secondary convection zone to form. These simulations are very interesting, but not yet mature, as the thermal timescale of the system is not covered.

5.2.6 Helling Model

The Helling et al model fundamentally differs from all the previous models as it is based on the analogy of a thunderstorm. In thunderstorms, large air-masses are convectively mixed upwards into cooler atmospheric layers where raindrops form. Dust grains nucleate and form in the cool upper region before sedimenting downwards, while growing in size, until they reach the hot, dense, deep layers where they evaporate.

Dust grain formation is described kinetically as a phase-transition: seed-formation, grain growth, sedimentation and element depletion of the gas-phase are all modelled for solid particles. Derived from the full rate-equations, these processes are described by a network of four dust moment equations following the number density, mean particle radius, surface area and volume of the dust grains.

The gas-phase is modelled in chemical equilibrium for 14 elements and 158 molecules. Solar elemental abundances are assumed at the lower boundary and element conservation equations follow the local abundances as they evolve due to nucleation, growth, evaporation and sedimentation of the dust grains.

The partial pressure of the gas phase compared to the partial pressure under chemical equilibrium gives the supersaturation ratio, S. Nucleation is modelled by the polymerisation. of TiO_2 molecules

via classical nucleation theory. These seed particles grow by condensing surface reactions for a network of 12 species. This implies the formation of core-mantle or "dirty" dust grains. Sedimentation causes dust grains to settle through the atmosphere, where they may continue to grow. Condensation takes place in a supersaturated medium, $S > 1$, but nucleation requires highly supersaturated gas, $S >> 1$. The dust opacity is calculated using Effective Medium and Mie theory to reflect the composition of dirty grains. Mixing, in this model, is treated using a parametrised mixing timescale based on convective overshooting, which exhibits an exponential decay with increasing height above the convection zone (Ludwig et al. 2002, 2006).

By considering quasi-static sub-stellar atmospheres, Helling et al. (2008) show how the micro-physical processes involved in dust formation may be included into the framework of stellar atmosphere codes. Employing an atmospheric structure from Allard et al, the dust model complex is solved, neglecting radiative feedback onto the thermal profile.

Results show a cloud deck strongly stratified by dust size, with small grains, $\sim 0.01\mu m$, at the top of the cloud deck while large particles, $\sim 200\mu m$, form at the base. Unlike decoupled models of dust species, Helling et al. (2008) find one single cloud layer, although the composition of the grains changes with height. Finally, the models show considerable depletion of seed forming elements but overall much less gas phase depletion than predicted by phase-equilibrium models.

Clearly, the most detailed model, in a micro-physical sense, the results are still subject to influence from the lack of feedback onto the thermal profile and assumptions made about overshooting efficiency.

5.3 Summary

In order to move to a multi-dimensional approach the dust model must not rely on inherently 1D assumptions. In this respect the models based on balancing up-mixing with sedimentation (Marley et al. and Cooper et al.) fail. The model of Tsuji et al. is based on a detailed balance argument as a static, stationary model is not a valid solution. However, the grain sizes that result from such a model are far too small to reproduce observations. The solution to this lies in the fact that these atmospheres are convective, meaning that dust grains can form, grow, rain-out and then be turbulently up-mixed again, allowing further growth and leading to larger grain sizes, consistent with observations. For this reason the Tsuji et al, model is discarded. The Allard et al. and Freytag et al. models are based on Rossow (1978), where competing processes are characterised by the timescale on which they operate. This model is implementable in 3D, but adds many free tunable parameters in the calculation of characteristic timescales and these are poorly constrained. By contrast, the model of Helling et al. is the most correct micro-physically, although also the most complex. The physical basis and lack of free parameters make this model appealing. It also has the advantage that it is the most easily extensible to study multiple species, dirty dust grains and even potentially charged processes that cause lightning.

Efforts to model dust in ultracool dwarf atmospheres have, evidently, been considerable. Currently, models successfully reproduce early L-dwarfs and late T-dwarfs. Early L dwarfs may be understood as dusty objects with a cloud deck that coincides with the photosphere. In contrast, T-dwarfs have cloudless photospheres, but show evidence of element depletion consistent with dust having formed

and precipitated out to a cloud deck that lies below the surface - locking away the refractory elements.

The transition between these objects is less well understood. The exact nature of the mixing mechanism operating in these objects has profound consequences for the type and size of dust found, but no consensus exists on this matter. 3D hydrodynamical simulations will be required to model the dust cycle consistently in order to resolve this question.

The size of the formed dust grains are ill-constrained by the present generation of models. Dust particle radii clearly depend on the assumptions made about their formation (e.g. pure or dirty composition, blocking dust formation or decoupled, convective or radiative region of the atmosphere). Such assumptions need to be relaxed, or at least their validity needs to be examined. In particular, nucleation is commonly found to be the bottleneck of the dust formation cycle and the assumptions made about it are critical as they lead directly to the dust number density. Equally the formation of a secondary convection fundamentally changes the nature of the physical problem being tackled and these issues must be settled if we are to construct a reliable model of the transition region from L to T.

Finally, both convection and dust clouds are manifestly 3D processes and to tackle these problems correctly a multi-dimensional approach is required.

Chapter 6

Dust model

The high density, low temperature environment that exists at the bottom of the stellar main sequence hosts the critical climate where condensation becomes stable. The dense oxygen-rich atmospheres of brown dwarfs provide favourable conditions for the gas-solid phase transition. The clustering of gas phase molecules proceeds by polymerisation and coagulation (sticking together of molecule clusters after a collision) creates dust in the atmosphere, which is entrained by stability considerations into a cloud deck in the atmosphere. The properties of these dust grains and cloud decks pose an interesting, if difficult, problem in understanding the appearance and evolution of these objects.

6.1 Why model in 3D?

At a fundamental level, ultracool dwarf atmospheres are the product of the interaction of convection and dust formation. Dust may remain in a stationary state in an atmosphere only if there is atmospheric mixing (Woitke & Helling 2004), that is a static stationary state is excluded. It is the replenishment of condensible species into the cool atmospheric layers that allows the dust formation to proceed.

In 1D atmosphere models this mixing is usually parametrised by mixing-length theory (Biermann 1932; Mihalas 1978) and its extension to model the effects of convective overshooting, see Castelli et al. (1997). This approach necessitates the addition of more free parameters, most notably, l/H_P, the mixing length and β, the gradient of the mixing timescale. The values adopted for these additional free parameters may significantly alter the properties of the resulting dust cloud.

Hydrodynamical studies of cool dwarfs show that the mixing length, l/H_P, can range from 1.5 to 3.5 Ludwig et al. (2002), with a value of 2.0 typically being assumed (Dehn 2007). Investigating the effect of l/H_P over this range Dehn (2007) finds that the nucleation rate varies by around 20% leading to a change in the resultant dust number density of a similar magnitude. Grain sizes are slightly more affected, leading to changes of ~25%. The gradient of the mixing timescale, β, is varied by ±10% resulting in a change to the dust number density of around 50% (Dehn 2007). A hydrodynamic model removes these uncertainties by modelling the convection correctly, without free tunable parameters.

It is the outermost, and therefore the coolest layers that are critical for dust formation, particularly when nucleation is considered (Tsuji et al. 1996a; Woitke & Helling 2004). These layers are also the

most sensitive to differences between 1D parametrisations of convection and the results of hydrodynamical models, see Chapter 3. The extension of the vertical velocity field in 3D, compared to the 1D model will significantly aid dust formation and is likely to affect the vertical extent of the dust cloud.

Static dust cloud models, that allow dust to form and remain *in situ*, like dust formed from the detailed balance arguments of Tsuji et al. (1996a), fail to reproduce the observations (Chabrier et al. 2000) and mean dynamical models of brown dwarf atmospheres are required.

Studying variability in these objects also requires a move to multiple dimensions as the hypothesis of the L/T transition being precipitated by inhomogeneous or partial cloud cover requires the breaking of azimuthal symmetry. Studies by Burgasser et al. (2002b) and (Marley et al. 2010) show that incomplete cloud cover is a plausible explanation but that further progress in this direction is inhibited by the lack of a multi-dimensional hydrodynamical model, coupled to dust formation.

6.2 Physical model

Adopting the kinetic description of Helling & Woitke, this work aims to model the full dust cycle (see Figure 6.1) of mixing, nucleation, growth, precipitation and evaporation (Woitke & Helling 2003, 2004; Helling et al. 2008; Helling & Woitke 2006). This model, a modified version of Helling et al. (2008), is a time-dependent description that employs a moment method to capture the essence of the problem, by following the number, size, surface area and volume of the dust in additional scalar fields, as well as enforcing the element conservation of the key dust-forming species. At present, this model considers only a single species for both nucleation and dust growth. Titanium dioxide in solid form, $TiO_2[s]$, is considered as it is the best candidate for physically meaningful nucleation, as it is both thermodynamically extremely stable, and formed from the monomer of titanium dioxide in the gas phase, $TiO_2[g]$, which according to chemical equilibrium calculations (Allard et al. 2001) is abundant Woitke & Helling (2004). Titanium dioxide is retained as the only grow species, at present, to allow a clear investigation of the properties of nucleation, but this model has the distinct advantage that many growth species may grow to form a dirty mantle on top of pure nucleation seeds, leading to a far more accurate model. For now, results regarding the size of dust grains should be regarded as lower limits, while the model dust number density is robust.

In addition, this model provides for gravitational settling or precipitation of dust grains through the atmosphere (offset from the gas motion) through the terminal (drift) velocity of the dust particle. This allows dust particles to nucleate high in the atmosphere, and grow while settling through the cool layers before being destroyed through evaporation in the hot deep layers.

The convection is naturally modelled by the hydrodynamics detailed in Chapter 2. The hydrodynamical equations are coupled to the dust moments via the gas density and velocity.

6.3 Nucleation

Nucleation is the first and key stage in the dust formation cycle, taking place in the cool upper region of the atmosphere. Dust will not form in an atmosphere, even if conditions for condensation are

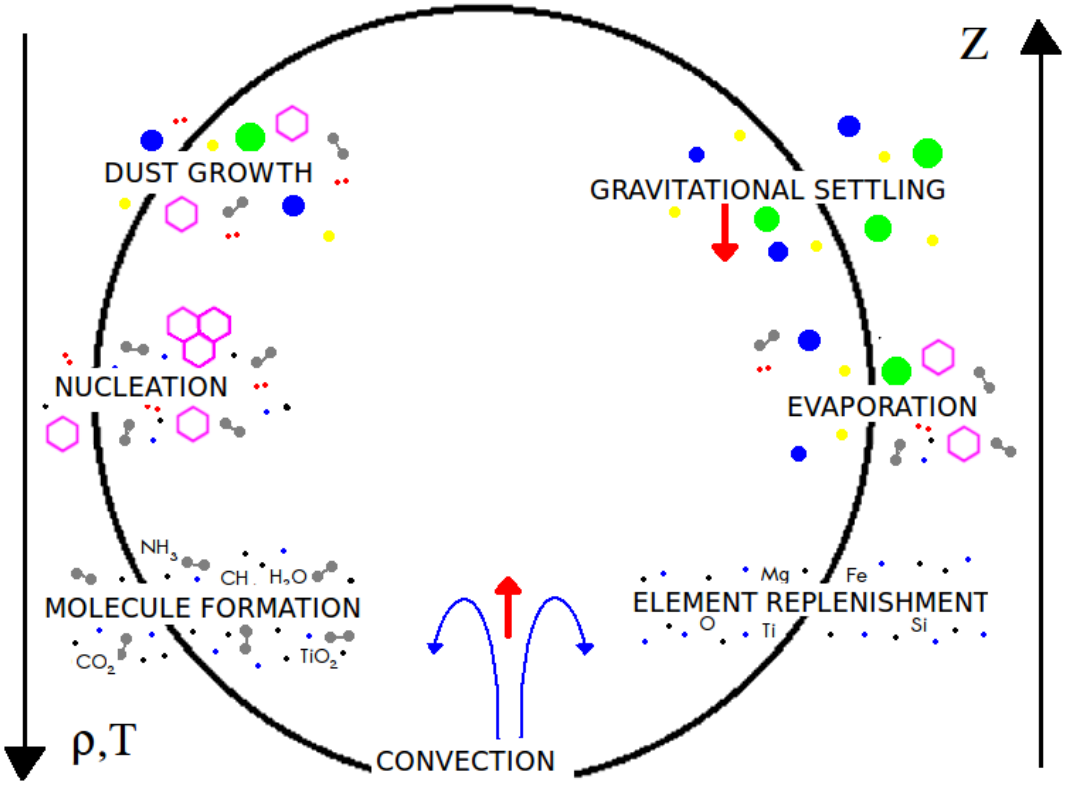

Figure 6.1: Full life cycle of a dust grain: molecule formation, then nucleation at cooler temperatures, dust grains then grow on top of these nucleation seeds until gravitational settling pulls the grains down to hotter layers where they evaporate replenishing the supply of condensible species, which is then mixed upwards by convection to begin the cycle again.

favourable, unless there are nucleation seeds to provide reaction sites for subsequent condensation. Nucleation governs the dust number density, while the dust grain size is determined by a balance of other considerations including the atmospheric mixing, the precipitation of heavy particles and the growth network of chemical reactions.

In terrestrial dust clouds, aerosols provide kernels for condensation reactions to occur meaning that dust can form and grow very close to where the partial pressure curve for that dust species crosses its saturation vapour pressure. In contrast, ultracool dwarf atmospheres cannot be assumed *a priori* to harbour such atmospheric impurities. The absence of these aerosols in the gas phase could lead to regions of highly supersaturated gas before conditions are appropriate for spontaneous nucleation.

Nucleation can proceed in a variety of ways: chemical nucleation, which consists of gas phase chemical reactions that produce nucleation seeds from vapour e.g. hetero-molecular nucleation consists of the reaction of two or more gases that have solution forming condensate phases; heterogeneous nucleation, where seed particles contain or form on the surface of other small aerosols; and homogeneous homo-molecular nucleation, where seed particles grow by polymerisation of monomers in the gas phase (Rossow 1978).

In the Earth's atmosphere, heterogeneous nucleation is dominant (Rossow 1978). Heterogeneous nucleation does not actually produce "new" seed particles, instead it may be understood as the activation

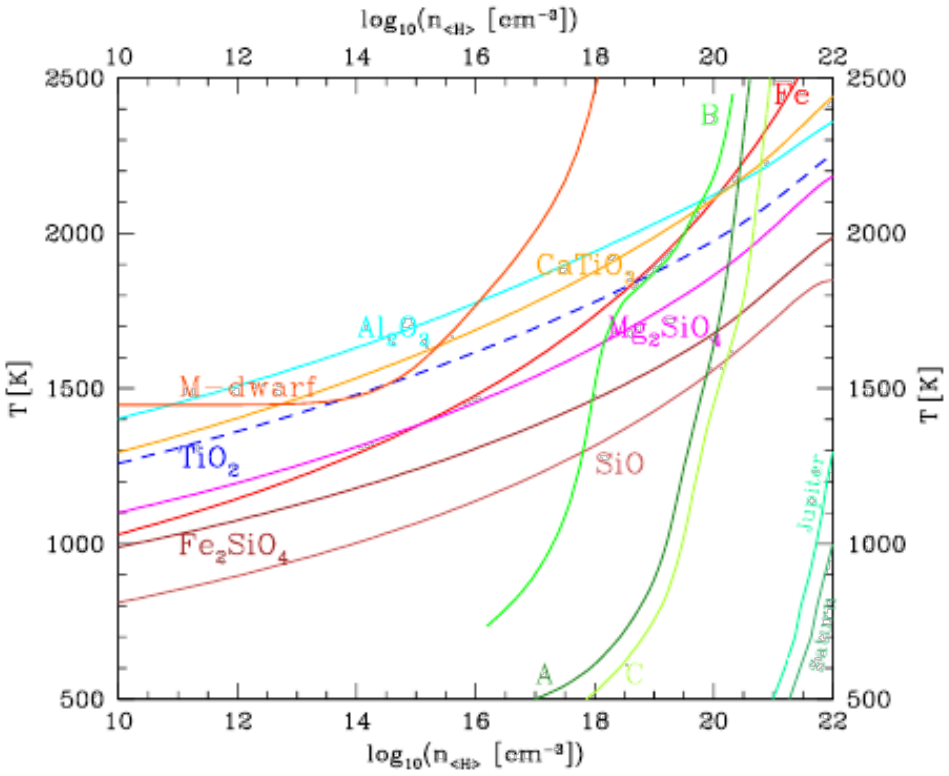

Figure 6.2: Sublimation temperature T of various solid compounds as a function of the total hydrogen density $n < H >$ in a gas of solar abundances. Depletion by dust formation is omitted; the pure stability of possible compounds is considered. (T, $n < H >$) trajectories for model atmospheres of typical M-dwarfs (Hauschildt, priv. com.), Brown Dwarfs (Tsuji et al. 1999); Model A dust free case, Model B dust included as opacity source, Model C dust serves only as element sink but not as opacity source; and gas planets (Fegley & Lodders 1994) are superimposed.

of a pre-existing population of cloud condensation nuclei or aerosols. As a result, while this type of nucleation may well operate, it is insufficient to model the formation of dust *ab initio*. Furthermore, in an atmosphere where the equilibrium vapour density of the condensing species is many orders of magnitude smaller than the atmospheric density, nucleation rates are controlled by the collision rates between molecules. Consequently, heterogeneous nucleation, which requires multiple reactants, becomes inefficient.

Chemical nucleation produces most of the sub-micron aerosols in the terrestrial atmosphere (Cadle & Grams 1975; Junge 1963). It refers to a gas phase chemical reaction which produces nucleation seeds from the vapour. As with heterogeneous nucleation, while efficient on Earth where reactant abundances are not extremely low in concentration (a result of metal-rich planetary rather than stellar initial elemental abundances), chemical nucleation is inefficient in ultracool dwarfs as the collision rates between the reactants are low.

Homogeneous homo-molecular nucleation is based on the kinetic theory of phase changes. The nucleation embryos are molecular aggregates, which form a Boltzmann distribution, and are formed by statistical density fluctuations in an isothermal gas (Gail et al. 1984). Experiments show that this process only proceeds under conditions of very high supersaturation, that is conditions for which the

partial gas pressure for a particular species exceeds the equilibrium gas pressure (S ∼ 5-8 for water (Mason 1971)). In contrast to heterogeneous and chemical nucleation, homogeneous homo-molecular nucleation may be expected to be efficient at nucleating seed particles in clean dwarf atmospheres, but only at very high supersaturation ratios, which means only in the very high, cool outer layers.

For convenience this model considers only a single nucleating species, rutile (TiO_2). This is sufficient as the first nucleating species has the strongest impact, due to its role in governing the dust cloud extension (Tsuji 2002), and the seed particles can serve as the underlying population for heterogeneous nucleation implicitly by providing a surface to catalyse other growth reactions. As an exemplary nucleating species, rutile has the advantage of being among the highest temperature solids (Helling et al. 2001), it is thermodynamically very stable, according to chemical equilibrium calculations the TiO_2 molecule exists abundantly in the gas phase and rutile forms easily by the primary reaction $TiO_2 + (TiO_2[s])_N \rightleftharpoons (TiO_2[s])_{N+1}$, where [s] denotes the solid phase. In contrast, other high temperature condensates have no stable monomer in the gas phase (Patzer et al. 1998), requiring three or more body collisions to nucleate. While stable at higher temperatures (See Figure 6.2) corundum, Al_2O_3, for example, requires a catalyst surface for condensation (Patzer et al. 1998), making it unsuitable for a primary nucleating species. Accordingly, rutile is considered in this work to be the most likely candidate for physically meaningful nucleation in the atmospheres of these objects, with only homogeneous homo-molecular nucleation considered explicitly.

Nucleation is initiated by the clustering of gas phase molecules, which grow by polymerisation into solid clusters of ∼ 100 molecules. These nuclei provide a site for surface reactions allowing the irreversible growth of the dust grains by condensation of additional gas species, forming a mantle around the seed particle core. Brown dwarf atmospheres are cool and very dense ensuring many intermolecular collisions. This implies that a classical equilibrium approach based on statistical mechanics is sufficient, unlike in supernovae dust models where the forward and backward rate reactions must be solved simultaneously (Cherchneff & Dwek 2010; Nozawa & Kozasa 2013).

The creation of a solid polymer particle proceeds along the energetically most favoured reaction pathway of the chemical network. Along this path, the least efficient reaction governs the formation of new stable seed nuclei. Beyond this critical reaction, all growth reactions are more efficient than the reverse reactions leading to rapid cluster growth. Consequently, it is sufficient to approximate the dust particle formation rate by polymerisation $J(V_l) \simeq J_*$ via the number density of the critical cluster n_s^*, where s denotes the solid species under consideration, and its growth timescale $\tau_{n_s^*}^{growth}$.

The stationary nucleation rate, J_*, is given by Gail et al. (1984)

$$J(V_l) \simeq J_* = \frac{n_x}{\tau} Z \exp\left[(N_* - 1)\ln S - \left(\frac{T_\theta}{T}\right)(N_* - 1)^{2/3}\right] \tag{6.1}$$

where n is the number density of species x, and τ is the seed growth timescale is $\tau = n_x v_{rel,x} N_*^{2/3} A_o$. N_* is the critical cluster size, A_0 is the hypothetical monomer surface of the critical cluster and $N_*^{2/3} A_0$ is the surface area of the critical cluster. The supersaturation ratio S is defined as $S = \frac{p_x}{p_{sat,x}}$ with $p_x = n_x kT$ the partial pressure of the species x, n_x the corresponding number density and $p_{sat,x}$ is the saturation vapour pressure of species x. Z is the well known Zeldovich factor,

$$Z = \left(\frac{1}{2\pi} \frac{\partial^2 \ln\left(n_1 \exp\{(N_* - 1)\ln S - \frac{T_\theta}{T}(N_* - 1)^{2/3}\}\right)}{\partial N^2} \bigg|_{N_*} \right)^{1/2} \tag{6.2}$$

where a_0 is the hypothetical monomer radius and σ the surface tension and $T_\theta = 4\pi a_o^2 \sigma / k$. The surface tension for nucleating clusters are determined from the size dependent thermodynamical data (Jeong

et al. 2000). A surface tension of $\sigma = 800\text{erg cm}^{-2}$ for $(TiO_2)_N$ is adopted. The relative velocity $v_{rel,x}$ is the thermal velocity between the grain of size N_* and gaseous nucleation species, implying :

$$v_{th,x} = \sqrt{\frac{kT}{2\pi\bar{\mu}}} = \sqrt{\frac{kT}{2\pi}\left(\frac{1}{m_x} + \frac{1}{m_{N_*}}\right)} \tag{6.3}$$

A more detailed account, including the derivation of this result, may be found in Gail et al. (1984).

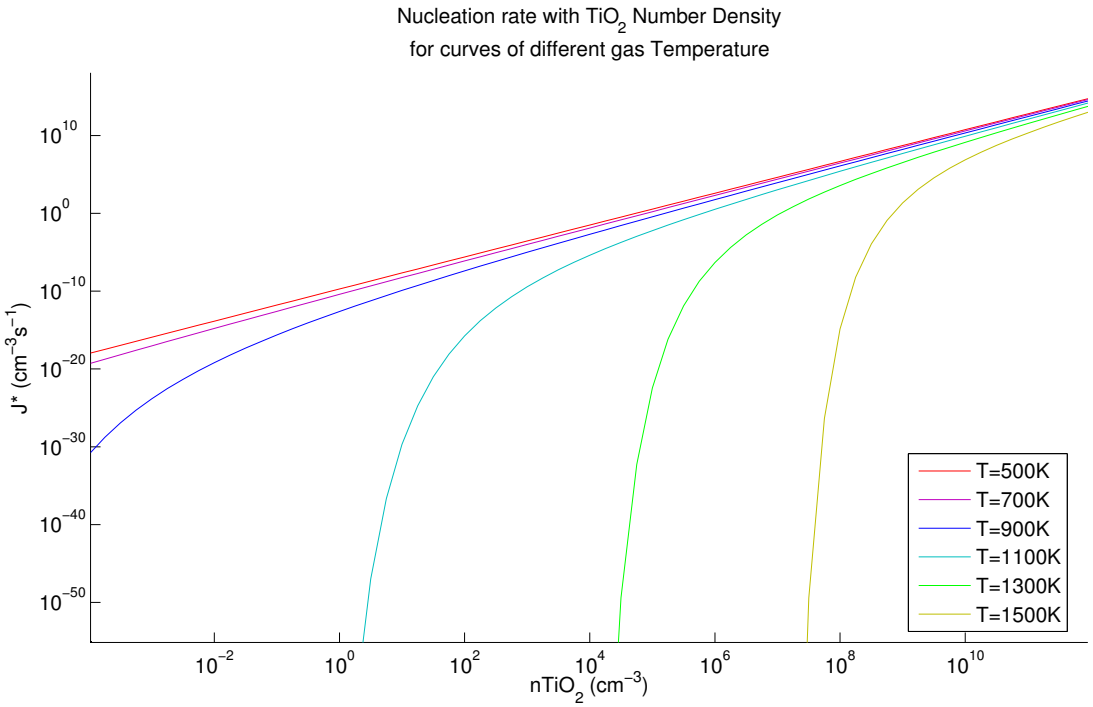

Figure 6.3: The nucleation rate, J_*, with the gas number density of TiO_2 molecules, $nTiO_2$. Individual curves correspond to isotherms of the gas temperature. The parameter space covered corresponds approximately with the properties of a brown dwarf atmosphere with an effective temperature of 2000K.

Figure 6.3 shows the nucleation rate with the atmospheric number density of gaseous titanium dioxide, $TiO_2[g]$, for curves of different gas temperature. As is to be expected, higher concentrations of the molecule in the gas result in a higher nucleation rate. The number densities range from $10^{-3} - 10^{10}$ particles per cm^3 covering typical atmospheric conditions encountered in a dwarf model atmosphere of effective temperature, $T_eff = 200K$ - where concentrations of $TiO_2[g]$ cover the range $\sim 1.5\dot{1}0^{-5} - 3.0\dot{1}0^{10} cm^{-3}$. At sufficiently low temperatures, or very high densities, the nucleation rate, J_*, is proportional to the square of the gas number density, $J_* \propto n(TiO_2[g])^2$, as the exponential term approaches unity. Curves for hotter temperatures show a marked reduction in the nucleation rate at low gas concentrations, as is to be expected from the less frequent collision rate of reactants, confirming that cool, dense gas provides the best environment for nucleating dust seed particles.

Figure 6.4 shows the nucleation rate with temperature with local gas temperature for a variety of curves of constant gaseous concentrations of titanium dioxide, $n(TiO_2[g])^2$. Naturally, higher gas temperatures suppress nucleation (rather strongly) and higher concentrations of the molecule in the gas phase correspond to higher nucleation rates. With temperature, the nucleation rate has a pronounced knee, whose position shifts towards higher temperatures for higher concentrations.

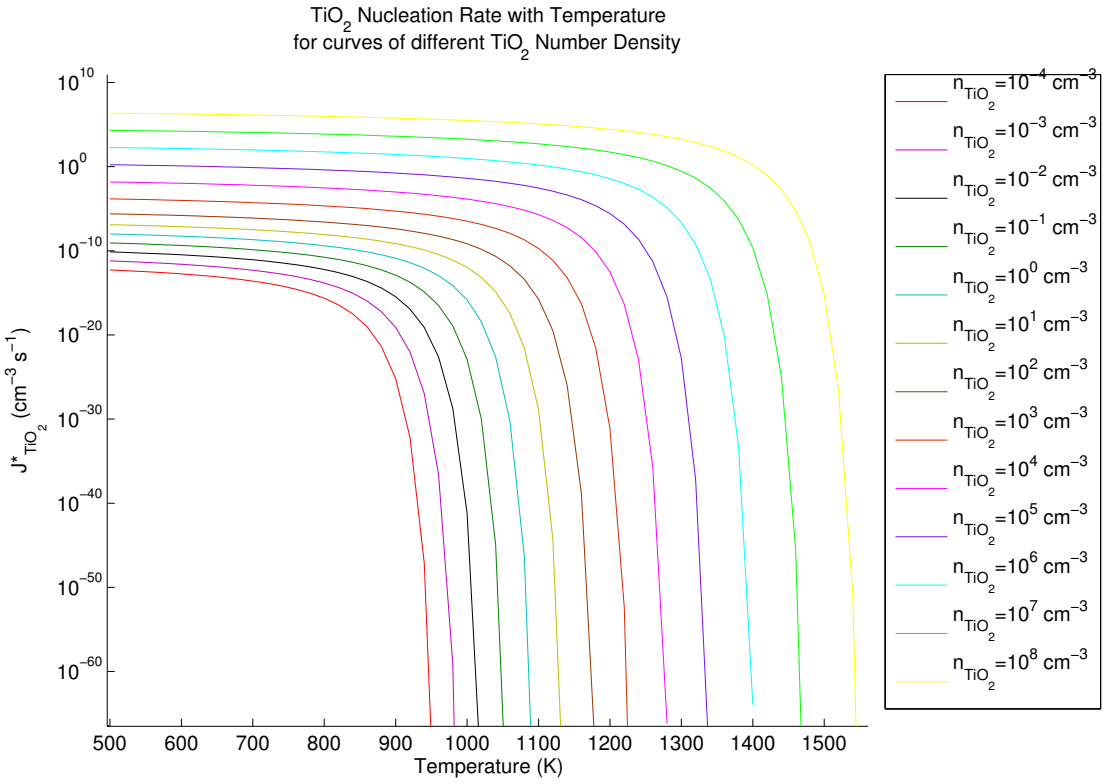

Figure 6.4: The nucleation rate, J_*, with the gas temperature, T. Individual curves correspond to a constant number density of TiO_2 molecule in the gas phase.

6.4 Growth and evaporation

Growth, and the reverse process of thermal evaporation, is critical to the formation, and destruction, of macroscopic dust grains in the atmosphere. Growth describes the condensation of gas phase refractory species directly onto the surface of a pre-existing dust grain. Consequently, the growth rate is governed by the collision rates of molecules with the dust grain. The atmospheres of ultracool dwarfs are dense ensuring rapid thermalisation of the gas, implying that molecules may be considered to follow a Maxwellian distribution. Reactions on the surface of a grain are essentially immediate once all the reactants are present as the characteristic timescale for chemical reactions is much shorter than the collision timescale. Collision rates for different molecules will vary and for each reaction there will be a reactant that collides least frequently; this is the 'key' species for this reaction. As all other reactants will collide more frequently, the growth rate of the key reactant closely approximates the growth rate for the individual species through collisions. The total growth rate is then given by the sum of all key reactant collision rates,

$$\frac{dV}{dt} = 4\pi a^2 \sum_{r}^{R} \Delta V_r n_r v_r^{rel} \alpha_r \tag{6.4}$$

where r is the general surface reaction index, ΔV_r is the increase of dust volume caused by reaction r, n_r is the number density of key species and v_r^{rel} is the relative velocity of the reactants defined by equation 6.3. The sticking parameter, $\alpha \in [0, 1]$, denotes the efficiency of the reaction. Not all

collisions will necessarily result in the physical absorption of the key reactant. Included here for clarity, a lack of laboratory data constraining the true value means that this model assumes collisions are completely efficient, $\alpha = 1$.

Evaporation acts in opposition to growth. The evaporation rate is the product of surface area and the dissociation probability of monomers. Under thermodynamic and chemical equilibrium, this can be expressed as a function of the grain growth and the supersaturation, S_r (Gauger et al. 1990; Woitke & Helling 2003).

Considering growth and evaporation simultaneously results in

$$\frac{dV}{dt} = 4\pi a^2 \sum_r^R \Delta V_r n_r v_r^{rel} \alpha_r (1 - \frac{1}{S_r}) \tag{6.5}$$

where evaporation is naturally accounted for when the gas phase becomes depleted and the result changes sign. For convenience in formulating the moment equations, this may be recast in terms of a linear net growth rate χ_{net}.

$$\chi_{net} = \sum_r^R \Delta V_r n_r v_r^{rel} \alpha_r (1 - \frac{1}{S_r}) \tag{6.6}$$

The summation here is over all reactions considered in the chemical network, which is not generally restricted to a single dust species. For simplicity, this model considers only a single dust species at present (see Table 6.1), but it is trivial to implement a larger network as required.

Index r	Solid s	Surface reaction	Key species
1	$TiO_2[s]$	$TiO_2 \rightarrow TiO_2[s]$	$TiO_2[s]$
2	rutile	$Ti + 2H_2O \rightarrow TiO_2[s] + 2H_2$	Ti
3		$TiO + H_2O \rightarrow TiO_2 + H_2$	TiO
4		$TiS + 2H_2O \rightarrow TiO_2[s] + H_2S + H_2$	TiS

Table 6.1: Data from Helling Woitke 2006

Surface chemical reactions release the latent heat of condensation, causing the heating of the dust grain. Friction further heats the grain, while radiation and inelastic collisions will act to cool it. For large particles, such heating may become significant and lead to the evaporation of the grain (Woitke & Helling 2003; Cooper et al. 2003). However, in the parameter space encountered in ultracool dwarfs, this effect will be no larger than $\Delta T \simeq 3.5K$, justifying the assumption of thermal equilibrium.

Coalescence, the low velocity collision and merging of two particles due to their relative gravitational settling is not considered here. Already thought to be a minor effect in most atmospheres (Rossow 1978; Cooper et al. 2003), the turbulent motions of the gas will largely disrupt this mechanism making the contribution of coalescing particles utterly negligible.

6.5 Drift velocity

Dust grains will not remain static in the atmosphere, rather they will be dragged along by the gas flow (given a sufficiently dense ambient medium), while the higher density of the grain compared to its

surroundings will cause the grain to sediment or settle gravitationally. The motion of the dust particle is governed by Newton's Law.

$$m_d\ddot{\mathbf{x}} = \mathbf{F_{grav}}(\mathbf{x}, a) + \mathbf{F_{rad}}(\mathbf{x}, a) + \mathbf{F_{fric}}(\mathbf{x}, a) \tag{6.7}$$

In principle, the grain may not be in equilibrium and accelerations ought to be taken into account, but it can be shown (Woitke & Helling 2003) that the acceleration phase for the parameter space encountered in ultracool dwarf atmospheres is always short compared to the hydrodynamical timescale $\tau_{hydro} \sim \frac{H_P}{v_{ref}} \sim 10s$, implying the sedimentation or precipitation velocity is always in equilibrium. Furthermore, the force from radiation pressure, while generally dominant in circumstellar envelopes of red giants, is negligible in ultracool dwarf atmospheres as the combination of a relatively weak radiation field and strong surface gravity mean that the radiative force never reaches more than 0.1% of the gravitational force, even in the 'worst' case of light but opaque grains (Woitke & Helling 2003).

$$\mathbf{F_{grav}}(\mathbf{x}, a)) + \mathbf{F_{fric}}(\mathbf{x}, a) = 0 \tag{6.8}$$

Thus, the problem reduces to balancing gravity and friction. Brown dwarf atmospheres are relatively compact, and like the hydrodynamic simulations, $g(x) \simeq g(R_*)$ implying that $F_{grav} = g(R_*)m_d = g(R_*)\frac{4\pi}{3}a_0^3\rho_{dust}$, leaving only the frictional force.

The gas flow around a moving dust particle in a brown dwarf atmosphere covers qualitatively different physical regimes depending on its size, velocity and/or the changing thermodynamic state of the gas. The parameter space covers both subsonic and supersonic motion, free molecular flows and flow through a viscous medium, and, laminar and turbulent flows. Such variety of physical conditions requires an appropriate description of the frictional or drag force under each regime. In order to quantify the physical behaviour of the gas flow it is useful to introduce the Knudsen number, a dimensionless number characterising the frequency of collisions.

The Knudsen number is defined as the ratio of the mean free path length to the flow scale under consideration, in this case the dust diameter, $2a$.

$$Kn = \frac{\bar{l}}{2a} = \frac{1}{2an\bar{\sigma}} \tag{6.9}$$

It quantifies the influence of molecular collisions. For low gas densities, inter-molecular collisions are rare (corresponding to a large Knudsen number ($Kn >> 1$)), therefore the (Schaaf 1963) formula for the drag force by freely impinging gas particles due to elastic collisions is appropriate in the high Knudsen number regime.

$$\mathbf{F_{fric}}^{Free\ \ flow} = -\pi a^2\rho|\mathbf{v_{dr}}|\mathbf{v_{dr}}\left[\left(1 + \frac{1}{s^2} + \frac{1}{4s^4}\right)erf(s) + (\frac{1}{s} + \frac{1}{2s^3})\frac{e^{-s^2}}{\sqrt{\pi}}\right] \tag{6.10}$$

where $s = |v_{dr}|/c_T$, the error function $erf(s) = \frac{2}{\pi} = \int_0^s e^{-s'^2}ds'$ and $c_T = \sqrt{2kT/\bar{\mu}}$

In contrast low Knudsen numbers correspond to frequent collisions requiring continuum theory descriptions. In this regime there exist well tested empirical formulae to describe the frictional force, assuming perfectly rigid spherical dust grains.

$$\mathbf{F_{fric}}^{Viscous\ \ flow} = -\pi a^2 c_D\frac{\rho}{2}|\mathbf{v_{dr}}|\mathbf{v_{dr}} \tag{6.11}$$

In general, the force is found by a simple interpolation scheme

$$\mathbf{F_{fric}}^{Viscous\ \ flow} = \left(\frac{\frac{Kn}{Kn_{cr}}}{\frac{Kn}{Kn_{cr}} + 1} \right)^2 \mathbf{F_{fric}}^{Free\ \ flow} + \left(\frac{1}{\frac{Kn}{Kn_{cr}} + 1} \right)^2 \mathbf{F_{fric}}^{Viscous\ \ flow} \tag{6.12}$$

where Kn_{cr} is the critical Knudsen number denote the change from one regime to the other. The sedimentation velocity not only depends on the particle position but also on the particle size, meaning that the system is coupled. Physically, the drift or precipitation velocity for initially stationary dust is a monotonic function of size, with larger particle precipitating more quickly than small ones.

As the dust grains are advected with the ambient gas, the true or absolute motion of the dust particles is found by adding this 'drift' velocity to the general gas velocity.

$$\mathbf{v_{dust}} = \mathbf{v_{gas}} + \mathbf{v_{drift}} \tag{6.13}$$

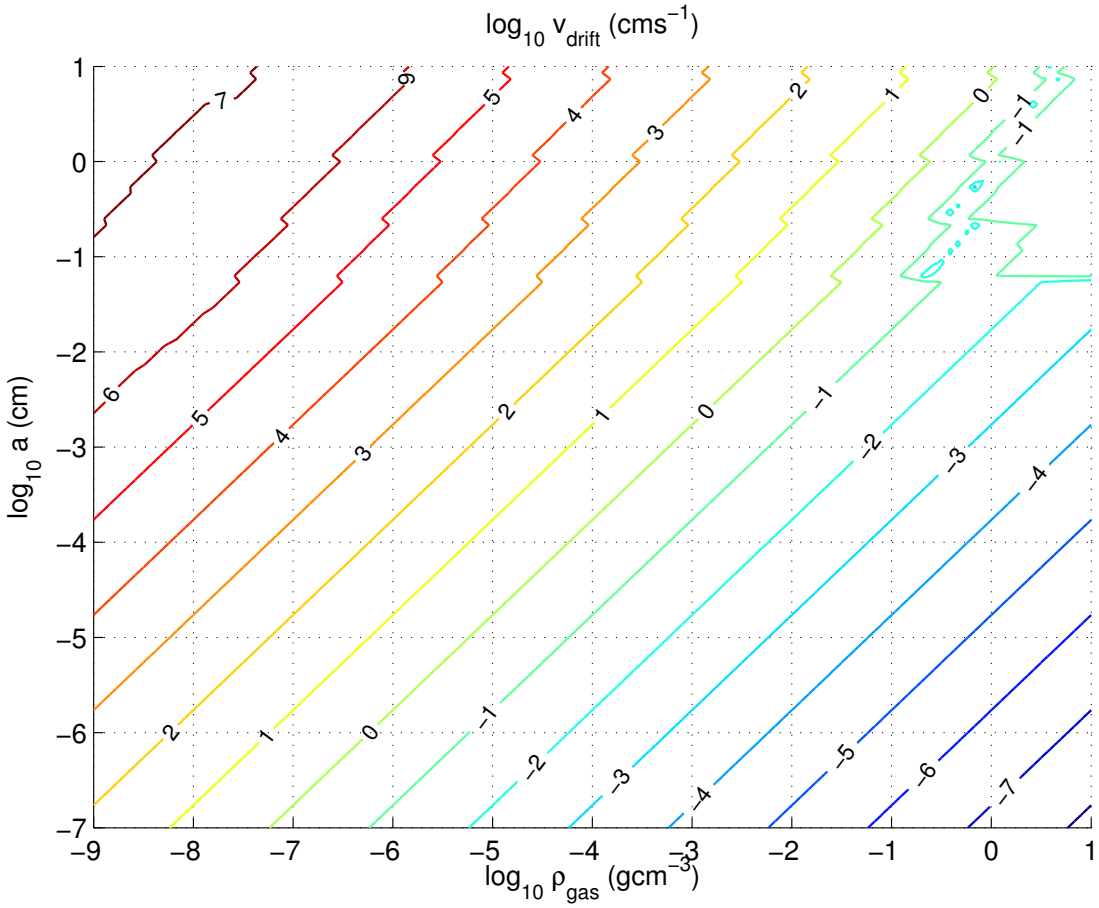

Figure 6.5: Logarithmic contour plot of the drift velocity on the gas density - dust radius plane.

Figure 6.5 shows the contour plot of the drift velocity on the gas density - dust radius plane. As expected, large dust particles drop quickly through a low density medium, while smaller, lighter particles settle more slowly. Similarly a denser medium leads to a lower drift velocity. The structure on the right hand side is associated with the change from laminar to turbulent flow. This plot compares well with Woitke & Helling (2003) Figure 1, where it is calculated for Quartz (SiO_2).

6.6 Dust Moments

The operating physical and chemical processes in the atmosphere occur simultaneously and may be strongly coupled. A true molecular dynamics approach to this problem is utterly intractable with current technology, so instead a system based on minimising the Gibb's Free Energy of the system that considers the mean powers of the particle radius is employed. To capture the essential elements of the system on the scales considered, only a few such averages are required.

For dust particle $\in [V, V + dV]$, the master equation is given by

$$\frac{\partial}{\partial t}\left(f(V)dV\right) + \nabla \cdot \left(\mathbf{v_{dust}} f(V)dV\right) = \sum_k R_k dV \tag{6.14}$$

where $f(v)[cm^{-6}]$ is the distribution function of dust in volume space. The summation on the right hand side describes the population and depopulation of the dust particles in this size bin due to the accretion or evaporation of molecules. By multiplying this equation with $V^{\frac{j}{3}}$ and integrating from $V = V_l$, the limiting dust volume, to $V \to \infty$ yields

$$\frac{\partial}{\partial t}\left(\rho L_j\right) + \nabla \cdot \left(\mathbf{v_{dust}} \rho L_j\right) = \int_{V_l}^{\infty} \sum_k R_k V^{\frac{j}{3}} dV \tag{6.15}$$

where the jth moment of the dust size distribution function $L_j[cm^j/g]$ is defined by

$$\rho L_j(\mathbf{x}, t) = \int_{V_l}^{\infty} f(V, \mathbf{x}, t) V^{\frac{j}{3}} dV \tag{6.16}$$

For free molecular flow under chemical and thermal equilibrium the right hand side can be shown to be

$$V_l^{\frac{j}{3}} J(V_l) + \frac{j}{3}\rho L_{j-1} \sqrt[3]{36\pi} \sum_r^R \Delta V_r n_r v_r^{rel} \alpha_r (1 - \frac{1}{S_r}) \tag{6.17}$$

where $J(V_l)$ is the nucleation rate of critically sized clusters of molecules, and the second term may be recognised from section 6.4 as the net growth speed of the dust grains, χ_{net}, with the dust moment and some numerical constants (Woitke & Helling 2003).

Laminar viscous flow (Woitke & Helling 2003) results in the analogous expression

$$V_l^{\frac{j}{3}} J(V_l) + \frac{j}{3}\rho L_{j-2} \sqrt[3]{48\pi^2} \sum_r^R \Delta V_r n_r D_r (1 - \frac{1}{S_r}) \tag{6.18}$$

where the diffusion coefficient is given by

$$D_i = \frac{\sqrt{\frac{8kT}{\pi}(\frac{1}{m_{H_2}} + \frac{1}{m_i})}}{3\pi(r_{H_2} + r_i)^2 n}. \tag{6.19}$$

Under normal circumstances, free molecular flow is appropriate for cool dwarf atmospheres.

The final moment equation is

$$\frac{\partial}{\partial t}\left(\rho L_j\right) + \nabla \cdot \left((\mathbf{v_{gas}} + \mathbf{v_{drift}^{\circ}})\rho L_j\right) = V_l^{j/3} J\left(V_l\right) + \frac{j}{3}\chi_{net}\rho L_{j-1} \tag{6.20}$$

with quantities defined as previously. Generally, the moment powers of interest are 0, 1, 2, and 3, corresponding physically to the number density of dust grains, the average radius of the grains, their average surface area and finally the volume of the grain.

The dust moment equations may be related back to the physical quantities of interest as follows.

$$n_d = \rho L_0 \qquad [\mathrm{cm}^{-3}] \tag{6.21}$$

$$< a > = \sqrt[3]{\frac{3}{4\pi}}\frac{L_1}{L_0} \qquad [\mathrm{cm}] \tag{6.22}$$

$$< A > = \sqrt[3]{36\pi}\frac{L_2}{L_0} \qquad [\mathrm{cm}^2] \tag{6.23}$$

$$< V > = \frac{L_3}{L_0} \qquad [\mathrm{cm}^3] \tag{6.24}$$

6.7 Element conservation

The formation of dust will deplete the gas phase in that region of the atmosphere ultimately limiting the dust growth. Depletion of the refractory elements modifies the gas chemistry, meaning that dust growth is retarded, resulting in a self-regulating growth mechanism. Overall, elemental abundances are perfectly conserved, but advection mixes the gas while nucleation and growth reactions lock up refractory elements resulting in a significantly modified abundance signature. The conservation equation of an element, e, considers the number density of that element, n_e, that is reduces by dust particles nucleating (1st term) and the growth upon such seed particles (2nd term)

$$\frac{dn_e}{dt} + \nabla \cdot (\mathbf{v_{gas}} n_e) = -\nu_{e,0} N_l J(V_l) - \sqrt[3]{36\pi}\rho L_2 \sum_{r=1}^{R} \nu_{e,r} n_r v_r^{rel} \alpha_r \left(1 - \frac{1}{S_r}\right) \tag{6.25}$$

where $\nu_{e,0}$ is the stoichiometric ratio of homogeneous nucleation and $\nu_{e,r}$ is the analogous ratio for surface reactions. An element conservation equation is required for each element involved in the dust cycle. Consequently, the chemical network of reactions initially considered by this model is restricted to titanium, Ti, and oxygen, O, compounds only.

In principle, only the titanium conservation equation is required as oxygen is more than three orders of magnitude more abundant than titanium (Asplund et al. 2009) and so even were the maximum possible dust mass to form then every titanium atom would be sequestered in dust while the remaining oxygen in the gas phase would be largely unaffected. This is true for this model while titanium dioxide (TiO_2) is the only dust species considered, but as the network of dust species expands to include other oxygen-bearing compounds then oxygen conservation or blocking of other oxygen gas and solid phase species may well become critically important.

6.7.1 Dust grain opacities

The opacity contribution of dust grain in ultracool dwarf atmospheres is critical not only to the spectral appearance but, through back-warming, even the structure of the atmosphere. The opacity of dust grains depends on their shape and size. Studies of dust grains in the interstellar medium suggest that

the grains might be elliptical in shape and easily charged. Such complications are beyond the scope of this work and superfluous until there is a clearer idea of the true shape of these grains. Instead, this model assumes homogeneous, neutral, spherical grains with cross-sectional area $\pi < a_{dust} >$.

Dust grains typically span the range $0.1\mu m - 100\mu m$ in size, which coincides with the wavelength of radiation in (mainly) the infrared, rendering the Rayleigh approximation inappropriate. Instead, Mie theory is applied to derive the effective extinction, absorption and scattering coefficients, Q_{ext}, Q_{abs} and Q_{sca}.

Mie theory involves the solution of Maxwell's equations for the absorption , scattering and re-emission of an electromagnetic field by homogeneous conducting spheres. It requires the wavelength dependent complex refractory index of the dust material, $m = n + ik$, and the related complex optical permittivity, $\epsilon = \epsilon_r + \epsilon_i$, which are related by

$$\epsilon_r = n^2 + k^2 \tag{6.26}$$

$$\epsilon_i = 2nk \tag{6.27}$$

The extinction, scattering and absorption coefficients are then given by

$$Q_{ext} = \frac{2}{x^2}\sum_{n=1}^{\infty}(2n+1)Re(a_n + b_n) \tag{6.28}$$

$$Q_{sca} = \frac{2}{x^2}\sum_{n=1}^{\infty}(2n+1)(|a_n|^2 + |b_n|^2) \tag{6.29}$$

$$Q_{abs} = Q_{ext} - Q_{sca} \tag{6.30}$$

with $x = 2\pi a/\lambda$,a is the grain size and λ the wavelength of light, and a_n, b_n are the Mie coefficients. These coefficients are simply multiplied with the geometrical cross-section of a spherical grain to find the effective cross section for absorption and scattering. The total opacity is then found by integrating over the grain size distribution, $f(V)$,

$$\chi_{dust} = \kappa_{dust} + \sigma_{dust} = \sqrt[3]{36\pi}\int_0^{\infty}(Q_{abs}(V) + Q_{sca}(V))f(V)V^{\frac{2}{3}}dV \tag{6.31}$$

Dust formation displays a hysteresis-type behaviour, as the availability of seed particles will affect the number density and the history of the dust grain will affect its size. Effectively, this means dust opacity depends on the grain size and dust number density in addition to both the shape discussed above and the thermodynamic properties of the gas that govern the gas phase opacity. To extend the pre-tabulated approach of the gas problem to the dust opacities would require extending the table from 4D to at least 6D, which starts to be very cumbersome to interpolate, as well as being extremely difficult to ensure the required parameter space coverage without allowing the table size to balloon. In addition these tabulated values would have to be integrated over wavelength in the same manner as the gas opacities, making computing the table massively time consuming and meaning this time was no longer offset by a speed up during the running of the hydrodynamic code. Instead, a hybrid scheme is adopted whereby the gas phase opacities are pre-tabulated and the dust opacities are calculated on-the-fly. The dust opacity is calculated for a typical wavelength, or a few typical wavelengths in each opacity bin and this is combined with the dust number density to give the total contribution from dust to the total opacity. The dust opacity contribution is then co-added to the gas opacities before the radiative transfer module is called. With this approach the comparatively flat behaviour of the

dust opacity with wavelength is exploited to create an efficient scheme incorporating the advantages of pre-tabulating the gas opacities with the necessity to correctly account for the more complexly coupled dust opacity.

6.8 Summary

The model presented here represents the first time that the full cycle of dust formation has been modelled self-consistently with convection. Such a model is long overdue (Allard et al. 1997; Burgasser et al. 2002b; Marley et al. 2010). Current models employ a suite of assumptions and this results in considerable variety in the resultant properties.

The current areas of contention between competing models are over the mixing mechanism, the grain size and the cloud inhomogeneity. Some groups argue that convective overshooting, as assumed by most models, is too weak to vigorously mix the atmosphere and as a result would retard dust formation and growth, while the 2D hydrodynamical model results of Freytag et al. (2010) suggest that gravity waves may significantly mix the medium. The assumptions made about the mixing mechanism directly impact the size of the dust grains that form. Weak mixing results in little condensible material available for dust formation and growth and therefore only small grains form, while strong mixing results in an abundance of dust-forming material and results in very large grains. In turn, grain size strongly affects the opacity of the dust and therefore its effect on the spectrum of the object. Small grains, as assumed by Tsuji et al have opacities which are almost independent of dust size, while for larger grains the effect on opacities scales as the square of the dust grain radius. The model developed here represents the strongest and most flexible tool to investigate these avenues. Only by removing key assumptions and allowing these quantities to emerge naturally from a simulation free of unconstrained free parameters can the mechanisms be thoroughly explored.

Moreover, this model is the first to allow 3D simulations of the dust formation, including the key nucleation phase, with realistic mixing and so it provides the best opportunity to study inhomogeneity in the atmosphere, and, in particular, investigate whether holes in the cloud deck could feasibly be responsible for the rapid transition between L and T dwarfs.

While complex and strongly coupled, this model does represent a sophisticated, powerful and flexible tool for investigating the diverse processes contributing to the atmospheres of ultracool dwarfs. Furthermore, it has the potential to form the basis for a complete understanding of stars, through brown dwarfs to extra-solar planets, which will become increasingly sought after as the observations of extra-solar planets improve and place more stringent constraints on the theoretical models.

Chapter 7

Micro-variability

Convection reaches the atmospheres of cool stars creating detectable variability in the photometry and spectrum of the star. Current 3D hydro-dynamical models of stellar convection in cool stars simulate only a small representative volume of the stellar atmosphere, typically covering some 10 granules horizontally. To derive observable quantities it is necessary to integrate these 'Box-in-a-star' models over the stellar disk. The integrated observable micro-variability induced by convection has critical implications for the detection of extrasolar planets by the radial velocity method. Convection on solar-type stars can induce ms^{-1} radial velocity shifts on timescales from $\sim$ 15 mins to a few days. In the era of ultra-precise spectrographs, like HARPS, that can theoretically determine radial velocities to sub-ms^{-1} precision (Pepe & Lovis 2008), it is necessary to address the the systematic errors introduced by noise sources like convection or oscillations (Dumusque et al. 2011b).

7.1 Introduction

Convection operating at the surfaces of cool stars fundamentally limits the stability of the stellar flux. This stochastic variability becomes increasingly important in the context of very precise spectra and radial velocity measurements as required by extrasolar planet searches and helioseismology.
Radial velocity measurements have now reached the level $\sim 1ms^{-1}$ (Pepe & Lovis 2008) . At this level of precision it becomes crucial to properly account for the systematic sources of noise associated with intrinsic stellar variability caused by granulation, oscillations and magnetic activity (Dumusque et al. 2011b).

Optimised observing strategies can remove much of the noise from oscillations, by averaging out its contribution (Dumusque et al. 2011a) leaving activity and convection the principal noise sources. Radial velocity searches employ either a cross-correlation function method, or a spectral Fourier space approach; both approaches require a reference spectrum against which the Doppler velocities are calculated. In many cases this is a composite of all the observations, however in other cases a model spectrum is used. By constraining the disk-integrated variability of the model spectrum caused by convection, it should be possible to obtain more accurate radial velocities, or at the very least a better quantitative characterisation of the uncertainties. This is ultimately of interest when searching for exoplanets, but could also be used to remove noise when searching for stellar oscillations.

Furthermore, in late-type non-active stars, gravitational redshifts and convective blue-shifts dominate the biases in determining radial velocity. These systematics, if ignored, can introduce errors of $\sim 0.5 \mathrm{km}^{-1}$, orders of magnitude larger than the instrumental precision of the current generation of ultra-precise spectrometers such as HARPS (Pepe & Lovis 2008). Gravitational redshifts may be constrained using accurate trigonometric parallaxes and stellar evolution models (Allende Prieto et al. 2009), while the use of 3D hydrodynamical models of surface convection naturally includes the convective blue-shifts. Convective blue-shifts are a consequence of surface convection, hot bright rising convective cells cover a larger surface area than the corresponding fast moving cool downdrafts and are hotter and therefore brighter meaning they dominate the observed flux creating a net blue-shift in the spectrum from on average stationary gas. 3D models naturally account for this blue-shift and the spectral lines derived from these models show asymmetric profiles, which agree well with observations, in contrast to 1D models which by construction can never have asymmetric line profiles.

Ideally when modelling the noise from the convective motions of a star one would like to model the full star. Sadly, the dynamic range of required spatial scales is so large as to make such an undertaking computationally prohibitive. Instead, state-of-the-art 3D surface convection simulations model a small but representative volume of the stellar atmosphere in detail resulting in the time series of emergent intensity as a function of emergent angle, $I(\nu, t, \mu, \phi)$. In recent years several groups have developed such 'Box-in-a-star' 3-D radiative hydrodynamic models of the upper convection zone and atmosphere of cool stars (Ludwig & Kučinskas 2012; Vögler et al. 2005; Trampedach et al. 2013)). Such simulations typically model $\sim$ 10 convective cells horizontally. In the case of the Sun the simulation box is typically a few Mm in each spatial dimension, requiring $\sim 10^5$ simulation boxes to cover the stellar surface.

The local model properties from these simulations are used to extrapolate to the full stellar disk quantities, for example flux. The statistical properties of spatial and temporal fluctuations derived from a time-series of simulation snapshots may be used to characterise the global variability. Previously suggested for white light and photometric centroid (Ludwig 2006), I extend this method to spectral lines, including the effects of stellar rotation. Better characterisation of this convective micro-variability would benefit velocity diagnostics for helioseismology, eg NiI 676.8nm, used by SOHO MDI (Jones 1989) and could be used to remove the 'noise' induced by convective motions in radial velocity planet searches.

7.2 Approach and basic statistical assumptions

3D radiative hydrodynamic models of stellar surface convection are computationally expensive, and so global models are ruled out. Instead, it is typical to simulate a section of the atmosphere covering of order 10 convective cells horizontally. Global properties from the simulations are derived by integrating these models over the stellar disk. By exploiting the statistical properties of the spatial distribution and temporal evolution of emergent intensity, not only the disk integrated spectrum and related properties, but also the expected variance of these as a result of the presence of convective motions may be derived.

In order to describe the brightness fluctuations of a star caused by convection I use the emergent radiation field and its temporal evolution from the simulation 'tile'. To progress, consider the visible hemisphere of the star as tiled by a large number of these simulation boxes. This tiling is not con-

sidered explicitly, as the geometric problems caused by the simulation tile shape coupled with the periodic horizontal boundary conditions would make this a formidable task. Instead merely consider that some such construction is theoretically possible.

As in Ludwig (2006), the following assumptions are made:

1. Each tile radiates statistically independently of all other tiles
2. Every tile on the stellar surface shares the same statistical properties
3. The spatial statistical properties may be used as a proxy for the temporal statistical properties

The first assumption is equivalent to assuming that the correlation length of the simulation is the dimension of the simulation tile. In practice, although convection is too weak to have long range correlation lengths, acoustic modes, for example, have correlation lengths which imply longer range coupling. This coupling could be treated separately (Ludwig 2006) as a perfectly correlated signal leaving the granulation signal for which the assumption holds.

The second assumption implies homogeneity, which might be violated by strong rotation or large-scale magnetic fields. Magnetic fields are neglected in this work, limiting its applicability to only weakly active stars and rotation is considered only as a bulk movement, not strong enough to cause changes in the convective pattern. While this works well for most stars, rapid-rotators and magnetically active stars require a more detailed consideration.

The final assumption should be robust as the chaotic nature of granular flows (Steffen & Freytag 1995) should ensure ergodic behaviour.

In general the method is limited by the available statistics provided by finite simulation runs and not the above assumptions, except in extreme cases like strongly magnetically active stars.

7.3 Radiative Hydrodynamic Models

The 3D radiative hydrodynamic (RHD) models consist of a plane-parallel box covering the photosphere and upper convection zone. The model solves the fluid equations of mass continuity, momentum and energy conservation. Radiative transfer is treated in detail, with several wavelength bands accurately modelling the wavelength dependence of radiative heating and cooling in the continuum and spectral line, while the geometry is accounted for by a ray-tracing technique. Realistic equations of state are used, e.g. Mihalas-Hummer-Däppen for *stagger* (Trampedach et al. 2006), and opacities are taken from the best opacity packages available, e.g. MARCS stellar atmosphere package for *stagger* (Gustafsson et al. 2008) and OPAL (among others) for CO^5BOLD (Iglesias & Rogers 1996).

The basic radiative output of a simulation tile, relevant for this application, is the surface average of the emergent intensity as a function of wavelength, λ, time, t, inclination angle, $\mu = cos(\theta)$ and azimuthal angle ϕ. In essence, this means the information about the detailed spatial intensity is reduced to correspond to the familiar 1D model atmosphere output, except there is time-series of this data. The restricted suite of inclinations and azimuthal angles reflects the computational expense of the calculation. For the data used here, there are 8 inclinations and 8 azimuthal angles. Figure

Figure 7.1: Definition of the inclination angle, μ, with respect to the surface geometry.

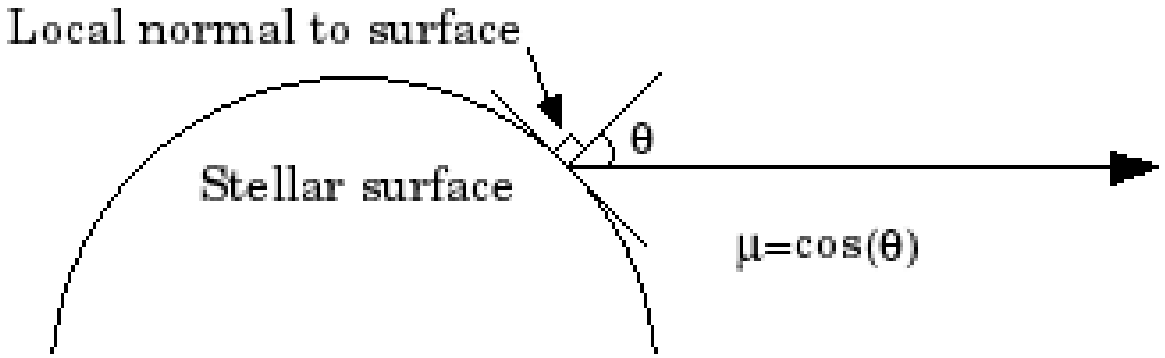

Figure 7.2: Normalised intensity of the neutral iron line at 542.7nm as a function of Doppler velocity from line centre, v (equivalent to wavelength), and inclination of viewing angle, μ.

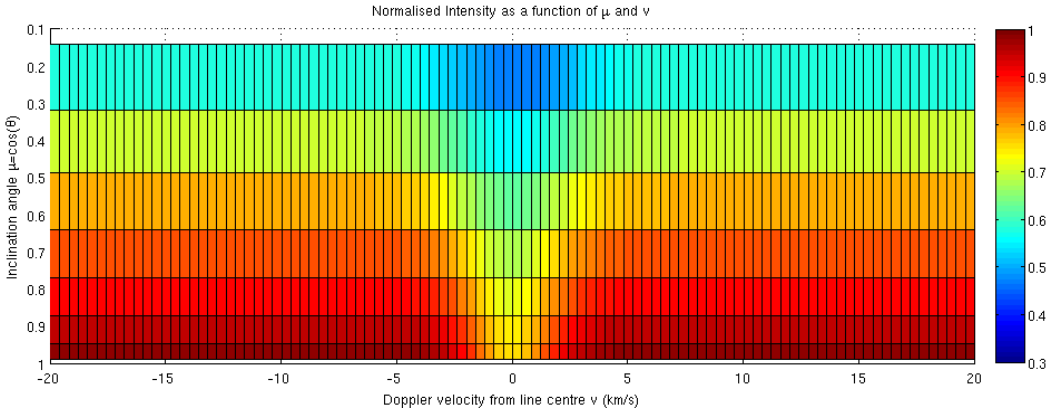

7.1 shows the definition of inclinations, μ while Figure 7.2 illustrates some example intensities as a function of μ and Doppler velocity from line centre, a proxy for ν.

7.4 Statistics of an individual tile

In order to derive expressions for the temporal average of the emergent spectral flux density, F_ν, and its standard deviation, σ_{F_ν} it is necessary to discretise the usual relation for spectral flux density as follows:

$$F_\nu = \int \mu I(\mu,\phi,\nu) d\Omega \tag{7.1}$$

$$= \int_0^{2\pi} d\phi \int_0^1 \mu I(\mu,\phi,\nu) d\mu \tag{7.2}$$

$$\simeq 2\pi \sum_{m=1}^{M}\sum_{k=1}^{N} \omega_{km}\mu_m I_{km}(\nu) \tag{7.3}$$

where ω_{km} is the fraction of solid angle of the hemisphere subtended at inclination μ_m and azimuthal angle, ϕ_k, and $I_{km}(\nu)$ is the specific intensity in that direction.The $\simeq$ highlights the transition from a continuous to a discrete description. In the limit of infinitely fine discretisation the full equality is recovered. The convection pattern is statistically horizontally isotropic, implying that ω_{km} for the same μ-ring ought to be equal. That is

$$\sum_{m=1}^{M}\sum_{k=1}^{N} \omega_{km} = \sum_{m=1}^{M} N(m)\omega_{km} = \sum_{m=1}^{M} \omega_m = 1 \tag{7.4}$$

Since ω_{km} and μ_m are not time dependent, but are fixed by the geometric setup, the temporal expectation value for the spectral flux density is

$$< F_\nu > \simeq 2\pi \sum_{m=1}^{M}\sum_{k=1}^{N} \omega_{km}\mu_m < I_{km}(\nu) > \tag{7.5}$$

The standard deviation may be found via the following:

$$\sigma_{F_\nu} = \sqrt{< F_\nu^2 > - < F_\nu >^2} \tag{7.6}$$

where

$$< F_\nu^2 > \simeq (2\pi)^2 \sum_{m=1}^{M}\sum_{m'=1}^{M}\sum_{k=1}^{N}\sum_{k'=1}^{N} \omega_{km}\omega_{k'm'}\mu_m\mu_{m'} < I_{km}(\nu) I_{k'm'}(\nu) > \tag{7.7}$$

At this point it is useful to introduce the linear correlation coefficient, $C[I_{km}(\nu), I_{k'm'}(\nu)]$, between $I_{km}(\nu)$ and $I_{k'm'}(\nu)$ obeying the relation:

$$< I_{km}(\nu) I_{k'm'}(\nu) > = < I_{km}(\nu) >< I_{k'm'}(\nu) > + \sigma_{I_{km}(\nu)}\sigma_{I_{k'm'}(\nu)} C[I_{km}(\nu), I_{k'm'}(\nu)] \tag{7.8}$$

Equation 7.7 can now be rewritten as

$$< F_\nu^2 > \simeq (2\pi)^2 \sum_{m=1}^{M}\sum_{m'=1}^{M}\sum_{k=1}^{N}\sum_{k'=1}^{N} \omega_{km}\omega_{k'm'}\mu_m\mu'_m \cdot$$
$$(< I_{km}(\nu) >< I_{k'm'}(\nu) > + \sigma_{I_{km}(\nu)}\sigma_{I_{k'm'}(\nu)} C[I_{km}(\nu), I_{k'm'}(\nu)]) \tag{7.9}$$

$$\simeq < F_\nu >^2 + (2\pi)^2 \sum_{m=1}^{M}\sum_{m'=1}^{M}\sum_{k=1}^{N}\sum_{k'=1}^{N} \omega_{km}\omega_{k'm'}\mu_m\mu'_m \sigma_{I_{km}(\nu)}\sigma_{I_{k'm'}(\nu)} C[I_{km}(\nu), I_{k'm'}(\nu)] \tag{7.10}$$

In general, the correlation function can take any value $\in [0, 1]$ at each point across the patch or stellar surface, but to simplify the problem I consider some analytical limiting cases:

i) The intensities of all elements of the solid angle are independent, that is completely uncorrelated,

$$C[I_{km}(\nu), I_{k'm'}(\nu)] = \delta_{mm'}\delta_{kk'} \quad \forall \quad m, m', k, k'. \tag{7.11}$$

ii) All intensities are perfectly positively correlated,

$$C[I_{km}(\nu), I_{k'm'}(\nu)] = 1 \quad \forall \quad m, m', k, k'. \tag{7.12}$$

iii) The intensities are correlated with height in the atmosphere, corresponding to azimuthal correlation within the same inclination, but are uncorrelated between different inclinations,

$$C[I_{km}(\nu), I_{k'm'}(\nu)] = \delta_{mm'} \quad \forall \quad m, m', k, k'. \tag{7.13}$$

The second case provides a reasonably good description of the actual behaviour of the intensities *within* an individual simulation tile, as neighbouring convective cells necessarily affect one another, while the final case also seems plausible as one would expect the correlation between different physical heights in the atmosphere to be lost before the azimuthal correlation at the same physical height in the atmosphere.

$$\sigma^2_{F_\nu} \simeq (2\pi)^2 \begin{cases} \sum_{m=1}^{M}\sum_{k=1}^{N} \omega_{km}^2\mu_m^2\sigma^2_{I_{km}(\nu)} & \text{if} \quad C[I_{km}(\nu), I_{k'm'}(\nu)] = \delta_{mm'}\delta_{kk'} \\ (\sum_{m=1}^{M}\sum_{k=1}^{N} \omega_{km}\mu_m\sigma_{I_{km}(\nu)})^2 & \text{if} \quad C[I_{km}(\nu), I_{k'm'}(\nu)] = 1 \\ \sum_{m=1}^{M}\sum_{k=1}^{N}\sum_{k'=1}^{N} \omega_{km}\omega_{k'm}\mu_m^2\sigma_{I_{km}(\nu)}\sigma_{I_{k'm}(\nu)} & \text{if} \quad C[I_{km}(\nu), I_{k'm'}(\nu)] = \delta_{mm'} \end{cases} \tag{7.14}$$

Table 7.1: Inclination angles μ_m and weighting factors ω_m for the flux integration

m	μ_m	ω_m	ω_{km}
1	0.1409	0.0506	0.0063
2	0.3189	0.1112	0.0139
3	0.4871	0.1569	0.0196
4	0.6390	0.1813	0.0227
5	0.7692	0.1813	0.0227
6	0.8734	0.1569	0.0196
7	0.9478	0.1112	0.0139
8	0.9900	0.0506	0.0063

For the individual tile, the variances and correlations could be found directly from the hydrodynamical data, but it is instructive to have these expressions to compare with the analogous disk-integrated expressions in the next section.

7.5 Statistics of disk-integrated spectral flux density

As for the individual simulation tile, the aim is to derive expressions for the expectation value and standard deviation of the disk integrated spectral flux density, f_ν. I adopt the discretisation found in

Figure 7.3: The geometry of stellar disk discretisation. The concentric circles define iso-μ rings which delineate the regions of constant μ. The red crosses show the representative μ considered for each region. The disk is symmetric and 6 azimuthal angles, ϕ are considered.

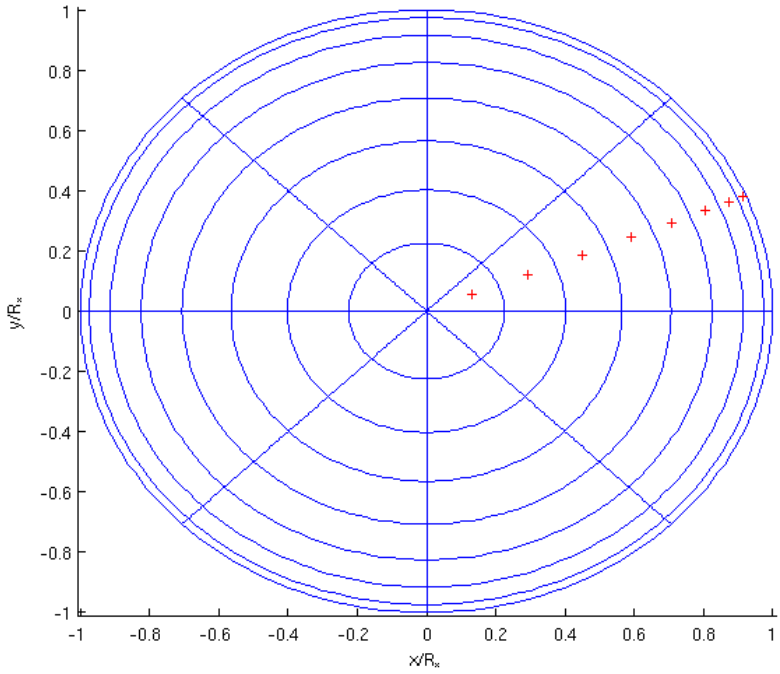

Table 7.1 from the hydrodynamic simulation and interpret this as a partitioning of the stellar disk, as shown in Figure 7.3.

The spectral flux density observed at distance D from a star with radius R_* is

$$f_\nu = \frac{R_*^2}{D^2} F_\nu \tag{7.15}$$

and since R_* and D are time independent, the expectation values of the two may be related

$$< f_\nu > \;=\; \frac{R_*^2}{D^2} < F_\nu > \tag{7.16}$$

$$\simeq\; \frac{2\pi R_*^2}{D^2} \sum_{m=1}^{M} \sum_{k=1}^{N} \omega_{km}\mu_m < I_{km}(\nu) > \tag{7.17}$$

again the expectation value of $< f^2(\nu) >$ is

$$< f_\nu^2 > \;\simeq\; (2\pi R_*^2/D^2)^2 \sum_{m=1}^{M} \sum_{m'=1}^{M} \sum_{k=1}^{N} \sum_{k'=1}^{N} \omega_{km}\omega_{k'm'}\mu_m\mu_{m'} \cdot$$
$$(< I_{km}(\nu) >< I_{k'm'}(\nu) > + \sigma_{I_{km}(\nu)}\sigma_{I_{k'm'}(\nu)} C[I_{km}(\nu), I_{k'm'}(\nu)]) \tag{7.18}$$

$$\simeq\; < f_\nu >^2 + (2\pi)^2 \left(\frac{R_*}{D}\right)^4 \sum_{m=1}^{M} \sum_{m'=1}^{M} \sum_{k=1}^{N} \sum_{k'=1}^{N} \omega_{km}\omega_{k'm'}\mu_m\mu_{m'}\sigma_{I_{km}(\nu)}\sigma_{I_{k'm'}(\nu)} C[I_{km}(\nu), I_{k'm'}(\nu)] \tag{7.19}$$

where I again introduce the linear correlation coefficient $C[I_{km}(\nu), I_{k'm'}(\nu)]$, defined by 7.8.

Finally we arrive at the disk-integrated variance under two of the limiting cases discussed previously:

$$\sigma^2_{f_\nu} \simeq 4\pi^2 \left(\frac{R}{D}\right)^4 \begin{cases} \sum_{m=1}^{M} \sum_{k=1}^{N} \omega^2_{km} \mu^2_m \sigma^2_{I_{km}(\nu)} & \text{if} \quad C[I_{km}(\nu), I_{k'm'}(\nu)] = \delta_{mm'}\delta_{kk'} \\ (\sum_{m=1}^{M} \sum_{k=1}^{N} \omega_{km} \mu_m \sigma_{I_{km}(\nu)})^2 & \text{if} \quad C[I_{km}(\nu), I_{k'm'}(\nu)] = 1 \\ \sum_{m=1}^{M} \sum_{k=1}^{N} \sum_{k'=1}^{N} \omega_{km} \omega_{k'm} \mu^2_m \sigma_{I_{km}(\nu)} \sigma_{I_{k'm}(\nu)} & \text{if} \quad C[I_{km}(\nu), I_{k'm'}(\nu)] = \delta_{mm'} \end{cases} \tag{7.20}$$

It would be natural to try to relate the simulation tile brightness fluctuations directly to the fluctuations of the disk-integrated brightness, $\sigma_f = R^2/D^2 \sigma_F$, analogously to the relation for the flux $< f >= R^2/D^2 < F >$, however this is only possible for the unrealistic situation of perfect correlation of intensities in a simulation tile *and* across the stellar disk. In general, reference must be made to the intensities themselves.

It should be pointed out explicitly that the above relations will also hold for integrals over a particular frequency range and recover the relations for white light in the limit of integration of the full spectrum.

7.6 Breaking the isotropy by rotation

Until now, I have considered a static stellar disk with perfect isotropy, but stars rotate. The rotation will shift the simulation intensities by a Doppler shift

$$d\nu = \nu dv_{patch}/c. \tag{7.21}$$

The Doppler velocity of the patch may be found by

$$dv_{patch} = \Omega(\lambda) cos(\alpha) \tag{7.22}$$

where $\Omega(\lambda)$ is the angular velocity at a latitude λ and $cos(\alpha)$ is the projection of the radius vector perpendicular to the rotation axis.

The statistical results derived in the previous sections still hold for each frequency, ν, however they must be applied to the *observed* frequency, which requires properly shifting the intensities due to rotation. The anisotropy introduced by the rotation requires that the integration over the azimuthal direction ϕ must be kept explicit, in contrast to Ludwig (2006) as $d\nu = d\nu(\mu, \phi)$.

While rotation breaks the isotropy, it should not be strong enough to affect the results of the RHD simulations, therefore the intensities need only be shifted from ν_0 in the simulations to ν

$$I(\nu_o, t, \mu, \phi) \rightarrow I(\nu_o + d\nu, t, \mu, \phi) = I(\nu, t, \mu, \phi) \tag{7.23}$$

This leads to a modified version of the flux integral, which adds a contour integral over frequency.

$$F(\nu) = \int \mu I(\nu) d\Omega = \int_0^1 d\mu \int_0^{2\pi} d\phi \mu \oint_{\nu=\nu'+d\nu=constant} I(\nu' + d\nu) d\nu' \tag{7.24}$$

$$\simeq 2\pi \sum_{m=1}^{M} \sum_{k=1}^{N} \omega_{km} \mu_m I_{km(\nu_o + d\nu)} \tag{7.25}$$

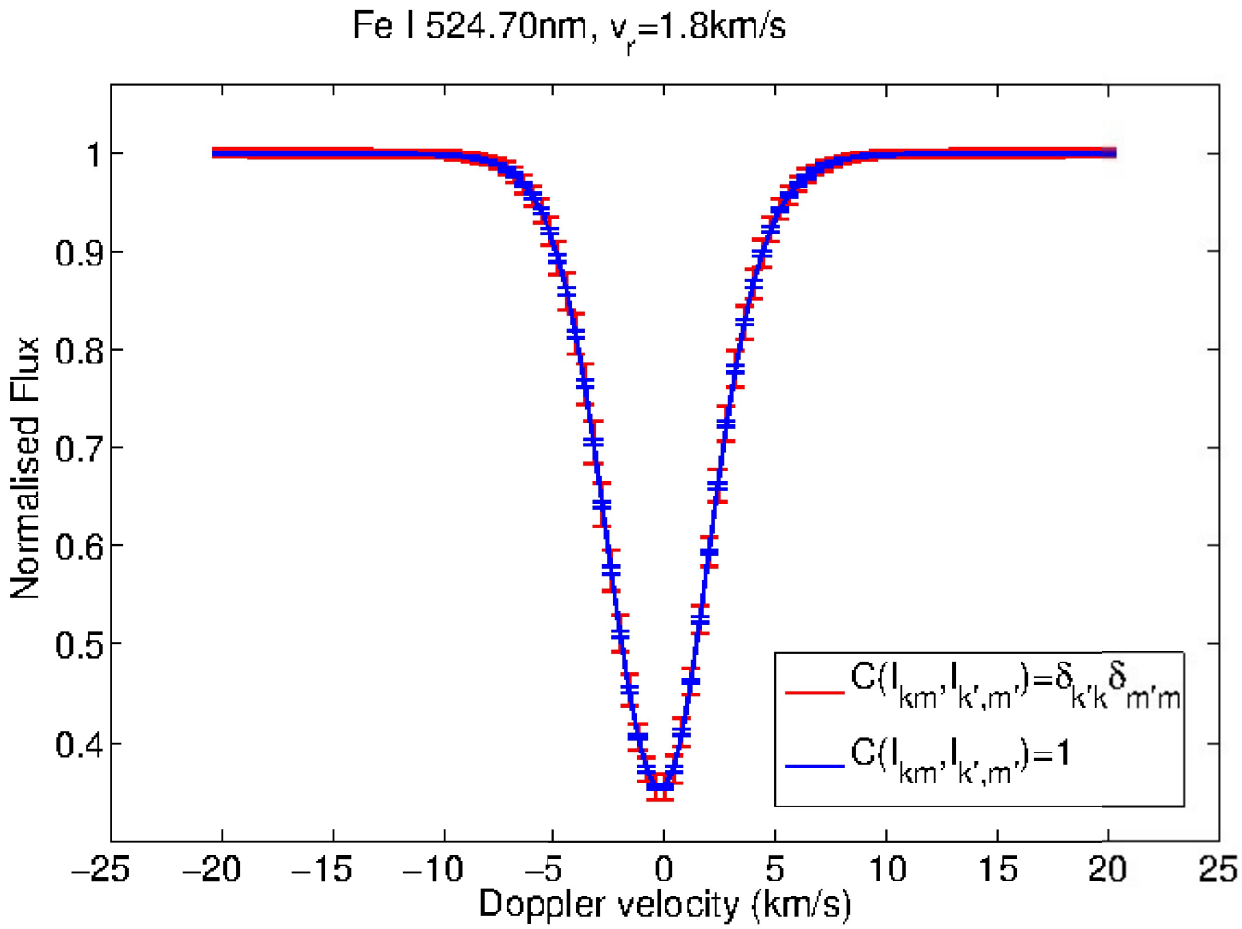

Figure 7.4: Fe I line at 524.70*nm* assuming solid body rotational at 1.8 kms^{-1}, for the solar 3D hydrodynamic model. The line profile is plotted and shown with errorbars, the red corresponds to a perfectly correlated signal, while the blue shows the tighter constraints for an uncorrelated signal on the length scale of the patch sizes in Figure 7.3.

The variance of the disk integrated spectrum, under the relevant limiting cases is again

$$\sigma^2_{f_\nu} \simeq 4\pi^2 \left(\frac{R}{D}\right)^4 \begin{cases} \sum_{m=1}^{M} \sum_{k=1}^{N} \omega^2_{km} \mu^2_m \sigma^2_{I_{km}(\nu)} & \text{if} \quad C[I_{km}(\nu), I_{k'm'}(\nu)] = \delta_{mm'}\delta_{kk'} \\ (\sum_{m=1}^{M} \sum_{k=1}^{N} \omega_{km} \mu_m \sigma_{I_{km}(\nu)})^2 & \text{if} \quad C[I_{km}(\nu), I_{k'm'}(\nu)] = 1 \end{cases} \tag{7.26}$$

where the final case of correlated inclinations μ is no longer considered. The correlation of inclinations is no longer a relevant case as the rotation breaks the symmetry and radiation from the same height contributes to the spectral flux density at a different wavelength due to the Doppler shifting of its frequency.

If the rotational profile of the stellar disk is known then the integration contours may be mapped,

7.7 Example

The method is applied to the Fe I line at 524.70*nm* assuming solid body rotational at the solar rotational velocity of 1.8 kms^{-1}. The simulation used was from the *Stagger* code with parameters to match the Sun. The simulation was at 400x400x200 resolution, covering physically 6Mm x 6Mm x 4Mm covering $\sim$ 1 hour stellar time: the same simulation has been used for detailed abundance analysis (Asplund et al. 2009).

From this, 12 snapshots were used and the radiative transfer computed for 8 inclination (μ) and 8 azimuthal (ϕ) angles for 101 frequencies spaced at 0.4 kms^{-1} (Doppler velocity equivalent). To highlight the advantage of this method I present the contrast between naive errorbars, corresponding to completely positively correlated patches and those computed by the method described. The results are independent of the particular geometry of the patches used. The temporal statistics allow the determination of the individual patch variance, while the spatial resolution gives independent measurements of the integrated disk flux errors. These operations are entirely symmetric, and equivalent. One can use the spatial information to derive the individual simulation box variances and then use the temporal snapshots to sample the expected patch variation or vice versa. These will yield the same results.

Figure 7.4 shows the Fe I line profile with errorbars corresponding to a perfectly correlated signal in red, which is the current standard, while the blue shows the case of an uncorrelated signal on the scale of the patches shown in Figure 7.3.

7.8 Extensions to the method

7.8.1 Centre of gravity

It would be desirable to extend this method to derived properties of spectral lines, particularly in the era of massive stellar spectral surveys, like SEGUE (Yanny et al. 2009) that surveyed 240,000 stars, which necessarily rely heavily on automatic parameter determination.

The centre-of-gravity, λ_{COG}, of a line profile, I_λ, is defined as the centroid of its residual intensity profile.

$$\lambda_{COG} = \frac{\int_\lambda \lambda(I_{cont} - I)d\lambda}{\int_\lambda (I_{cont} - I)d\lambda} \tag{7.27}$$

This is particularly useful as λ_{COG} is linearly related to the line-of-sight velocity at the atmospheric height where the line forms (Uitenbroek 2003). Accurate theoretical models describing this could be invaluable in large-scale planet hunting surveys and stellar oscillation monitoring.

Unfortunately, the λ_{COG} of a line depends on the detailed shape of the line profile and cannot be reconstructed by the linear combination of individual profile centres-of-gravity, even including information about the continuum intensity. As a result this method is fundamentally inapplicable to this spectral diagnostic.

7.8.2 Clouds

The results derived in Sections 7.4,7.5, and 7.6 are predicated on inhomogeneous, temporally evolving convective cells limiting the photometric and spectral stability. However, the relation will hold for any statistically homogeneous dynamical surface pattern. In particular, the dust model developed in Chapters 4,5 and 6, will result in inhomogeneous clouds or cloud coverage. This is particularly pertinent as it is the variability induced by these clouds that is being searched for in the Spitzer proposal of Apai et al. (2012). The statistical results presented here will be applicable whether the variability turns out to be a result of a secondary dust dominated convection zone with inhomogeneity in the thickness of the cloud deck or broken cloud coverage, as long as the surface coverage of clouds fulfils the original assumptions about the spatial, temporal and statistical properties of the surface pattern. On Jupiter, for example, differential rotation significantly affects the cloud structure leading to a banded appearance, for which this method would be inapplicable without modification.

7.8.3 Activity

The photometric and spectral signature of activity on the stellar surface represents another source of noise for accurate radial velocity determinism. While the statistical properties of starspots may lend themselves to this kind of analysis, active regions are not expected to be homogeneously distributed over the stellar surface but to follow belt-like zones, as in the solar case.

However, it is likely that a semi-quantitative connection will still remain between the activity-induced brightness fluctuations so that rough estimates of variability are possible from magneto-hydrodynamic models, or further investigation might yield an extension to this method that correctly accounts for the expected spatial correlation of spots along the belts.

7.9 Discussion

Further improvements are possible by assuming a more realistic correlation length or by increasing the resolution of the radiative transfer. Reducing the correlation length to be the simulation tile size of around 10 granules rather than the patch size the errorbars could be significantly reduced whilst accounting for the correlation of neighbouring granules. This method encounters fundamental limits when the number of convective cells on a hemisphere is small, such as for red supergiants (Chiavassa et al. 2011). Additionally other sources of variability may dominate over the convective signal, for example inhomogeneity caused by activity or correlation caused by pulsations. Nevertheless this remains a useful tool for studying the convection induced micro-variability of cool stars.

In conclusion I have extended the method of Ludwig (2006) to handle strongly wavelength dependent fluxes, such as spectral lines. Rotational broadening can then be superimposed and spectral lines recovered by contour integrals over constant frequency. In particular better constraints on the convective component of the variability of the NiI 676.8 nm line used by SOHO MDI would allow better calibration and treatment of the uncertainty propagation from the use of this line as a velocity diagnostic for helioseismology.

Chapter 8

Conclusions

The age of three-dimensional hydrodynamic modelling of stellar atmospheres has arrived and is here to stay. Late-type stars have convective envelopes immediately below their photospheres and this convection significantly affects the appearance of their surfaces, the atmospheric structures of these stars and their emergent spectra.

Hydrostatic one-dimensional models of stellar atmospheres are becoming increasingly sophisticated, while the fundamental assumptions underlying them are often and severely violated. In this thesis I have simulated a sequence of six cool dwarf stars using a 3D hydrodynamic code, resulting in relaxed models of the stars' convective envelopes and photospheres. The emergent intensity maps I present show clearly that the stellar surface is strikingly inhomogeneous in the horizontal plane, as a result of the presence of convective cells. I confirm the findings of Magic et al. (2013) that there is a trend of root mean square intensity fluctuations with effective temperature, but show that the slope is steeper. Decomposition of emergent intensities may be resolved into a cool dim component coming from the downflowing intergranular lanes and a second component corresponding to the convective cells that is hot and bright. I demonstrate that towards cooler dwarfs these components become more sharply defined and that the relative peaks shift from hot objects where the cool component has a higher amplitude peak to cooler objects where the opposite is true. The inhomogeneity in photosphere and underlying layers is critical to understanding these objects and I further show that the physical modelling of the convective zone leads to a revised and shallower temperature structure in the photospheres of the more physically realistic 3D models than the hydrostatic models, even when the inhomogeneities are averaged out. The natural inclusion of convective overshooting without artificial parametrisation means I can demonstrate that velocity fields and turbulent pressure remain sizable out into layers classically considered stable against convection, in contrast to previous hydrostatic models, and these velocity fields will broaden the spectral lines formed in this region. Additionally, the energy fluxes in these atmospheres alter importantly in 3D, with convective overshooting meaning that motion propagates out into line forming layers and that the switchover from convectively dominated flux to the radiatively dominated flux in the outer atmosphere is more gradual than that predicted by 1D models. Energy transport in these objects is fundamental to our understanding of their properties and structure as the emergent spectra are the only probe we have of their structure[1], therefore changes in the energy transport have serious consequences in terms of changing the boundary conditions for internal structural models of these objects. I further show that the emergent spectra in these objects are impacted by

[1] Asteroseismology has not yet been applied to these cool dwarf stars.

these differences, and that due to the height-dependent nature of spectral line formation these changes do not form a systematic shift but are intricately connected with the details of the atmospheric structure. Additionally, I show that the differences between 1D and the mean 3D can differ by typically 30-50K for the same input model parameters, while in the line centres, that are particularly sensitive to the lack of broadening from velocity fields in the atmosphere, the differences can be substantially greater. I conclude overall, that while the spectral studies I perform are not highly sophisticated, the results suggest that inhomogeneity and the convective overshooting that are the natural consequences of a 3D model are critical in understanding these objects and 1D hydrostatic models are no longer sufficient to model these objects properly.

Stellar atmosphere modelling depends sensitively on the physical data that is incorporated to describe the equation of state of the gas and the gas opacities. While hydrogen, ionised metals and neutral metals are most crucial for modelling the Sun, the suite of considered opacities must reflect the physical conditions found in the atmosphere of the star and therefore moving to cooler models requires the addition of a plethora of molecular species and their lines. For this reason I adapted the more complete at low temperature suite of opacity data from the PHOENIX collaboration to be compatible with the *stagger* code, which by default uses the MARCS collaboration opacities that are designed to be used with hotter stars. I demonstrate that the two raw datasets are similar for conditions encountered in the mean solar model, but that at lower temperatures likely, to be encountered in models of cooler effective temperature, the PHOENIX suite of opacities has more complete coverage of the molecular opacities, which are particularly important at the red end of the spectrum. I designed and wrote software that processes the raw opacities using the τ-sorting multi-group method to bin the opacities. Pre-tabulated opacity is necessary as radiative transfer in 3D hydrodynamic codes is expensive and monochromatic radiative transfer would render this type of problem insoluble, even with current supercomputers. I compare and contrast the raw opacities with a view to understanding the resultant differences in the binned opacity tables, which are a result of resolution, small differences in the equations-of-state and intrinsic differences in the raw opacities caused by differing sources and poorly constrained measured or theoretical opacity calculations. Using the mean solar model, I show that for solar conditions the two datasets recover similar Rosseland opacities, although not identical for the reasons outlined above. Opacities, and even more-so multi-group binned opacities are valid (calculated or measured) for a particular set of atmospheric conditions, therefore the equation-of-state plays a crucial role and in a stellar atmosphere code the opacities and equation-of-state must be compatible. By changing from the MARCS opacity package, which works with the MHD equation-of-state, to the PHOENIX opacity suite, the equation-of-state must also be changed to ACES, the corresponding one for PHOENIX. The two equations-of-state are not calculated in the same variables, therefore a transformation must be made and the re-fixing of the energy zero. I show that the two equations-of state are significantly different in their parameter space coverage but similar in thermodynamic variables, particularly in the high temperature range where they are both well-tested. The implementation of this new more sophisticated equation-of-state and substantially more complete opacity suite means that the previous barrier to modelling cooler stars with the *stagger* code has been removed.

While the new opacities extend the range of effective temperatures that may be modelled, at the coolest end of the stellar main sequence the condensation of molecules into dust poses an interesting new regime. Dust strongly affects the atmospheric structure and constitutes a major opacity source. This differs from the normal gas hydrodynamic problem in that dust grains exhibit a hysteresis type behaviour with the dust radius depending on the grain history as well as the local thermodynamic conditions. I developed the first three-dimensional model of cool stellar atmospheres that simultane-

ously considers the full (including nucleation) dust cycle and naturally includes the true mixing by convection and overshooting. Resolving both dust and convection simultaneously on a reasonable simulation timescale requires the splitting of the radiative transfer into the gas and molecular component, which may be pre-tabulated, and the dust grain opacity that depends on a greater number of variables. The dust opacity is calculated 'on-the-fly' at each cell and timestep then co-added to the gas and molecular opacity in each of the multi-group bins to give a hybrid scheme that minimises the code runtime. Other important assumptions include the advection of dust with the local gas velocity field offset only by the gravitational settling velocity, which allows the multi-fluid system to be treated as a single fluid. Using a moment method of the dust radius, the key properties of the dust may be followed with each micro-physical process being correctly considered. The mutual blocking of species is included via a chemical equilibrium solver. While nucleation and growth currently model only a single dust species, the framework has been set up to efficiently model multiple species and dirty dust grains. The new code is a substantial leap forward in our ability to model ultracool dwarfs in a meaningful way that considers the coupled physical processes operating rather than parametrisations of decoupled timescale arguments.

Inhomogeneous surface features caused by convection operating in atmospheres of late-type stars imply there is a fundamental limit to the photometric stability of these objects. Such micro-variability becomes increasingly important in the context of extra-solar planet searches and characterisation. Using the realistic 3D hydrodynamic simulations of surface convection in cool stars, it is possible to better characterise the expected background micro-variability from convection. I develop the necessary statistical relations to constrain the observable photometric variability based on the restricted 'box-in-a-star' models that are the current state-of-the-art, including for the first time the ability to incorporate rotation and even a more complex rotation profile than a rigid rotator. I examine the extension of this method to centre of gravity of line profiles and conclude it is not possible. I note that these relations are valid for any statistically independent surface inhomogeneity; in particular dust clouds on ultracool dwarfs and extra-solar planets might be a fruitful application where this method could be used to constrain the many free parameters in the cloud modelling. Magnetic activity, though correlated, could be decomposed into a correlated component and a stochastic signal, if the activity correlations were well enough known[2] these relations could be applied to the uncorrelated signal.

As a body of work, this thesis pushes 3D atmospheric modelling down into cooler effective temperatures than ever before and sets the groundwork for the detailed modelling of coupled convection and dust formation in ultracool dwarf atmospheres, paving the way for a better understanding of the continuum between cool main-sequence stars, brown dwarfs and planets, and in particular the poorly understood transition between the L and T spectral classes.

[2]In the Sun the magnetic activity is confined to particular bands, but within these may be considered as an inhomogeneous surface feature.

Chapter 9

Outlook and extendability

9.1 3D hydrodynamic models

3D hydrodynamic models are extremely successful in reproducing the observed spectra of cool stars (e.g. Asplund et al. 2000) without recourse to additional free parameters like micro- or macroturbulence. The dynamical nature of convection has important consequences for the velocity fields present in the atmosphere and therefore the expected mixing. As observations improve, more rigorous constraints will be placed on atmosphere models and the assumptions inherent in 1D models will have to be relaxed or removed. Chapter 3 explores the properties of a sequence of M dwarf models in effective temperature and shows interesting and significant differences in structure and energy transport between static 1D modelling and the dynamic 3D counterpart.

At present, there exist 3D models for only a short sequence in effective temperature, $T_{eff} = 4500 - 3800K$, but surface gravity and metallicity also have a strong influence on the atmosphere. In order to understand the effect of these parameters, future work should explore this parameter space. Considering only cool and ultracool dwarfs will naturally restrict the surface gravity to a relatively narrow range, but the longevity of these stars and brown dwarfs means that the metallicity range will be rather wide. A similar parameter space exploration has been carried out for hotter models (Magic et al. 2013) leading to the identification of trends in the entropy, granule size, root mean square intensity fluctuations and vertical mixing velocity. Further to this, the implementation of the new equation-of-state and opacity suite allows the effective temperature sequence to be extended significantly, from $\sim 3800K$ down as far as $\sim 1200K$ without further modification. This range is appropriate for studying M, L and T dwarfs as well as the transitions in between and will be particularly interesting around $\sim 1600K$ where the transition occurs.

In addition, the PHOENIX-ACES equation-of-state and opacity package is now implemented in the same hydrodynamical code as the MARCS-MHD, meaning that for the first time a direct comparison of the results obtained with the two equations-of-state and opacities can be made. By comparing these results to observations, a detailed study may be able to discriminate between different opacity calculations or measurements. Many astrophysical opacities are highly uncertain, some by more than an order of magnitude and detailed comparisons between observed and synthetic spectra, with differing absorption coefficients derived from different sources, would provide a strong test as to the preferred values.

9.1.1 Spectra of $< 3D >$ models

The radiation field emitted by a gas depends sensitively on a number of physical properties, most prominently the gas temperature, pressure, the chemical composition of the gas and the velocity fields present. These properties combine to govern the shapes and depths of both absorption and emission lines, as well as governing the formation of the continuum. Spectral lines can therefore be used to determine stellar parameters (e.g. Barklem et al. 2000) or chemical composition of an object (e.g. Asplund et al. 2009). The velocity fields present may be investigated via spectral line bisectors. Under the assumption of mixing-length theory, spectral line profiles would be perfectly symmetric and therefore the bisectors straight lines. Observationally, line profiles show both C-like profiles and inverse C-profiles (e.g. Ramírez et al. 2009), which can be reproduced by 3D hydrodynamic models without invoking the free parameters of micro- and macro-turbulence (Asplund et al. 2000). Several studies have used line bisectors to probe the velocity fields in cool star atmospheres (e.g. Dravins & Nordlund 1990; Asplund et al. 2000; Allende Prieto et al. 2002; Ramírez et al. 2009), although as yet these studies have not been applied to M stars or cooler. A detailed understanding of velocity fields and mixing in these objects is critical to understanding their structure and chemistry. Arguably this becomes even more pronounced in the coolest objects where velocity fields and mixing operate on dust clouds, whose formation, location, thickness and composition is determined by these processes.

At present the hydrodynamics code employs the multi-group binning method to approximate the strong frequency dependence of the opacities. By sorting the millions of spectral lines into a small number of bins the computational load is drastically reduced, although this does place limits on the accuracy of the atmospheric structure and under this assumption the effects of velocity fields cannot be included (e.g. Vögler 2004; Hayek 2010). Opacity sampling is the current state-of-the-art for 1D models (Gustafsson et al. 2008). It samples the wavelength range in a statistical manner to capture the essence of the spectral shape, but requires sampling at $\sim 10^5$ wavelengths, meaning it is hugely more computationally expensive. The rapidly increasing performance of large-scale massively-parallel supercomputers means that while not yet quite feasible, in the next few years this will become realistic.

The accuracy of the radiative transfer in these models continues to be limited by the assumption of local thermodynamic equilibrium (LTE). Analyses of non-LTE effects on 1D hydrostatic stratifications (Anderson 1989; Short & Hauschildt 2005) suggest that over-ionisation of the iron-group elements with respect to Saha equilibrium strongly affects the atmosphere leading to higher temperatures above the surface. Implementing the consistent atomic models necessary to study departures from LTE in 3D radiative hydrodynamic simulations will be extremely challenging as the strong coupling between the atmospheric structure, the radiation field and the state of the atomic model will be difficult to handle in multiple dimensions, even if the analysis is restricted to only the most important elements and transitions, although Leenaarts & Wedemeyer-Böhm (2006) and Leenaarts et al. (2007) published the first efforts to treat hydrogen ionisation for the Sun.

A more tractable approach to non-equilibrium effects is to decouple them from the dynamical model and study instead the detailed non-equilibrium line formation using a post-processing spectral synthesis code on the mean stratification from the 3D radiative hydrodynamical models (Bergemann et al. 2012b)

9.1.2 Magnetic fields

Magnetic fields have not been considered in this work but can play a significant role in determining the atmospheric structure, cool star spots being perhaps the most apparent example. In solar-like stars magnetic fields are typically weak and they can be neglected even for the Sun (Asplund et al. 2009; Hayek 2010). M dwarfs are thought to be more magnetically active and so future work exploring the differences that occur when magnetic fields are considered would be important. In general, though, magnetic fields are far more significant in the chromospheres and coronas, where they are included even in solar models (Pereira et al. 2013). Ultimately, moving to cooler effective temperatures leads to increasingly neutral atmospheres, suggesting that the influences of magnetic fields will wane for L and T spectral types and can be safely neglected. Current work (Thaler priv. comm) is focused on the effect of magnetic fields in 3D on the Sun, which provides a strong and detailed test of the code and models.

9.1.3 Abundance

The formation of spectral lines in stars is dependent on the chemical composition of the atmosphere. Spectral synthesis may be used to facilitate comparison with observed spectra in order to determine the chemical composition of the object. Reanalysis of the abundances in the Sun with 3D radiative hydrodynamic models instead of 1D hydrostatic, led to the revision of the solar abundances (Asplund et al. 2005). The downward revision of the solar abundances was partly due to 3D effects and partly due to non-LTE effects. This has particular relevance to ultracool dwarfs as abundance analysis could be used to determine the object formation mechanism, giving an easier, but more importantly observable and non-degenerate way to assign planet or brown dwarf status to an object. The current IAU definition of a planet states that it must orbit the parent star, have achieved hydrostatic equilibrium and have cleared the neighbourhood around its orbit, but this definition fails to account for brown dwarfs captured by a planetary system, is ambiguous about very low mass binaries and planets ejected from their host system would not be classified correctly.

9.2 Dust

The mixing mechanism that operates in these atmospheres is of principal interest. Current models adopt a number of assumptions, most commonly convective overshooting, but it is unclear whether this would be strong enough (Tsuji et al. 1996a). Mixing by radiative diffusion is very week (Ackerman & Marley 2001), but gravity waves that can only be considered in multi-dimensional models may provide a solution (Freytag et al. 2010). Determination of the mixing mechanisms that operate and their relative importance would be a significant step towards understanding these objects.

The mixing mechanism strongly affects the grain sizes produced in these models. At present, the dust grain sizes span around four orders of magnitude from $0.01\mu m$(Tsuji et al. 1996a) to $300\mu m$ (Cooper et al. 2003). Dust sizes in these atmospheres are important as small dust particles remain suspended in the atmosphere over long timescales, while large, heavy particles rain-out quickly, requiring further strong convection for dust to remain in the atmosphere, as is observed for L dwarfs (e.g. Kirkpatrick 2005). In addition, dust sizes influence the opacity behaviour. Small grains $\sim 0.01\mu m$ have opacities

which are almost size independent, while for large grains the opacities strongly depend on the dust size. Dust size, through the dust opacity, will directly affect the resultant spectrum, so in addition to exploring the emergent dust sizes, an investigation comparing the synthetic spectra with observed spectra would be interesting and be a strong test of the validity of the simulations.

Another impact of dust grain size would be that if the opacities were large, this could set up strong feedback, heating the atmosphere and creating a stronger temperature gradients, which might lead to the development of a secondary convection zone. The coupling in this system is such that convection would lead to the dust grain being sustained in the upper atmosphere for longer, and having the opportunity to grow still further. This could represent the physical mechanism for a sudden increase in dust growth efficiency necessary for explaining the rapid transition from L to T dwarfs.

Cloud inhomogeneity, or indeed incomplete dust cloud coverage is a natural result from these hydrodynamical models, providing a direct testing of this as the mechanism behind the L-T transition. Holes in the cloud deck are not strictly necessary for strong inhomogeneity, any relatively large scale variation in the cloud thickness would break the azimuthal symmetry of the atmosphere and be an explanation for the observed variability on rotational timescales (e.g. Radigan et al. 2012).

The current version of the dust formation model considers only a single dust species. In reality, the dust grains will constitute a dirty mantle composed of islands of pure dust accumulated on a nucleated seed particle. The single dust species results will yield the correct dust number density, but neglecting the agglomeration of other species onto this particle will result in only a lower estimate for the dust grain size. Care has been taken to allow the quick and simple extension to considering additional dust species. Expanding the network of dust species requires only the inclusion of the formation reactions in the chemical network and accounting for the element consumption in the appropriate element conservation equation. It should be noted that the computational effort for this, in terms of 3D datacubes, scales only as the number of elements involved in dust formation, not by the number of dust species, meaning many species can be efficiently modelled. The extension to dirty grains would increase the grain size of the dust and consequently strongly affect the dust opacity.

The dust opacity is currently modelled using Mie theory of spherical dust grains, Dirty dust grains will consist of a composite material and thus require Effective Medium theory in order to derive mean material properties to give an extinction coefficient appropriate for the amalgam. This is a simplification as the true extinction coefficient will depend on the shape of the grain and the distribution of pure material islands making up the grain. As the grain shape is uncertain, with some studies suggesting that grains may be elliptical, the assumption of the simplest shape is not particularly critical, but in more detailed future models it must be kept in mind.

Th current chemical equilibrium network is relatively small, considering only $\sim$ 50 of the most important gaseous species. It has the distinct advantage of very rapid convergence and high accuracy, deviating from the large chemical network with stronger convergence criteria by less that 5%. However, in the longer term, as more dust species are considered, it is important that chemical equilibrium network for the gas expands appropriately to ensure the correct abundances of molecules that participate in or block dust formation.

While the atmospheres of L and T dwarfs are increasingly neutral, as lower temperatures result in a lesser degree of ionisation, dust forms in these atmospheres and dust particles acquire charge easily on relative small scales. Charged processes have already been considered in this context (Helling et al. 2011b,a, 2013; Stark et al. 2013) and dust clouds in brown dwarf atmospheres could easily charge

enough to create lightning. As on Earth, the charging depends on the mixing in the atmosphere and would operate on a similar scale to the convective cells on the surface of the stars. As a long-term project , this would be a fascinating avenue to explore.

9.3 Longer term

In seeking to model the transition from stars to planets, the consideration of irradiation becomes important. Not considered in the current 3D model, irradiation from a binary companion or a parent star would significantly alter the chemistry and atmospheric structure. Irradiation breaks the azimuthal symmetry by illuminating one hemisphere of the object, while the other side is in shadow. The scale of this asymmetry is global, requiring global models (Showman et al. 2009) as the incident radiation affects the photochemistry of the atmosphere and heats the day-side, setting up thermal gradients that lead to strong winds. Such considerations are far beyond current capabilities and are more akin to the global models of supergiants (Chiavassa et al. 2013).

Likewise rotation operates on a global scale and could affect the convection pattern. Unlike irradiation, this is unlikely to be a major effect as the Rossby numbers, ratio of inertial to Coriolis force, for these atmospheres are large meaning that box-in-a-star models are justified and that rotation may be superimposed post-processing as it little affects the dynamics.

9.4 Summary

In conclusion, 3D radiative hydrodynamic models of stellar atmospheres are here to stay. The accelerating performance of computers and access to massively parallel clusters creates a climate where models of increasing sophistication are possible. Observationally, the increasing wealth of photometry and spectra from these objects place tighter constraints on such models. The ultimate goal of this field is a complete understanding of the atmospheres of cool objects spanning the star to planet divide. The complexity of the inherent physical processes and the strong coupling between them mean that 3D atmosphere modelling is the best chance for progress.

Bibliography

Ackerman, A. S. & Marley, M. S. 2001, ApJ, 556, 872

Allard, F., Guillot, T., Ludwig, H.-G., et al. 2003, in IAU Symposium, Vol. 211, Brown Dwarfs, ed. E. Martín, 325

Allard, F. & Hauschildt, P. H. 1995, ApJ, 445, 433

Allard, F., Hauschildt, P. H., Alexander, D. R., & Starrfield, S. 1997, ARA&A, 35, 137

Allard, F., Hauschildt, P. H., Alexander, D. R., Tamanai, A., & Schweitzer, A. 2001, ApJ, 556, 357

Allende Prieto, C., Asplund, M., García López, R. J., & Lambert, D. L. 2002, ApJ, 567, 544

Allende Prieto, C., Koesterke, L., Ramírez, I., Ludwig, H.-G., & Asplund, M. 2009, Mem. Soc. Astron. Italiana, 80, 622

Anderson, L. S. 1989, ApJ, 339, 558

Apai, D., Buenzli, E., Flateau, D., et al. 2012, Spitzer Proposal, 90063

Artigau, É., Bouchard, S., Doyon, R., & Lafrenière, D. 2009, ApJ, 701, 1534

Asplund, M. 2005, ARA&A, 43, 481

Asplund, M., Grevesse, N., & Sauval, A. J. 2005, in Astronomical Society of the Pacific Conference Series, Vol. 336, Cosmic Abundances as Records of Stellar Evolution and Nucleosynthesis, ed. T. G. Barnes, III & F. N. Bash, 25

Asplund, M., Grevesse, N., Sauval, A. J., & Scott, P. 2009, ARA&A, 47, 481

Asplund, M., Nordlund, Å., Trampedach, R., Allende Prieto, C., & Stein, R. F. 2000, A&A, 359, 729

Bailer-Jones, C. A. L. & Mundt, R. 2001, A&A, 367, 218

Barklem, P. S., Piskunov, N., & O'Mara, B. J. 2000, A&A, 363, 1091

Barklem, P. S., Stempels, H. C., Allende Prieto, C., et al. 2002, A&A, 385, 951

Barman, T. in prep.

Basri, G. 2000, ARA&A, 38, 485

Bastian, N., Covey, K. R., & Meyer, M. R. 2010, ARA&A, 48, 339

Behara, N. T., Bonifacio, P., Ludwig, H.-G., et al. 2010, A&A, 513, A72

Béjar, V. J. S., Martín, E. L., Zapatero Osorio, M. R., et al. 2001, ApJ, 556, 830

Bergemann, M. & Cescutti, G. 2010, A&A, 522, A9

Bergemann, M. & Gehren, T. 2008, A&A, 492, 823

Bergemann, M., Kudritzki, R.-P., Plez, B., et al. 2012a, ApJ, 751, 156

Bergemann, M., Lind, K., Collet, R., & Asplund, M. 2011, Journal of Physics Conference Series, 328, 012002

Bergemann, M., Lind, K., Collet, R., Magic, Z., & Asplund, M. 2012b, MNRAS, 427, 27

Bergemann, M., Pickering, J. C., & Gehren, T. 2010, MNRAS, 401, 1334

Berrington, K. 1995, in Astronomical Society of the Pacific Conference Series, Vol. 78, Astrophysical Applications of Powerful New Databases, ed. S. J. Adelman & W. L. Wiese, 19

Biermann, L. 1932, ZAp, 5, 117

Blum, J. & Wurm, G. 2008, ARA&A, 46, 21

Böhm, K.-H. 1954, ZAp, 34, 182

Böhm-Vitense, E. 1958, ZAp, 46, 108

Brandenburg, A. 2003, Computational aspects of astrophysical MHD and turbulence, ed. K. Zhang, A. Soward, & C. Jones, 269–344

Burgasser, A. J., Geballe, T. R., Golimowski, D. A., et al. 2003, in IAU Symposium, Vol. 211, Brown Dwarfs, ed. E. Martín, 377

Burgasser, A. J., Kirkpatrick, J. D., Brown, M. E., et al. 2002a, ApJ, 564, 421

Burgasser, A. J., Marley, M. S., Ackerman, A. S., et al. 2002b, ApJ, 571, L151

Burrows, A., Heng, K., & Nampaisarn, T. 2011, ApJ, 736, 47

Burrows, A., Hubbard, W. B., Lunine, J. I., & Liebert, J. 2001, Reviews of Modern Physics, 73, 719

Burrows, A., Marley, M., Hubbard, W. B., et al. 1997, ApJ, 491, 856

Burrows, A. & Sharp, C. M. 1999, ApJ, 512, 843

Burrows, A., Sudarsky, D., & Hubeny, I. 2006, ApJ, 640, 1063

Cadle, R. D. & Grams, G. W. 1975, Reviews of Geophysics and Space Physics, 13, 475

Castelli, F., Gratton, R. G., & Kurucz, R. L. 1997, A&A, 318, 841

Castelli, F. & Kurucz, R. L. 2004, ArXiv Astrophysics e-prints

Cauble, R., Perry, T. S., Bach, D. R., et al. 1998, Physical Review Letters, 80, 1248

Chabrier, G., Baraffe, I., Allard, F., & Hauschildt, P. 2000, ApJ, 542, 464

Chabrier, G., Baraffe, I., Allard, F., & Hauschildt, P. H. 2005, ArXiv Astrophysics e-prints

Chandrasekhar, S. 1935, MNRAS, 96, 21

Cherchneff, I. & Dwek, E. 2010, ApJ, 713, 1

Chiavassa, A., Bigot, L., Kervella, P., et al. 2012, A&A, 540, A5

Chiavassa, A., Freytag, B., & Plez, B. 2013, in EAS Publications Series, Vol. 60, EAS Publications Series, ed. P. Kervella, T. Le Bertre, & G. Perrin, 145–153

Chiavassa, A., Pasquato, E., Jorissen, A., et al. 2011, A&A, 528, A120

Clarke, F. J., Hodgkin, S. T., Oppenheimer, B. R., Robertson, J., & Haubois, X. 2008, MNRAS, 386, 2009

Collet, R., Asplund, M., & Trampedach, R. 2007, A&A, 469, 687

Collet, R., Hayek, W., & Asplund, M. 2011a, in Astronomical Society of the Pacific Conference Series, Vol. 448, 16th Cambridge Workshop on Cool Stars, Stellar Systems, and the Sun, ed. C. Johns-Krull, M. K. Browning, & A. A. West, 819

Collet, R., Hayek, W., Asplund, M., et al. 2011b, A&A, 528, A32

Cooper, C. S., Sudarsky, D., Milsom, J. A., Lunine, J. I., & Burrows, A. 2003, ApJ, 586, 1320

Dehn, M. 2007, PhD thesis, Universitaet Hamburg, Hamburg, Germany

Di Mauro, M. P., Christensen-Dalsgaard, J., Rabello-Soares, M. C., & Basu, S. 2002, A&A, 384, 666

Dravins, D. 2008, A&A, 492, 199

Dravins, D. & Nordlund, A. 1990, A&A, 228, 203

Dumusque, X., Santos, N. C., Udry, S., Lovis, C., & Bonfils, X. 2011a, in IAU Symposium, Vol. 276, IAU Symposium, ed. A. Sozzetti, M. G. Lattanzi, & A. P. Boss, 527–529

Dumusque, X., Udry, S., Lovis, C., Santos, N. C., & Monteiro, M. J. P. F. G. 2011b, A&A, 525, A140

Enoch, M. L., Brown, M. E., & Burgasser, A. J. 2003, AJ, 126, 1006

ESA. 1997, VizieR Online Data Catalog, 1239, 0

Faherty, J. K., Burgasser, A. J., Walter, F. M., et al. 2012, ApJ, 752, 56

Fegley, Jr., B. & Lodders, K. 1994, Icarus, 110, 117

Fegley, Jr., B. & Lodders, K. 1996, ApJ, 472, L37

Ferguson, J. W., Alexander, D. R., Allard, F., et al. 2005, ApJ, 623, 585

Freytag, B., Allard, F., Ludwig, H.-G., Homeier, D., & Steffen, M. 2010, A&A, 513, A19

Freytag, B., Steffen, M., & Dorch, B. 2002, Astronomische Nachrichten, 323, 213

Fuhrmann, K., Axer, M., & Gehren, T. 1993, A&A, 271, 451

Gail, H.-P., Keller, R., & Sedlmayr, E. 1984, A&A, 133, 320

Gail, H.-P. & Sedlmayr, E. 1988, A&A, 206, 153

Gauger, A., Sedlmayr, E., & Gail, H.-P. 1990, A&A, 235, 345

Geballe, T. R., Knapp, G. R., Leggett, S. K., et al. 2002, ApJ, 564, 466

Gelino, C. R., Marley, M. S., Holtzman, J. A., Ackerman, A. S., & Lodders, K. 2002, ApJ, 577, 433

Goldman, B., Bouy, H., Zapatero Osorio, M. R., et al. 2008, A&A, 490, 763

Golimowski, D. A., Leggett, S. K., Marley, M. S., et al. 2004, AJ, 127, 3516

Gray, D. F. 2005, The Observation and Analysis of Stellar Photospheres

Gudiksen, B. V., Carlsson, M., Hansteen, V. H., et al. 2011, A&A, 531, A154

Gustafsson, B., Bell, R. A., Eriksson, K., & Nordlund, A. 1975, A&A, 42, 407

Gustafsson, B., Edvardsson, B., Eriksson, K., et al. 2008, A&A, 486, 951

Hauschildt, P. H., Allard, F., Ferguson, J., Baron, E., & Alexander, D. R. 1999, ApJ, 525, 871

Hayashi, C. 1961, PASJ, 13, 450

Hayashi, C. & Nakano, T. 1963, Progress of Theoretical Physics, 30, 460

Hayek, W., Asplund, M., Carlsson, M., et al. 2010, A&A, 517, A49

Hayek, W. S. 2010, PhD thesis, Australian National University, Canberra, Australia

Helling, C., Jardine, M., & Mokler, F. 2011a, ApJ, 737, 38

Helling, C., Jardine, M., Stark, C., & Diver, D. 2013, ApJ, 767, 136

Helling, C., Jardine, M., Witte, S., & Diver, D. A. 2011b, ApJ, 727, 4

Helling, C., Oevermann, M., Lüttke, M. J. H., Klein, R., & Sedlmayr, E. 2001, A&A, 376, 194

Helling, C. & Woitke, P. 2006, A&A, 455, 325

Helling, C., Woitke, P., & Thi, W.-F. 2008, A&A, 485, 547

Höfner, S., Gautschy-Loidl, R., Aringer, B., & Jørgensen, U. G. 2003, A&A, 399, 589

Hubeny, I. 1988, Computer Physics Communications, 52, 103

Hubeny, I. & Lanz, T. 1995, ApJ, 439, 875

Hummer, D. G. & Mihalas, D. 1988, ApJ, 331, 794

Husser, T.-O., Wende-von Berg, S., Dreizler, S., et al. 2013, A&A, 553, A6

Hyman, J. M. 1979, in Advances in Computer Methods for Partial Differential Equations - III, 313–321

Iglesias, C. A. & Rogers, F. J. 1996, ApJ, 464, 943

Jeans, J. H. 1902, Royal Society of London Philosophical Transactions Series A, 199, 1

Jeong, K. S., Chang, C., Patzer, A. B. C., Sedlmayr, E., & Sülzle, D. 2000, in Astronomische Gesellschaft Meeting Abstracts, Vol. 17, Astronomische Gesellschaft Meeting Abstracts, ed. R. E. Schielicke, 29

Johnson, J. A., Winn, J. N., Albrecht, S., et al. 2009, PASP, 121, 1104

Jones, H. P. 1989, Sol. Phys., 120, 211

Jones, H. R. A. & Tsuji, T. 1997, ApJ, 480, L39

Jørgensen, U. G. 1997, in IAU Symposium, Vol. 178, IAU Symposium, ed. E. F. van Dishoeck, 441–456

Junge, C. E. 1963, J. Geophys. Res., 68, 3849

Kirkpatrick, J. D. 2005, ARA&A, 43, 195

Kirkpatrick, J. D., Allard, F., Bida, T., et al. 1999a, ApJ, 519, 834

Kirkpatrick, J. D., Henry, T. J., & McCarthy, Jr., D. W. 1991, ApJS, 77, 417

Kirkpatrick, J. D., Kelly, D. M., Rieke, G. H., et al. 1993, ApJ, 402, 643

Kirkpatrick, J. D., Reid, I. N., Liebert, J., et al. 1999b, ApJ, 519, 802

Knapp, G. R., Leggett, S. K., Fan, X., et al. 2004, AJ, 127, 3553

Koen, C. 2003, MNRAS, 346, 473

Koen, C. 2004, MNRAS, 354, 378

Koen, C. 2005, MNRAS, 360, 1132

Koen, C., Matsunaga, N., & Menzies, J. 2004, MNRAS, 354, 466

Koen, C., Tanabé, T., Tamura, M., & Kusakabe, N. 2005, MNRAS, 362, 727

Kumar, S. S. 1963a, ApJ, 137, 1126

Kumar, S. S. 1963b, ApJ, 137, 1121

Kurucz, R. 1993a, Atomic data for opacity calculations. Kurucz CD-ROM No. 1. Cambridge, Mass.: Smithsonian Astrophysical Observatory, 1993., 1

Kurucz, R. 1993b, Diatomic Molecular Data for Opacity Calculations. Kurucz CD-ROM No. 15. Cambridge, Mass.: Smithsonian Astrophysical Observatory, 1993., 15

Kurucz, R. 1993c, Opacities for Stellar Atmospheres: [+0.0],[+0.5],[+1.0]. Kurucz CD-ROM No. 2. Cambridge, Mass.: Smithsonian Astrophysical Observatory, 1993., 2

Kurucz, R. L. 1979, ApJS, 40, 1

Leenaarts, J., Carlsson, M., Hansteen, V., & Rutten, R. J. 2007, A&A, 473, 625

Leenaarts, J. & Wedemeyer-Böhm, S. 2006, A&A, 460, 301

Leggett, S. K., Golimowski, D. A., Fan, X., et al. 2002, ApJ, 564, 452

Leggett, S. K., Toomey, D. W., Geballe, T. R., & Brown, R. H. 1999, ApJ, 517, L139

Lodders, K. & Fegley, B. 2002, Icarus, 155, 393

Loidl, R., Höfner, S., Jørgensen, U. G., & Aringer, B. 1999, A&A, 342, 531

Ludwig, H.-G. 1992, PhD thesis, Universitaet Kiel, Germany

Ludwig, H.-G. 2006, A&A, 445, 661

Ludwig, H.-G., Allard, F., & Hauschildt, P. H. 2002, A&A, 395, 99

Ludwig, H.-G., Allard, F., & Hauschildt, P. H. 2006, A&A, 459, 599

Ludwig, H.-G., Jordan, S., & Steffen, M. 1994, A&A, 284, 105

Ludwig, H.-G. & Kučinskas, A. 2012, A&A, 547, A118

Lunine, J. I., Hubbard, W. B., Burrows, A., Wang, Y.-P., & Garlow, K. 1989, ApJ, 338, 314

Magic, Z., Collet, R., Asplund, M., et al. 2013, A&A, 557, A26

Marley, M. 2000, in Astronomical Society of the Pacific Conference Series, Vol. 212, From Giant Planets to Cool Stars, ed. C. A. Griffith & M. S. Marley, 152

Marley, M. S., Saumon, D., & Goldblatt, C. 2010, ApJ, 723, L117

Marley, M. S., Seager, S., Saumon, D., et al. 2002, ApJ, 568, 335

Mashonkina, L., Korn, A. J., & Przybilla, N. 2007, A&A, 461, 261

Mashonkina, L., Zhao, G., Gehren, T., et al. 2008, A&A, 478, 529

Mason, B. J. 1971, The Physics of Clouds (Monographs on Meterology

Mayor, M. & Queloz, D. 1995, Nature, 378, 355

Mihalas, D. 1967, ApJ, 149, 169

Mihalas, D. 1978, Stellar atmospheres /2nd edition/

Mihalas, D., Dappen, W., & Hummer, D. G. 1988, ApJ, 331, 815

Milne, E. A. 1921, MNRAS, 81, 361

Mohanty, S., Basri, G., Shu, F., Allard, F., & Chabrier, G. 2002, ApJ, 571, 469

Morales-Calderón, M., Stauffer, J. R., Kirkpatrick, J. D., et al. 2006, ApJ, 653, 1454

Muthsam, H. J., Kupka, F., Löw-Baselli, B., et al. 2010, New A, 15, 460

Nahar, S. N. 2004, Phys. Rev. A, 69, 042714

Nakajima, T., Oppenheimer, B. R., Kulkarni, S. R., et al. 1995, Nature, 378, 463

Nakajima, T., Tsuji, T., & Yanagisawa, K. 2004, ApJ, 607, 499

Nordlund, A. 1982, A&A, 107, 1

Nordlund, A. & Dravins, D. 1990, A&A, 228, 155

Nordlund, Å., Stein, R. F., & Asplund, M. 2009, Living Reviews in Solar Physics, 6, 2

Nozawa, T. & Kozasa, T. 2013, ArXiv e-prints

Oppenheimer, B. R., Kulkarni, S. R., Matthews, K., & van Kerkwijk, M. H. 1998, ApJ, 502, 932

Patzer, A. B. C., Gauger, A., & Sedlmayr, E. 1998, A&A, 337, 847

Pepe, F. A. & Lovis, C. 2008, Physica Scripta Volume T, 130, 014007

Pereira, T. M. D., Asplund, M., Collet, R., et al. 2013, A&A, 554, A118

Pereira, T. M. D., Asplund, M., & Kiselman, D. 2009, Mem. Soc. Astron. Italiana, 80, 650

Peytremann, E. 1974, A&A, 33, 203

Radigan, J., Jayawardhana, R., Lafrenière, D., et al. 2012, ApJ, 750, 105

Ramírez, I., Allende Prieto, C., Koesterke, L., Lambert, D. L., & Asplund, M. 2009, A&A, 501, 1087

Rebolo, R., Zapatero Osorio, M. R., & Martín, E. L. 1995, Nature, 377, 129

Reid, I. N. & Cruz, K. L. 2002, AJ, 123, 466

Reiners, A., Homeier, D., Hauschildt, P. H., & Allard, F. 2007, A&A, 473, 245

Rosenthal, C. S., Christensen-Dalsgaard, J., Nordlund, Å., Stein, R. F., & Trampedach, R. 1999, A&A, 351, 689

Rossow, W. B. 1978, Icarus, 36, 1

Saumon, D. & Marley, M. S. 2008, ApJ, 689, 1327

Saumon, D., Marley, M. S., Lodders, K., & Freedman, R. S. 2003, in IAU Symposium, Vol. 211, Brown Dwarfs, ed. E. Martín, 345

Schaaf. 1963, Taschenbuch der Physik

Seaton, M. J. 1995, The opacity project

Short, C. I. & Hauschildt, P. H. 2005, ApJ, 618, 926

Showman, A. P., Fortney, J. J., Lian, Y., et al. 2009, ApJ, 699, 564

Skartlien, R. 2000, ApJ, 536, 465

Smalley, B. & Kupka, F. 2003, in IAU Symposium, Vol. 210, Modelling of Stellar Atmospheres, ed. N. Piskunov, W. W. Weiss, & D. F. Gray, 10P

Smith, W. & Missen, R. 1982, Chemical reaction equilibrium analysis: theory and algorithms

Stark, C. R., Helling, C., Diver, D. A., & Rimmer, P. B. 2013, ApJ, 776, 11

Steffen, M. & Freytag, B. 1995, Chaos Solitons and Fractals, 5, 1965

Steffen, M., Ludwig, H.-G., & Kruess, A. 1989, A&A, 213, 371

Stein, R. F. & Nordlund, A. 1998, ApJ, 499, 914

Stempels, H. C., Piskunov, N., & Barklem, P. S. 2001, in Astronomical Society of the Pacific Conference Series, Vol. 223, 11th Cambridge Workshop on Cool Stars, Stellar Systems and the Sun, ed. R. J. Garcia Lopez, R. Rebolo, & M. R. Zapaterio Osorio, 878

Stephens, D. C., Leggett, S. K., Cushing, M. C., et al. 2009, ApJ, 702, 154

Strom, S. E. & Kurucz, R. 1966, AJ, 71, 181

Trampedach, R., Asplund, M., Collet, R., Nordlund, Å., & Stein, R. F. 2013, ApJ, 769, 18

Trampedach, R., Däppen, W., & Baturin, V. A. 2006, ApJ, 646, 560

Troyer, J., Moses, J. I., Fegley, B., et al. 2007, in Bulletin of the American Astronomical Society, Vol. 39, AAS/Division for Planetary Sciences Meeting Abstracts #39, 450

Tsuji, T. 2002, ApJ, 575, 264

Tsuji, T. 2005a, ApJ, 621, 1033

Tsuji, T. 2005b, in ESA Special Publication, Vol. 560, 13th Cambridge Workshop on Cool Stars, Stellar Systems and the Sun, ed. F. Favata, G. A. J. Hussain, & B. Battrick, 1001

Tsuji, T. & Nakajima, T. 2003, ApJ, 585, L151

Tsuji, T., Nakajima, T., & Yanagisawa, K. 2004, ApJ, 607, 511

Tsuji, T., Ohnaka, K., & Aoki, W. 1996a, A&A, 305, L1

Tsuji, T., Ohnaka, K., & Aoki, W. 1999, ApJ, 520, L119

Tsuji, T., Ohnaka, K., Aoki, W., & Nakajima, T. 1996b, A&A, 308, L29

Uitenbroek, H. 2003, ApJ, 592, 1225

van Altena, W. F., Lee, J. T., & Hoffleit, D. 1995, VizieR Online Data Catalog, 1174, 0

Visscher, C., Lodders, K., & Fegley, Jr., B. 2006, ApJ, 648, 1181

Visscher, C., Lodders, K., & Fegley, Jr., B. 2010, ApJ, 716, 1060

Vögler, A. 2004, A&A, 421, 755

Vögler, A., Bruls, J. H. M. J., & Schüssler, M. 2004, A&A, 421, 741

Vögler, A., Shelyag, S., Schüssler, M., et al. 2005, A&A, 429, 335

Vrba, F. J., Henden, A. A., Luginbuhl, C. B., et al. 2004, AJ, 127, 2948

Whitworth, A. P. & Stamatellos, D. 2006, A&A, 458, 817

Williamson, J. H. 1980, Journal of Computational Physics, 35, 48

Witte, S. 2011, PhD thesis, Universitaet Hamburg, Hamburg, Germany

Witte, S., Helling, C., & Hauschildt, P. H. 2009, A&A, 506, 1367

Woitke, P. & Helling, C. 2003, A&A, 399, 297

Woitke, P. & Helling, C. 2004, A&A, 414, 335

Wuchterl, G. 2004, in IAU Symposium, Vol. 202, Planetary Systems in the Universe, ed. A. Penny, 167

Yanny, B., Rockosi, C., Newberg, H. J., et al. 2009, AJ, 137, 4377

Zapatero Osorio, M. R., Martín, E. L., Béjar, V. J. S., et al. 2007, ApJ, 666, 1205